

MECHANICS AND STRUCTURE OF DISLOCATIONS INDUCED
BY THERMAL MISMATCH IN COMPOSITE MATERIALS

by

DAVID CHRISTOPHE DUNAND

Diplomierter Werkstoffingenieur ETHZ (1986)

Submitted to the Department of
Materials Science and Engineering
in Partial Fulfillment of the Requirements for the Degree of

DOCTOR OF PHILOSOPHY IN METALLURGY

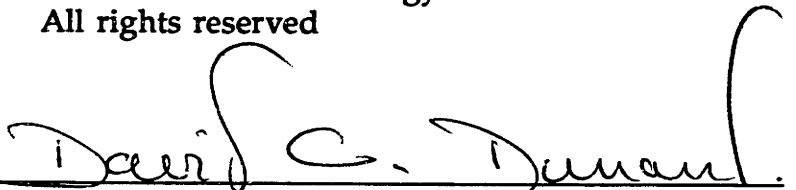
at the

MASSACHUSETTS INSTITUTE OF TECHNOLOGY

February 1991

© Massachusetts Institute of Technology 1991
All rights reserved

Signature of Author



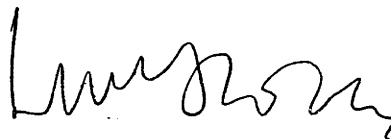
Department of Materials Science and Engineering
January 11, 1991

Certified by



Andreas Mortensen
Thesis Supervisor

Accepted by



Linn W. Hobbs
Chairman, Departmental Committee on Graduate Students

MASSACHUSETTS INSTITUTE
OF TECHNOLOGY

MAR 08 1991

LIBRARIES

ARCHIVES

MECHANICS AND STRUCTURE OF DISLOCATIONS INDUCED BY THERMAL MISMATCH IN COMPOSITE MATERIALS

by

DAVID CHRISTOPHE DUNAND

Submitted to the Department of Materials Science and Engineering on
January 11, 1991 in partial fulfilment of the requirements for the degree of
Doctor of Philosophy in Metallurgy.

ABSTRACT

Cast silver chloride containing alumina or glass spheres, particles or fibers is used as a model material for metal matrix composites to study thermally induced plasticity around large inclusions. Matrix dislocations, resulting from the thermal mismatch between reinforcement and matrix upon quenching of the composite, are decorated at room temperature in the bulk through photodissociation of the matrix and observed by optical microscopy. The plastic zone is found to take the form of (i) a deformed region surrounding the inclusion and containing a high density of dislocation tangles, (ii) rows of prismatic, interstitial dislocation loops punched into the matrix and extending at a large distance from the interface. From the number of loops punched by spheres and that punched radially by fibers, the highest temperature at which slip is operative is found to be 400 ± 30 K. The residual elastic stress in the plastic zone around fibers is determined from the radius of curvature of pinned dislocations, leading to the conclusion that the matrix is strain-hardened. Using these two results, a simple model is proposed to predict the radius of the plastic zone around mismatching inclusions embedded in a strain-hardening matrix. The model matches well the experimental data for spheres, particles and fibers.

Another model predicting the number of loops punched at fiber ends is developed. The longitudinal stress in the fiber is derived for a plastic and elastic interface for which the shear-lag theory is used. There is a maximum fiber length above which the number of punched loops is constant because the central part of the fiber is strained by elasto-plastic interfacial shear until it exhibits no mismatch with the matrix. The backstress of the loops on the fiber is derived and the effect of the fiber stress field on the loop arrangement in the row is estimated. The length of the row is calculated from the number of loops and predictions of the above model are found to match satisfactorily the experimental data, as does another existing model based on a mismatching ellipsoid. Finally, the geometry of dislocations punched by a mismatching fiber is discussed based on microstructural observations for the case where the fiber axis does not correspond to the glide direction.

Thesis Supervisor: Dr. Andreas Mortensen.

Title: ALCOA Associate Professor of Metallurgy.

TABLE OF CONTENTS

| | |
|--|----|
| ABSTRACT | 2 |
| TABLE OF CONTENTS | 3 |
| LIST OF ILLUSTRATIONS AND FIGURES | 6 |
| LIST OF TABLES | 12 |
| ACKNOWLEDGEMENTS | 13 |
| 1. INTRODUCTION | 15 |
| 2. LITERATURE SURVEY | 18 |
| 2.1 Dislocations in metal matrix composites | 18 |
| 2.1.1 Observation of dislocations | 18 |
| 2.1.2 Modelling of dislocation structure | 24 |
| 2.2 Selected properties of silver halides | 26 |
| 2.2.1 Physical properties | 27 |
| 2.2.2 Mechanical properties | 29 |
| 2.3 Observation of dislocations in silver halides | 30 |
| 2.3.1 Decoration and optical microscopy | 31 |
| 2.3.2 Indirect methods | 36 |
| 2.4 Observation of stresses in silver halides | 38 |
| 2.5 Conclusions of literature survey | 40 |
| 3. THEORY | 42 |
| 3.1 Plastic zone size around a sphere and an infinite cylinder | 42 |
| 3.2 Plastic zone size around a particle of irregular form | 50 |
| 3.3 Micromechanics of a row of punched prismatic loops | 54 |
| 3.3.1 Row relaxed configuration | 54 |
| 3.3.2 Row backstress on an inclusion | 61 |
| 3.4 Longitudinal emission of loops at fiber end | 64 |

| | |
|--|-----|
| 3.4.1 Elastic interface | 66 |
| 3.4.2 Plastic-elastic interface | 69 |
| 3.4.3 Plastic-elastic-unstrained interface | 74 |
| 3.4.4 Effect of fiber residual stresses on punching distance | 76 |
| 3.4.5 Parametric study and discussion of model | 80 |
| 3.5 Figures | 89 |
| 4. EXPERIMENTAL PROCEDURES | 113 |
| 4.1 Sample preparation for decoration experiments | 115 |
| 4.2 Other experiments pertaining to silver chloride decoration | 120 |
| 4.3 Sample preparation for photoelastic experiments | 123 |
| 4.4 Figures | 125 |
| 5. RESULTS | 128 |
| 5.1 Dislocation microstructure and micromechanics | 129 |
| 5.1.1 Spherical inclusions | 130 |
| 5.1.2 Particulate inclusions | 131 |
| 5.1.3 Fibrous inclusions | 132 |
| 5.2 Photoelasticity | 136 |
| 5.3 Figures | 137 |
| 6. DISCUSSION | 159 |
| 6.1 Dislocation microstructure | 159 |
| 6.1.1 Spherical inclusions | 160 |
| 6.1.2 Particulate inclusions | 162 |
| 6.1.3 Fibrous inclusions | 165 |
| 6.1.3.1 Punching by fiber ends | 166 |
| a. Fiber axis parallel to punching direction | 166 |
| b. Fiber axis not parallel to punching direction | 168 |
| c. Punching of pairs of rows | 171 |

| | |
|---|-----|
| 6.1.3.2 Punching by fiber sides | 173 |
| 6.2 Dislocation micromechanics | 176 |
| 6.2.1 Spherical inclusions | 176 |
| 6.2.1.1 Determination of ΔT | 176 |
| 6.2.1.2 Plastic zone size | 178 |
| 6.2.2 Particulate Inclusions | 178 |
| 6.2.3 Fibrous Inclusions | 179 |
| 6.2.3.1 Flow stress of the dislocations | 179 |
| 6.2.3.2 Plastic zone size | 181 |
| 6.2.3.3 Punching distance | 182 |
| 6.2.3.4 Number of side-punched dislocations | 187 |
| 6.3 Photoelasticity | 189 |
| 6.4 Figures | 192 |
| 7. CONCLUSIONS | 197 |
| 8. SUGGESTIONS FOR FUTURE WORK | 199 |
| 8.1 Decoration experiments | 199 |
| 8.2 Photoelastic experiments | 200 |
| APPENDIX 1 | 202 |
| APPENDIX 2 | 207 |
| APPENDIX 3 | 215 |
| APPENDIX 4 | 217 |
| APPENDIX 5 | 222 |
| APPENDIX 6 | 227 |
| BIBLIOGRAPHY | 231 |

LIST OF ILLUSTRATIONS AND FIGURES

| | | |
|--------------|--|----|
| Figure 3.1.1 | Fictitious hole expanded from zero radius to radius a producing a plastic zone of radius c and a matrix displacement of Δr at the surface of the inclusion of radius r . | 89 |
| Figure 3.1.2 | Schematic of prismatic dislocation loops punched in the $\langle 110 \rangle$ directions of a f.c.c. lattice from a cylinder. | 90 |
| Figure 3.1.3 | Schematic of prismatic dislocation loops punched in the $\langle 110 \rangle$ directions of a f.c.c. lattice from a sphere. | 91 |
| Figure 3.1.4 | Plastic zone radius around a SiC cylinder (c) and sphere (s) in a 99.5 % aluminium matrix after a temperature change of 200 K. | 92 |
| Figure 3.2.1 | Schematic drawing of a particle and its projection with relevant variables. | 93 |
| Figure 3.3.1 | Steady-state configuration of a moving row of n bodies, each submitted to a friction force. | 94 |
| Figure 3.3.2 | Equivalent configuration of a row of n circular, prismatic loops repelling each other in a lattice with a non-zero friction stress. The first loop is blocked. | 94 |
| Figure 3.3.3 | Dimensionless distance from the origin for a row of 100 loops for two values of v , as calculated from Eq. [3.3.9] and as computed. | 95 |
| Figure 3.3.4 | Dimensionless minimum spacing between two loops (first two loops) as a function of the number of loops in the row | 96 |
| Figure 3.3.5 | Dimensionless length of a row as a function of the number of loops for different values of v . | 97 |
| Figure 3.3.6 | Plot of parameters A'' and v , Eq. [3.3.11]. | 98 |

| | | |
|-----------------|--|-----|
| Figure 3.3.7 | Dimensionless maximum spacing between two loops (two last loops) as a function of v . | 99 |
| Figure 3.3.8 | Configuration of two rows of prismatic loops of opposite Burgers' vector, located symmetrically on each side of the origin. The first loop of each rows is blocked. | 100 |
| Figure 3.3.9 | Relative difference in loop spacings between the undisturbed row (Fig. 3.3.2) and the corresponding disturbed row | 101 |
| Figure 3.3.10 | Particle with "greased" interface pushing a row of loops against the loop friction stress. | 102 |
| Figs. 3.4.1a-c | Schematic diagrams for the interface displacement u , the interfacial shear stress t and the fiber longitudinal stress as a function of the distance x from the center of the fiber. (a) purely elastic interface, (b) plastic-elastic interface, (c) plastic-elastic-unstrained interface | 103 |
| Figs. 3.4.2 a&b | Schematic diagram of matrix with hole, fiber and matrix with fiber before (a) and after (b) the temperature change ΔT . | 104 |
| Figure 3.4.3 | Diagram for the interfacial shear stress for a fiber of length L in the plastic-elastic regime. | 105 |
| Figs. 3.4.4 a&b | Diagrams for the interfacial shear stress (a) and the fiber longitudinal stress (b) for three different fiber lengths L_p , L , L_u . | 106 |
| Figure 3.4.5a | Number of loops punched as a function of the fiber diameter d , all other parameters in Table 3.4 being constant. | 107 |
| Figure 3.4.5b | Number of loops punched as a function of the fiber length L , all other parameters in Table 3.4 being constant. | 108 |
| Figure 3.4.5c | Number of loops punched as a function of the fiber elastic modulus E_f , all other parameters in Table 3.4 being constant. | 109 |

| | | |
|---------------|--|-----|
| Figure 3.4.5d | Number of loops punched as a function of the matrix critical interfacial stress t_c , all other parameters in Table 3.4 being constant. | 110 |
| Figure 3.4.5e | Number of loops punched as a function of the temperature excursion ΔT , all other parameters in Table 3.4 being constant. | 111 |
| Figure 3.4.6 | Dimensionless plot of the two critical lengths L_p and L_u as a function of the temperature excursion ΔT . | 112 |
| Figure 4.1.1a | Apparatus used to purify the AgCl melt. | 125 |
| Figure 4.1.1b | Apparatus used to filter the AgCl melt. | 125 |
| Figure 4.1.2 | Procedure used to fabricate AgCl composites. | 126 |
| Figure 4.1.3 | Zone melter used to remelt samples made in oven shown in Fig. 4.1.2. | 127 |
| Figure 5.1.1 | Decorated prismatic loops in AgCl punched by a glass sphere. Unresolved tangles are visible in the directions where no loops were emitted. | 137 |
| Figure 5.1.2 | Unresolved dislocations forming a spherical plastic zone around glass spheres embedded in AgCl. | 137 |
| Figure 5.1.3 | Glass sphere in AgCl matrix surrounded by an irregular zone of unresolved, decorated dislocations and having emitted prismatic loops. | 137 |
| Figure 5.1.4 | Glass spheres in AgCl matrix surrounded by tangled, decorated dislocations in a plastic zone forming lobes. | 137 |
| Figure 5.1.5 | Total number of prismatic dislocations loops punched by glass spheres in AgCl as a function of the sphere diameter. | 138 |
| Figure 5.1.6 | Radius of plastic zone surrounding a sphere in an AgCl matrix as a function of the radius of the corresponding sphere. | 139 |

| | | |
|---------------|---|-----|
| Figure 5.1.7 | Decorated prismatic loops in AgCl punched by two glass particles | 140 |
| Figure 5.1.8 | Partially resolved, decorated dislocations in AgCl forming a plastic zone around a glass particle located at the intersection of three grain- or subgrain boundaries. | 140 |
| Figure 5.1.10 | Glass particle in AgCl matrix surrounded by an irregular zone of unresolved, decorated dislocations and having emitted prismatic loops, some of which form an helix. | 140 |
| Figure 5.1.9 | Schematics of particles and their associated plastic zone traced by hand from enlarged micrographs. | 141 |
| Figure 5.1.11 | Plot of the frequency of the punching angle for non-equiaxed particles. | 142 |
| Figure 5.1.12 | Equivalent radius of the plastic zone surrounding glass particles in AgCl as a function of the equivalent radius of the corresponding particle. | 143 |
| Figure 5.1.13 | Decorated, pinned dislocations in the plastic zone surrounding an alumina fiber in an AgCl matrix. | 144 |
| Figure 5.1.14 | Decorated rows of prismatic loops punched from a short alumina fiber in an AgCl matrix. | 144 |
| Figure 5.1.15 | Peanut-shaped plastic zone around an alumina fiber embedded in AgCl. | 144 |
| Figure 5.1.16 | Row of decorated, prismatic loops emitted by a glass fiber in AgCl. A dark zone formed of unresolved dislocation tangles surrounds the fiber. 1500x. | 145 |
| Figure 5.1.17 | Row of decorated prismatic loops punched from the end of a glass fiber in AgCl. | 145 |

| | | |
|---------------|--|-----|
| Figure 5.1.18 | Glass fiber with emitted row of prismatic loops punched at an angle in AgCl. The fiber is also surrounded by a plastic zone formed of unresolved dislocations. 1500x. | 145 |
| Figure 5.1.19 | Glass fiber in AgCl with decorated dislocation structure | 146 |
| Figure 5.1.20 | Two rows of decorated loops punched by the tip of a glass fiber in AgCl. Loops are on non-adjacent glide systems. 1300x. | 146 |
| Figure 5.1.21 | Rows of elongated, decorated dislocations emanating from the tip of a glass fiber in AgCl. | 146 |
| Figure 5.1.22 | Two glass fibers in AgCl showing the same dislocation structure | 147 |
| Figure 5.1.23 | Three glass fiber having emitted decorated dislocations in AgCl. | 148 |
| Figure 5.1.24 | Glass fiber in AgCl with elongated, decorated loops emitted by its sides. | 148 |
| Figure 5.1.25 | Long, decorated loops emitted by the sides of a long glass fiber in AgCl. | 149 |
| Figure 5.1.26 | Decorated dislocations forming the plastic zone surrounding a long glass fiber in AgCl. | 149 |
| Figure 5.1.27 | Plot of the frequency of the angle between the axis of the punched row of loops and that of the emitting alumina fiber. | 150 |
| Figure 5.1.28 | Plot of the frequency of the angle between the axis of the punched row of loops and that of the emitting glass fiber. | 151 |
| Figure 5.1.29 | Stress of pinned dislocations as calculated from Eq. [5.1.2] in the plastic zone surrounding alumina fibers in an AgCl matrix (see Fig. 5.1.13) as a function of radial distance from the interface. | 152 |
| Figure 5.1.30 | Plot of the row length divided by the loop diameter versus glass fiber aspect ratio for two values of the friction stress. | 153 |

| | | |
|----------------|--|-----|
| Figure 5.1.31a | Plot of the row length divided by the loop diameter versus glass fiber aspect ratio for small fiber diameters. | 154 |
| Figure 5.1.31b | Plot of the row length divided by the loop diameter versus glass fiber aspect ratio for large fiber diameters. | 155 |
| Figure 5.1.32 | Plot of the maximum number of loops emitted by the sides of glass fibers as a function of the fiber diameter. | 156 |
| Figure 5.2.1 | Large glass fibers in AgCl matrix. One grain shows slip bands visible as parallel region of alternating contrast while the other grain does not show any slip. | 157 |
| Figure 5.2.2 | Stress concentration at the tip of alumina fibers 3 μm in diameter embedded in AgCl | 157 |
| Figure 5.2.3 | Stress concentration at the tip of alumina fibers 20 μm in diameter embedded in AgCl | 158 |
| Figure 5.2.4 | Stress concentration at the tip of a glass fiber 80 μm in diameter embedded in AgCl | 158 |
| Figure 5.2.5 | Stress concentration at the tip of a glass fiber 80 μm in diameter embedded in AgCl | 158 |
| Figure 6.1.1 | Schematics of a mismatching fiber in a crystalline matrix deforming by slip. | 192 |
| Figure 6.1.2 | Schematic of fiber punching elongated dislocation loops along the six directions $\langle 110 \rangle$. | 193 |
| Figure 6.1.3 | Schematic drawing proposed as an explanation for the structure of Fig. 5.1.22. | 194 |
| Figure 6.1.4 | Proposed mechanism of nucleation of prismatic loops to explain structure in Fig. 5.1.24 and 25. | 195 |
| Figure 6.1.5 | Variation of Fig. 6.1.4, with formation of the shear loop on another glide plane. | 196 |

LIST OF TABLES

- Table 3.1: Physical and mechanical parameters of matrix materials (high purity silver bromide and chloride and 99.5 % aluminium). 85
- Table 3.2: packing ratio, critical volume ratio, dislocation density and increase of yield stress in shear for different arrays of mismatching SiC spheres and cylinders in aluminum. 86
- Table 3.3: Exact values of constant K for regular bodies. 87
- Table 3.4: Thermal, mechanical and geometric parameters of the matrix and fibers used in the parametric study. 88

ACKNOWLEDGEMENTS

It is my pleasure to express my gratitude to everyone who contributed to the completion of this work and especially to acknowledge the following:

Prof. Andreas Mortensen, my adviser, for his faith in taking me as his first student, for his technical and scientific guidance throughout this thesis, teaching me to do research, and for the generosity with which he shared his many ideas and insights;

Prof. K. C. Russell for his interest in this work and enlightening discussions;

Prof. J.W. Mitchell for pioneering the field of silver halide and sharing his extensive experience in the processing of these tricky materials;

Prof. R.G. Ballinger for permission to use his microscope;

Dr. Jim A. Cornie for his contagious enthusiasm for metal matrix composites, and for sharing (and supplying !) countless liters of very European, very strong expresso coffee;

Maria Wehrle-Due for the enthusiasm, generosity and efficiency with which she helped me (as well as many generations of students) in the lab;

Jackie Isaacs for the support when this thesis was little more than an idea trying to be realized, the helpful discussions and the friendship;

Eric Klier for his friendship and for showing me that (almost) any technical difficulty can be solved through hard work;

Brent Chambers for sharing the lab with me and for always lending a hand (or a vacuum oven) when I needed it;

Liz Earhart for reading this thesis and making many helpful comments, and for starting to carry on some of the future work connected with this research;

my family, which always showed full support for my work and especially my mother, for unquestionably believing in me, supporting and encouraging me at

every step on the road to higher education, as well as my grand-father, Dr. C. H. Wakker, metallurgist, scientist, engineer and entrepreneur, who first awakened my scientific interest and still inspires me, after more than twenty years of formal education;

Jan Eberly for her unfailing support, her invigorating optimism and her caring understanding.

Finally, I am very grateful to the Swiss National Foundation and to International Business Machines for scholarships as well as to MIT for many hours of free computing on the ATHENA network.

David C. Dunand

Cambridge, Massachusetts

August 1990

1. INTRODUCTION

Metal matrix composites (MMCs) are a new class of materials which has been the focus of considerable scientific and technological activity in the last twenty years. Recently, reinforced metals have been produced on a large scale, thus breaking for the first time the commercial barrier inherent to any new material which relegated MMCs to applications - such as military and aeronautical hardware - where cost is of secondary importance. One of the most interesting properties of MMCs is their high stiffness and strength to density ratios at ambient and elevated temperature, leading to potential structural applications in the aerospace and automotive industries. Another promising market is electronic packaging where MMCs offer a unique combination of low thermal expansion and high electrical and thermal conductivity. If MMCs are to be accepted and used in the engineering community, their processing, microstructure, properties and performances must be thoroughly understood in order to derive general constitutive laws describing them. A data base approach is not sufficient due to the staggering number of parameters which influence MMCs; elementary mechanisms common to all MMCs must be recognized and modelled in order to accurately predict from theoretical principles optimal microstructures and properties.

MMCs consist of two phases, the reinforcement and the matrix. The reinforcement is usually a ceramic phase (carbide, nitride, oxide, boride, etc.) or an element (beryllium, boron, carbon, tungsten, etc.) which exhibits desirable properties such as strength, stiffness, hardness, density, thermal expansion, temperature and environmental stability, thermal and electrical conductivity, superconductivity, etc.. The reinforcement shape can be equiaxed (particles) or elongated (whiskers, fibers); the latter geometry allows anisotropic properties

upon orientation of the reinforcement in the composite. The other phase, the metallic matrix, is used as a binder for the reinforcement and also contributes a set of desirable properties such as high toughness and ductility, high thermal and electrical conductivity, good processibility, good high-temperature and environmental resistance, etc..

One of the unique properties of MMCs compared to polymeric or ceramic matrix composites is the ability of the matrix to deform plastically by dislocation nucleation and motion. The ductile behavior of the matrix has far-reaching consequences for the mechanical and physical properties (and therefore performance) of MMCs since stresses can be relaxed by plastic flow of the matrix. Stresses in composites can be induced by an external force or by a change of temperature if the coefficient of thermal expansion (CTE) of matrix and reinforcement are different, as is the case in most MMCs of practical interest. Upon temperature change, the expansion (or shrinkage) of each phase will be different, leading to a thermal mismatch strain. In composites where both phases are brittle (such as ceramic matrix composites or certain polymer matrix composites), these stresses can lead to the failure of one of the phases or the interface. In the case of MMCs, however, thermal stresses can be relieved by dislocations nucleation and glide in the matrix. This phenomenon has practical importance since most MMC systems are fabricated at a high temperature from which they are cooled. Unlike single-phase metals, the matrix of an annealed MMC will therefore contain a high density of dislocations. Finally, many MMCs are candidates for high temperature applications, with or without temperature cycling, where thermal mismatch can be expected as well. The study of these thermally induced dislocations is thus of importance since they are an unavoidable feature of MMCs and since they will influence such important

properties as the internal stress state, strain-hardening, diffusion, aging, recovery, recrystallization, etc.

The purpose of this thesis is to contribute to the basic understanding of the micromechanics and microstructure of dislocations produced by thermal mismatch in reinforced metals, using both a theoretical and experimental approach. The first half of the literature survey is devoted to the subject of dislocations in MMCs, while the second half reviews relevant data of silver chloride as a model material to investigate plasticity of metals. Experimental methods and results are given in the next two chapters. The subsequent chapter presents theoretical micromechanical considerations which are compared to the experimental data in the following discussion chapter, which also includes the interpretation of micrographs showing dislocation microstructures. Finally, the findings are summarized in the conclusion and suggestions are made for future work.

2. LITERATURE SURVEY

This survey is divided in two main areas: metal matrix composites and unreinforced silver halides. The observation and modelling of dislocations in MMCs is first addressed. The properties of silver halides are then described, including observations of plastic and elastic strains.

2.1 Dislocations in metal matrix composites

While a great number of theoretical and experimental papers have been written on the interaction of submicroscopic inclusions or precipitates and a metallic matrix upon thermal and mechanical loading, much less is known about the corresponding interaction between reinforcement and matrix in MMCs. Some of the reasons why the modelling of precipitation hardening cannot be directly used for MMCs, are that the size, volume fraction, geometry and interface of the reinforcement in MMCs are different from those of two-phase alloys. Some information on dislocations in MMCs has been indirectly deduced by measurements of mechanical properties affected by the presence of dislocations, e.g. strain-hardening, Bauschinger effect, etc. This work is not surveyed here; only previous work on direct observation and modelling of dislocation mechanisms in particle, fiber or whisker reinforced metals are described in what follows.

2.1.1 Observation of dislocations

Hancock and Grosskreutz (1968) found that, in 2024 aluminum reinforced with stainless steel fibers, the average dislocation density after solution treatment and

quenching was greater than that in the unreinforced alloy in the same state; they also reported that the dislocation density was highest close to the fiber. On the other hand, Hancock (1967) in an earlier study did not report any significant difference in dislocation densities between reinforced and unreinforced quenched specimens. Pinnel and Lawley (1970) too reported that, for a 99.99 aluminum-stainless steel composite, the dislocation density and configuration was independent of the distance from the matrix interface for a given level of strain and reinforcement. For a given strain (including the as-pressed condition without any mechanical deformation), they also found that the dislocation density and configuration was the same with or without fibers; they reported the same result for the creep behavior of this system (Pinnel and Lawley 1971). Pattnaik and Lawley (1974) found no difference in the matrix substructure (grain and subgrain boundaries, dislocations) between the reinforced and the unreinforced aluminium samples, which had been annealed at 550 °C and 625 °C prior to deformation. In contrast to these findings, Chawla and Metzger (1972, 1977) found by an etch pitting technique in copper reinforced with tungsten wires an increased dislocation density (which was more pronounced in the vicinity of the fibers), compared to unreinforced copper. This was confirmed by TEM data on SiC whisker-2124 aluminum (Harding *et al.* 1987), showing that the highest dislocation density was close to the surface of the whisker in both deformed and undeformed samples, as received or in the T6 condition. Average dislocation densities were the same for unloaded and impact loaded specimens ($5 \times 10^{13} \text{ m}^{-2}$) but higher for quasi-statically loaded specimens ($3 \times 10^{14} \text{ m}^{-2}$). Williams and Fine (1985) studied the dislocation density in SiC whisker-2124 aluminum in the T6 condition using TEM. Prior to deformation, the density was highly non-uniform, with dislocations piled up along one side of the observed whiskers but

not the other. The structure became uniform after fatigue. They made the hypothesis that pile-ups of dislocations promote fatigue crack initiation.

In annealed and slowly cooled 6061 Al reinforced with SiC whisker and SiC powders respectively, Arsenault and Fisher (1983a, 1983b) observed high dislocation densities in the range of 10^{14} to $4 \cdot 10^{14} \text{ m}^{-2}$, more than an order of magnitude higher than an unreinforced alloy hot-rolled to a strain of 50%. Dislocations were clustered around the fibers, forming low angle cell boundaries. Decoration of the dislocations by GP zones was also observed. The precipitates as well as the increased dislocation density were given as an explanation for the higher than expected strength of the composites. Vogelsang *et al.* (1986) investigated the dislocation dynamics of the same material with thin foils which were heated during TEM observation. One sample viewed axially showed only rearrangement of the dislocations in polygonized regions upon heating and no multiplication upon cooling. When viewed longitudinally, the dislocations disappeared at high temperatures and reappeared on cooling, more so at the ends of the whiskers. In another sample, dislocations upon cooling were seen emanating from the interface and forming tangles in subgrains. The dislocation density was higher in the composite matrix than in an unreinforced control sample. Greater densities were observed close to the whiskers, especially at their ends. Large whiskers were surrounded by larger dislocation densities than small whiskers.

Arsenault and Shi (1986) investigated Al 6061 reinforced with 20 vol.% platelets of SiC. They performed *in situ* TEM observations of thin foils submitted to thermal cycling. They again observed that dislocations disappeared at high temperature and were generated at the interface Al/SiC upon cooling. The density of dislocations observed was, however, lower by an order of magnitude than that in bulk thermally cycled composites ($10^{14} [\text{m}^{-2}]$), a result the authors

attributed to dislocation loss at the TEM surface. The same observation was made in the study mentioned above (Vogelsang *et al.* 1986).

Arsenault *et al.* (1986) investigated the fracture of this material and concluded that thermally induced dislocations had an influence on the deformation due to the expansion of the plastic zone upon deformation. They measured by TEM dislocation densities as a function of distance from the fracture surface in composites with 5 and 20 vol.% whiskers and particles as well as an unreinforced control alloy.

Arsenault and Wu (1988) compared SiC/aluminium composites fabricated by powder metallurgy to the same specimen which had been remelted. They did not find any significant difference in dislocation density (or strength) before and after remelting. This might indicate that thermal mismatch dislocations are the largest population of dislocations initially present in the matrix at room temperature.

Chin (1987) observed in an as-cast alumina reinforced magnesium specimen dislocation densities in the order of 10^{14} [m⁻²]. Upon heat treatment for 95 h at 450 °C, polygonization of dislocations occurred, resulting in dislocation-free subgrains.

In magnesium AZ91C reinforced with graphite fibers, Rawal *et al.* (1986) found high dislocation densities close to the fiber; dislocation networks were also observed close to the interface. Diffusion-bonded specimens exhibited linear dislocations which were oriented crystallographically in the matrix while specimens processed by metal infiltration showed tangles of dislocations, as did cast specimens with an aluminium matrix. In a later article, Rawal *et al.* (1987) found a lower dislocation density in the cast material than in the diffusion-bonded material. TEM pictures of fatigued 6065 aluminum reinforced with graphite fibers (Allard *et al.* 1986) show tangles of dislocations at the fiber-matrix

interface and in narrow matrix regions between two fibers. The latter observation was confirmed by Fox and Flowers (1987) on an undeformed Al-Mg specimen with alumina fibers.

Li *et al.* (1989) performed a high resolution TEM study on SiC-coated graphite fiber - aluminum composites and found an extensive dislocation network in the vicinity of the fiber, i.e., within 0.1 μm of the interface. High resolution images do not however show any dislocations in the immediate vicinity of the interface (i.e., within 20 nm of the interface) and the authors propose that dislocations in this region dissociated to widths greater than the extinction distance, as observed by Liu and Balluffi (1984) at the interface between aluminium and amorphous alumina. Misfit dislocations with a spacing of about 9 nm were observed using lattice images at the interface between niobium and alumina (Rühle and Evans 1988).

Liu *et al.* (1989) observed a larger dislocation density after annealing in the vicinity of whiskers in a powder metallurgically produced Al/SiC composite.

Quite a large number of TEM investigations has been performed on directionally solidified eutectic composites. The dislocation structure can be different from the cases described above, because there is very often a crystallographic relationship between fiber and matrix, and because fibers can be faceted. Breinan *et al.* (1972) studied the creep of Al-Al₃Ni composites. Dislocation loops and tangles were observed at all stages of deformation. At low plastic strain, no substructure was visible, whereas in specimens tested to rupture, a dense dislocation cell structure was observed at the interface. Williams and Garmong (1975) investigated Ni-W composites and found that the fiber-matrix interface acted as a source which emitted dislocations into the matrix upon quenching of the specimen. These dislocations were concentrated around

the fibers. Also, discontinuities at the interface such as ledges were found to act as stress concentrators which allowed dislocation multiplication. Contrast experiments showed that these dislocations were not prismatic. The interpretation was however complicated by the fact that the dislocations were absorbed by a precipitates of $W\text{Ni}_4$ in the matrix; precipitation took place more rapidly in the vicinity of the W fibers, in accord with the observation that dislocations were more numerous there. In the same system, Garmong and Williams (1975) observed rows of dislocations emitted on a single slip plane by the fiber upon quenching and slight straining. When the specimen was strained more extensively, dislocation arrays became less planar and formed tangles, due to a tendency to cross-slip and due to the obstacles formed by the fibers. When the matrix was aged, shear bands were observed upon monotonic loading. The fatigued structure is the same as the uniaxially deformed one: diffuse slip in the as-quenched condition and highly planar slip in the aged condition.

A TEM investigation of a nickel base TaC composite (Walter 1982) showed that the matrix changed its mode of deformation with increasing fiber density, from well defined slip bands to a forest of dislocations with patches of higher density. Also observed were the dislocations formed by the fracture of a fiber; the dislocations did not follow the direction of the slip bands in the matrix. In a Ni-TaC composite tested in fatigue (Blank and Stoloff 1987), dislocation tangles were observed; they were due to bowing out of loops in the matrix which reacted with each other. An increasing dislocation density with decreasing testing frequency was also observed.

A TEM study made on an ordered nickel aluminide matrix reinforced with molybdenum fibers deformed under creep (Funk and Blank 1988) showed long straight dislocations parallel to the fibers. Loops around the fibers were thought to be the product of the recombination of dislocations of opposite sign running

against the fiber from opposite sides. The regularity of the dislocation network was disturbed at the ends of broken fibers where the density was higher. In samples with larger fibers and volume fraction, slip bands confined to only a few slip planes were observed. Pile-ups of over one hundred parallel dislocations were observed parallel to a TaC fiber in a cobalt base matrix (Stohr and Khan 1982). It was also shown that thermal cycling of Ni-TaC composites leads to high dislocation densities close to the fibers.

2.1.2 Modelling of dislocation structure

In the previous section, widely varying dislocation observations were reported: this is due to the fact that different authors investigated various composite systems with different thermal and mechanical histories. A small number of investigators have tried to go beyond and have modelled their observations. A great deal of work has been done on the modelling of the matrix of MMCs upon large mechanical deformations, where the effect of large numbers of dislocations in the matrix is treated globally. Two recent papers (Pedersen 1988, Humphreys 1988) review some of these models. In what follows, only those models dealing with individual dislocations from an atomistic point of view are reported. No published information could be found on how dislocations are created at the interface or how they interact with each other or with the reinforcement.

Walter *et al.* (1969) studied dislocations at the interface of chromium fibers grown *in situ* in a NiAl matrix. They observed square networks, the Burgers vectors of which they measured and matched to a geometrical model. They calculated the network strain energy and its contribution to matrix strengthening. Occasionally, hexagonal networks were also seen.

Arsenault and Fisher (1983a & b) and Arsenault (1984) proposed that a large part of the strengthening in particle and whisker reinforced aluminum was due to the thermally induced dislocations in form of tangles or rearranged in subgrains. Flom and Arsenault (1985) proposed a model for the extent of the plastic zone around a fiber on cooling which they compared to observations of slip lines on a model composite with a SiC fiber of 1 mm diameter. A simple model of a SiC parallelepiped particle (modelling a particle or a whisker) punching dislocations on all faces was then proposed and used in many publications (Arsenault and Shi 1986, Arsenault 1986, Arsenault 1988). Complete relaxation of the mismatching particle was assumed and the density of dislocations was calculated after assuming that the loops punched had the same dimension as the sides of the parallelepiped; however, the crystallographic nature of slip and the orientation of the particle with the slip directions were not taken into account. Dislocation densities as a function of volume fraction, size and morphology were obtained, and the corresponding matrix strengthening was predicted.

Mori and Taya (1986) and Taya and Mori (1987) presented a model predicting the punching distance of loops emitted at the end of a short fiber; their model ignored the discrete nature of the loops and considered instead the extent of the plastic zone. They equated the change in the work done by the movement of a prismatic loop with the change in total potential energy of the composite due to thermal mismatch. The punching distance was calculated as a function of fiber stiffness, temperature change, frictional stress and fiber aspect ratio. They found that for certain critical values of these parameters, the punching of loops was completely suppressed, and they predicted fiber rupture if no other relaxation process was operative to reduce the internal stress. The model is briefly summarized in Appendix 5. Using this model, Christman and Suresh (1988)

calculated that the punching distance due to a regular array of SiC whiskers (13.2 vol%) in an aluminum matrix was sufficient to cover 75% of the matrix. Their TEM observation of such a system quenched and aged showed a significantly higher dislocation density, as well as a greater number of helical dislocations in the composite matrix than in a control alloy. The dislocations were homogeneously distributed in the matrix with no preference for the interface.

Stanford-Beale and Clyne (1988) proposed models for the relaxation at high temperatures of mechanical and thermal stresses by diffusive mass transport and dislocation motion assisted by cross-slip and/or climb. They noted that vacancies would drift from the ends of the fibers to their mid-point at high temperature.

Kim *et al.* (1990a & b) investigated by TEM the plastic relaxation of 2024 aluminum reinforced with SiC or TiC particles of different size and volume fraction which had been annealed at 515 °C. They measured the dislocation density as a function of the distance from the interface and proposed a theoretical model taking into account the volume fraction. They observed that, with increasing volume fraction, the dislocation density increased and the dislocations became more tangled. Reinforcement size and elastic modulus were also found to affect the dislocation density. A good agreement between theory and data was reached if it was assumed that the fractional amount of plastic strain energy stored in form of dislocations was 50%. The authors do not, however, justify this value, nor note that it is much higher than in macroscopic metallic samples where the stored energy is on the order of 10% (Bever *et al.* 1973).

2.2 Selected properties of silver halides

Much is known about silver halides since they are used industrially as photosensitive emulsions on photographic film. A wealth of information can be found in reference books (Gmelin Institut 1971 and 1972), photography monographs (Frieser *et al.* 1968, Mees and James 1966) or materials science series (Javornicky 1974, Sprackling 1976). In what follows, only selected properties which seem pertinent to the subject of this thesis are described; if no specific reference is made to an author, the information comes from the six books mentioned above. Throughout this thesis, the term "silver halide" will be used to describe silver chloride and silver bromide, thus excluding the fluoride and iodide which are of little experimental value for the simulation of metals.

2.2.1 Physical properties

Some physical properties are listed in Table 3.1 for silver bromide, silver chloride and, as a point of comparison, aluminum (Boyer and Gall 1985). Both halides crystallize in the NaCl lattice which can be visualized as two shifted f.c.c. lattices of cations and anions. The main point defects are Frenkel defects on the silver sublattice; Schottky defects are present in much smaller concentration. At room temperature, only the Frenkel defects are mobile. Due to the thermal formation of vacancies, the coefficient of thermal expansion at temperatures close to the melting point increases more than linearly with the temperature.

Silver halides are ionic conductors; at room temperature, the current is due to movement of interstitial silver ions, while the chloride ions are immobile. The electronic conductivity is smaller than the ionic conductivity by many orders of magnitude. Silver halides also exhibit photoconductivity: the photoelectrons have a lifetime of 3 ns. in ultra-pure silver chloride crystals. Oxygen ions in the lattice increase this life time to 10 μ s. The photoeffect is strongest in the region of

strong light absorption, e.g., 365 nm. for silver chloride and 450 nm. for silver bromide. This peak shifts to shorter wavelengths at lower temperatures.

Silver halides have high refraction indices and are transparent to infrared and optical light (silver chloride is colorless and silver bromide is yellow), but absorb strongly in the UV region. When heated, silver chloride becomes slightly yellow whereas silver bromide turns orange. Copper additions to silver chloride increase the absorption in the violet and blue region. Silver halides also exhibit stress birefringence.

Even though there has been a great number of investigations on the subject, the elementary processes of photodissociation and silver speck formation are not yet fully understood. According to the Guernsey-Mott theory, a photon liberates an electron from a halide ion. This electron is then captured by a sensitivity center (silver oxide, sulfide etc.) which becomes negative. It attracts an interstitial silver cation, which is reduced to silver. This mechanism repeats itself until a silver aggregate is formed. It is assumed that the mobility of the electron is significantly smaller than that of the silver ion. The Mitchell theory assumes, on the other hand, that no sink for electrons is present at the beginning of the exposure. Groups of three silver atoms are formed and absorb a silver ion, so that a tetrahedric positive group is formed. It will attract a photoelectron and become neutral again. The process is repeated until a speck of silver is formed. For a discussion of these different theories of photographic sensitivity and image formation, the reader is referred to papers by Mitchell (1957b, 1983, 1987a & b).

Schematically, the photodissociation process for AgCl can be described as follows:

1. Creation of a photoelectron at the surface upon absorption of a photon and formation of chlorine:



The chlorine is liberated as a gas molecule and the electron is captured by a sensitivity center, the identity of which is different depending on the theory, as described above.

2. Reduction of silver at the sensitivity center:



The sum of Eqs. [2.1] and [2.2] gives:



The chlorine is liberated at the surface, while the silver is deposited where the electron is captured, i.e., at the surface if sinks exist there, in the volume if the electron diffuses there or is attracted by a sink. The silver will precipitate preferentially at structural defects, possibly because the stress field of the precipitate is minimized there or because electron sinks are attracted by the defects.

2.2.2 Mechanical properties

Both mono- and polycrystalline silver halide crystals are very ductile and behave mechanically in most ways as pure metals do. This is to be expected, since silver halides exhibit mobile dislocations. Many typically metallic phenomena have been reported for silver halides: strain-hardening, texture, slip bands,

Luder's bands, necking, ductile fracture, internal friction, slip band extrusion in fatigue, diffusion controlled creep, recovery and recrystallization. One of the main differences in the deformation behavior of silver halides is caused by the ionic nature of the lattice; certain dislocation movements are restricted for electrical reasons and the dislocation core structure is different. Also, dislocations can be electrically charged and interact with both anions and cations as well as their vacancies. But at large, the similarities of mechanical behavior between the silver halides and pure metals are striking, and this explains why silver halides have been used for decades as transparent models for metals.

Silver halides deform by pencil glide (as does iron) in the $\langle 110 \rangle$ direction. Many slip planes are operative, the principal ones being $\{110\}$, $\{100\}$ and $\{111\}$. This leads to wavy slip lines at room temperature; at $-196\text{ }^\circ\text{C}$, cross-slip is inhibited and straight glide surfaces are observed in silver chloride. The deformation behavior of silver chloride is independent of the grain size at room temperature, but not at $-196\text{ }^\circ\text{C}$. A strong increase of tensile strength is observed after 25% cold working of silver chloride. Table 3.1 lists a few mechanical properties of the silver halides, which differ from those of aluminum by only a factor of 2 to 4.

2.3 Observation of dislocations in silver halides

The very first direct observations of dislocations in any material was made by decoration of subgrain boundaries in silver bromide (Hedges and Mitchell 1953a), at a time where TEM was not yet a proven analytical technique. TEM is difficult to perform on silver halides due to decomposition in the electron beam (Pashley 1950). While used by some investigators (e.g., Skillman and Berry 1964, Hamilton 1967, Brady *et al.* 1968), it is chiefly applied to emulsions. X-Ray diffraction has

also been used to resolve dislocations in silver halides (see for example Lang 1959, Newkirk 1959). TEM and X-Ray methods are not discussed further in this section, nor is etch pitting, which is another direct method used by many authors (e.g., Vavra 1969, Sprackling 1964, 1968, 1980). Nuclear magnetic resonance and conductivity measurements are indirect techniques giving information of statistical nature. Unlike the four direct methods mentioned above, these indirect methods do not image dislocations. In this section, decoration and indirect methods are reviewed.

2.3.1 Decoration and optical microscopy

In a series of papers stretching over a decade, J.W. Mitchell and coworkers explored the room temperature decoration of dislocations in silver halide. In a paper dealing essentially with the photographic sensitivity of silver bromide under different treatment, Hedges and Mitchell (1953a) decorated polyhedral substructures of dislocations by separation of photolytic silver in annealed samples. They also observed that the regular polygonized structure was destroyed upon deformation of the annealed crystals (*ibid.*, 1953b). Clark and Mitchell (1956) describe the synthesis and treatment of the silver halide from which thin plates of silver bromide were fabricated, annealed, and exposed to the light of a mercury lamp. This paper again mostly deals with the problem of photographic sensitivity, but the experimental procedures described in great detail were used in all subsequent papers by Mitchell and co-workers in the investigation of dislocations in silver halides. They are used with some modifications in this thesis as well.

Mitchell (1957) observed tilt and twist subgrain boundaries as well as fields of curved dislocations decorated with a load applied. The deformed structure is

thus "frozen" by the decoration and can be later investigated under the microscope.

Barber *et al.* (1957) decorated potassium and sodium chloride at high temperature with gold and observed individual dislocations on slip planes and arranged in subgrain boundaries. They also reported the formation of rows of circular dislocations or helices emitted from an inclusion. The three-dimensional structure of these dislocations can be rendered by series of micrographs focused at different depths in the crystal. Due to the very small depth of field of high resolution optical microscopy, only a small volume of material is in focus and "slices" of materials can be photographed.

Jones and Mitchell (1957) showed that there was no absolute correspondence between etch pits and decorated dislocations. They also observed dislocation structures in plastically deformed crystals. They also established that decoration does not alter the dislocation structure.

By annealing at high temperatures and recrystallization of the samples, Mitchell (1958) showed that it was possible to produce crystals with a very low density of dislocations. He also observed dislocation loops produced by the differential contraction of a glass sphere embedded in a matrix of silver chloride, thus duplicating the same observation made in sodium chloride containing unspecified inclusions which had punched dislocation loops (Barber *et al.* 1957). The superiority of silver chloride for this application is immediately apparent since decoration is possible at room temperature.

Jones and Mitchell (1958) observed a whole range of dislocation structures emitted at the interface of a misfitting glass sphere in silver chloride: prismatic loops, helical dislocations, figure eights, etc. They describe the mechanisms of formation at the sphere surface of such dislocations by assuming that the screw components of a shear loop rotate around the glide cylinder. If the two screw

ends of the shear loop meet after a turn, they annihilate and form a simple prismatic loop; if, on the other hand, they turn many times before meeting, figure-eights and double helixes are formed. The authors also report the effect of the stress field of other spheres on the loops forming a row. They noted that the loop diameter is usually slightly smaller than the sphere diameter.

Bartlett and Mitchell (1958) investigated gold-sensitized silver chloride which they strained, exposed to light and annealed at low temperature: they found that gold particles decorate dislocations and concluded that prismatic loops are punched along the twelve $\langle 110 \rangle$ directions passing through the center of misfitting inclusions such as growing precipitates. They note that this observation may be relevant to precipitation-hardened alloys.

Sensitization by cuprous and cupric chloride was investigated by Parasnis and Mitchell (1959). They reported that traces of cuprous chloride increase the photosensitivity of silver chloride while cupric chloride precipitates along dislocations and other defects upon cooling from the annealing temperature. They show series of micrographs (the plane of which is normal to a $[100]$ and $[111]$ direction respectively) featuring rows of dislocations punched from growing particles of silver along all twelve $\langle 110 \rangle$ directions. In a separate paper, Mitchell (1959) discusses this phenomena in silver and alkali halides which have different types of defects and thus different mechanisms of relaxation.

In silver chloride doped with cupric chloride and annealed at a temperature close to the melting point, evidence of dislocation climb was observed by Parasnis *et al.* (1963). They report lozenge shaped dislocations crystallographically oriented so that a configurational electrostatic charge would be expected. The authors suggest that the charge is neutralized by cupric ions adsorbed on the dislocation.

When exposed to light, plastically strained silver bromide crystals sensitized with silver iodide showed decorated surface terraces and associated dislocation loops, from which the dislocations glide planes and Burgers vector could be determined (Bartlett and Mitchell 1960a).

The combination in silver bromide of two dislocations of Burgers vector $1/2\langle 110 \rangle$ to form a single dislocation of vector $\langle 110 \rangle$ was also observed by Bartlett and Mitchell (1960b), in possibly the first paper to experimentally establish dislocation interactions.

The same authors (*ibid.* 1961) also report the interaction of dislocations with different Burgers vector and furnish direct experimental evidence for pencil glide in silver bromide.

Mitchell (1962) compares different methods of dislocation imaging in a review article in which he also mentions that the limited decoration depth of silver halide can be circumvented by dissolution of the decorated layer and subsequent decoration.

Finally, Mitchell (1980) summarizes his research in a review article which also gives an historical perspective to the pioneering work his group performed in the late fifties, leading to the first proven observation of dislocations.

While the Mitchell group was the most active in the area of dislocation imaging in silver halide, their results were repeated by other investigators. Kanzaki (1955) published micrographs of coarsely decorated subgrain boundaries. This author studied the correlation between etch pits and decorated dislocations in annealed silver chloride (Kanzaki 1956a) and strained specimens (Kanzaki 1956b). The quality of decoration is however much lower than that achieved by the Mitchell group. Subgrain boundaries and polygonized dislocations were also decorated in silver chloride by Süptitz (1959).

One of the limitations of the technique used by the above investigators is the limited depth of material which can be decorated (about 30 μm). This relatively shallow depth is not a drawback if the size of the substructure to be investigated is smaller than this depth - for example if misfitting second phases are smaller than 10 μm . Also, a crystal decorated throughout its volume is much less transparent and the achievable resolution is reduced due to the large scattering taking place. If, however, it is desired to decorate at great depth, photoelectrons produced at the surface can be swept by an electrical field into the volume where they recombine with silver ions. The electrical field must be pulsed to avoid its rapid decay, since silver halides are conductive materials. In other words, the electrical field pulse must be long enough to appreciably move the photoelectrons but short enough to not influence the ions forming the crystal. Early investigators using this technique were mainly interested by the electron dynamics in silver halides. Haynes and Shockley (1951) used a stroboscope connected to a high voltage generator and measured the Hall and drift mobility of photoelectrons in silver chloride. Süptitz (1958) using the same type of apparatus, measured the drift mobility, lifetime and recombination rate of photoelectrons in silver chloride crystals of different purities. Hamilton *et al.* (1956) carried the same kind of investigations on electrons and holes in photographic grains which were also studied using TEM. Webb (1955) designed a air-driven turbine with a spark-gap switch to allow simultaneous illumination and electric field application on the sample. He dragged electrons in silver chloride over distances counted in millimeters. Castle (1957) measured the dislocation density in the bulk in as-grown crystals as $10^9 \text{ [m}^{-2}\text{]}$ and observed dislocation length on the order of 100 μm . In a series of papers, Slifkin and coworkers published excellent micrographs of decorated dislocations in silver chloride. The use of the pulsed method seems to inhibit completely the "fog" (or

random precipitation of silver in the volume) visible in all micrographs published by the Mitchell group. Childs and Slifkin (1960) and Slifkin and Childs (1961) reported that pulsed decoration followed by aging for several days at room temperature yields very sharp decoration; in the latter paper, they published micrographs showing dislocation polygonized in square and hexagonal patterns. Layer *et al.* (1962) published a micrograph showing trains of prismatic loops punched from both tips of an elongated inclusion about 10 μm long, located 300 μm below the surface of the specimen of silver chloride. Finally, Childs and Slifkin (1965) published a series of micrographs of stunning quality in a paper mostly dealing with the use of silver chloride as a nuclear particle track detector where they show that the disturbed region produced by energetic particles can be decorated in silver chloride and yields better results than stacks of photographic emulsions. Their micrographs include a 200 μm long dislocation bowing between pinning points, dislocation cusps in lightly deformed material, elongated loops (25 μm long and a few microns high), interacting dislocations with small inclusions showing how the former pass the latter, lozenge-shape vacancy condensation loops about an inclusion which also punched prismatic loops, one of which grew considerably. Finally, two micrographs are of particular importance for this thesis: the first shows a fiber-like inclusion about 30 μm long which punched two rows of loops at its tips; the longer row is about 100 μm long, while the shorter one is about 25 μm long. The second micrograph shows a shorter elongated inclusion, the orientation of which does not correspond to a slip direction. This inclusion punched two trains of prismatic loops at its tips as well as two pairs of trains on its sides.

2.3.2 Indirect methods

Mechanical deformation was found by many authors to increase the ionic conductivity of silver halides (Ninomiya and Sonoike 1958, Matejec 1961 and 1962, Matta and Vavrinec 1970). W.G. Johnston (1955) extensively studied this phenomenon on monocrystalline silver bromide; his findings are summarized in what follows. The conductivity increased linearly with strain up to deformations of 6%. The activation energy of this increase was close to that of the migration of interstitial silver ions. After unloading the sample, the conductivity recovered according to the same law that Cottrell and Aytakin (1950) used to fit data for the recovery of the yield stress of zinc. The conductivity also recovered following Andrade's $t^{1/3}$ law when a strained specimen was allowed to creep under load. Finally, the conductivity increase was 40% greater parallel to the slip plane of single crystals, than perpendicular to it. A frequency dependence of the conductivity measurement was also observed, consistent with regions of high conductivity separated by regions of lower conductivity.

All the evidence above suggests that the increase of conductivity was due to pipe conduction along dislocations. Interstitial silver ions are the most mobile defects and are expected to move much more quickly by pipe migrations along dislocation line, than by volume migration in the bulk. If the conductivity is assumed to be proportional to the number of piled-up dislocation in the crystal, Mott's model of work hardening predicts the observed linear strain-conductivity relationship, and the observed time dependence for recovery of conductivity during transient creep. Polycrystalline samples were also tested and showed the same qualitative behavior as single crystals. The conductivity was however systematically shifted to higher values, probably due to a constant contribution from grain boundary conduction.

Many researchers have used nuclear magnetic resonance (NMR) to investigate defects, as well as impurities in silver halides (for an overview, see Frieser *et al.* 1968). But only one investigator (Hohne 1964) extended this method to the study of dislocations in silver bromide. By locally changing the lattice distance, dislocations produce a spreading of the main peak during quadrupole resonance. Hohne showed that this effect could be calibrated to a dislocation density, and he used this technique to measure the change of dislocation density of a deformed sample as a function of annealing time, annealing temperature, previous deformation and impurity content. He successfully fitted his results to known models of recovery. The weakness inherent to NMR measurements (i.e. single dislocations cannot be imaged) can be turned into an advantage when high dislocation densities are involved: dislocation counting from TEM pictures becomes difficult due to cell formation or unresolved tangles. Methods such as NMR or conductivity, which both rely on the indirect effect of dislocations on a physical property, can therefore be used when changes in large dislocation densities must be measured, e.g., during recovery and creep.

2.4 Observation of stresses in silver halides

Internal stresses in metals are usually investigated by X-Ray methods, which feature poor spatial resolution and limited penetration. Silver halides are photoelastic and this property can be used to study stresses in a cubic material with mechanical properties very similar to metals. The fact that silver halides deform plastically by dislocation movement makes the stress distribution observed by birefringence directly comparable to the stresses present in metals; on the other hand, results on transparent polymers are only relevant for metals in the elastic region.

To the best of our knowledge, Nye (1948, 1949a&b) first systematically investigated the plasticity of silver chloride by stress birefringence. He determined the glide planes and directions of dislocations, and suggested the pencil glide deformation mode for silver chloride. He studied the effect of grain boundaries on slip propagation and the types of residual stresses within the grains. He also investigated the glide bands and the stress state of a deformed crystal, as well as the sign of dislocations in glide bands. Goodman and Sutherland (1953) showed that the birefringence of silver chloride was due to stress and not strain. They also measured the stress-optical coefficient of silver chloride and found it to be independent from stress well into the plastic region. Nye *et al.* (1957) also studied deformation in tension of single crystal bars of silver chloride and found that the plastic deformation was greatest near the surface of the specimen. In bending, plastic deformation was found to propagate longitudinally along the bars. The stress distribution was explained with a dislocation model. They also found that the ratio of the shear stress needed to move dislocations to that necessary to generate them was less than 0.6. Sprackling (1960) found no evidence of inhomogenous deformation upon reverse bending of silver chloride bars, unlike what happens upon the first bending; he proposed a simple dislocation model for this result. Kuznetsov (1956) studied the plastic and elastic stress distribution in notched and smooth specimens with large grains. Zhitnikov and Stepanov (1958a, b, c) measured the stress distribution in a textured plate of silver chloride, which was subjected to different stresses, and compared it to calculations. They also used a Babinet compensator to study the elastic-plastic transition of silver chloride in tension and bending (Zhitnikov and Stepanov 1958d). Stowell (1962) studied the structure of kink bands in uniaxial tension, and presented a dislocation model for their data. Sprackling (1966) studied yield phenomena in silver chloride and

found that the stress at which birefringent glide bands move is lower than the macroscopic yield stress by about 25 %. The former stress which they associate to the dislocation nucleation stress was found to be about 1.5 MPa in tension. Ogin and Brown (1980) found that the persistent slip bands which formed in cyclically loaded silver chloride were comparable to those observed in metals; the internal stresses had principal axes perpendicular and parallel to the plane of the bands. Dietz (1986), in a study of the engineering use of silver chloride to simulate metals plasticity, performed test on notched rods, silver chloride screw threads and cold-formed blanks. He concludes that such silver chloride parts submitted to the same deformation history as metal parts can bring experimental information on the plastic regions and the stress state of the metallic part.

2.5 Conclusions of literature survey

Except for early studies, investigators agree on the fact that dislocations are more numerous in MMCs than in unreinforced metals and that their density is higher close to the reinforcement, after both thermal and mechanical deformation. However, the data present in the literature was gathered in composites of engineering significance, which complicates its interpretation for several reasons: (i) chemical interaction between the fiber and the matrix affecting their properties or producing a third phase, (ii) complex matrix composition derived from conventional alloys, leading to extraneous phenomena (such as precipitation or phase transformation) influencing and influenced by dislocations, (iii) coherent and semi-coherent interfaces as well as grown-in dislocations in the case of, the directionally grown eutectic *in-situ* composites. While many investigators have observed dislocations in MMCs as part of broader investigations, few have focussed on the dislocations

microstructure and geometry or on elementary mechanisms of plastic deformation around large inclusions. As a consequence, very few models exist which can explain and predict the micromechanics of plastic deformation in MMC, even in the least complicated case of thermal excursion, unlike the extensive models existing for two-phase alloys.

Silver chloride and bromide deform under extensive dislocation movement and exhibit macroscopic breaking strains of up to 300% (Stepanov 1934). These materials have been used for more than half a century as "transparent metals" and they show dislocation mechanisms in a great number of ways similar to that in metals. Their excellent transmission in the range of optical wavelengths allows the observation of the bulk by transmission optical microscopy. Microstructural defects - particularly dislocations and grain boundaries - can be decorated at room temperature by photodissociation of the crystal. The dislocation substructure can therefore be examined along the whole sample to a depth of about 30 μm without further preparation. Another useful property of the silver halides is their stress birefringence, thus allowing the optical observation of elastic and plastic stresses with the optical microscope. This is a powerful method when used in conjunction with the observation of plastic deformation by decoration. Finally, the dislocations in silver halides can be investigated by other complementary methods such as conductivity measurements and NMR. The properties listed above as well as their low melting point and the good wettability of ceramic fibers make silver bromide and chloride excellent candidates as a model materials for the matrix of MMCs.

3. THEORY

In this section, we present micromechanical calculations for the extent of the plastic zone around mismatching inclusions of different shapes. In the first paragraph, we derive simple approximate expressions predicting the size of the plastic zone in a strain-hardening matrix resulting from a mismatching sphere as well as an infinite cylinder where only radial mismatch is considered. In the second paragraph, we extend this model to particles of irregular shape. In the following paragraph, the problem of a row of prismatic loops is considered, the solution of which is used in the last paragraph to derive the extent of the plastic zone due to longitudinal stresses in a fiber.

3.1 Plastic zone size around a sphere and an infinite cylinder

The formation of a plastic zone around an inclusion embedded in metal has been modelled by various authors using a continuum approach (e.g., Hill 1950, de Silva and Chadwick 1969, Hoffman 1973, Garmong 1974, Lee *et al.* 1980, Earmme *et al.* 1981, Dutta *et al.* 1988, Kim *et al.* 1990 a&b). In what follows, we propose an alternative method to calculate the size of the plastic zone surrounding inclusions of simple shape, namely spheres and cylinders embedded in a monocrystalline, elastically isotropic single-phase matrix. Our approach uses continuum plasticity as well, but takes into account the influence of dislocation density on flow stress.

Hill (1950) solved the problem of the expansion of a cylindrical or spherical cavity into an infinite, isotropic, linear elastic, non work-hardening plastic matrix from zero radius to end radius a . Assuming a Tresca yield criterion in the

matrix, the radius of the plastic zone c_c and c_s for a cylinder and sphere of respective radius a_c and a_s are respectively given as:

$$c_c = a_c \cdot \left(\frac{2 \cdot E}{(5 - 4\nu) \cdot \sigma_y} \right)^{1/2}, \quad [3.1.1a]$$

$$c_s = a_s \cdot \left(\frac{E}{3 \cdot (1 - \nu) \cdot \sigma_y} \right)^{1/3}, \quad [3.1.1b]$$

where E is the matrix elastic modulus, ν the matrix Poisson's ratio and σ_y the matrix yield tensile stress.

These results can be used to find the plastic zone radius due to the differential contraction of an infinite matrix around an inclusion. Consider a sphere or an infinitely long cylinder embedded in an infinite matrix which deforms by slip. Upon cooling from elevated temperature, the matrix is first able to alleviate misfit stresses that result from the differential thermal contraction of the reinforcement by diffusion or other creep mechanisms. These mechanisms will operate as long as their rate is on a par with that of cooling. At low temperatures, creep cannot relieve thermal stresses, which build up and induce plastic deformation by slip in the matrix that surrounds the inclusion. The transition from creep to slip is assumed to take place at a single temperature T_c , above which all thermal mismatch strains are relieved by diffusion, and below which dislocations form at the interface and glide within the matrix to relieve thermal mismatch stresses higher than the yield stress of the matrix. Thus, upon cooling from a high annealing temperature T_a to a lower temperature T_o , stresses will be relieved first by diffusion and/or creep at high temperatures until temperature T_c is reached. At this temperature, the inclusion and the matrix are assumed to

be stress-free. Upon further cooling to T_0 , elastic stresses build up in both phases until the matrix yield stress is reached and slip begins in the matrix. It is assumed that the stress for nucleation of dislocations at the interface is at most equal to the friction stress of the matrix. Given the relatively low yield stress of silver halides (and most metals) and the high modulus of the inclusions of interest, the latter is assumed to be perfectly rigid. The total mismatch strain ϵ_m between matrix and inclusion to be relieved by slip is

$$\epsilon_m = \Delta\alpha \Delta T , \quad [3.1.2]$$

where

$$\Delta T = T_c - T_0 , \quad [3.1.3]$$

and $\Delta\alpha$ is the absolute value of the difference of CTE between matrix and inclusion. The displacement Δr of the matrix due to the presence of an inclusion of radius r at its surface is then known, and given as

$$\Delta r = \Delta\alpha \cdot \Delta T \cdot r . \quad [3.1.4]$$

By using Eqs [3.1.1], the radius of a fictitious cylindrical or spherical hole of radius a_c and a_s , respectively, which would produce in an unreinforced matrix a displacement Δr at the inclusion surface can be calculated (Fig. 3.1.1). Since the stress and strain state, as well as strain history of the matrix outside the inclusion, are identical for these two cases of a thermally mismatching inclusion and a growing hole, the size of the plastic zone can be found by deriving a_c or a_s , and using Eqs. [3.1.1]. The radii a_c and a_s are most easily derived from conservation of volume, neglecting the elastic compressive strain within the

inclusion volume in the growing hole configuration. Neglecting higher orders of Δr , one obtains for the cylinder and the sphere, respectively:

$$\pi \cdot a_c^2 = 2 \cdot \pi \cdot r_c \cdot \Delta r , \quad [3.1.5a]$$

$$\frac{4}{3} \pi \cdot a_s^3 = 4 \cdot \pi \cdot r_s^2 \cdot \Delta r . \quad [3.1.5b]$$

Inserting Eq. [3.1.5a] and [3.1.5b] into Eq. [3.1.1a] and [3.1.1b] respectively and taking Eq. [3.1.4] into account, the radius of the plastic zone produced by differential thermal contraction of the matrix around a cylinder (c_c) and a sphere (c_s) is respectively given by:

$$c_c = r_c \cdot \left(\frac{4 \cdot \Delta \alpha \cdot \Delta T \cdot E}{(5 - 4\nu) \cdot \sigma_y} \right)^{1/2} , \quad [3.1.6a]$$

$$c_s = r_s \cdot \left(\frac{\Delta \alpha \cdot \Delta T \cdot E}{(1 - \nu) \cdot \sigma_y} \right)^{1/3} . \quad [3.1.6b]$$

Equations [3.1.6a] and [3.1.6b] predict the extent of the plastic zone in a matrix showing no strain-hardening. From data presented below and measurements on pure silver chloride (Stepanow 1934, 1935), however, it is known that this material exhibits strain-hardening, as most metals do. Use of macroscopic relations giving flow stress as a function of strain history is inappropriate given the microscopic dimensions of plastic flow. We assume that the matrix is monocrystalline, elastically isotropic and single-phased, and make use of the more "microscopic" relationship between dislocation density ρ and flow stress of the matrix τ_y given by the classical equation (Taylor 1934)

$$\tau_y = \tau_{y0} + A G b \sqrt{\rho}, \quad [3.1.7]$$

where τ_{y0} is the intrinsic flow stress of the matrix, G its shear modulus, b the Burgers vector of dislocations in the matrix and the strain-hardening constant A has a value between 0.3 and 0.6 for metals (Bailey and Hirsch 1960, Keh 1962, Livingston 1962, Venables 1962, Mader *et al.* 1963, Hansen 1977) and 0.4 for NaCl (in der Schmitt and Haasen 1961). We assume for the case of interest here - namely the formation of a cylindrical or spherical plastic zone of tangled dislocations surrounding the inclusion - that the impeding effect of one dislocation upon motion of another can be represented by Eq. [3.1.7]. We make the added assumptions that flow stress and dislocation density are uniform within the plastic zone and that the plastic zone size always increases with increasing ΔT . To calculate the extent of the plastic zone around inclusions, we can then use Eqs. [3.1.6] derived above with

$$\sigma_y = 2 \tau_y. \quad [3.1.8]$$

The dislocation density ρ is estimated as the total length of punched prismatic dislocation loops that are needed to relieve the thermal mismatch strains in simple configurations divided by the plastic zone volume. For the sphere, we adopt the model described by Hull and Bacon (1984) wherein it is assumed that loops are punched out along all twelve $\langle 110 \rangle$ directions on glide cylinders intersecting the sphere along circles where the resolved shear stress is maximum (Fig. 3.1.2); the glide cylinders have then a diameter of $\sqrt{2}r_s$. For the cylinder, it is assumed that the axis of the cylinder is aligned along one of the $\langle 111 \rangle$ directions and that infinitely long loops are emitted in the six $\langle 110 \rangle$ directions. We assume

that, as with the sphere, these loops are emitted where the resolved shear stress is maximum, resulting in a loop width of $\sqrt{2}r_c$ (Fig. 3.1.3). Deviation of the particular fiber orientation from $\langle 111 \rangle$ will increase the number of loops if no Burgers vectors perpendicular to the fiber axis is available. For this reason, and because a series of loops of same width but shorter length might be generated instead, the present estimate is most likely a lower bound for the actual dislocation density around a cylindrical inclusion.

The number of dislocation loops in the plastic zone around the cylinder n_c and the sphere n_s is now obtained by dividing the volume of the material to be displaced to relieve thermal mismatch by the volume of material removed by each loop:

$$n_c = \frac{2 \cdot \pi \cdot r_c \cdot \Delta \alpha \cdot \Delta T \cdot r_c}{\sqrt{2} \cdot r_c \cdot b} = \frac{\sqrt{2} \cdot \pi \cdot r_c \cdot \Delta \alpha \cdot \Delta T}{b}, \quad [3.1.9a]$$

$$n_s = \frac{4 \cdot \pi \cdot r_s^2 \cdot \Delta \alpha \cdot \Delta T \cdot r_s}{\pi \cdot \frac{r_s^2}{2} \cdot b} = \frac{8 \cdot r_s \cdot \Delta \alpha \cdot \Delta T}{b}. \quad [3.1.9b]$$

Dividing the total dislocation length by the volume of the plastic zone, the dislocation densities around a cylinder and a sphere are then respectively:

$$\rho_c = \frac{2 \cdot n_c}{\pi \cdot (c_c^2 - r_c^2)} = \frac{2 \cdot \sqrt{2} \cdot \Delta \alpha \cdot \Delta T}{b \cdot r_c \cdot (x_c - 1)}, \quad [3.1.10a]$$

$$\rho_s = \frac{3 \cdot n_s \cdot r_s}{2 \cdot \sqrt{2} \cdot (c_s^3 - r_s^3)} = \frac{6 \cdot \sqrt{2} \cdot \Delta \alpha \cdot \Delta T}{b \cdot r_s \cdot (x_s - 1)}, \quad [3.1.10b]$$

where

$$x_c = \left(\frac{c_c}{r_c}\right)^2, \quad [3.1.11a]$$

$$x_s = \left(\frac{c_s}{r_s}\right)^3. \quad [3.1.11b]$$

Inserting Eqs. [3.1.7], [3.1.8] and [3.1.10] into Eq. [3.1.6] leads to equations for the radius of the plastic zone in a strain-hardening matrix for the cylinder and the sphere respectively:

$$\tau_{y0} + A \cdot G \cdot \sqrt{\frac{2 \cdot \sqrt{2} \cdot \Delta \alpha \cdot \Delta T \cdot b}{r_c \cdot (x_c - 1)}} - \frac{2 \cdot \Delta \alpha \cdot \Delta T \cdot E}{(5 - 4\nu) \cdot x_c} = 0, \quad [3.1.12a]$$

$$\tau_{y0} + A \cdot G \cdot \sqrt{\frac{6 \cdot \sqrt{2} \cdot \Delta \alpha \cdot \Delta T \cdot b}{r_s \cdot (x_s - 1)}} - \frac{\Delta \alpha \cdot \Delta T \cdot E}{2 \cdot (1 - \nu) \cdot x_s} = 0. \quad [3.1.12a]$$

After some algebraic manipulations, these two equations can be transformed into cubic equations:

$$x^3 - x^2(1 + C_1 + 2C_2) + x(C_2^2 + 2C_2) - C_2^2 = 0 \quad [3.1.13]$$

where for the cylinder $x = x_c$ and C_1 and C_2 are dimensionless constants given below:

$$C_1 = \frac{2 \cdot \sqrt{2} \cdot \Delta \alpha \cdot \Delta T \cdot b}{r_c} \left(\frac{A \cdot G}{\tau_{y0}}\right)^2, \quad [3.1.14a]$$

$$C_2 = \frac{\Delta\alpha \cdot \Delta T \cdot G \cdot (1+\nu)}{\tau_{y0} \cdot (1-\nu)} \quad , \quad [3.1.14b]$$

and where, for the sphere, $x = x_s$, and

$$C_1 = \frac{6 \cdot \sqrt{2} \cdot \Delta\alpha \cdot \Delta T \cdot b}{r_s} \left(\frac{A \cdot G}{\tau_{y0}} \right)^2 \quad , \quad [3.1.15a]$$

$$C_2 = \frac{\Delta\alpha \cdot \Delta T \cdot E}{2 \cdot (1-\nu) \cdot \tau_{y0}} \quad , \quad [3.1.15b]$$

For the particular cases explored numerically here (AgCl/Al₂O₃, AgCl/glass and Al/SiC), these equations generally yield three roots, two of which are extraneous. With the strain-hardening constant A equal to zero - corresponding to a non strain-hardening matrix - the cubic equation yields an extraneous root $x=1$ and a double root equal to the value found using Eqs. [3.1.6] with $\sigma_y = 2\tau_{y0}$ (reference value). With $A > 0$ (i.e. for a strain-hardening matrix), the smallest root is still equal to 1 and is discarded since it is non-physical. Of the other two roots, one is larger than the reference value and hence physically absurd, the other is smaller than the reference value and therefore retained.

The critical volume fraction v^* of inclusions for which plastic zones impinge is then for the cylinders and spheres, respectively:

$$v_c^* = \frac{P_c}{x_c} \quad , \quad [3.1.16a]$$

$$v_s^* = \frac{P_s}{x_s} \quad , \quad [3.1.16b]$$

where P_c and P_s are the packing ratios for cylinders and spheres respectively. Since Eqs. [3.1.1] were developed for a single inclusion in an infinite matrix, the volume fractions derived above are larger than the upper limit for the range of validity of Eqs. [3.1.12].

Results from this model for SiC spheres and cylinders of radius $1.5 \mu\text{m}$ in a 99.5% pure aluminium matrix for an arbitrary value for ΔT of 200 K are given in Fig. 3.1.4, using CTE value for SiC of $3.4 \cdot 10^{-6} [\text{K}^{-1}]$ and constants given in Table 3.1. The choice of slightly alloyed aluminium for this example rather than the pure metal was dictated by the fact that, even for the thermal strain rates achievable by quenching, very pure aluminium deforms by slip only at temperatures below 300 K.

The plastic zone radius that results from use of Eqs. (3.1.6) with $\sigma_y = 2 \tau_y$ for a non strain-hardening matrix is given in the same figure. The critical volume fraction and dislocation density are given in Table 3.2 for cylinders and spheres under the same conditions as above. Also listed in Table 3.2 is the increase of yield stress in shear due to the dislocations present in the matrix (Eq. [3.1.7]). Due to strain-hardening, the value of the yield stress in the plastic zone around cylinders and spheres is respectively over 1.5 and 2 times the intrinsic flow stress measured by Hansen (1977).

3.2 Plastic zone size around a particle of irregular form

To the best of our knowledge, all models available in the literature (and the model described above is no exception) use simple, idealized shapes such as spheres or ellipsoids to describe particles in MMC. However, the commercially available particulate reinforcement used in most MMC usually exhibits irregular form and sharp angles. To model such a system would necessitate a complex

statistical treatment as well as a thorough knowledge of the geometrical parameters best describing the particles. Due to the complexity of such an approach, investigators have assumed that irregular shapes are adequately represented by the mathematically tractable simple geometric bodies mentioned above. In what follows, we make the assumption that a particle of irregular shape and a sphere with the same volume both generate a plastic zone of same volume. We thus assume that the average dislocation density around a particle is equal to that of a sphere of the same volume as the particle. This is reasonable if the size of the emitted loops is about the same in both cases, since the volume of matrix to be "displaced" at the interface by dislocation nucleation is dictated by the total thermal mismatch, which is itself independent of the shape of the particle.

From the assumption of equality of volumes between bodies of irregular shape and spheres made above, we now define the equivalent radius of the particle r_e as the radius of the sphere having the same volume,

$$r_e = \left(\frac{3 V_p}{4 \pi} \right)^{1/3} , \quad [3.2.1]$$

and the equivalent radius of the plastic zone around the particle c_e as the radius of the spherical plastic zone around the sphere,

$$c_e = \left(\frac{3 (V_p + V_z)}{4 \pi} \right)^{1/3} , \quad [3.2.2]$$

where V_p is the particle volume and V_z is the plastic zone volume. If the volume of a particle is known, its equivalent radius can be calculated using Eq. [3.2.1]. Eq. [3.1.13] then predicts the equivalent radius of the plastic zone from

which the volume of the plastic zone around the particle can be calculated using Eq. [3.2.2]. In a system containing a distribution of particles of different shapes, the only knowledge necessary is therefore the distribution of volumes. A straightforward method to obtain such information is by direct size measurement of a statistically large number of particles. For small particles, this can be done by direct inspection of the projection of the opaque particles on photomicrographs from the transmission optical microscope.

While the volume of a sphere can be very simply determined from the surface of its projection, the same is not true for bodies of irregular form. Certain general topological relationships hold, however, for a system of convex bodies of single shape and size randomly oriented in space (Underwood 1972). The volume V of a body is a function of its mean projected area $\overline{A'}$ and its mean intercept length \overline{L}_3 ,

$$V = \overline{A'} \cdot \overline{L}_3 \quad . \quad [3.2.3]$$

The mean projected area can be expressed by two other projected values, the mean intercept length of the projected area \overline{L}_2' and the mean projected height of the body \overline{H}' (Fig. 3.2.1),

$$\overline{A'} = \overline{L}_2' \cdot \overline{H}' \quad . \quad [3.2.4]$$

The mean intercept length \overline{L}_3 is a three-dimensional property which cannot be expressed in term of two-dimensional projected values only. This reflects the fact that information is lost in the passage from a three-dimensional object to a two-dimensional projection, unless the shape of the object is known independently. We define a constant K such that

$$\bar{L}_3 = K \cdot \bar{L}_2' \quad [3.2.5]$$

This shape-dependent constant is calculated in Table 3.3 for different regular bodies, starting from the values of V , \bar{A}' and \bar{H}' given by Underwood (1970). Eqs. [3.2.3] - [3.2.5] can then be combined into an expression for the volume which contains only projected variables:

$$V = \frac{K \cdot \bar{A}'^2}{\bar{H}'} \quad [3.2.6]$$

Since the particles are randomly oriented in the matrix, the area projected in the image plane of the microscope is taken as the mean projected area and the mean projected height is approximated as the mean projected height of the projected area. Both above assumptions are valid if a large enough number of particles is considered. Since the shape of the particle is not known, the average of the minimum and maximum values for K given in Table 3.3 is taken ($K=0.69$). This approximation induces a relative error of 28% if the true shape of the particle is that of the bodies in Table 3.3 with the maximum or minimum K values. The actual error will probably not exceed much this value if the shape of the particles is not too drastically different from that of the regular bodies listed in Table 3.3. Eq. [3.2.6] can thus be used to approximate the volume of the particles and their plastic zone needed in Eq. [3.2.1] and [3.2.2].

3.3 Micromechanics of a row of punched prismatic loops

3.3.1 Row relaxed configuration

Consider a circular prismatic dislocation of diameter d and Burgers' vector b lying in the plane $z=0$ with its centre at the origin of a cylindrical coordinate system r, ϕ and z . The shear stress $\tau_{rz}(\rho, \zeta)$ induced by this loop in the infinite, isotropic crystal is given by Kroupa (1960) and Bullough and Newman (1960) as:

$$\tau_{rz}(\rho', \zeta) = \frac{bG}{d(1-\nu)} \int_0^{\infty} J_1(2t\rho') J_1(t) t^2 \exp(-2t\zeta) dt, \quad [3.3.1]$$

with

$$\begin{aligned} \zeta &= \frac{z}{d} \\ \rho' &= \frac{r}{d} \end{aligned}, \quad [3.3.2]$$

where G is the shear modulus, ν the Poisson's ratio and J_1 the Bessel function of first order. Eq. [3.3.1] can be rewritten as a function of complete elliptical integrals E and K . The shear stress on the glide cylinder $\tau_{rz}(1/2, \zeta)$ is then (Kroupa, 1960):

$$\tau_{rz}\left(\frac{1}{2}, \zeta\right) = \frac{bG}{2\pi d(1-\nu)} \cdot \frac{\zeta \cdot K\left[\left(\zeta^2 + 1\right)^{-1/2}\right] - \left(\zeta - \zeta^{-1}\right) \cdot E\left[\left(\zeta^2 + 1\right)^{-1/2}\right]}{\left(\zeta^2 + 1\right)^{3/2}}. \quad [3.3.3]$$

This shear stress on the glide cylinder decays rapidly with distance and increases with decreasing loop diameter. Bullough and Newman (1960) used Eq. [3.3.1] to determine loop spacings in a row of coaxial, prismatic dislocation loops of diameter d in the half space $z \geq 0$, the first loop being fixed and located at the

origin. They calculated the dimensionless position ζ for each loop within a row of ten loops for three different values of the dimensionless parameter v :

$$v = \frac{2 \pi d (1-v) \tau_c}{b G}, \quad [3.3.4]$$

where τ_c is the local critical shear stress (or loop friction stress) needed to move the dislocation constituting the loop against the lattice friction. The equilibrium configuration of such a row is reached when the shear stress on each and every loop (except the last punched loop) due to its neighbours is equal to τ_c .

The choice of the number of neighbours to be considered in the stress computation can be made arbitrarily, as did Bullough and Newman (1960). Mathematically, all neighbouring loops should be considered since the elastic stress field has an infinite reach; this n-body equilibrium problem however leads to prohibitively long calculation times for a large number of loops in the row. As a compromise, we consider only neighbours which exert a stress larger than the critical shear stress on the loop to be equilibrated. We expect this assumption to be at possible fault only at the ends of the row, where the stress fields of distant loops do not cancel one another. When this situation occurs at the blocked end of the row, the relative error is small since nearest neighbour loop spacings are at their smallest. The stress due to nearest neighbours is therefore very large compared to τ_c . At the other "free" end, loop spacings are generally large, so the stresses due to higher order neighbouring loops is most likely to decay rapidly below the loop friction stress.

A first-order approximation is to consider only nearest neighbour interactions. The problem then has a mathematically simple solution, which is most easily derived by considering a physically equivalent, and conceptually simpler,

situation. Imagine a row of n identical solid bodies, aligned on a single axis, and only able to move along that axis. Each body is connected to its two nearest neighbours by a non-linear spring (Fig. 3.3.1), which exerts a repulsive force F_S :

$$F_S(\Delta\zeta) = \pi d b \tau_{rz}(1/2, \Delta\zeta) , \quad [3.3.5]$$

where $\tau_{rz}(1/2, \Delta\zeta)$ is given by Eq. [3.3.3] and $\Delta\zeta$ is the distance between the body and its neighbour. Motion of each body is opposed by a constant friction force F_F :

$$F_F = \pi d b \tau_c . \quad [3.3.6]$$

The first body is pushed towards its neighbours until all bodies move at steady state along the axis. Now, consider the i^{th} body in this row of n bodies, $i=1$ denoting the body on which the external force is applied. The spring between body i and its neighbour $i+1$ - which are separated by a distance $\Delta\zeta_i$ - must oppose a force equal to the friction of the $(n-i)$ bodies that are moving ahead of it

$$F_S(\Delta\zeta_i) = (n-i) \cdot F_F , \quad [3.3.7]$$

or, after introducing Eqs. [3.3.5] and [3.3.6] in Eq. [3.3.7]:

$$\tau_{rz} (1/2, \Delta\zeta_i) = (n-i) \cdot \tau_c . \quad [3.3.8]$$

The spacing is then found by inserting Eq. [3.3.3] in Eq. [3.3.8] and solving for $\Delta\zeta_i$.

Since all governing equations are the same, the configuration of the row of moving bodies is identical to that of the row of loops under consideration (Fig. 3.3.2). The position of loop i , ζ_i , measured from the blocked loop, is:

$$\zeta_i = \sum_{j=1}^{i-1} \Delta\zeta_j . \quad [3.3.9]$$

The total train length is ζ_n . It is noted that the position of loop i measured from the opposite, "free" end of the train, $\zeta_n - \zeta_i$, is independent of the total number of loops n in the train.

The problem is therefore solved by successive solution of equation [3.3.8], the n -body solution being constructed as a superposition of $(n-1)$ two-body solutions.

A computer program listed and explained in Appendix 2 was written to find the equilibrium configuration of a row of loops, using Eq. [3.3.3] and a numerical solution for elliptical integrals given by Abramovitz and Stegun (1972). Eq. [3.3.8] was used to generate the initial loop positions. The computational algorithm was designed to seek equilibrium positions of each loop in a row, starting with the last "free" one, by changing loop position until the stress to which it is subjected falls in the range $\tau_c \pm 0.005 \cdot \tau_c$. This iterative procedure was stopped when the equilibrium condition was satisfied for all loops in the row (except the first one), and no loop in the row was moved in the last iteration by both more than 0.5% of the distance to the origin, and more than an absolute value of $\Delta\zeta = 10^{-3}$.

Different initial conditions were also tried to check for chaotic behaviour. Results were identical provided that the shear stress on each loop in the initial configuration was larger than the critical shear stress, i.e., provided that each

loop was initially submitted to a stress pushing it in the positive direction of the z-axis away from the blocked loop. It was also found that the computation time was significantly decreased by using an initial condition based on results from previous computations for $n' < n$ for the first n' loops, and Eq.[3.3.8] for the remaining loops. This initial condition was used in most of this work.

While considering all relevant neighbours makes the calculation significantly more lengthy than using the second-nearest neighbour assumption made by Bullough and Newman (1960), results differ significantly at small loop spacings. An example for a row of 100 loops is given in Fig. 3.3.3 with the parameter v equal to 0.1 and 1, and compared with those of the nearest neighbour solution (Eq. [3.3.8]). It is found that Eq. [3.3.8] constitutes an excellent approximation for values of v smaller than 0.1.

The minimum distance between two loops in a row $\Delta\zeta_1$ is found to decrease exponentially with the total number of loops n in the row (Fig. 3.3.4). This minimum distance is of interest since it defines the maximum number of loops for which the present calculation is meaningful: since Eqs. [3.3.1] and [3.3.3] are based on continuum mechanics, they are only valid for loop spacings much larger than a Burgers vector, i.e. when $\Delta\zeta_1$ is much larger than b/d .

Fig. 3.3.5 displays the length of the row, i.e., the position of the last loop ζ_n . It is found that, for the values of v and n explored, the length of a row is closely approximated by a power-law function of the total number of loops:

$$\zeta_n = A n^C, \quad [3.3.10]$$

where A'' and C are functions of v . It is also found that, for $0.05 \leq v \leq 5$, the exponent C is roughly constant (Fig. 3.3.5) and A'' is a power-law function of v (Fig. 3.3.6).

A two-parameter best-fit relationship for both parameters n and v , valid for $0.05 \leq v \leq 5$ and values of n plotted in Fig. 3.3.3 was then calculated using the computer program listed in Appendix 3:

$$\zeta_n = 1.74 v^{-0.64} n^{0.34} \quad [3.3.11]$$

The relative error when using this expression is on average 14%, the maximal deviation found being 25%. Thus, if the length and number of loops of a row are known experimentally, the parameter v and therefore the loop friction stress can be found. In practice however, it can be difficult to determine the exact number of loops in a row either because of lack of resolution (as in X-ray topography and decoration techniques) or because the field of view is smaller than the row length (as in transmission electron microscopy). An equally suitable and more convenient parameter to determine v is then the spacing $\Delta\zeta_{n-1}$ between the last and the penultimate loops of a row. This spacing is virtually independent of the total number of loops in the row n , but is sensitive to v (Fig. 3.3.7). Curve-fitting yields:

$$\log v = 0.866 - 1.08 \Delta\zeta_{n-1} + 0.102 \Delta\zeta_{n-1}^2 \quad [3.3.12]$$

The average dislocation density ρ in the volume defined by the glide cylinder and the first and last loop is then

$$\rho = \frac{4n}{dL_r}, \quad [3.3.13]$$

or, introducing Eq. [3.3.11] into Eq. [3.3.13]:

$$\rho = \frac{2.30 v^{0.64} n^{0.66}}{d^2} \quad [3.3.14]$$

Due to the unequal spacing of the loops, this density is not constant in the glide cylinder, being higher than average close to the fiber and lower at the other end of the row.

We now turn to the problem of two rows of prismatic loops, respectively of interstitial atoms and vacancies, placed symmetrically on each side of the plane $z=0$ and prevented from annihilating by locking of the leading loop of each row, held a reduced distance $\Delta\zeta_0$ apart (Fig. 3.3.8). This problem has been treated by Head (1959) for straight dislocations of infinite length. The solution to this problem is the same as that of a row perpendicular to a free surface with the first loop held at a distance $\Delta\zeta_0^*/2$ from the surface (Hirth and Lothe, 1982). Alternatively, the double train can arise when, upon shearing of a two-phase material, an inclusion produces two rows of geometrically necessary loops of opposite Burgers' vector on each of its sides (Hirsch, 1957).

The relative difference in loop spacings δ_i in the undisturbed row $\Delta\zeta_i$ and the corresponding spacing in the double row $\Delta\zeta_i^*$:

$$\delta_i = \frac{\Delta\zeta_i - \Delta\zeta_i^*}{\Delta\zeta_i}, \quad [3.3.15]$$

is shown in Fig. 3.3.9 for two values of v and $\Delta\zeta_0^*$. The program used is listed in Appendix 4. The disturbance decays more rapidly for the larger value of v , since the overall distance from the origin of each loop is larger and thus the attraction of the opposite train is smaller. As expected, the smaller value of $\Delta\zeta_0$ leads to a larger disturbance for the first loops of the train and a larger number of loops which are significantly disturbed. The absolute value of the departure is, however, small for all loops, even for the small values of $\Delta\zeta_0$. The attractive effect might hardly be noticeable experimentally, except for the very first closely spaced loops of the row. This implies, for example, that the loop friction stress can be measured with adequate precision using Eq. 3.3.12, which was derived for a single row of loops in an otherwise stress-free crystal.

3.3.2 Row backstress on an inclusion

To calculate the backstress on a cylindrical inclusion by a row of n loops in a crystal with friction stress τ_f , we consider a hypothetical crystal with zero friction stress. Assume that this crystal contains the same inclusion which has punched the same row of n coaxial, circular, prismatic loops of length l and Burgers vector b . If the loop were free to move, they would repel each other and glide an infinite distance away from the inclusion, since there would be no friction stress to stop them. Imagine now that the hypothetical crystal is subjected to an external shear stress τ which prevents the loops from escaping to infinity. If the loops are assimilated to straight edge dislocations of the same length, the force F on the inclusion by the pile-up is (Eshelby 1957):

$$F = n \tau b l . \quad [3.3.16]$$

If the value of this external shear stress is chosen as that of the friction stress of the real lattice τ_f , the spacing of the loops and therefore the backforce F_B on the inclusion is the same in both cases:

$$F_B = n \tau_f b l . \quad [3.3.17]$$

The real crystal with a friction stress τ_f has thus been replaced by an hypothetical crystal with zero friction stress but an external shear stress τ_f . Since the spacings of the loop is the only parameter determining the magnitude of the backforce, it is identical in both situations. Assuming that the loops of length πd exert a force $F_B = \sigma_B \pi d^2 / 4$ at the end of the fiber of same diameter, the backstress σ_B is calculated from Eq. [3.3.17] as

$$\sigma_B = \frac{4 n \tau_f b}{d} . \quad [3.3.18]$$

The same result can be reached using a virtual work argument, described below for the more general case where the shape of the source of the row is not assumed to be cylindrical. Consider an equilibrated row of n dislocation loops, emanating from an inclusion of second phase material, the surface of which is "greased" so that it can move freely through the crystal while atoms in the vicinity of the interface relocate reversibly by diffusion to allow motion of the inclusion at no energy cost. Suppose now that the inclusion is slowly pushed by a force F_B toward the equilibrated row of loops, by a distance dx larger than several interatomic spacings (Fig. 3.3.10). Since they are at equilibrium, the loops move with the particle, the end-result being a translation by a distance dx of the entire system particle/row of loops.

The work dW_b spent in the operation

$$dW_b = F_B dx \quad [3.3.19]$$

is equal to the energy dW_f dissipated by the n loops moving against the friction force F_f

$$dW_f = n F_f dx , \quad [3.3.20]$$

since the particle is assumed to move reversibly.

Assuming that the force on the inclusion induces an average stress σ_b :

$$\sigma_b = F_B/A , \quad [3.3.21]$$

where A is the cross-sectional area of the inclusion, the average backstress is found by introducing Eqs. [3.3.6] and [3.3.21] into Eqs. [3.3.20] and [3.3.19] respectively which are then equated:

$$\sigma_b = \frac{n \tau_f b \pi d}{A} . \quad [3.3.22]$$

Introducing into Eq. [3.3.22] the value $A=\pi d^2/4$ for the cylinder yields Eq. [3.3.18]. It is noted that, while the form and range of the stress field will determine the spacing of the equilibrated row, it has no influence on the backstress on the inclusion. The above derivation is only valid in an infinite crystal with a single inclusion and row of loops. For closely spaced inclusions with interacting rows of loops, Ashby's derivation (1966, 1970) of the average backstress should be used.

We also note that a similar derivation can be used to ascertain that the force exerted by a pile-up of n dislocations of length L on an obstacle in an applied shear stress field τ much higher than the loop friction stress, is $n\tau b L$. Repeating the thought experiment described above in the non-zero stress field, the work dW done against the stress field is:

$$dW = n \tau b L dx . \quad [3.3.23]$$

The force exerted by the dislocations on the inclusion is therefore $n \tau b L$ (Hirth and Lothe 1982), and the backstress on the particle is found by replacing τ_f in Eq. [3.3.22] by τ .

These simple derivations are approximate because changes in the stress state of the inclusion induced by "greasing" the interface (which relaxes interfacial stresses) are neglected. Also, the results say nothing about the local stress distribution inside the inclusion.

3.4 Longitudinal emission of loops at fiber end

In this section, we present a theoretical model describing the emission of prismatic loops at fiber ends due to the longitudinal thermal mismatch of a cylindrical fiber in a matrix deforming by slip. We use both continuum mechanics and the dislocation equilibrium results derived in the previous paragraph to derive the number of loops punched by the fiber when the interface is elasto-plastic. We also give expressions for the fiber longitudinal stress and the interface shear stress after punching. We finally perform a parametric study on the system Al/Al₂O₃ to illustrate the model and compare it to another by Taya and Mori (1987).

Consider a perfectly elastic fiber in a matrix capable of plastic deformation by dislocation movement. Upon cooling from an elevated temperature, thermal stresses will develop due to the CTE mismatch between the fiber and the matrix. We neglect the radial stresses, which are small compared to the axial stresses for a slender body, and we assume an elastic, perfectly plastic matrix showing no strain-hardening. At high temperature, the fiber is embedded in the matrix and both phases are initially stress-free. Upon cooling, the matrix shrinks more than the fiber if we assume that the matrix CTE is larger than that of the fiber (as is the case in most MMC systems). This results in a stressed interface with the fiber in compression and the matrix in tension. At first, the interface is stressed elastically by shear along the whole length of the fiber. As the temperature decreases, the total mismatch strain between fiber and matrix increases and the interfacial shear stress increases proportionally. At some temperature, for certain fiber lengths, the interfacial shear stress may equal the matrix plastic flow stress, at which point dislocation motion is induced in the matrix. This changes the nature of the stress distribution along the fiber, just as it does in a short fiber composite in tension (Kelly and Macmillan, 1986a). Whatever the nature of the stress at the interface, so long as there is no debonding (a situation which we exclude here), stress builds up in the fiber as the result of load transfer from the matrix. The resulting fiber strain reduces the local mismatch between fiber and matrix.

In summary, three different local situations are possible at the fiber/matrix interface, which may occur along the same fiber:

- unstrained interface: the fiber is stressed elastically to a strain equal to the CTE mismatch strain.

- elastic interface: both fiber and matrix are stressed elastically; the interfacial shear stress is everywhere lower than the critical shear stress at which slip is initiated.

- plastic interface: the critical shear stress is reached, thus inducing slip at the interface.

3.4.1 Elastic interface

Consider a cylindrical fiber of length L , diameter d , parallel to the x -axis and centered at the origin. We use the shear lag model developed by Cox (1952) for a single fiber embedded in a matrix submitted to an uniaxial strain e at infinity applied along the same direction as the main axis of the fiber. In this model, it is assumed that

$$\frac{dp}{dx} = H'' (u-w) , \quad [3.4.1]$$

where p is the load on the fiber, H'' is a constant, u is the longitudinal displacement in the fiber and w is the hypothetical displacement at the same point in the absence of the fiber. The axial stress in the fiber $\sigma(x)$ can then be expressed as

$$\sigma(x) = E_f e \left[1 - \frac{\cosh(\beta \cdot x)}{\cosh(\beta \cdot L / 2)} \right] , \quad [3.4.2]$$

while the interfacial shear stress τ_x is

$$\tau(x) = \frac{E_f \cdot d \cdot e \cdot \beta}{4 \cdot \cosh(\beta \cdot L/2)} \sinh(\beta \cdot x) , \quad [3.4.3]$$

where

$$\beta = \frac{4}{d} \sqrt{-\frac{G_m}{E_f \ln(v_f)}} , \quad [3.4.4]$$

and E_f is the fiber elastic modulus, x the distance from the origin, G_m the matrix shear modulus and v_f the fiber volume fraction. Eqs. [3.4.2] and [3.4.3] are related by

$$\frac{d\alpha(x)}{dx} = -\frac{4}{d} \tau(x) . \quad [3.4.5]$$

This analysis, which was later refined by Dow (1963), was found to be experimentally correct by Tyson and Davies (1965) for a 4 mm diameter cylinder embedded in a photoelastic polymer, except close to the ends of the fibers (about two diameters from the extremity), where the measured shear stress was higher than predicted by Eq. [3.4.3] due to stress concentration at the end faces discontinuity. Schuster and Scala (1964) embedded a sapphire whisker in a polymeric birefringent matrix and also found a good correlation with the model above. Fig. 3.4.1a shows schematically the interfacial displacement and the interfacial shear stress which are zero at the fiber center and maximum at its ends. Since the fiber longitudinal stress is built up from the shear stress transfer from the matrix, it is zero at fiber ends (assuming no load transfer from the end faces) and maximum at the fiber center.

We assume that Eq. [3.4.1] is valid for the case where the matrix shrinks (or expands) around a fiber, neglecting the radial strains. The same equations used for the shear-lag model (Eqs. [3.4.2] - [3.4.4]) can then be used if the external strain e is assimilated to the thermal mismatch strain:

$$e = \Delta\alpha \cdot \Delta T , \quad [3.4.6]$$

with

$$\Delta\alpha = \alpha_m - \alpha_f , \quad [3.4.7]$$

where α_m and α_f are respectively the matrix and fiber coefficient of thermal expansion and ΔT is the temperature difference between the higher temperature (stress-free state) and the lower temperature (stressed state). The axial fiber stress and the interfacial shear stress are found by inserting Eq. [3.4.6] into Eqs. [3.4.2] and [3.4.3].

As can be seen from Eq. [3.4.2], the fiber longitudinal stress increases as x decreases and is maximum at the fiber center. Simple inspection of Eq. [3.4.2], however, shows that the maximum fiber stress (at $x=0$) will never reach the value $E_f e$ for a fiber of finite length L . Thus, in the purely elastic case, an unstrained interface cannot occur under the present assumptions, except of course at the exact center of the fiber.

The interfacial shear stress is maximum at the fiber end ($x=L$) and increases as L increases. At some critical fiber length L_p , the critical shear stress τ_c is reached at the end of the fiber where plastic flow and dislocation emission begin. Introducing Eq. [3.4.6] as well as the values

$$\tau = \tau_c , \quad [3.4.8a]$$

$$x = L_p/2 , \quad [3.4.8b]$$

$$L = L_p , \quad [3.4.8c]$$

in Eq. [3.4.3] gives an equation for L_p :

$$L_p = \frac{2}{\beta} \operatorname{arctgh} \left[\frac{4 \cdot \tau_c}{\beta \cdot E_f d \cdot \Delta \alpha \cdot \Delta T} \right] . \quad [3.4.9]$$

If the fiber is longer than L_p , the interface at the ends of the fiber is plastic. We now consider the case when this happens.

3.4.2 Plastic-elastic interface

In the unstrained state at a higher temperature, the fiber of length L_0 can be thought of as occupying a hole of same length in the matrix (Fig. 3.4.2a). Upon cooling by a temperature interval of ΔT , the fiber length - if it were outside the matrix - would become L_f while the hole in the matrix in absence of the fiber would have a length L_m . Fitting the fiber in the hole will force both the fiber and the hole to adopt a length L , which is intermediate between L_f and L_m (Fig. 3.4.2b).

It is assumed that slip is the only relaxation mechanism in the temperature interval ΔT , and that the fiber axis is oriented along a slip direction. Plasticity originates from the fiber end because the shear stress is maximum there and because the fiber end corner acts as a stress concentrator. The end of the fiber then acts like a punch and creates a pair of prismatic dislocation loops with opposite Burgers vector parallel to the fiber axis. One of these is a prismatic interstitial loop which glides away from the fiber end into the matrix, repelled by the local stress field of the fiber and that of subsequently formed interstitial loops.

The vacancy loop can be thought as gliding in the other direction along the interface away from the fiber end and relaxing the stressed interface. The glide length defines the plastic zone. In reality, it is more probable that the vacancy loops are delocalized along the whole length of the plastic zone, i.e., the atomic planes shift slightly due to the addition of an additional plane at the interface, leading to a reduction of the elastic stress at the fiber end. The plastic zone can be thought of as the interfacial length where this shift is appreciable. The fiber thus relaxes its interface and emits in the matrix along the x-axis a row of coaxial, circular, interstitial, prismatic dislocation loops of diameter d . Since each loop carries away a disk of matrix material of thickness equal to its Burgers vector b , the number of loops n punched at each end is, by conservation of volume:

$$n = \frac{L - L_m}{2 \cdot b} . \quad [3.4.10]$$

Now, Hooke's law applied to the elastic fiber gives

$$\frac{L_f - L}{L} = \frac{\bar{\sigma}}{E_f} , \quad [3.4.11]$$

where the average stress in the fiber is

$$\bar{\sigma}(L) = \frac{2}{L} \int_0^{L/2} \sigma(x) dx , \quad [3.4.12]$$

while the CTE equations yield

$$\frac{L_0 - L_m}{L_m} = \alpha_m \cdot \Delta T , \quad [3.4.13]$$

$$\frac{L_0 - L_f}{L_f} = \alpha_f \Delta T, \quad [3.4.14]$$

assuming the CTE's are isotropic and temperature independent. Combining Eqs. [3.4.7], [3.4.10], [3.4.11], [3.4.13] and [3.4.14] then gives

$$n = \frac{L}{2 \cdot b \cdot (1 + \alpha_m \cdot \Delta T)} \left[\Delta \alpha \cdot \Delta T - (1 + \alpha_f \Delta T) \frac{\bar{\sigma}(L)}{E_f} \right]. \quad [3.4.15]$$

Thus, one only needs to evaluate the average stress $\bar{\sigma}(L)$ defined in Eq. [3.4.12] to find through Eq. [3.4.15] the number of loops punched at the end of the fiber. This necessitates a knowledge of the function $\sigma(x)$ or equivalently of $\tau(x)$ (Eq. [3.4.5]).

The fiber longitudinal stress is shown schematically in Fig. 3.4.3. The integral of this stress function can be decomposed in four parts (right hand side of Eq. [3.4.16]) labelled 1 to 4 in Fig. 3.4.3:

$$\bar{\sigma}(L) = \frac{2}{L} \cdot \int_0^{L_p/2} \sigma_e(x) dx + \frac{(\sigma^* - \sigma_B)}{2 \cdot L} \cdot (L - L_p) + \frac{(\sigma^* - \sigma_B)}{L} \cdot L_p + \sigma_B, \quad [3.4.16]$$

where σ^* is the fiber longitudinal stress at the point where the interfacial shear stress reaches the critical shear stress, σ_B is the backstress on the end face of the fiber by the punched loops and $\sigma_e(x)$ is the contribution by the elastic interface to the fiber longitudinal stress. In what follows, we calculate these three variables.

We first evaluate the integral of $\sigma_e(x)$. The elastic stress profile $\sigma_e(x)$ is independent of the fiber total length in the elastic/plastic regime. In other words, the stress diagrams of fibers of different lengths in that regime will match

when superimposed. Fig. 3.4.4a shows the superimposed diagrams of the interfacial shear stress for three fibers of length L_p , L and L_u such that $L_p \leq L \leq L_u$, the length L_u corresponding to the boundary between the elastic-plastic and the elastic-plastic-unstrained regimes. It follows from Eq. [3.4.5] that the fiber longitudinal stress diagrams can also be superimposed, with a shift of the coordinate system due to the integration variable. This is shown schematically in Fig. 3.4.4b for the same three fiber lengths as in Fig. 3.4.4a (the backstress σ_B increases with the length of the fiber and is derived in section 3.3.2). The first term of the right hand side of Eq. [3.4.16] is thus independent of the fiber length and can be calculated by integrating Eq. [3.4.2] with $L=L_p$. This yields after introduction of Eqs. [3.4.6] and [3.4.9]

$$\frac{2}{L} \cdot \int_0^{L_p/2} \sigma_e(x) dx = E_f \cdot \Delta\alpha \cdot \Delta T \cdot \frac{L_p}{L} - \frac{8 \cdot \tau_c}{\beta^2 \cdot d \cdot L} \quad [3.4.17]$$

We now determine σ^* , the stress induced in the fiber by the plastic interfacial region. Considering the fiber of length $L > L_p$, the interfacial shear stress and fiber stress gradient in the plastic interface region, i.e., for values of x between $L_p/2$ and $L/2$ are respectively (Fig. 3.4.4b):

$$\tau(x) = \tau_c \quad , \quad [3.4.18]$$

$$\frac{d\sigma(x)}{dx} = 2 \cdot \frac{\sigma^* - \sigma_B}{L - L_p} \quad [3.4.19]$$

Inserting Eqs. [3.4.18] and [3.4.19] into Eq. [3.4.5] then gives an expression for σ^* :

$$\sigma^* = \frac{2 \cdot \tau_c}{d} (L - L_p) + \sigma_B . \quad [3.4.20]$$

Inserting Eqs. [3.4.17] and [3.4.20] into [3.4.16] finally yields

$$\bar{\alpha}(L) = E_f \Delta\alpha \cdot \Delta T \cdot \frac{L_p}{L} + \frac{\tau_c}{d \cdot L} (L^2 - L_p^2 - 8 \cdot \beta^{-2}) + \sigma_B , \quad [3.4.21]$$

where σ_B is given by Eq. [3.3.18]. It appears from inspection that, even for large values of n , the terms containing σ_B are small compared to the other terms in these equations. The backstress of the loops on the fiber has thus a minor effect on the stress state of the fiber and the interface.

Inserting Eqs. [3.4.21] and [3.3.18] into Eq. [3.4.15] gives an equation for n as a function of geometrical and thermomechanical parameters, all assumed to be isotropic and temperature independent:

$$n = \left(1 + \frac{(1 + \alpha_f \Delta T) 2 \cdot L \cdot \tau_c}{(1 + \alpha_m \Delta T) \cdot d \cdot E_f} \right)^{-1} n' , \quad [3.4.22]$$

where

$$n' = \frac{L}{2 \cdot b \cdot (1 + \alpha_m \Delta T)} \left\{ \frac{\tau_c}{d \cdot E_f} (1 + \alpha_f \Delta T) \left(L_p^2 + \frac{8}{\beta^2} - L^2 \right) + \Delta\alpha \cdot \Delta T \cdot [L - L_p \cdot (1 + \alpha_f \Delta T)] \right\} \quad [3.4.23]$$

is the solution of Eq. [3.4.21] for $\sigma_B=0$. For most systems of interest, σ_B is very small and thus n and n' are almost equal (Eq. [3.4.21]).

3.4.3 Plastic-elastic-unstrained interface

In the elastic/plastic regime, the maximum fiber stress in the central fiber region increases with increasing fiber length since the length of the plastic region increases too, loading the fiber linearly from the fiber ends (Eqs. [3.4.5] and [3.4.18]). Above a certain critical length L_u , the fiber will be strained by the matrix to such a degree that a region in the middle of fiber forms which exhibits no strain mismatch with the matrix. The interfacial displacement and shear stress are zero in that region, and the fiber strain has a value of $\Delta\alpha\Delta T$.

L_u is thus the critical length of the fiber between the two regimes plastic/elastic and plastic/elastic/unstrained, corresponding to the fiber length where the maximum strain $\Delta\alpha\Delta T$ is reached at the center of the fiber. The interfacial shear stress and fiber stress are shown in Fig. 3.4.4b (lower fiber stress diagram). The fiber stress at the origin is maximum and has the value

$$\alpha(0) = E_f \Delta\alpha \cdot \Delta T \quad , \quad [3.4.24]$$

From Fig. 3.4.4a

$$\alpha(0) = \sigma_{e,max} + \sigma_{max}^* \quad , \quad [3.4.25]$$

where $\sigma_{e,max}$ and σ_{max}^* are the stress contributions from the elastic and plastic interface regions respectively. Inserting Eq. [3.4.2] (with $x=0$ and $L=L_p$), Eq. [3.4.20] (with $L=L_u$ and $\sigma_B=\sigma_{Bmax}$) and Eq. [3.4.24] into Eq. [3.4.25] yields

$$L_u = L_p + \frac{E_f d \cdot \Delta \alpha \cdot \Delta T}{2 \cdot \tau_c \cdot \cosh(\beta \cdot L_p / 2)} - d \cdot \frac{\sigma_{Bmax}}{2 \cdot \tau_c} , \quad [3.4.26]$$

where σ_{Bmax} is the backstress on the fiber of length L_u .

Inserting $L=L_u$ as given by Eq. [3.4.26] into Eqs.[3.4.23] or [3.4.22] gives the maximum number of punched loops. Any fiber of length larger than L_u will punch this maximum number of loops regardless of its length, since the unstrained length in its center part does not contribute to the strain mismatch.

In summary, depending upon the length of the fiber and the values of the thermomechanical properties of the fiber and the matrix, three main global regimes can be distinguished for a fiber:

a. elastic interface: the whole interface is elastic; the interfacial shear stress is everywhere below the critical shear stress and no dislocation loops are created.

b. plastic/elastic interface: both ends of the fiber have a plastic interface while the interface in the central region is elastic. The plastic interface forms when the fiber tip creates pairs of prismatic loops of vacancy and interstitial character respectively. The interstitial loop is punched from the fiber end into the matrix and glides away from the fiber. It leaves behind a vacancy loops which glides in the opposite direction along the fiber interface to relieve the interfacial mismatch.

c. plastic/elastic/unstrained interface: the interface at both ends of the fiber is stressed plastically and then elastically; the load transfer is such that the central part of the fiber is elastically strained to the point that there is no local mismatch with the matrix, leading to an unstrained interface.

Figs. 3.4.1a-c schematically show the interface displacement, interfacial shear stress and fiber axial stress for the three cases cited above; only half of the fiber is

represented since these functions are symmetric with respect to the origin. We note that an elastic zone always exists because the interfacial displacement and thus the shear stress are zero at the fiber center.

3.4.4 Effect of fiber residual stresses on punching distance

In what follows, we estimate the shear stress in the vicinity of a fiber with residual stresses and its effect on the punching distance. Even after punching, the fiber and the interface are stressed elastically as shown in the previous paragraphs, thus inducing a shear stress on the glide cylinder which can alter the equilibrium position of the row of loops and therefore the row length. As illustrated in Fig. 3.3.9, large perturbations in the stress state at the row end closest to the blocked loop do not significantly change the row length. On the other hand, perturbations at the "free" end of the row have much larger effects on the local loop spacings and thus the row length.

We do not seek to evaluate the stress close to the sharp corner formed by the end of the cylinder. It is likely to be high in the immediate vicinity of the singularity and to decay rapidly away from it. For instance, Schneider and Conway (1969) found that, at a distance of 0.14 diameter from the end of a flat-end rectangular fiber, the shear stress was only a third of the uniform tensile stress applied at infinity. Similarly, Atkinson *et al.* (1982) found that the shear stress decays very rapidly in the matrix close to the end of a partially embedded fiber subjected to a pull-out test. Except in the small region close to the stress singularity, the matrix stress is dominated by the contribution of the residual fiber stress; this matrix shear stress is calculated in what follows on the glide cylinder where the loops are located.

Let us represent the fiber by a semi-infinite cylinder of diameter d , the end of which is at the origin of a cylindrical coordinate system z, r, θ . It is assumed that the interfacial shear stress along the fiber is constant and equal to its maximal value τ_c , corresponding to a fully plastic interface. These two assumptions, of semi-infinite fiber and fully plastic interface, will yield an upper bound for the matrix shear stress since actual fibers are finite in length and since the interfacial shear strength can only be constant up to the middle of the fiber where its sign is reversed. Following Phan-Thien (1979), the fiber is considered as a slender body which can be approximated by a suitable distribution of "Kelvinlets" or point forces. For the conditions stated above, the relevant Kelvinlets are:

$$dF_z = -\pi \cdot d \cdot \tau_c \cdot dz , \quad [3.4.27]$$

$$dF_r = 0 , \quad [3.4.28]$$

$$dF_\theta = 0 , \quad [3.4.29]$$

Landau and Lifshitz (1959) give the displacement field u at a point x due to a force F applied at the origin of a cartesian coordinate system x_1, x_2, x_3 as:

$$du_i(x) = \frac{1}{16 \cdot \pi \cdot G \cdot (1-\nu)} \left[\frac{3-4\nu}{(x_1^2+x_2^2+x_3^2)^{1/2}} \delta_{ij} + \frac{x_i \cdot x_j}{(x_1^2+x_2^2+x_3^2)^{3/2}} \right] \cdot dF_j , \quad [3.4.30]$$

where δ_{ij} is the Kronecker symbol, G the matrix shear modulus and ν its Poisson's ratio. Introducing Eqs. [3.4.27]-[3.4.29] into Eq. [3.4.30] and using cylindrical coordinates yields:

$$du_z = - \frac{d \cdot \tau_c}{16 \cdot G \cdot (1-\nu)} \cdot \frac{r \cdot z}{(r^2 + z^2)^{3/2}} dz , \quad [3.4.31]$$

$$du_r = -\frac{d \cdot \tau_c}{16 \cdot G \cdot (1-\nu)} \cdot \left[\frac{3-4\nu}{(r^2+z^2)^{1/2}} + \frac{r^2}{(r^2+z^2)^{3/2}} \right] dz \quad [3.4.32]$$

The shear strain is given by

$$d\epsilon_{rz} = \frac{1}{2} \left(\frac{\partial du_z}{\partial r} + \frac{\partial du_r}{\partial z} \right) \quad [3.4.33]$$

The overall shear strain due to the distribution of Kelvinlets is then

$$\epsilon_{rz} = \int_0^{\infty} d\epsilon_{rz} \quad , \quad [3.4.34]$$

or, introducing Eqs. [3.4.31] - [3.4.33] into Eq. [3.4.34] and rearranging:

$$\epsilon_{rz} = -\frac{d \cdot \tau_c}{32 \cdot G \cdot (1-\nu)} \int_{-\infty}^0 \frac{z-s}{[r^2+(z-s)^2]^{5/2}} [4\nu(z-s)^2 - 3(z-s) + (4\nu-3)r^2] ds \quad [3.4.35]$$

Solving Eq. [3.4.35] and introducing the result into

$$\tau_{rz} = 2 \cdot G \cdot \epsilon_{rz} \quad , \quad [3.4.36]$$

yields the final result

$$\tau_{rz} = -\frac{3-4\nu}{16(1-\nu)} \tau_c \frac{d}{\sqrt{z^2+r^2}} \quad [3.4.37]$$

Eq. [3.4.37] is the exact solution for the problem stated above, thus giving an upper bound for the shear stress induced by a fiber with residual stresses after dislocation punching, at a distance far enough from the end of the fiber for the corner singularity to be neglected and for the fiber to be satisfactorily approximated by a line of point forces. For a typical value of $\nu = 0.3$, the shear stress on the glide cylinder $r = d/2$ at a distance of one diameter away from the fiber end ($z = d$) is equal to $0.072 \tau_c$, i.e., an order of magnitude less than the minimum stress necessary to move a dislocation in the lattice, if it is assumed that τ_c is about equal to τ_f , the lattice friction stress. This leads to the conclusion that, apart from the stress induced by the singularity at the end of the fiber, the shear stress on the glide cylinder is negligible. Even if it is fully loaded through the interface, the fiber will have very little effect upon the dislocations away from its immediate vicinity. The first loop will therefore be very close to the end of the fiber and we conclude that the length of the loops row as given by Eq. [3.3.11] is an adequate measure of the punching distance.

It is of interest to compare the above result to the similar situation of the backstress due to a sphere of radius r_s located at the origin of a cartesian coordinate system. The matrix shear stress on the glide cylinder ($x=r_s/2$) due to a sphere subjected to an elastic, hydrostatic strain ϵ is given by Johnson and Lee (1983) as

$$\tau(\xi) = 96 \cdot \sqrt{2} \cdot G \cdot \beta' \cdot \epsilon \frac{\xi}{(2 \cdot \xi^2 + 1)^{5/2}}, \quad [3.4.38]$$

where $\xi = z/r_s$ and β' is a constant containing the matrix Poisson's ratio as well as the matrix and inclusion bulk moduli.

It is apparent that, as expected, the shear stress decays more rapidly than in the case of the cylinder. To allow a further quantitative comparison, we calculate the stress on the glide cylinder when the residual stress in the sphere is such that the critical shear stress is reached at the intersection of the glide cylinder and the sphere. If the backstress due to the other loops is neglected, this is the maximal residual stress possible in the sphere since any higher stress would nucleate a loop at the interface. Introducing $\tau = \tau_f$ and $\xi = \sqrt{3}/2$ into Eq. [3.4.38] gives a value for the maximum strain which, after introduction into Eq. [3.4.38] yields an equation for the shear stress on the glide cylinder:

$$\tau^*(\xi) = 8 \tau_f \frac{\xi}{(2 \cdot \xi^2 + 1)^{5/2}} . \quad [3.4.39]$$

Choosing again a value of ν equal to 0.3 and a distance of two radii away from the interface ($\xi = 3$) yields a value for τ^* equal to 0.013 τ_f .

It can therefore be concluded that, in the case of the sphere as in the case of the cylinder, the backstress of the inclusion with a residual strain present after emission of loops is negligible at short distances away from the interface. This conclusion is supported by experimental observations of spherical and cylindrical inclusions reported in what follows with the last punched loop located very close to the interface.

3.4.5 Parametric study and discussion of model

A parametric study was performed to investigate the influence of different variables on the number of punched loops n and the two critical length L_u and

L_p . The system aluminium/alumina was chosen as an example, the properties of which are given in Table 3.4.

Each of the parameters in Table 3.4 was varied while keeping all the other constant. It was found that only $\Delta\alpha\Delta T$, L , d , τ_c , E_f had a significant influence on n , L_u or L_p . The length L_p as calculated from Eq. [3.4.9] was always small. In particular, the volume fraction of fibers had a very small effect on these parameters. It must be however kept in mind, since this model was developed for a single fiber, it is only valid for small volume fractions.

Figs. 3.4.5a-e show the effect of these parameters on the number of punched loops, using Eq. [3.4.23] (full curves). Also shown in the same figures is the value predicted by Taya and Mori (1987) (Eqs. [1] and [2], App. 5), whose model is briefly summarized in Appendix 5.

Eqs. [3.4.9] and [3.4.26] giving the two critical lengths L_p and L_u (with $\sigma_B = 0$, see section 3.4.2) can be rewritten in dimensionless form:

$$\frac{\beta \cdot L_p}{2} = \operatorname{arctgh}\left(\frac{\theta}{\Delta T}\right) \quad , \quad [3.4.40]$$

$$\frac{\beta \cdot L_u}{2} = \operatorname{arctgh}\left(\frac{\theta}{\Delta T}\right) + \sqrt{\left(\frac{\Delta T}{\theta}\right)^2 - 1} \quad , \quad [3.4.41]$$

where the intrinsic temperature θ is given by

$$\theta = \frac{4 \cdot \tau_c}{E_f \cdot \beta \cdot d \cdot \Delta \alpha} = \frac{\tau_c}{\Delta \alpha} \sqrt{-\frac{\ln(v_f)}{G_m \cdot E_f}} \quad . \quad [3.4.42]$$

Fig. 3.4.6 shows a dimensionless plot of the critical lengths L_p and L_u as a function of the temperature interval ΔT , for all other parameters being constant

(Eqs. [3.4.40] and [3.4.41]). The two curves delimit the three regions described above, i.e., elastic, elastic/plastic and elastic/plastic/unstrained interfaces. Similar projections can be done for the other variables defining L_p and L_u , introducing the appropriate intrinsic variables corresponding to θ .

It is apparent from Fig. 3.4.6 that, for $\Delta T > \theta$, a short fiber interface is completely elastic, a longer fiber interface is elastic/plastic while an even longer fiber interface is elastic/plastic/unstrained. For $\Delta T < \theta$ however, all fibers will have an entirely elastic interface. With the parameters chosen for the parametric study (Table 3.4), θ is equal to 7.8 K. It is also clear from Fig. 3.4.6 that there is a critical fiber length L^* (corresponding to the minimum of the $L_u - \Delta T$ curve and found by derivation of Eq.[3.4.41]), below which no temperature interval, however large, will produce an unstrained interfacial region:

$$\frac{\beta \cdot L^*}{2} = \operatorname{arctgh} \left[\left(\frac{\sqrt{5} + 1}{2} \right)^{1/2} \right] + \left(\frac{\sqrt{5} - 1}{2} \right)^{1/2} = 1.847 . \quad [3.4.43]$$

For the parameters in Table 3.4, L^* is equal to 19 μm .

The results above also show that the critical length L_p is small: for the parameters of Table 3.4, it is equal to 0.4 μm . In typical fiber reinforced metals subjected to large temperature variations, the prevailing regimes will thus be elastic/plastic or elastic/plastic/unstrained, i.e., relaxation by slip along part of the fiber will be observed. It follows that the first term in Eq. [3.4.26] can be neglected and since the third term is negligible (because σ_B is typically smaller than τ_c), Eq. [3.4.26] reduces to

$$L_u \approx \frac{E_f d \cdot \Delta \alpha \cdot \Delta T}{2 \cdot \tau_c} . \quad [3.4.44]$$

The boundary between the elastic/plastic regime and the elastic/plastic/unstrained regime is marked by an arrow in Figs. 3.4.5a-e. For small values of L , τ_c and ΔT , and large values of E_f and d , the value of n calculated from Eq. [3.4.23] tends toward that predicted by Eq. [2] of Appendix 5 which represents an upper bound value; as must be the case, this value is never exceeded.

An important qualitative and quantitative discrepancy is observed between our model and that of Taya and Mori (1987), since Eq. [3.4.23] does not predict a set of critical parameters for which punching is suppressed (except when the interface is completely elastic for $L < L_p$, at which point punching has not yet been activated). The punching suppression in Taya and Mori's model (1987) is due to the implicit assumption that the loops are punched *all at once* rather than one after the other. As the number of loops to be simultaneously punched increases, so does the total energy needed for punching, until it exceeds the energy released during the relaxation of the ellipsoid, thus suppressing all punching. If loops are punched sequentially rather than simultaneously, such a situation does not occur, as predicted by our model where the fiber is at no time too long to punch loops. Rather, long fibers reach a critical length L_u , above which *subsequent* punching is inhibited (Fig. 3.4.5b). From a physical point of view, it seems that coaxial loops of same diameter should be nucleated and punched one after the other when the nucleation stress is reached at the end of the cylindrical fiber. This is because the location where nucleation takes place is limited to a single circle corresponding to the edge of the fiber ends. In Taya and Mori's model, on the other hand, each loops is nucleated at a different place along the surface of the ellipsoid and has therefore a different diameter. The assumption of simultaneous punching is therefore geometrically possible for an ellipsoid and might happen physically for inclusions of that shape when the cooling rate is

much higher than the rate of loop nucleation. The root of the discrepancy between the two models thus seems to lie in the different assumptions made concerning the nature of the dislocation punching process (simultaneous punching in Taya and Mori's model (1987), sequential punching in ours) as well as the geometry of the fiber (prolate spheroid in Taya and Mori's model (1987), cylinder in ours).

| Parameter | Unit | AgBr | AgCl | Al |
|-------------------|------------------------------------|---------|---------|--------|
| crystal type | [-] | B1 NaCl | B1 NaCl | A1 fcc |
| density | [kg/dm ³] | 6.47 | 5.56 | 2.7 |
| melting point | [K] | 705 | 728 | 933 |
| boiling point | [K] | 2033 | 1373 | 2900 |
| heat conductivity | [W/mK] | 1 | 1.1 | 238 |
| CTE | [10 ⁶ K ⁻¹] | 36 | 30 | 23 |
| refractive index | [-] | 2.25 | 2.07 | - |
| elastic modulus | [GPa] | 32 | 26 | 62 |
| shear modulus | [GPa] | 7.2 | 6.9 | 23 |
| Poisson's ratio | [-] | 0.37 | 0.343 | 0.33 |
| UTS | [MPa] | 24.5 | 17 | 55 |
| τ_{y0} | [MPa] | | 0.5 | 8.8 |
| A | [-] | | | 0.625 |
| rupture strain | [%] | > 38 | > 50 | > 55 |
| Burgers vector | [nm] | 0.407 | 0.384 | 0.286 |

Table 3.1: Physical and mechanical parameters of matrix materials (high purity silver bromide and chloride and 99.5 % aluminium) from Sprackling (1965), Gmelins (1971, 1972), Hansen (1977) and Boyer *et al.* (1985). τ_{y0} : intrinsic shear flow stress; A: strain-hardening constant.

| | array | P | v* [%] | ρ [m ⁻²] | AGb $\sqrt{\rho}$ [MPa] |
|----------|--------|-----------------|--------|---------------------------|-------------------------|
| sphere | fcc | $\sqrt{2}\pi/6$ | 6.1 | $5.9 \cdot 10^{12}$ | 10 |
| | bcc | $\sqrt{3}\pi/8$ | 5.6 | $5.9 \cdot 10^{12}$ | 10 |
| | cubic | $\pi/6$ | 4.3 | $5.9 \cdot 10^{12}$ | 10 |
| cylinder | hex. | $\sqrt{3}\pi/6$ | 5.1 | $1.7 \cdot 10^{12}$ | 5.4 |
| | square | $\pi/4$ | 4.4 | $1.7 \cdot 10^{12}$ | 5.4 |

Table 3.2: packing ratio, critical volume ratio (Eqs. [3.1.16]), dislocation density (Eqs. [3.1.10]) and increase of yield stress in shear (Eq. [3.1.7]) for different arrays of silicon carbide spheres and cylinders of radius 1.5 μm in a strain-hardening 99.5 % aluminium matrix submitted to a change of temperature $\Delta T = 200\text{K}$.

| body | K |
|--------------------------------|-------------|
| rhombic dodecahedron | 0.88 |
| sphere | 0.85 |
| truncated octahedron | 0.76 |
| octahedron | 0.74 |
| pentagonal dodecahedron | 0.72 |
| cube | 0.67 |
| cylinder | 0.64 |
| tetrahedron | 0.57 |
| square rod | 0.50 |

Table 3.3: Exact values of constant K for regular bodies.

| Parameter | Al | Al ₂ O ₃ |
|-------------------------|-------|--------------------------------|
| E [GPa] | 72.5 | 300* |
| G [GPa] | 30.1 | — |
| ν [-] | 0.362 | 0.21 |
| τ_c τ_f [MPa] | 5 | — |
| α [10^6 /K] | 23.5 | 9* |
| b [nm] | 0.286 | — |
| L [μ m] | — | 200 |
| d [μ m] | — | 3* |
| ν_f [-] | — | 0.1 |
| σ_B [MPa] | 0 | |
| ΔT [K] | 200 | |

Table 3.4: Thermal, mechanical and geometric parameters of the matrix and fibers used in the parametric study (* : Saffimax™ values).

3.5 Figures

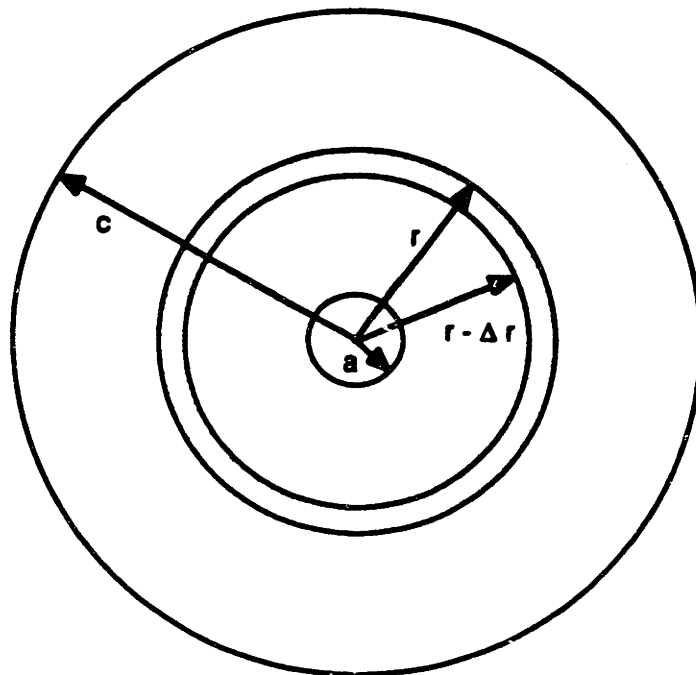


Figure 3.1.1 Fictitious hole expanded from zero radius to radius a producing a plastic zone of radius c and a matrix displacement of Δr at the surface of the inclusion of radius r . Cylindrical or spherical case.

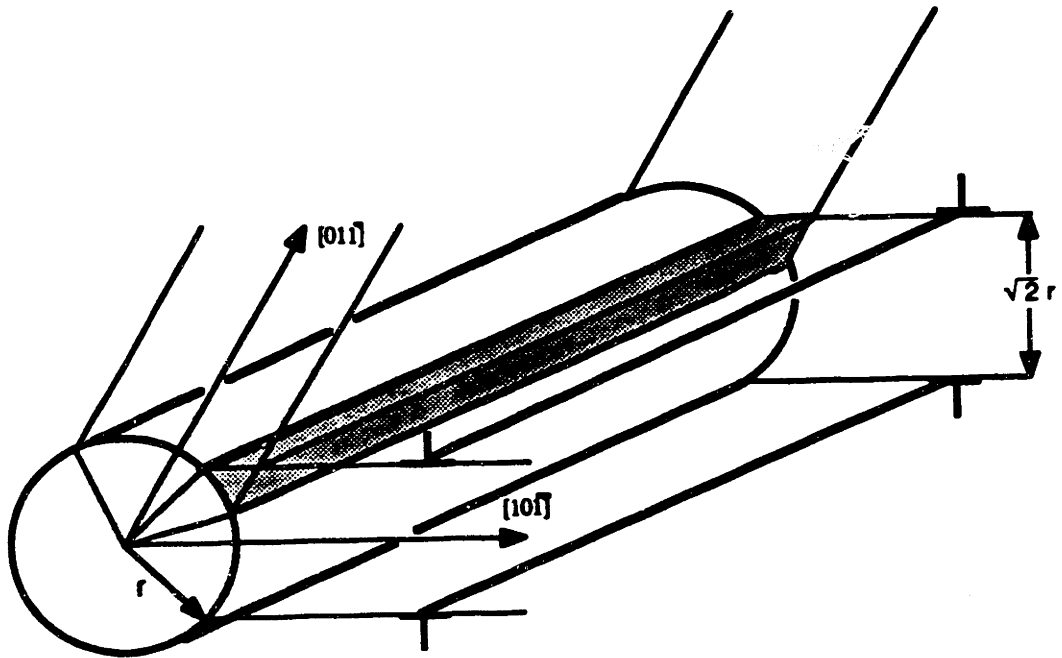


Figure 3.1.2 Schematic of prismatic dislocation loops punched in the $\langle 110 \rangle$ directions of a f.c.c. lattice from a cylinder. The shaded volumes represent the intersection of adjacent glide systems.

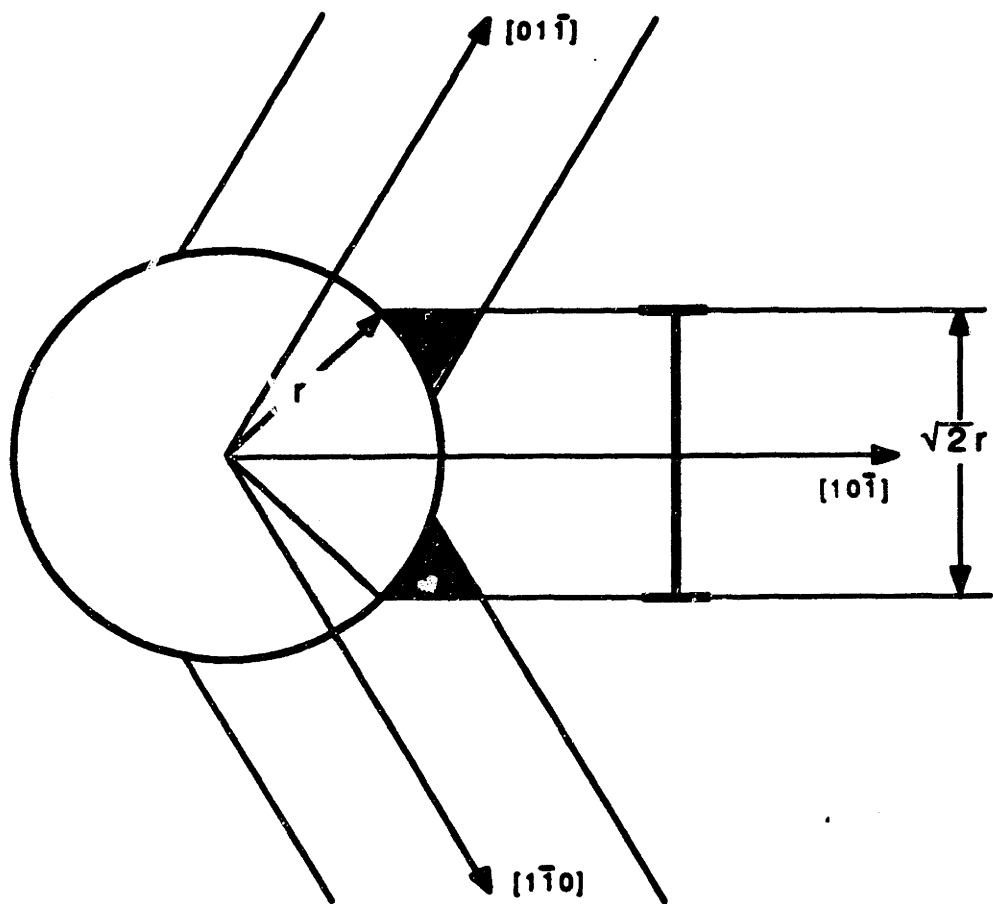


Figure 3.1.3 Schematic of prismatic dislocation loops punched in the $\langle 110 \rangle$ directions of a f.c.c. lattice from a sphere. The shaded volumes represent the intersection of adjacent glide systems.

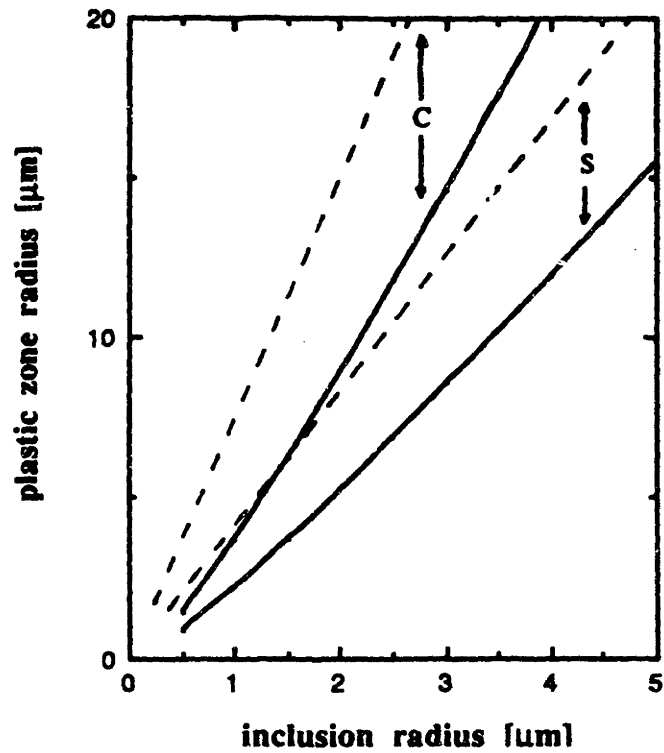


Figure 3.1.4 Plastic zone radius around a SiC cylinder (c) and sphere (s) in a 99.5 % aluminium matrix after a temperature change of 200 K. Full curves: strain-hardening matrix (Eqs. [3.1.12]). Dotted curves: non strain-hardening matrix (Eqs. [3.1.6]).

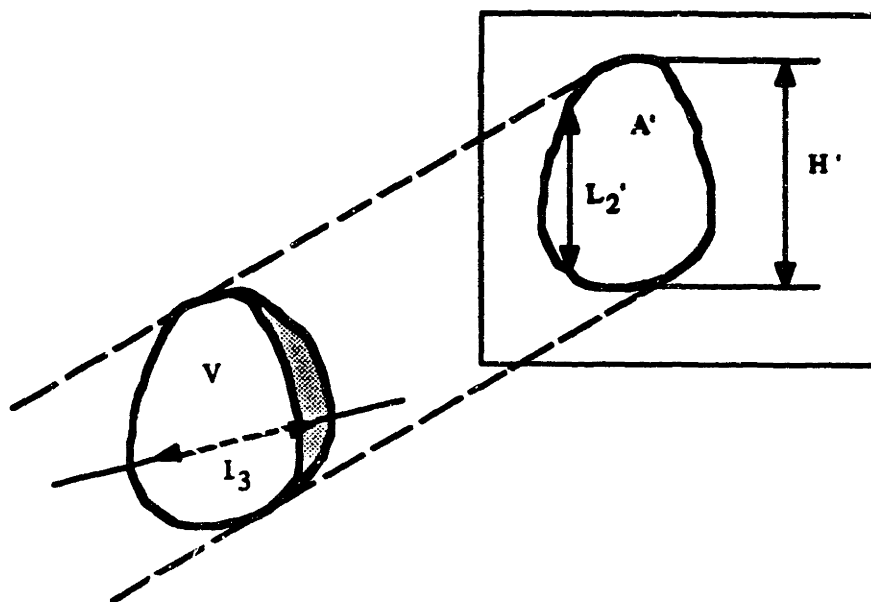


Figure 3.2.1 Schematic drawing of a particle and its projection with relevant variables.

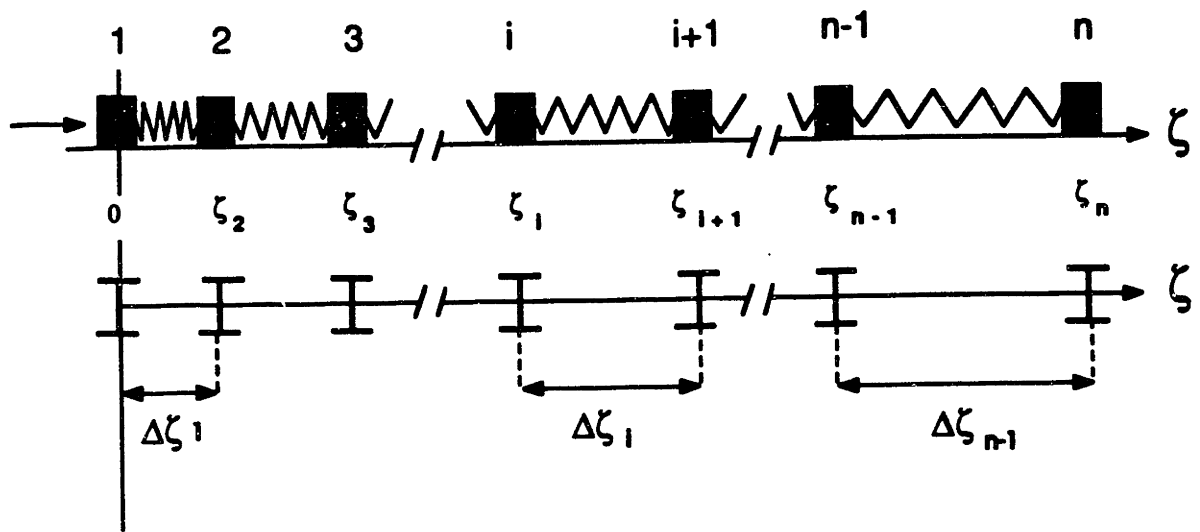


Figure 3.3.1 Steady-state configuration of a moving row of n bodies, each submitted to a friction force.

Figure 3.3.2 Equivalent configuration of a row of n circular, prismatic loops repelling each other in a lattice with a non-zero friction stress. The first loop is blocked.

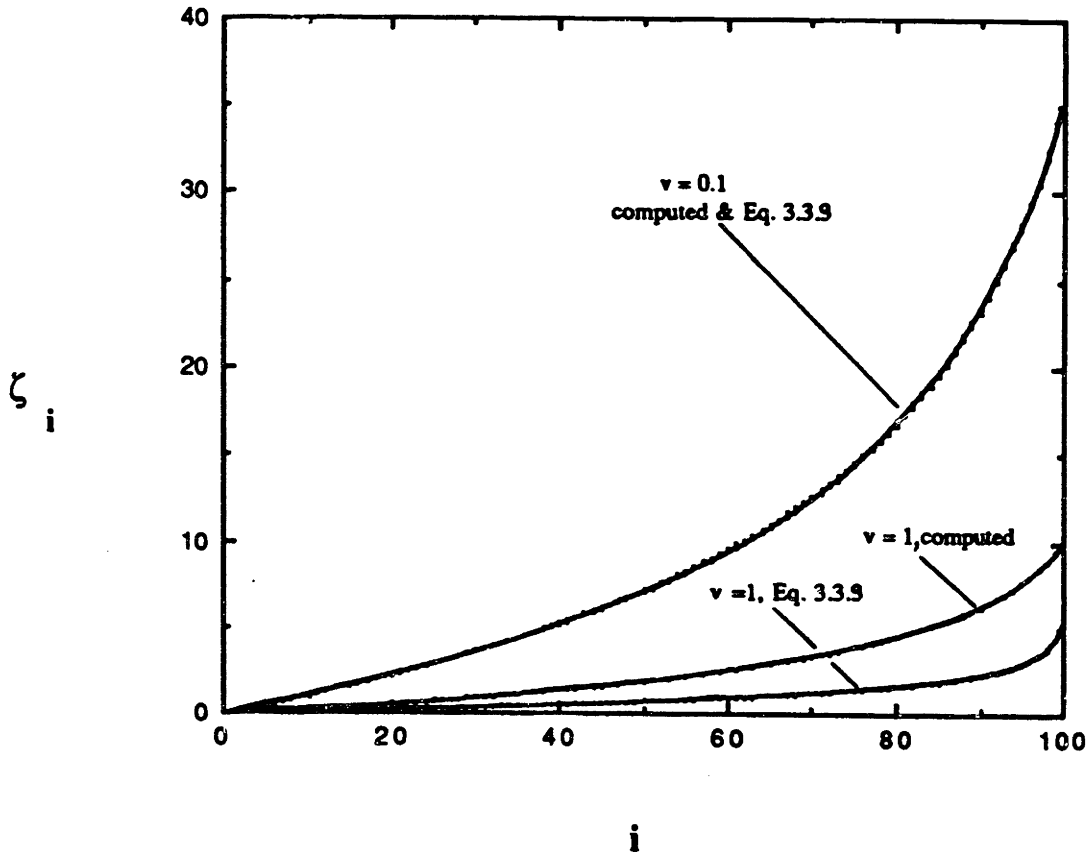


Figure 3.3.3 Dimensionless distance from the origin for a row of 100 loops for two values of ν , as calculated from Eq. [3.3.9] and as computed.

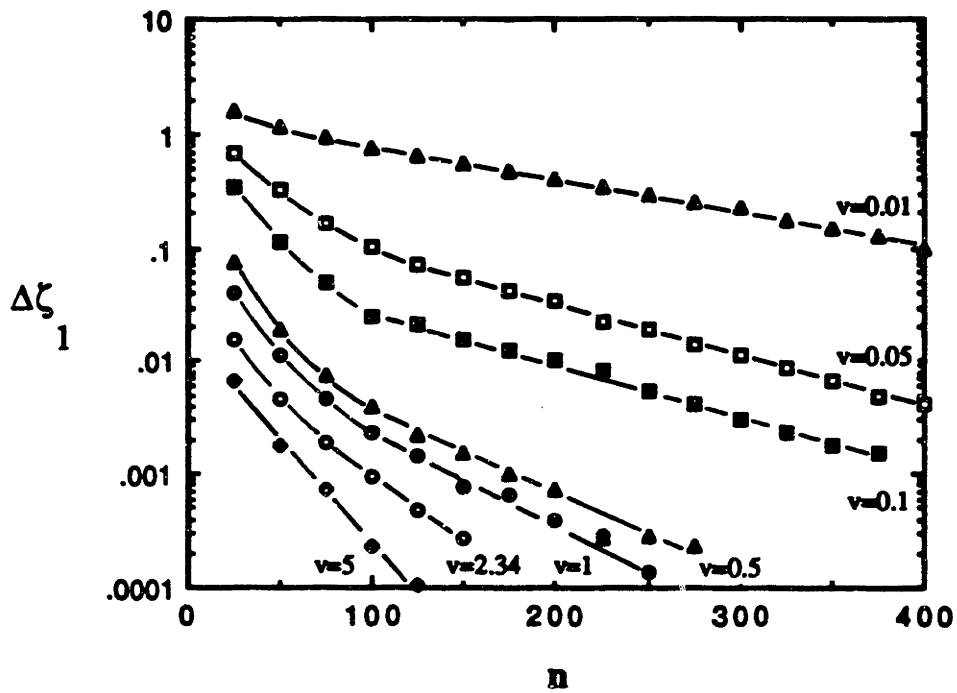


Figure 3.3.4 Dimensionless minimum spacing between two loops (first two loops) as a function of the number of loops in the row for different values of ν .

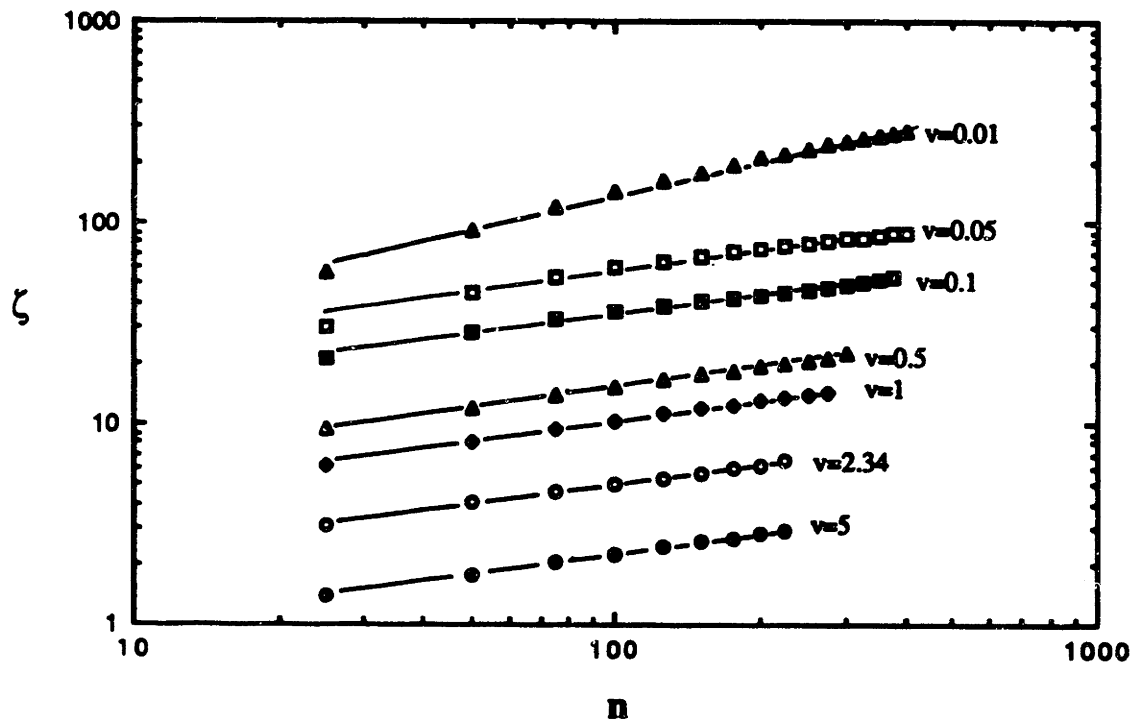


Figure 3.3.5 Dimensionless length of a row as a function of the number of loops for different values of v .

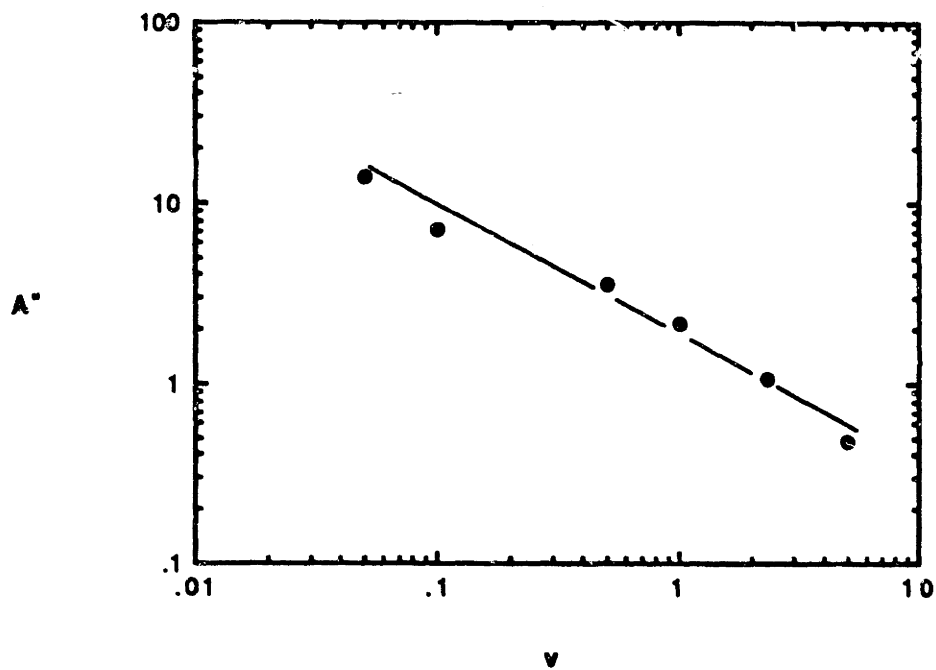


Figure 3.3.6 Plot of parameters A'' and v , Eq. [3.3.11].

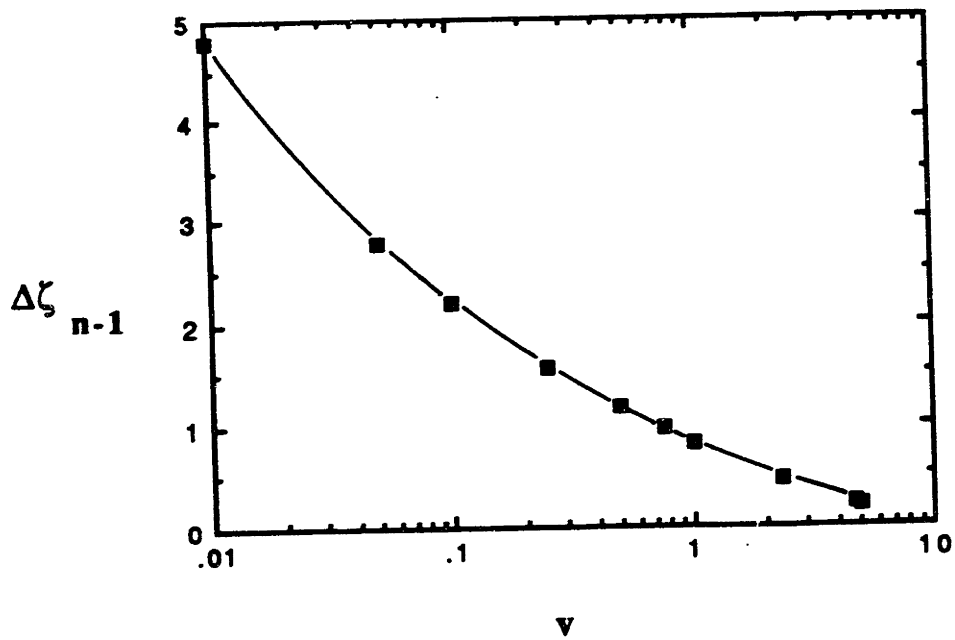


Figure 3.3.7 Dimensionless maximum spacing between two loops (two last loops) as a function of v .

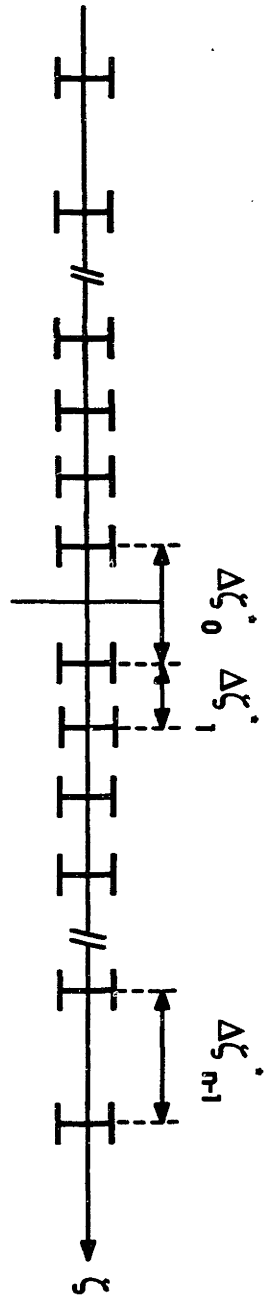


Figure 3.3.8 Configuration of two rows of prismatic loops of opposite Burgers' vector, located symmetrically on each side of the origin. The first loop of each row is blocked.

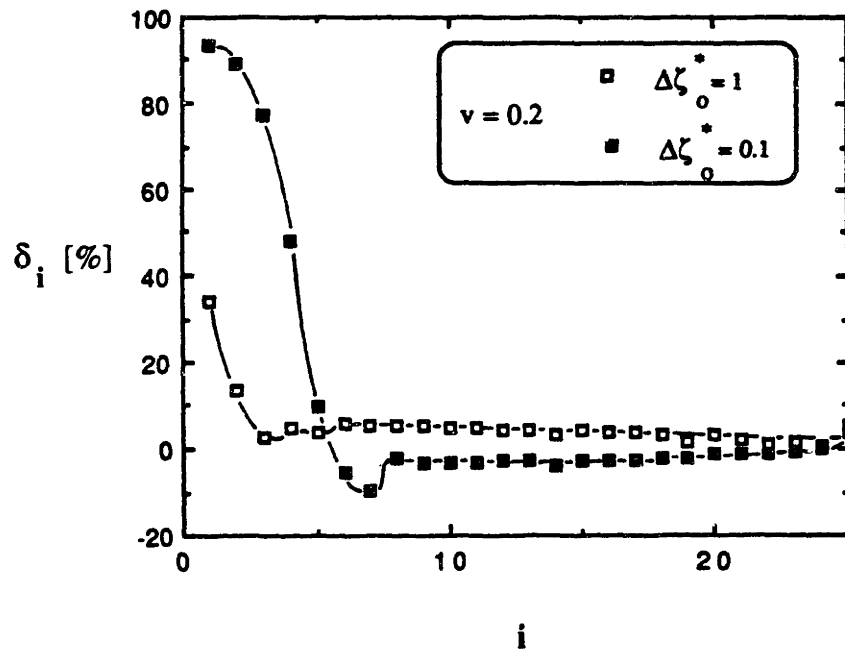
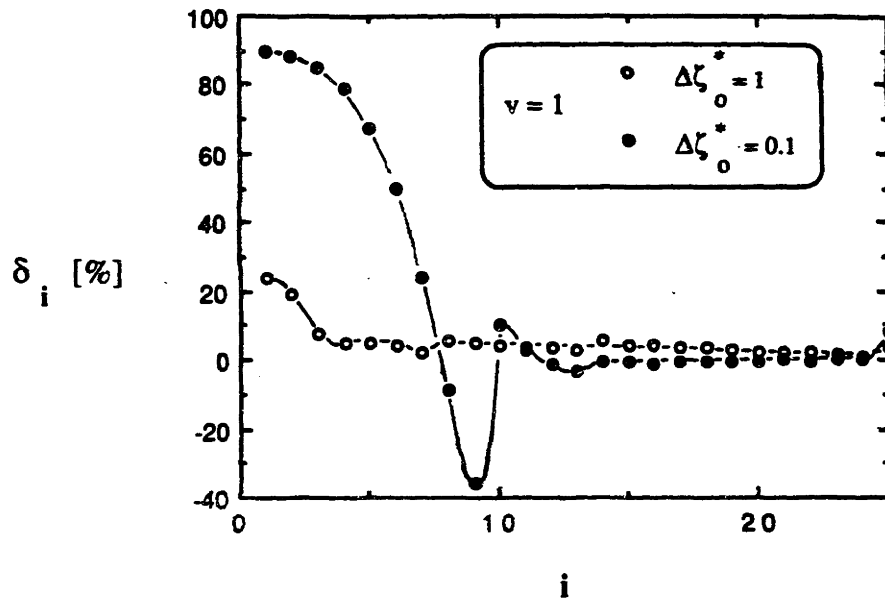


Figure 3.3.9 Relative difference in loop spacings between the undisturbed row (Fig. 3.3.2) and the corresponding disturbed row (Fig. 3.3.8, $\zeta > 0$) for two values of v and $\Delta\zeta_o$.

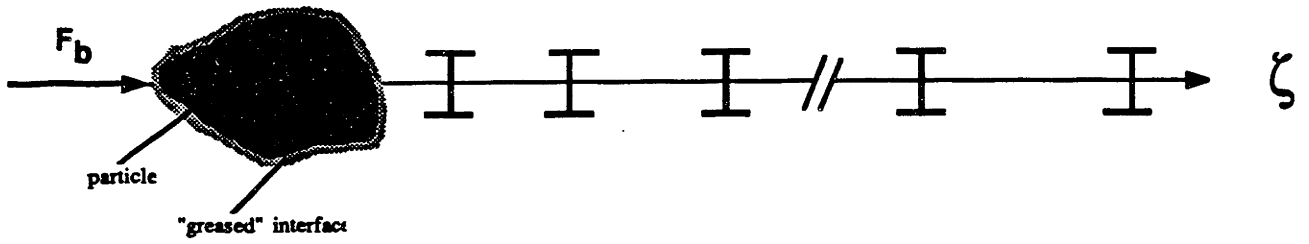
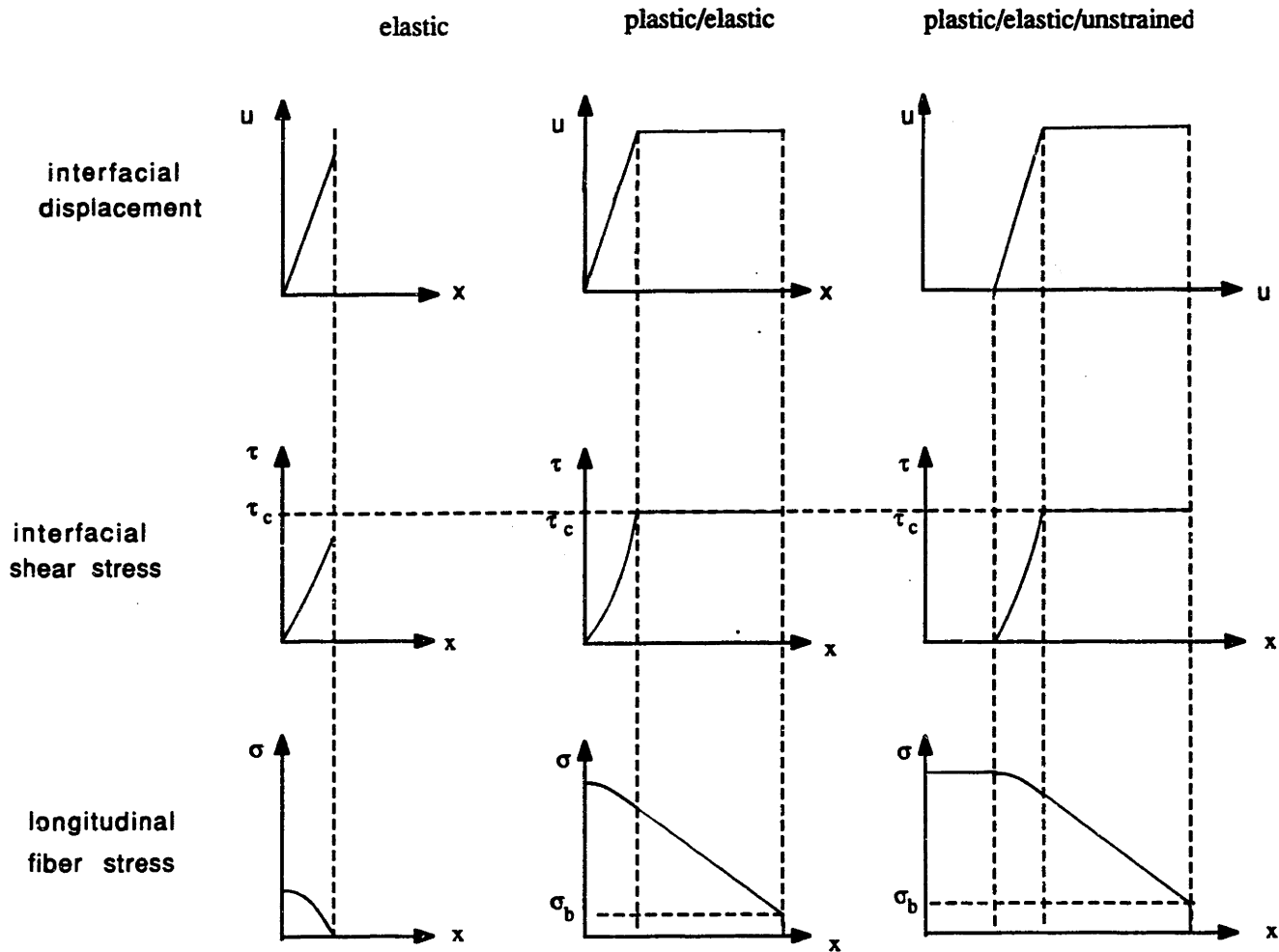
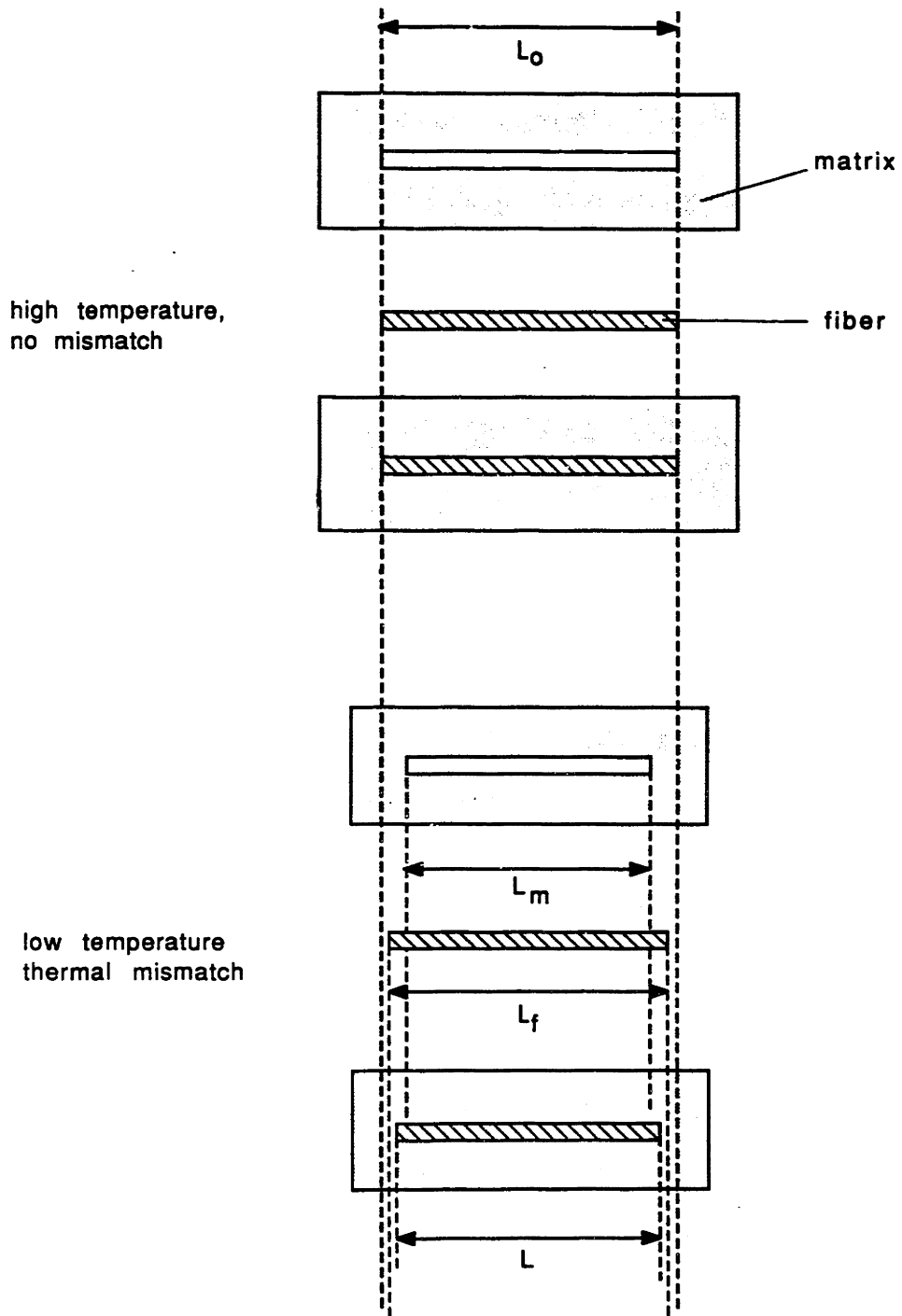


Figure 3.3.10 Particle with "greased" interface pushing a row of loops against the loop friction stress.



Figs. 3.4.1a-c Schematic diagrams for the interface displacement u , the interfacial shear stress τ and the fiber longitudinal stress as a function of the distance x from the center of the fiber. (a) purely elastic interface, (b) plastic-elastic interface, (c) plastic-elastic-unstrained interface



Figs. 3.4.2 a&b Schematic diagram of matrix with hole, fiber and matrix with fiber before (a) and after (b) the temperature change ΔT .

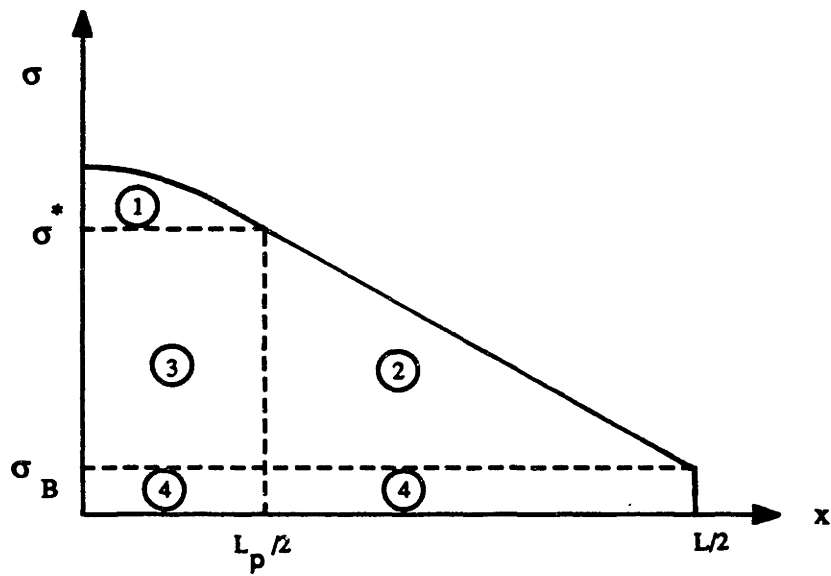
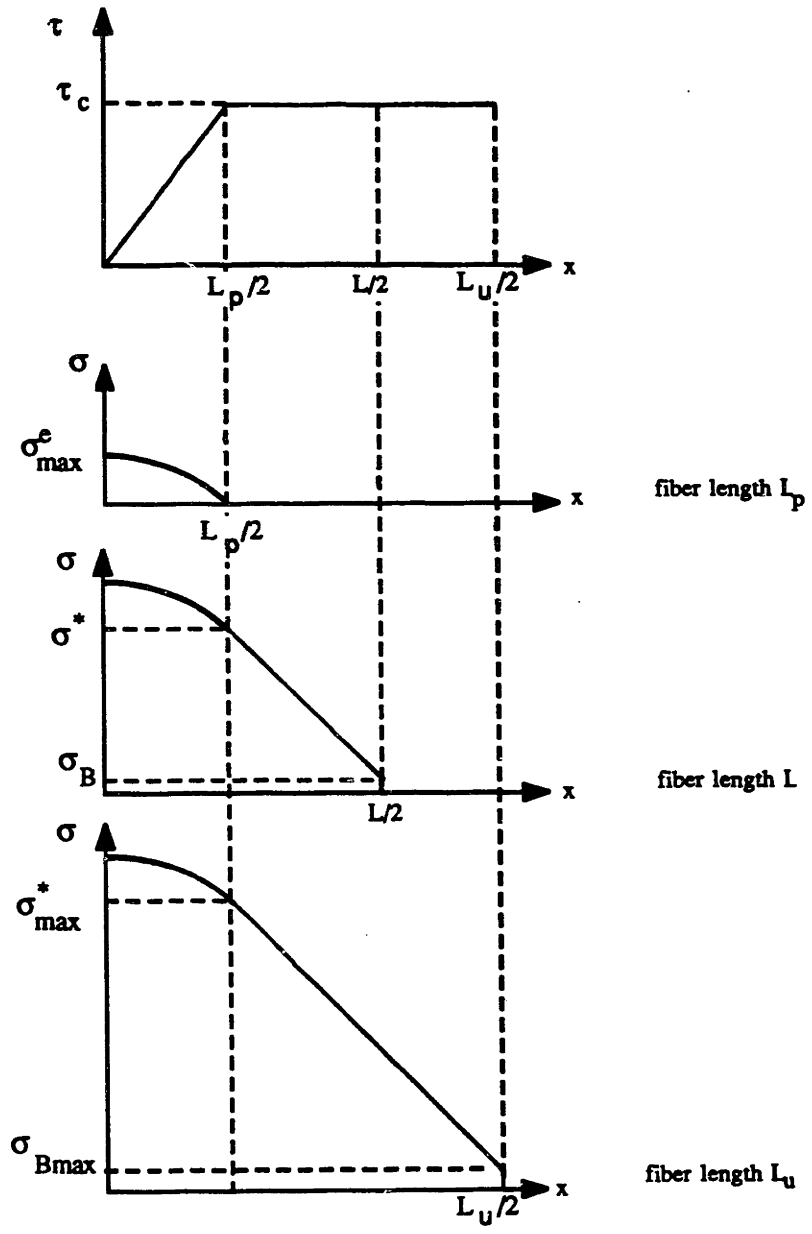


Figure 3.4.3 Diagram for the interfacial shear stress for a fiber of length L in the plastic-elastic regime.



Figs. 3.4.4 a & b Diagrams for the interfacial shear stress (a) and the fiber longitudinal stress (b) for three different fiber lengths L_p , L , L_u .

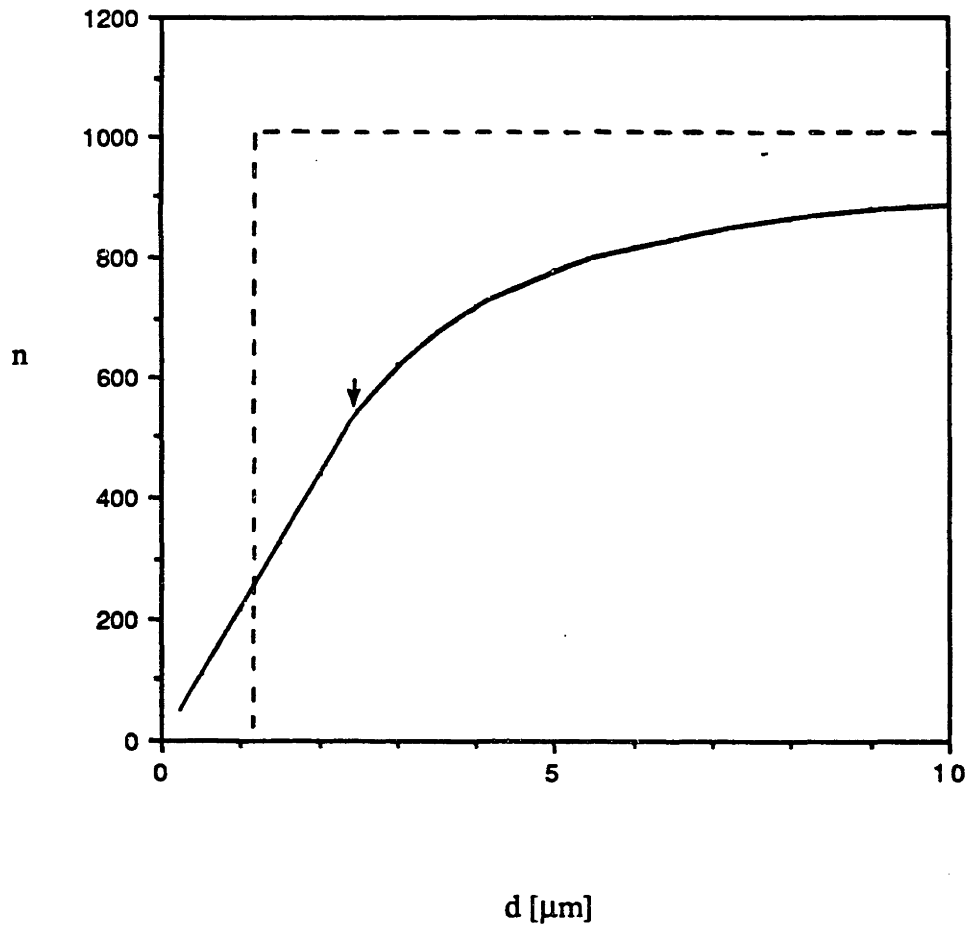


Figure 3.4.5a Number of loops punched as a function of the fiber diameter d , all other parameters in Table 3.4 being constant. Full curve : this model (Eq. [3.4.23]). Dotted curve : Taya and Mori's model (Eqs. [1] and [2] App. 5).

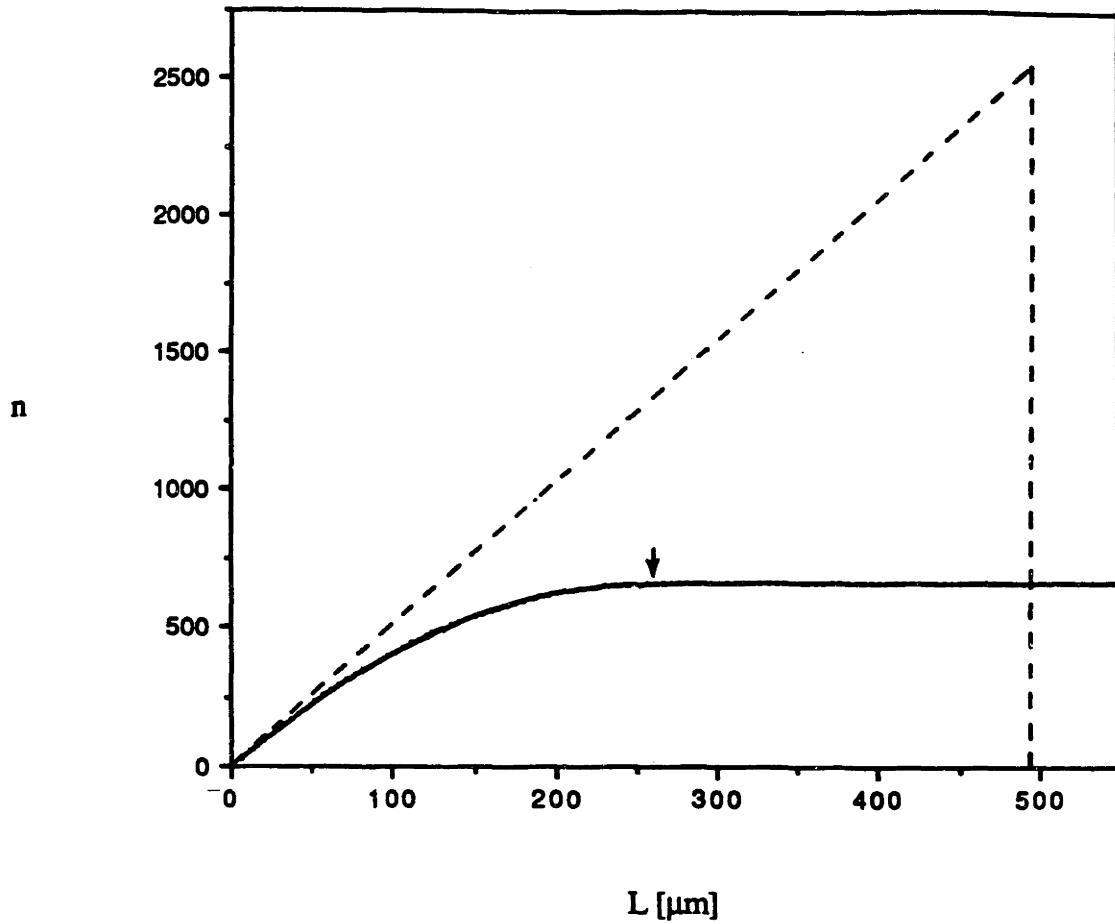


Figure 3.4.5b Number of loops punched as a function of the fiber length L , all other parameters in Table 3.4 being constant. Full curve : this model (Eq. [3.4.23]). Dotted curve : Taya and Mori's model (Eqs. [1] and [2] App. 5).

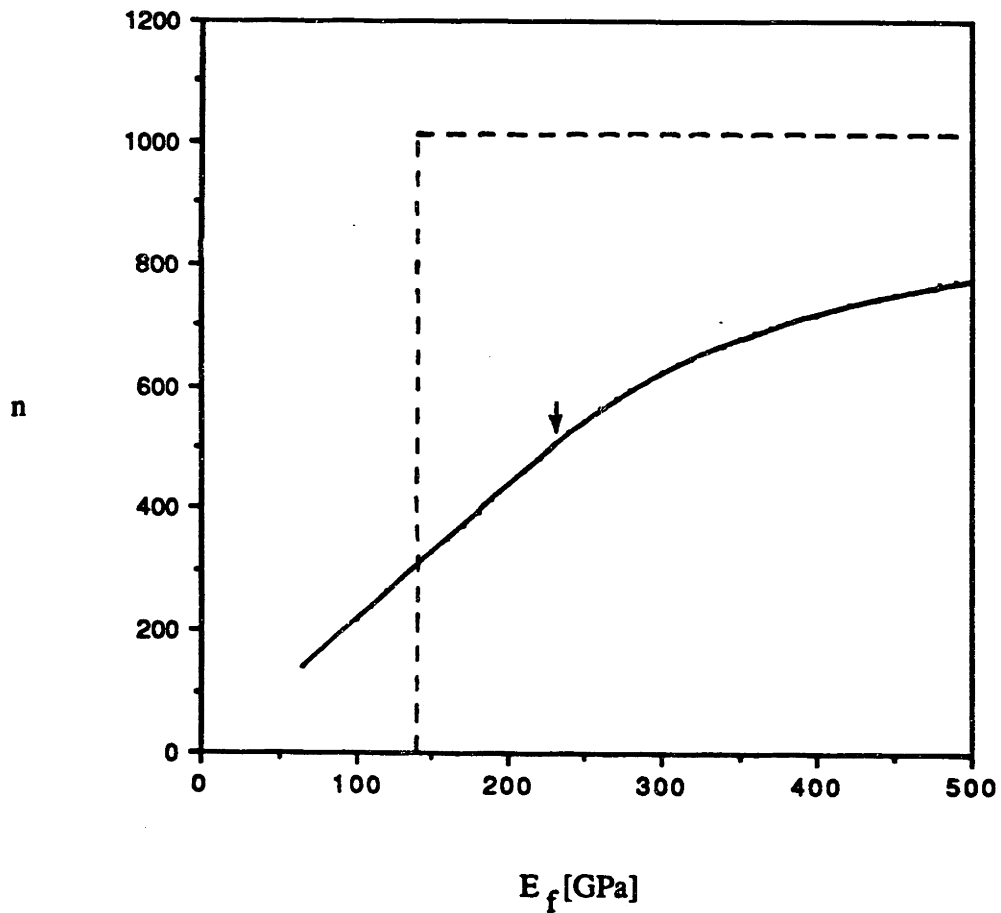


Figure 3.4.5c Number of loops punched as a function of the fiber elastic modulus E_f , all other parameters in Table 3.4 being constant. Full curve : this model (Eq. [3.4.23]). Dotted curve : Taya and Mori's model (Eqs. [1] and [2] App. 5).

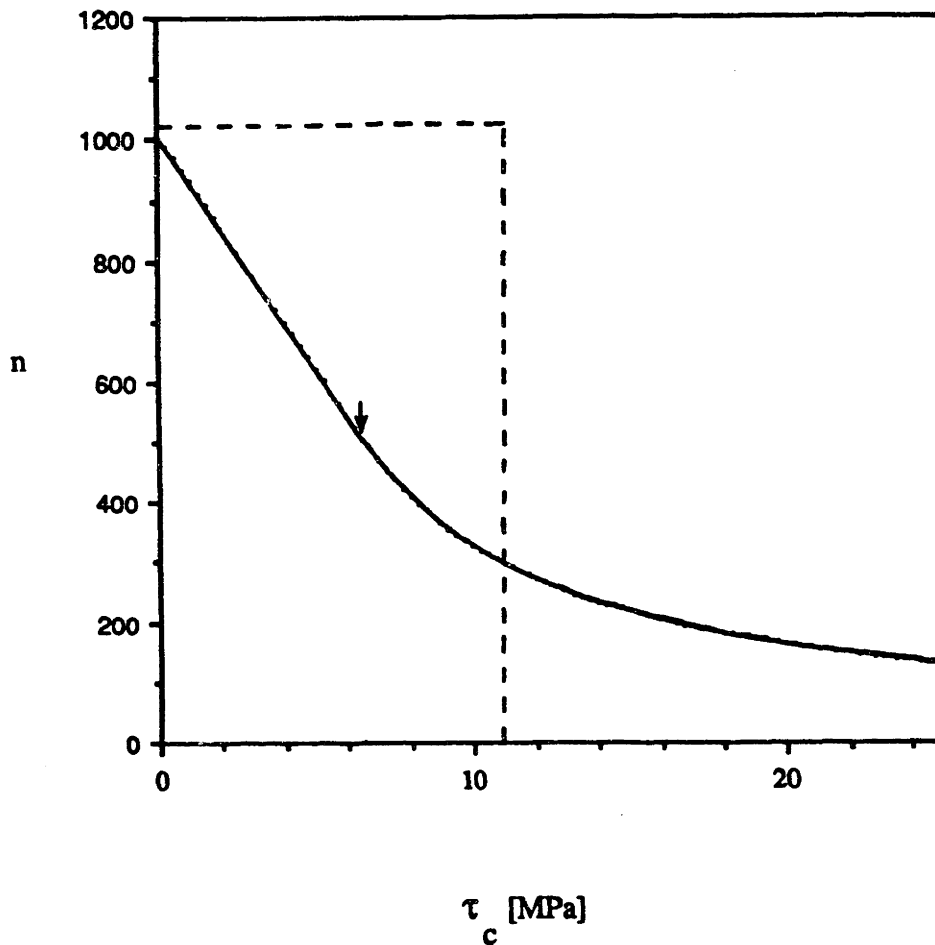


Figure 3.4.5d Number of loops punched as a function of the matrix critical interfacial stress τ_c , all other parameters in Table 3.4 being constant. Full curve : this model (Eq. [3.4.23]). Dotted curve : Taya and Mori's model (Eqs. [1] and [2] App. 5).

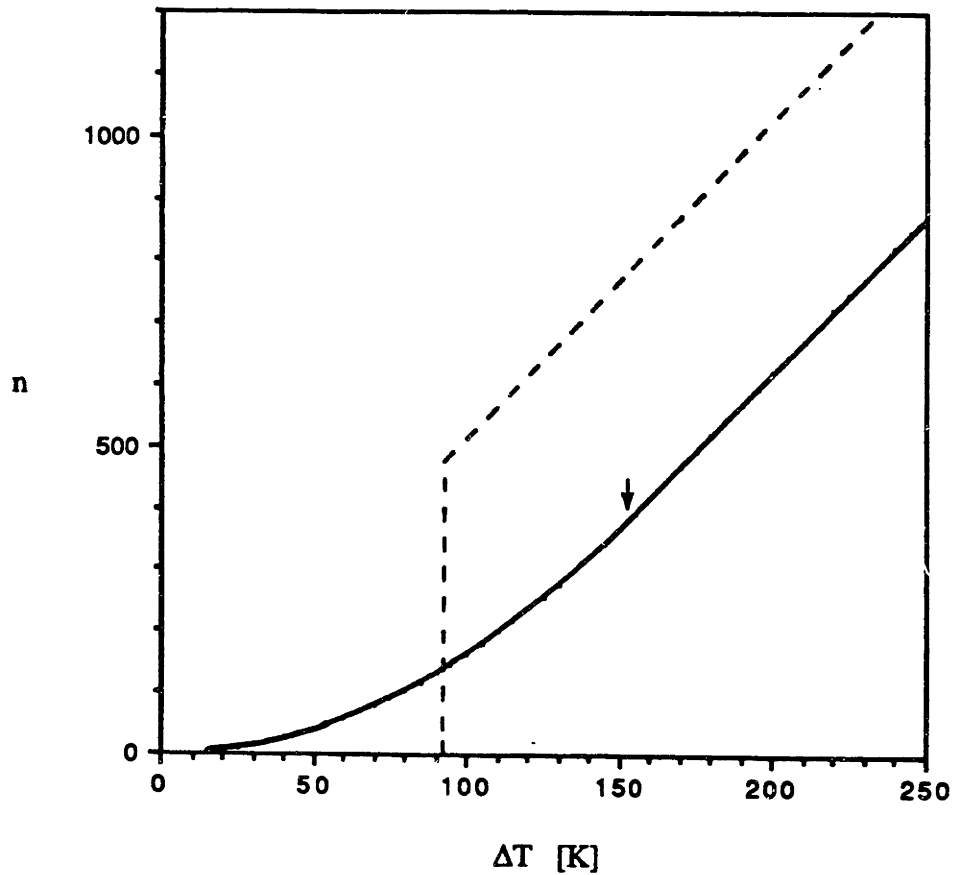


Figure 3.4.5e Number of loops punched as a function of the temperature excursion ΔT , all other parameters in Table 3.4 being constant. Full curve : this model (Eq. [3.4.23]). Dotted curve : Taya and Mori's model (Eqs. [1] and [2] App. 5).

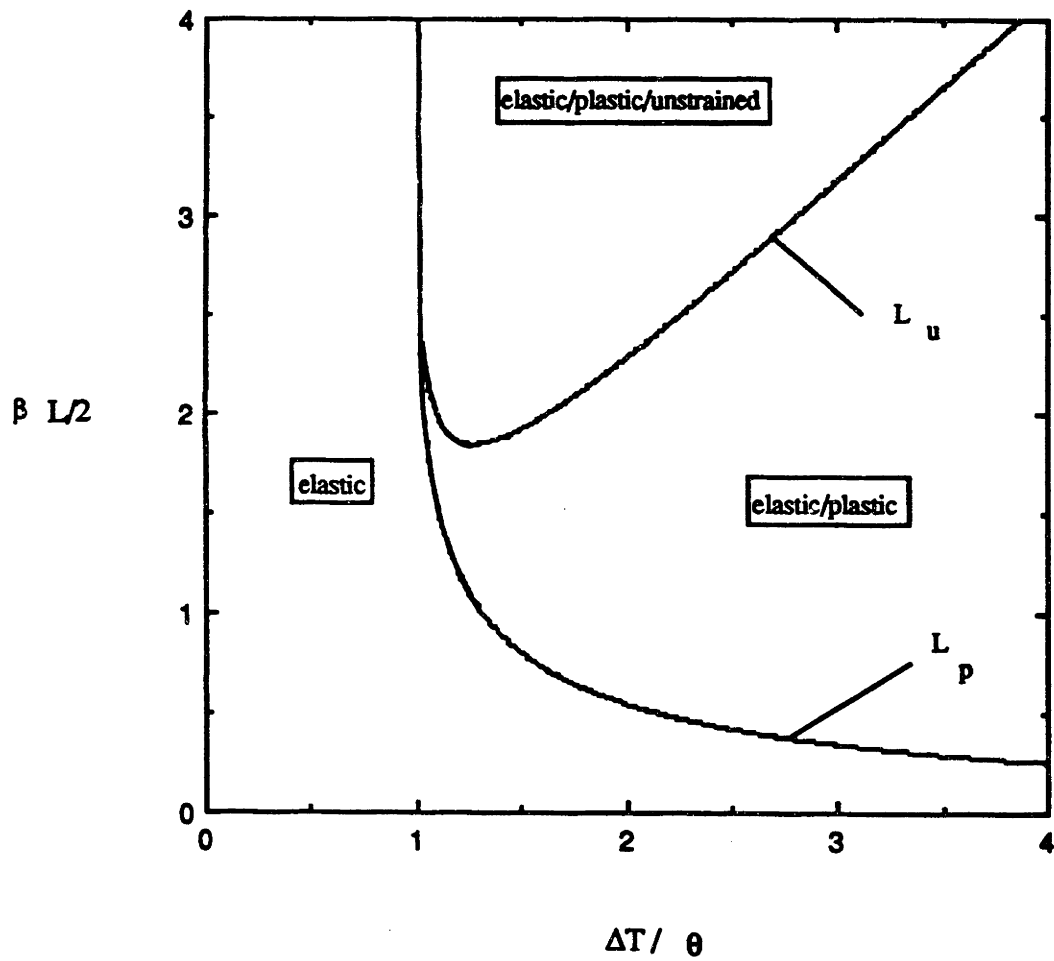


Figure 3.4.6 Dimensionless plot of the two critical lengths L_p and L_u as a function of the temperature excursion ΔT .

4. EXPERIMENTAL PROCEDURES

The method of choice to investigate dislocations in metals is transmission electron microscopy (TEM) since it allows a very high resolution; it has been used extensively in metals containing submicroscopic second phases. In most MMCs however, the typical size of the reinforcement and its associated plastic zone is much larger than the thin area, both in terms of thickness and of width of the electron-transparent region. This hinders the investigation of some typical dislocation structure found in MMCs, such as long dislocations along the sides of fibers, or entire rows of punched dislocations extending far from the reinforcement. Also, dislocations can be added during sample preparation which make use of mechanical ablation; ion-milling also often induces thermal excursion of the sample by beam heating or excessive cooling when a cold stage is used, leading to extraneous thermal mismatch dislocations. Finally, dislocations can be lost and their structure disturbed by the free surfaces of the electron-thin area, as observed by Vogelsang *et al.* (1985) and Arsenault and Shi (1986). The perturbation of the elastic stresses and the dislocations by a free-surface is also of concern for such techniques as etch pits or slip line observation which are also unable to observe the bulk.

To circumvent these limitations, we use silver chloride as a transparent model matrix for MMCs. As described in the literature survey, this transparent salt has been used by many investigators to simulate metal plasticity since it exhibits dislocation mechanisms which are in most cases similar to those found in metals, leading to typically metallic properties such as strain-hardening, high ductility or recovery. Upon exposure to actinic light at room temperature, dislocations can be decorated within bulk silver chloride by photodissociation and preferential precipitation of metallic silver on dislocation lines. These can

then be imaged by high resolution transmission optical microscopy, provided the dislocation density is sufficiently low. In practice, silver halides must be chemically sensitized, in order to reach the maximum decoration depth of about 30 μm . This allows the observation of decorated dislocations associated with reinforcements of large dimension typically found in MMCs.

Interest in this technique for imaging dislocations quickly waned after its development by Mitchell and coworkers thirty years ago with the development of the transmission electron microscope, which allows direct observation of dislocations in metals at high resolution. While decoration techniques for examination in the optical microscope do not allow imaging of individual dislocations when their density is high, we believe that they present distinct advantages over alternative techniques mentioned above for the study of the plastic zone around supramicroscopic reinforcements typically used in MMCs, because the whole plastic zone can be examined. Furthermore, the equilibrium configuration of low density dislocation structures which extend far from the reinforcement, such as prismatic loop rows, can be examined in their entirety.

The main disadvantage of decoration of silver halides is its low resolution. The average width of the decorated dislocations must be on the order of 0.4 μm for detection in the optical microscopy. Areas of high densities of dislocations (on the order of the inverse of the square of the decoration width, $6 \cdot 10^{12} [\text{m}^{-2}]$) will therefore appear as black regions where dislocations cannot be resolved. Decoration also pins dislocations down, therefore making impossible the observation of their movement or even of two of their successive positions. Finally, the decoration depth is limited to about 30 μm ; this depth can be increased by the application of a pulsed electrical field as described in the Literature Survey. While, in part due to these shortcomings, decoration of silver halides has fallen out of fashion for the investigation of dislocation phenomena

in favor of TEM, we think these materials constitute a splendid tool for experimental investigation of matrix behavior in MMCs when dislocation densities in the matrix are low. Elementary dislocation phenomena can be viewed in three dimensions along entire fibers and with no interference from sample free surfaces - unlike what has been achieved so far with TEM or etch pitting - in a material that has been extensively proven to accurately replicate such phenomena as they occur in metals.

In what follows, we first describe the experimental procedures which lead to an optimal decorated microstructure in silver chloride containing a second phase. In the next paragraph, we mention other less successful trials, in the hope that, if these experiments are repeated or extended, some of the problems encountered during this research can be avoided. We finally describe the sample preparation procedures explored for the fabrication of thick reinforced samples suitable for photoelastic experiments.

4.1 Sample preparation for decoration experiments

We mostly follow the experimental methods developed by Mitchell and co-workers summarized in the literature review, with some modifications dictated by experience. Great care must be exercised in each of the steps to obtain good microstructures, since a single non-optimal step will generally completely ruin the sample.

Blocks of silver chloride of 99.999% purity were purchased from Engelhard (Ohio) and stored in a dessicator in their original wrapping of polyethylene covered by dark paper. Some of the as-received material was sent for chemical

analysis to Luvak Inc. (Massachusetts) to check the potentially harmful elements copper, iron, cobalt and nickel, all of which were found to be below the sensitivity limit of 3 ppm. The analysis from the manufacturer takes however into account neither the possible decomposition of the chloride into silver nor oxygen contamination, both of which are visible by a slight gray or violet coloration of the otherwise transparent crystal. Decomposition can be minimized by shielding the samples from visible and ultraviolet light. If the crystals are very pure however, photodecomposition is very slow (Mitchell 1988).

When needed, silver chloride was manipulated using polymeric or glass instruments due to the reactivity of the chloride with metallic materials. If the blocks were too thick to be cut by hand (using gloves), they were cut into suitable pieces with a clean razor blade on a Teflon™ substrate. This was the only time that the chloride was in contact with metal, and it was cleaned immediately afterwards since it reacts quickly with most metals, forming the metal chloride and silver, both of which are detrimental for the sensitization of the chloride. Blades were used only once since a thick layer of corrosion product forms on their surface after the contact with chloride. The chloride was manipulated with clean polyethylene gloves to avoid any contamination with finger grease. Powdered rubber gloves were avoided since the talcum can contaminate the sample. When not manipulated, the chloride was stored in a glass beaker covered with a glass funnel to avoid contamination with air-born dusts. All operations described below involving the reactive molten silver chloride were performed in Pyrex or quartz glassware, previously aged in boiling nitric acid for 15 minutes, thoroughly rinsed in distilled water and dried with nitrogen prior to each experiment in order to avoid contamination by leached metallic ions.

The chloride was cleaned for about 10 minutes in a 10% HCl aqueous solution, rinsed in distilled water and dried in an air oven at about 400 K in a covered glass beaker. Another drying technique was to blow the water with a stream of nitrogen from a compressed tank. The cleaned cuttings were charged in a Pyrex crucible and melted under dry nitrogen by heating the glass apparatus shown in Fig. 4.1.1a with an oxygen-gas flame, making sure that the heat was applied evenly. High purity dry nitrogen from Airco was used, containing 0.5 ppm oxygen, 2 ppm water, 2 ppm hydrogen, 0.5 ppm carbon mono- and dioxide, 0.5 ppm hydrocarbons. The melt was purified by slowly bubbling 99.9% pure chlorine (lecture bottle purchased from Mattewson) for about 15 minutes, to transform silver oxide or metallic silver into chloride. This operation was stopped when no oxide layer was visible at the top of the melt. The chlorine was flown through monel, Teflon™ and glass tubes and was thus never in contact with materials with which it could react and thus contaminate the melt. After bubbling through the melt, the chlorine was bubbled through three washing bottles containing sodium hydroxide or sodium thiosulfate aqueous solutions in order to minimize the emission of chlorine in the hood. The melt was then degassed for about 15 minutes by bubbling dry nitrogen, solidified and cooled to room temperature under the same atmosphere in the crucible which was tipped to avoid solidification of the melt around the capillary. The ingot was transferred to a capillary filter (Fig. 4.1.1b), heated in dry nitrogen until a drop of liquid ran down the capillary and sealed it by solidifying at its tip, and was then completely melted. The melt was then run through the capillary into a cold crucible by melting the small drop of chloride blocking the capillary tip. Any solid particles, silver oxide or colloidal silver present in the melt were deposited on the walls of the filter. This filtering operation was repeated until no residues were left on the walls of the filter.

The silver chloride was then doped with 0.1% cuprous chloride (99.999% purity powder purchased from Strem Chemicals, Massachusetts), by melting both compounds in a crucible under dry nitrogen, and thoroughly mixing them in the liquid state by shaking the apparatus. The previous degassing operation is crucial for the success of this last step since any free chlorine will transform the cuprous chloride into cupric chloride, with a subsequent loss of sensitization (Mitchell 1988). The resulting master "alloy" had a distinct yellow color and was quite brittle, since grains would fragment when the sample wrapped in Teflon™ was hit with a hammer. It was stored in the dark in a plastic box prior to the fabrication of a plate, at which point a fragment of about 200 to 300 mg was rinsed in distilled water, dried, and put in a capillary together with a piece of rinsed and dried non-doped chloride of the same mass. The chloride pieces were then melted under flowing dry nitrogen, the melt shaken and solidified 3 to 5 times to thoroughly mix the cuprous chloride which was then present in silver chloride in a concentration of 500 ppm.

The reinforcements used were glass microspheres (borosilicate Corning glass 7070) with a diameter range of 1-5 μm , glass particles (borosilicate glass BK10) in the same dimension range, glass continuous fibers (strontium oxide glass) with a diameter range from 0.8 to 2 μm , all purchased from MoSci Corp. (Rolla, Missouri). Chopped Safimax™ alumina fibers 3 μm in diameter were also used (Imperial Chemical Industries, Runcorn, UK). A slurry of the reinforcement in pure acetone was spread on two quartz plates which were then laid on top of each other so that the reinforcement would be on the inside surfaces. Quartz capillary tubes of 170 μm diameter were used as spacers. Great care was exerted to avoid dust contamination. The quartz plate were heated in the plate oven shown in Fig. 4.1.2 to about 823 K. The doped silver chloride prepared in the

capillary was remelted under flowing dry nitrogen and poured onto one of the bottom quartz plates while the other was held with steel tweezers. The melt was then immediately topped by the top quartz plate which was slowly moved in a circular motion to induce a turbulent flow and engulf the reinforcement on the plates. The sandwich was then pushed at a speed of about 10 $\mu\text{m/s}$ onto a water-cooled chill, thus directionally solidifying the composite silver halide plate. In another configuration used for certain samples, the bottom quartz plate was directly attached to a water-cooled arm itself connected to the motor which pulled the sample out of the hot zone. The solidification front was visible since the molten chloride is red while the solid chloride at the melting point has an orange color. The front was found to be perpendicular to the growing direction. After the whole sample was solidified, it was immersed while hot in distilled water. This usually helped remove at least one of the plates and expose the sample which was dried under a flow of nitrogen and immediately checked under the microscope. The other plate could be removed after further immersion in water for about 10 min. If it was still attached to the plate, the pH of the water was reduced to 6 using HCl and the sample kept for some more time. Stubborn adhesion was usually a sign of the presence of silver oxide at the sample surface, which destroyed the sensitivity of the sample. Silver oxide was formed after the transfer of the melt on the quartz plate if it was not promptly covered with the hot top plate, but was also found in improperly prepared feed material.

The large as-cast plates were then cut into smaller samples with a clean razor blade. The contamination at the edges was minimal due to the small thickness of the sample and since the sample was not remelted. Cleaning in HCl was avoided since it lead to a reduced sensitivity of the sample, probably by diffusion

of chlorine ions having reacted with the cuprous chloride. The cut samples were laid on a quartz plate and annealed to remove the dislocations introduced by the differential contraction of the quartz plates and the specimen. The annealing was done in a tube furnace under flowing dry nitrogen for two hours at 673 K, and the samples were then gas quenched to room temperature at a rate of about 1 K/s. The quartz plate was carefully removed from the oven and the undisturbed samples immediately exposed to the unfiltered light of a stroboscope (model 510AL, Electronic Brazing Company) with the following characteristics: Xe tube, 60 flashes/second, integrated illuminance per flash: 35 lux/s. Immediately thereafter, the samples were mounted on a microscope slide using Permunt mounting medium (Fisher Sci.) and a thin cover plate; the decorated substructure was observed without delay in transmitted light using a Zeiss inverted microscope Z/M 35 with a 100x oil immersion lens of numerical aperture 1.25 or an Olympus metallurgical microscope AH2 with a 100 x dry lens of numerical aperture 0.95. Photomicrographs were taken using a 35 mm camera fitted to the microscope and the films used were Ilford PanF (50 ASA) and Ilford FP4 (125 ASA) under white or green light. The negatives were developed and printed by an outside photographic shop. All pictures in this thesis were printed at MIT using high contrast glossy paper.

4.2 Other experiments pertaining to silver chloride decoration

Many experiments were performed using silver chloride powder as starting material (Cerac AgCl 99.999). Even though the chemical purity of the powder was high, the chlorination and filtering operations could never eliminate the coloration of the resulting ingot; this was probably due to the the large amount of metallic silver and silver oxide present on the surface of the fine powders.

Vacuum melting was attempted without significant improvement of the crystal quality. A white deposit was always observed in the cooler part of the oven and could have been condensed chloride, since AgCl in powder form is white. When chemical contamination was present, colored deposits were found on the cool part of the vacuum oven.

In order to try to degas the melt, purified and filtered chloride was melted under nitrogen after which a vacuum was pulled on the melt. As expected, large bubbles formed and raised to the surface of the melt which was subsequently solidified under vacuum. When remelted, more bubbles would slowly form, possibly due to a reaction with the glassware. Even when many cycles of degassing and solidification in vacuum were performed, the plates made from this material did not show significantly less bubbles.

The developer described by Hedges and Mitchell (1953) was used to try to predict the quality of treated silver chloride. Pure reagents were mixed in distilled water (the reagent described as *metol* in the above paper is 4-methyl-amino-phenol-sulfate) and pieces of chloride at different stages of chlorination, filtration and sensitization dipped for 1 to 2 seconds. The surface of the specimen became completely black when the chloride was oversensitized by oxygen; but even after a treatment which produced decorated specimens, the developer induced some black spots visible under the microscope on the sample surface. The developer was thus a good indicator of the effectiveness of chlorination (a well purified sample showed only a few spots after developing) but did not reliably predict the decorability of the specimens.

A series of experiments were performed on silver bromide rather than chloride since decoration is easier to achieve in that salt (Mitchell 1988). Nitrogen was bubbled through liquid bromine at ambient temperature prior to the bubbling in

the AgBr melt, but otherwise the experiments were performed in the same way as described for AgCl.

Many experiments were performed to try to sensitize the samples with oxygen rather than with copper. Filtered silver bromide was melted and brominated; low purity nitrogen containing oxygen as a natural impurity (or in certain cases air rather than nitrogen) was then bubbled through the melt. Its contact angle would then change from non-wetting to wetting as more oxygen dissolved. It was never possible to find an optimum in decorability even by monitoring the wetting angle: either the sample were undersensitized and did not show any decoration upon exposure to actinic light, or the samples were oversensitized and the surface became black when exposed. Annealing of oversensitized samples in bromine atmosphere was tried but did not yield any good results. Similarly, dissolution of the top surface with a 0.1 N KCN aqueous solution was tried without improvement of the decorability. Good decoration was only achieved by addition of cuprous bromide in a similar manner to the experimental procedures described above for silver chloride doped with cuprous chloride. To reduce the number of variables, silver bromide was not used in this study; it is however a satisfactory alternative to silver chloride.

Following the description of Mitchell and coworkers, the light of a 250 W high pressure mercury vapor lamp (with or without outer glass envelope) was used to decorate samples for a duration of 1 to 10 seconds, depending on the sensitivity of the specimens. It was difficult to avoid overexposure of the top surface which would then hide the decorated bulk. Much better results were obtained with the stroboscope described in the previous paragraph. An attempt was also made to use a pulsed system where light from the stroboscope and an electrical field across the sample were applied simultaneously. An electronic pulse generator was custom-made at MIT to trigger the stroboscope described in the previous

paragraph as well as a DC 200 V power supply. The sample was placed between a copper electrode and a glass plate on which a thin layer of gold had been evaporated, forming a transparent electrode through which the light of the stroboscope could illuminate the sample. However, experiments on sensitized samples produced very little decoration. It seems that the glass electrode decreased the intensity of light reaching the sample since samples exposed between the electrodes but without the pulsed field exhibited very little decoration. This line of research was not pursued since good decoration could be achieved with the stroboscope alone.

4.3 Sample preparation for photoelastic experiments

Some experiments were performed to investigate the photoelasticity of composite silver halide. The samples produced had however many bubbles that disturbed the stress field produced by the reinforcement. Some samples were prepared using the same procedures described above. About ten glass fibers 80 μm in diameter were arranged parallel to each other and separated by spacers from each quartz plate. The sandwich was heated in the furnace described above and a large drop of molten chloride was deposited on the bottom plate as well as the offset top plate. Due to capillarity forces the chloride was drawn between the two plates, engulfing the fibers. Directional solidification was performed as described above, resulting in a sample containing bubbles. The same experiment was performed vertically in a muffle furnace under nitrogen and showed fewer bubbles. Another sample was prepared horizontally as above, except that the fibers were inserted between two rolled pieces of silver chloride and the sandwich thus formed melted. The resulting sample exhibited a large number of bubbles, probably from entrapped air.

In an attempt to eliminate the bubbles, some of the samples described above were not separated from the quartz plate but slowly passed vertically through a zone melter (Fig. 4.1.3), starting with the bottom part of the sample. Some of the bubbles could thus be eliminated but new ones formed at the sample surface. Very large grains were observed in the remelted zone.

The samples were observed in transmission at low magnification with cross-polarized nichols with the metallurgical microscope Olympus in section 4.1. Some of the samples were strained because they were still adhering to one of the quartz plate which had shrunk less than the sample upon cooling from fabrication temperature. Another technique used was to glue aluminum tabs with cyanoacrylate glue (Davcon) directly to the silver chloride. The tensile specimens were mounted on a tensile rig designed to allow observation in transmission and the rig mounted in the microscope. The specimen was strained by slowly turning a screw displacing one of the heads in the rig.

4.4 Figures

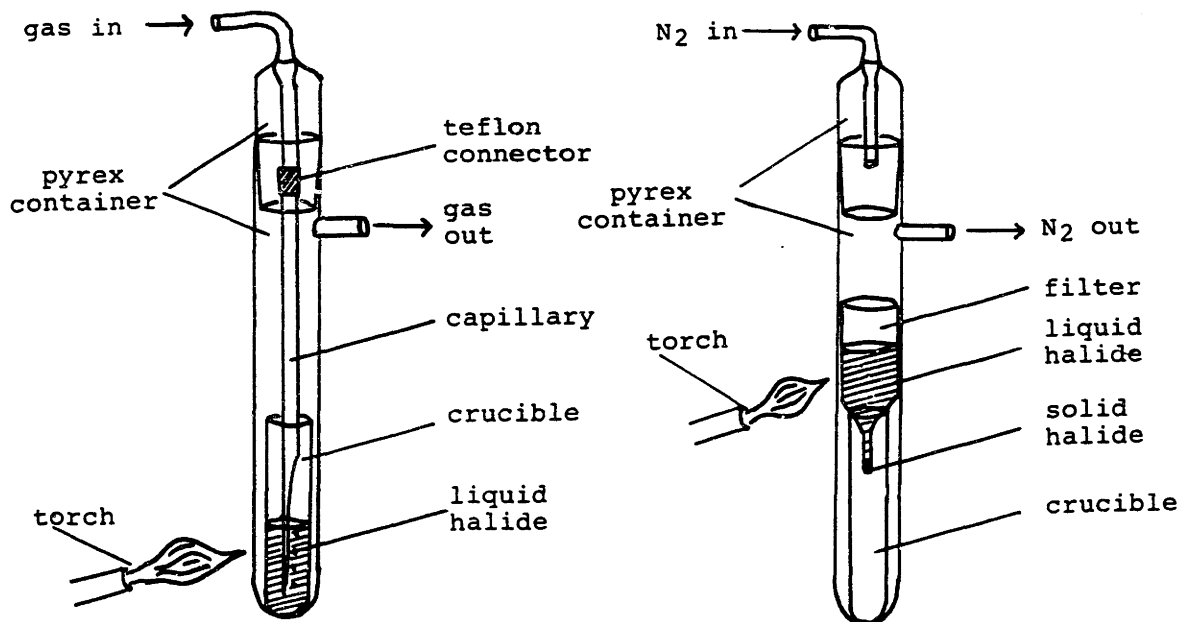


Figure 4.1.1a Apparatus used to purify the AgCl melt.

Figure 4.1.1b Apparatus used to filter the AgCl melt.

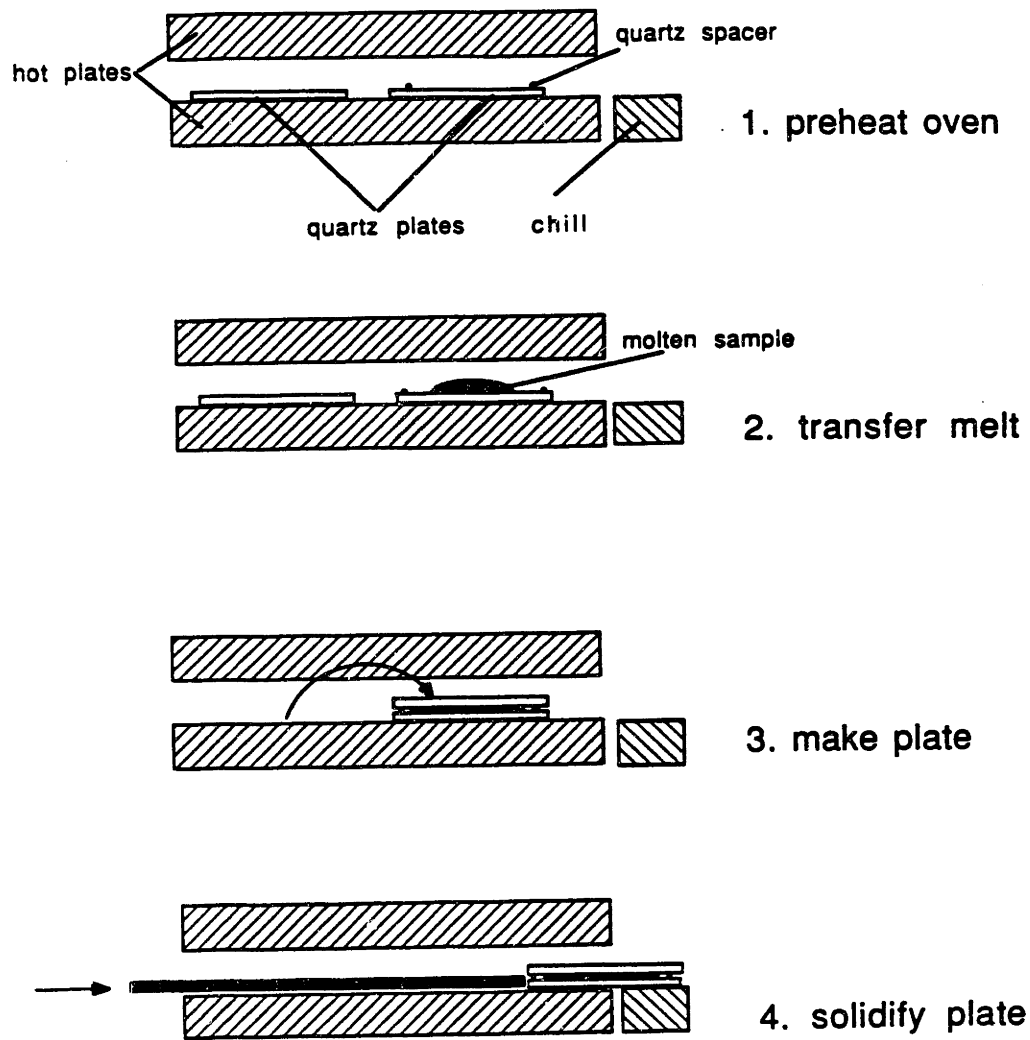


Figure 4.1.2 Procedure used to fabricate AgCl composites.

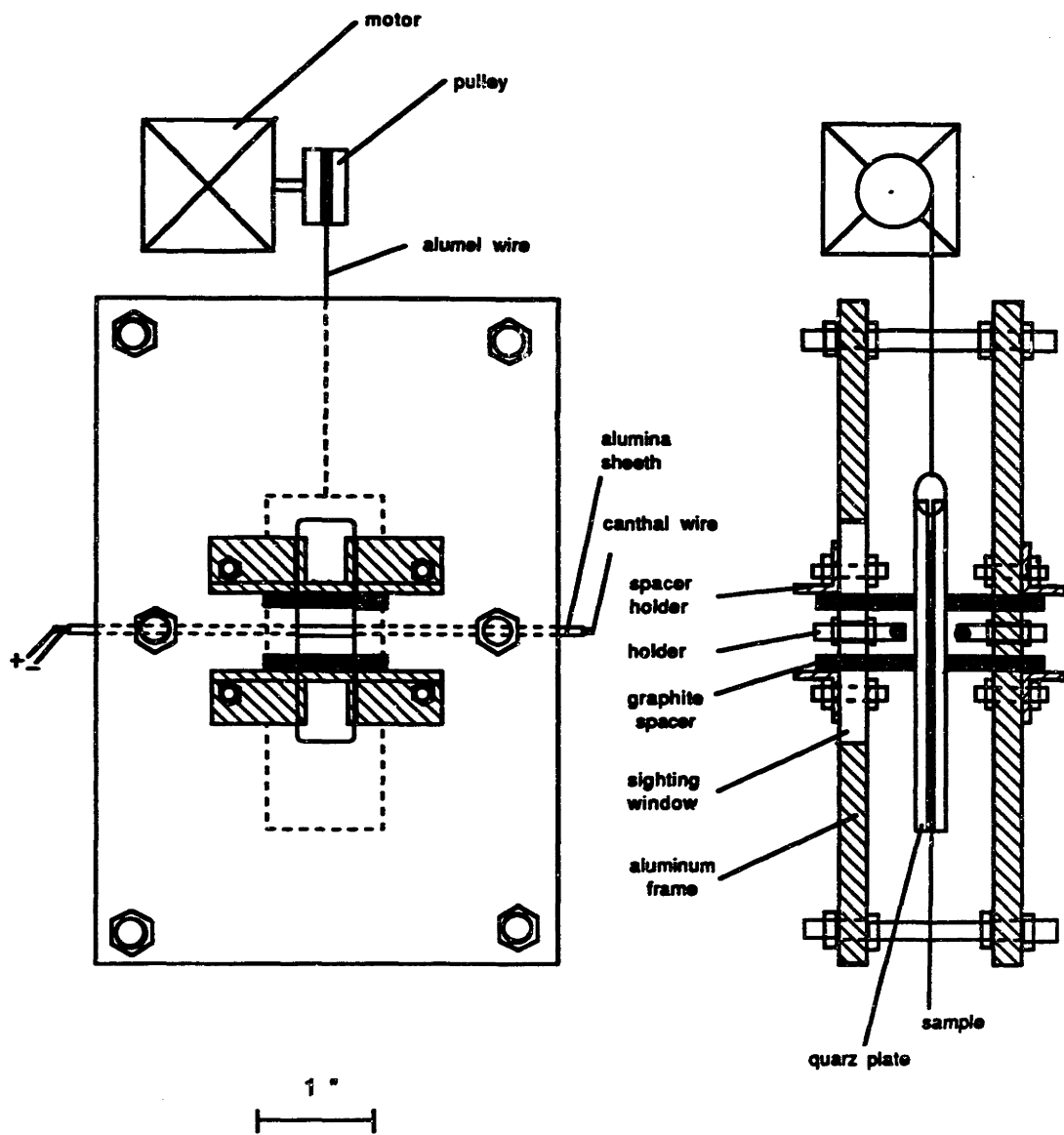


Figure 4.1.3 Zone melter used to remelt samples made in oven shown in Fig. 4.1.2.

5. RESULTS

Density differences between the melt and the reinforcement did not induce any separation of the two phases in the time needed for solidification. Even with the smallest glass spheres, no particle pushing by the solidification front was observed.

A recurrent imperfection found in the as-cast sample was the presence of bubbles which could be due to (i) shrinkage upon solidification, (ii) dissolved gas rejected by the melt, (iii) air entrapped during the squeezing of the melt between the quartz plates and/or (iv) evolution of chlorine due to decomposition of the chloride. Shrinkage porosities - usually 20 to 200 μm long - were recognizable by their elongated pear or tear shape and their orientation parallel to the growth direction. They could be minimized by a slow growth rate and a steep temperature gradient but would nevertheless be present in most samples in a plane halfway between the two surfaces, probably formed by the junction of solid silver chloride growing from the top and bottom quartz plates. This morphology indicated that the solidification front was microscopically not plane, even though visual inspection showed a straight solid-liquid interface. The shrinkage pores were too deep to interfere with the decorated region. It is interesting to note that they could not be eliminated even when the samples were solidified vertically and/or submitted to vibrations. Millimeter-sized round bubbles were always found in some number and could sometimes be seen in the melt after the top plate was in place; these were probably formed by mechanism (iii). Since their volume fraction was small, they did not disturb the observation of the microstructure. Smaller bubbles were often found in the middle plane as well and could have formed by the mechanisms (ii) and (iv). Improperly cleaned or scratched quartz plates would also create surface pores with irregular, angular

shapes of different dimensions. Other defects which were sometimes observed in the bulk were black small precipitates of various shapes, including 1 to 5 μm long rods oriented along crystallographic directions, wavy lines 1 to 3 μm in diameter seemingly showing the outline of dendrites and root- or spider-like tangles. They almost always occurred in non-sensitive samples and might have formed from the reaction with some contaminant. Round, black precipitates on the surface were typical of overheated samples. Etch pits were sometimes found in sample kept in water for more than about an hour. Wavy slip lines at the surface indicated that the sample had been deformed upon removal from the plates. All reinforcements used were found to be wetted by the melt and the interface of the as-cast specimen was free of any visible defect.

5.1 Dislocation microstructure and micromechanics

After annealing and quenching, all the sensitized samples showed small black surface precipitates which must have been due to the copper present in the samples, since non-sensitized control samples did not exhibit such a behavior. These precipitates only occurred at the surface and did not seem to interfere at all with the microstructure in the bulk. Pulsed light of high intensity from the stroboscope was found to yield better decoration of the samples than continuous exposure to the light of a mercury vapor lamp used by some previous investigators. In all samples, random precipitation of silver took place within the silver chloride upon exposure to actinic light, resulting in the "fog" visible in all figures. Grain boundaries and subgrain boundaries were always decorated first; when the samples were properly decorated and only slightly deformed, individual dislocations within the subgrains could be resolved. In most samples, decoration was found to fade in a matter of hours or days, or even more quickly

when the samples were exposed to the intense light of the microscope. Subsequent exposure to the stroboscopic light did not restore the decoration but rather increased the background fog.

5.1.1 Spherical inclusions

High dislocation densities were observed in the vicinity of the glass spheres. The configuration of the resulting plastic zone surrounding the spheres fell in two main categories. In the first, the dislocations were clearly resolved as trains of prismatic loops emanating from the spheres along crystallographic directions. Unresolved tangles were almost always visible, but only along the sides where no loops were punched (Fig. 5.1.1). In the other category, the plastic zone was composed of unresolved dislocation tangles surrounding the inclusion as a continuous shell of variable regularity (Fig. 5.1.2), on occasions coexisting with one or two trains of emitted loops (Fig. 5.1.3). In some cases of intermediate character between these two types (Fig. 5.1.4), an irregular plastic zone was observed featuring lobes that extended along the glide directions (these directions were determined by observing loop rows punched by other spheres within the same subgrain).

Measurements were also performed directly on the micrographs. Fig. 5.1.5 shows the total number of punched prismatic loops as a function of the sphere diameter, for rows of loops which were not separated from the sphere by any tangled dislocations.

The sphere radius and that of its unresolved plastic zone (Fig. 5.1.2) are plotted against each other in Fig. 5.1.6. Only cases where the spheres were isolated from neighbours and where the plastic zone was spherical were considered.

5.1.2 Particulate inclusions

The matrix around the irregularly shaped particles exhibited much higher densities of decorated dislocations than the bulk of the matrix. In rare cases, the only dislocations visible were in form of rows of prismatic loops punched along crystallographic directions (Fig. 5.1.7), a configuration found around microspheres as well (see previous paragraph). The linear structure in Fig. 5.1.7 is a subgrain boundary consisting of dislocations perpendicular to the image plane. They can be resolved as points at the lower right corner of the micrograph and, by changing the focus of the microscope, can be followed in the crystal. Also visible in the same figure is a small particle surrounded by a dark decorated zone consisting of tangled dislocations. Another example of this plastic zone geometry is shown in Fig. 5.1.8, where the dislocations in the tangles are partially resolved. This plastic zone morphology was by far the most common in the sample investigated and its shape in most cases did not resemble the shape of the corresponding particle. Schematic examples of particles and their associated plastic zones as seen in the transmission optical microscope given in Fig. 5.1.9 illustrate this point. Fig. 5.1.10 is an example of a mixed plastic zone morphology: the particle is surrounded by a decorated plastic zone of unresolved dislocation tangles and has also emitted a row of loops which extends at a large distance beyond the interface.

Fig. 5.1.11 is a plot of the frequency of the punching angle ϕ measured on micrographs. The angle was measured between the axis of the punched row of loops and the largest dimension of elongated glass particles.

The projected areas of the particles and their associated plastic zones were cut and weighed from enlarged micrographs; the mean projected length was

measured directly on the enlargements. The relative error for each of these measurements is estimated at 5% for the smallest particles, less for the larger ones. Taking into account the maximum error in the constant K estimated above as 28 %, the maximum relative error on the calculation of the volume using Eq. [3.2.6] due to measurements and the averaged value of K is therefore about 43% for the small particles, less for the large ones. The maximum error on the equivalent sphere radii in Fig. 5.1.12 is thus on the order of 15%. The equivalent radii of the particles and their plastic zones are plotted against each other in Fig. 5.1.12. The only particles considered were those which had clearly defined plastic zones and which were far enough from neighbouring particles so that their plastic zones were not in contact.

5.1.3 Fibrous inclusions

Observations were made on samples with alumina as well as glass fibers. In all cases, the dislocation density was found to be significantly higher close to the fibers than elsewhere in the matrix. The microstructure around the alumina fibers (Fig.5.1.13-15) was usually more complicated and less illustrative in terms of elementary dislocation mechanisms. This is probably because the diameter of the alumina fibers was larger and thus both the number and length of dislocations were larger, leading to more frequent entanglement.

We first describe the dislocation structure around alumina fibers. Fig. 5.1.13 shows dislocation tangles along the sides of a long fiber. Some of the dislocations have been pinned and are bowed due to the local stress field. In most cases, however, single dislocations could not be resolved within the plastic zone surrounding the fibers. The plastic zone could be seen as a dark cylindrical region of precipitated silver around the fiber. This region usually ended abruptly

and was very often separated from the undeformed matrix by decorated subgrain boundaries.

In numerous cases, rows of prismatic loops were seen emanating from the ends of the fibers. In Fig. 5.1.14, a train of loops is shown which bursts through a subgrain boundary and continues in the next subgrain with a slightly different orientation, reflecting the change in crystallographic orientation between the two subgrains. Partially resolved tangles are also visible along the sides of the same fiber. Fig. 5.1.15 shows a fiber surrounded by a dark plastic zone of unresolved dislocations. The plastic zone is larger at the ends of a fiber than at its middle, a morphology frequently observed around other fibers. Due to the directional solidification of the samples, very large grains on the order of a square centimeters were formed. Within these grains, subgrain boundaries - visible as dark continuous lines in Figs 5.1.1,2, 14 and 15 - were always associated with regions of the sample containing reinforcement.

In what follows, we briefly describe the micrographs with glass fibers. Fig. 5.1.16 and 17 are example of fibers punching rows of loops at their tip. Fig. 5.1.18 is an illustration of the more frequent situation in which the axes of the fiber and of the row of loops form an angle. Fig. 5.1.19 presents a fiber which punched elongated loops at each of its tips; the loops are clearly emanating from the sides of the fiber. Tangles of unresolved dislocations form a sheath around the fiber; a subgrain boundary is also visible on either side of the fiber. Fig. 5.1.20, for which the plane of focus is just below the 1 μm diameter fiber, shows a fiber which punched two rows of loops at its tip, both in such a direction as to relax the longitudinal fiber stress. Fig. 5.1.21 shows the tip of a fiber which has emitted what seems to be parallel non-coaxial elongated dislocations which rotate and merge into a subgrain boundary. Fig. 5.1.22 presents a peculiar dislocation structure encountered in many instances: the tip of both fibers in this

micrograph have punched a pair of coaxial rows on either side of the fiber. The outward row is clearly detached from the fiber and similar to those presented earlier while the inward row is always attached to the fiber. In Fig. 5.1.23, three fibers can be seen with their associated dislocation structures: fiber A has punched rows of loops at both of its tips, fiber B emitted four rows at 90°, two of which are blocked by fiber A and C. Fiber C is surrounded by tangles in which some bowed dislocations can be distinguished. Fig. 5.1.24 similarly shows a thin fiber which has emitted elongated dislocations, some of which are still attached to the fiber. A similar situation is found in Fig. 5.1.25, where all the dislocations are pinned and bowed due to the stress of the fiber. Finally, in Fig. 5.1.26, tangles around a thin glass fiber are visible, with some of the dislocations in the plastic zone discernible. This configuration is similar to that observed for the larger diameter alumina fibers (Fig 5.1.13).

Measurements were performed on the micrographs. Fig. 5.1.27 and 28 report the frequency of the angle between the fiber axis (alumina and glass respectively) and that of the row of loops. Fig. 5.1.29 is a plot of the stress to which pinned dislocations are subjected, as a function of the radial distance from the fiber; the radius of curvature was calculated assuming that the pinned dislocations formed a segment of a circle. By measuring on enlarged micrographs the distance between the anchor points L_b as well as the maximum deflection h from the line running through the two anchor points, the radius of curvature R can be calculated from (Beyer 1979)

$$R = \frac{L_b^2}{8 \cdot h} + \frac{h}{2}, \quad [5.1.1]$$

from which it is possible to derive the local stress σ_b (Hirth and Lothe, 1982), assumed constant along the dislocation line:

$$\sigma_b = \frac{G \cdot b}{4 \cdot \pi \cdot R \cdot (1-\nu)} \left\{ \frac{\nu}{2} - 1 + \left[1 - \frac{\nu}{2} (3 - 4\cos^2\beta'') \right] \cdot \ln \left(\frac{L_b}{R_0} \right) \right\}, \quad [5.1.2]$$

where G is the matrix shear modulus, ν its Poissons ratio, R_0 the core distance of the dislocation and β'' the angle between the dislocation line and the Burgers vector. The angle β'' being unknown, the square of its cosine is taken as 0.5 (the average of \cos^2x). The core distance is taken as 33% the value of the Burgers vector, as determined by Puls and So (1980) for sodium chloride. These two parameters have little influence on the numerical result. The Burgers vector was assumed to be along $\{110\}$, the main slip direction in silver chloride (Sprackling 1976). The Poisson's ratio was taken as 0.343, the average of the values of elastic constants determined by three investigators (Stepanov and Eidus 1955, Vallin 1967, Hidshaw *et al.* 1967); other materials data are listed in Table 3.1.

The length of the row of loops normalized to its diameter as a function of the aspect ratio of the corresponding punching glass fiber is plotted in Fig. 5.1.30 for fibers with a row of loops at each of their tips and in Fig. 5.1.31 for those with a row at only one end. The former case was observed much less frequently than the latter. Only rows for which no visible obstacles (such as subgrain boundaries or other fibers) had interacted with the punched loops were considered. Nearly all alumina fibers exhibited rows which were blocked by subgrain boundaries (Fig. 5.1.14 is an example of such a case) and therefore no data is presented for these fibers.

In Fig. 5.1.32, the maximum number of radially punched, elongated loops (such as those in Fig. 5.1.25) is plotted as a function of the glass fiber diameter. The average number was usually 25 to 50% smaller. The only fibers considered had no tangled plastic zones and showed dislocations far away from the tip to minimize the effect of longitudinal stresses. The dislocation lines were counted radially on both sides of the fiber; usually, one side had punched significantly more dislocations than the other.

5.2 Photoelasticity

As-cast samples still adhering to one or both of the quartz plates used during fabrication were observed in the optical microscope in transmission between crossed nichols, with or without a compensating $\lambda/4$ plate introduced in the optical train. All samples exhibited strong birefringence due to the stresses from the differential contraction between the sample and the quartz or pyrex plate(s). Grains were visible as areas of different contrast. Inside some of the grains, slip bands were visible as systems of parallel bands 10 to 50 μm thick with alternating contrast. In certain cases, two slip band systems were found superimposed; slip bands in different grains had different orientations. Sometimes, as in Fig. 5.2.1, only one of two adjacent grains exhibits slip bands. Figs. 5.2.2 and 3 show the photoelastic contrast observed at the end of alumina fibers 3 μm and 20 μm in diameter respectively, while Figs. 5.2.4 and 5 illustrate large glass fibers 80 μm in diameter.

5.3 Figures

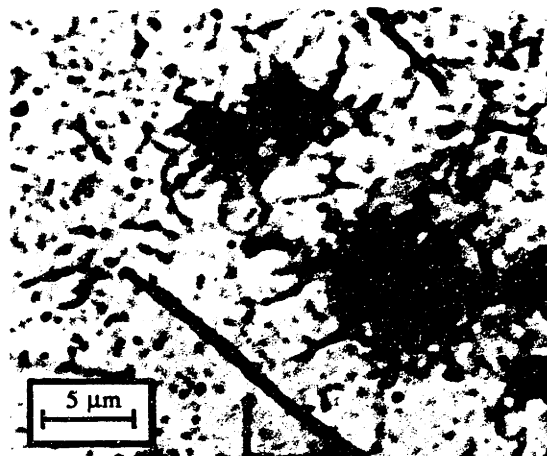


Figure 5.1.1 Decorated prismatic loops in AgCl punched by a glass sphere. Unresolved tangles are visible in the directions where no loops were emitted.

Figure 5.1.2 Unresolved dislocations forming a spherical plastic zone around glass spheres embedded in AgCl.

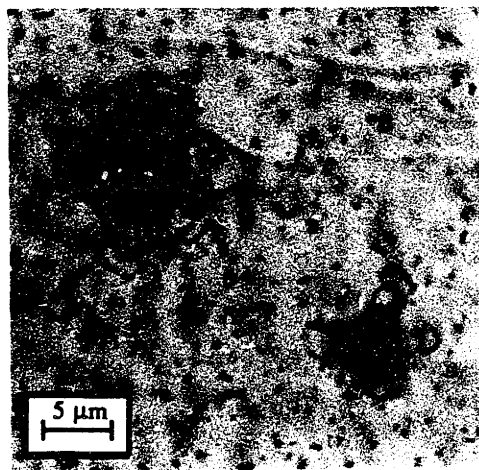
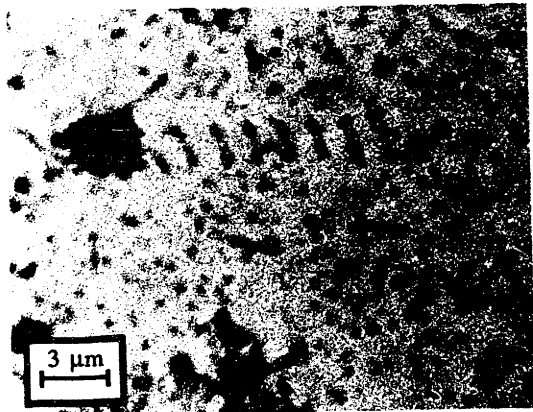


Figure 5.1.3 Glass sphere in AgCl matrix surrounded by an irregular zone of unresolved, decorated dislocations and having emitted prismatic loops.

Figure 5.1.4 Glass spheres in AgCl matrix surrounded by tangled, decorated dislocations in a plastic zone forming lobes.

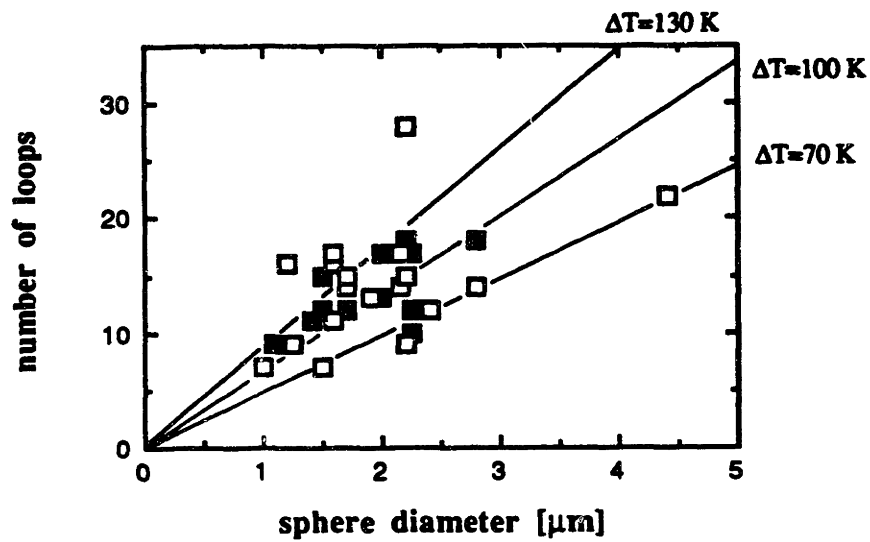


Figure 5.1.5 Total number of prismatic dislocations loops punched by glass spheres in AgCl as a function of the sphere diameter. Open squares : single row of loops. Filled square : double rows of loops. Lines : calculations from Eq. [5.2.3] for different values of ΔT .

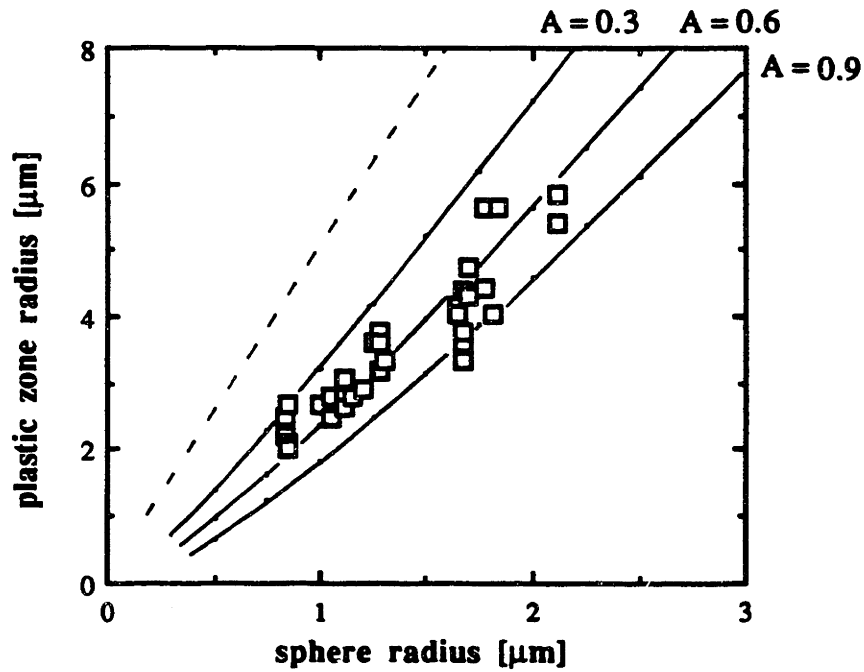


Figure 5.1.6 Radius of plastic zone surrounding a sphere in an AgCl matrix as a function of the radius of the corresponding sphere. Squares : experimental data. Full curve : strain-hardening matrix with $A=0.6$ (Eq. [3.1.12b]); dotted curves : non strain-hardening matrix (Eq. [3.1.6b]).

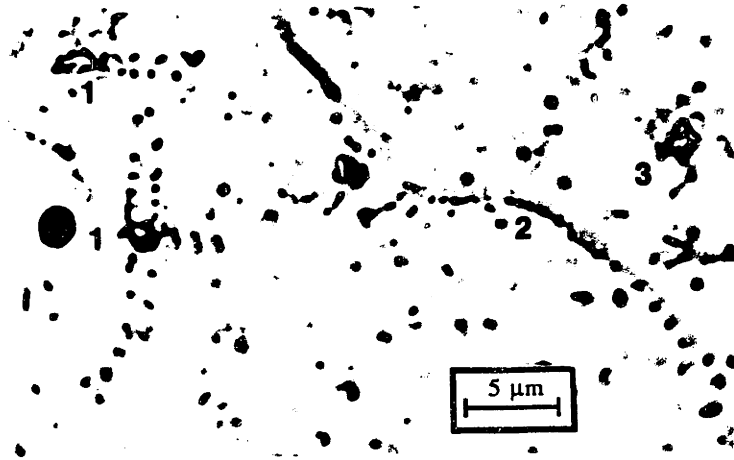


Figure 5.1.7 Decorated prismatic loops in AgCl punched by two glass particles (1). A wall of dislocations perpendicular to the image plane form a subgrain boundary (2). Unresolved tangles are visible around another particle (3).

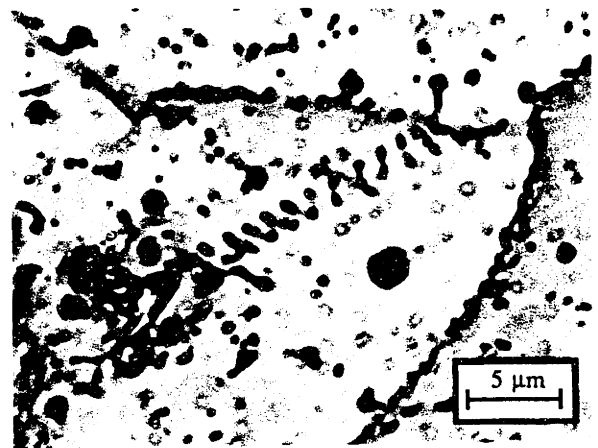
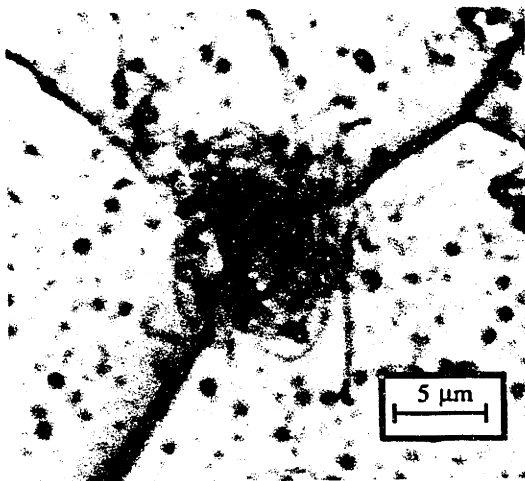


Figure 5.1.8 Partially resolved, decorated dislocations in AgCl forming a plastic zone around a glass particle located at the intersection of three grain- or subgrain boundaries.

Figure 5.1.9 See next page

Figure 5.1.10 Glass particle in AgCl matrix surrounded by an irregular zone of unresolved, decorated dislocations and having emitted prismatic loops, some of which form an helix. The row of dislocations is blocked at a subgrain boundary.

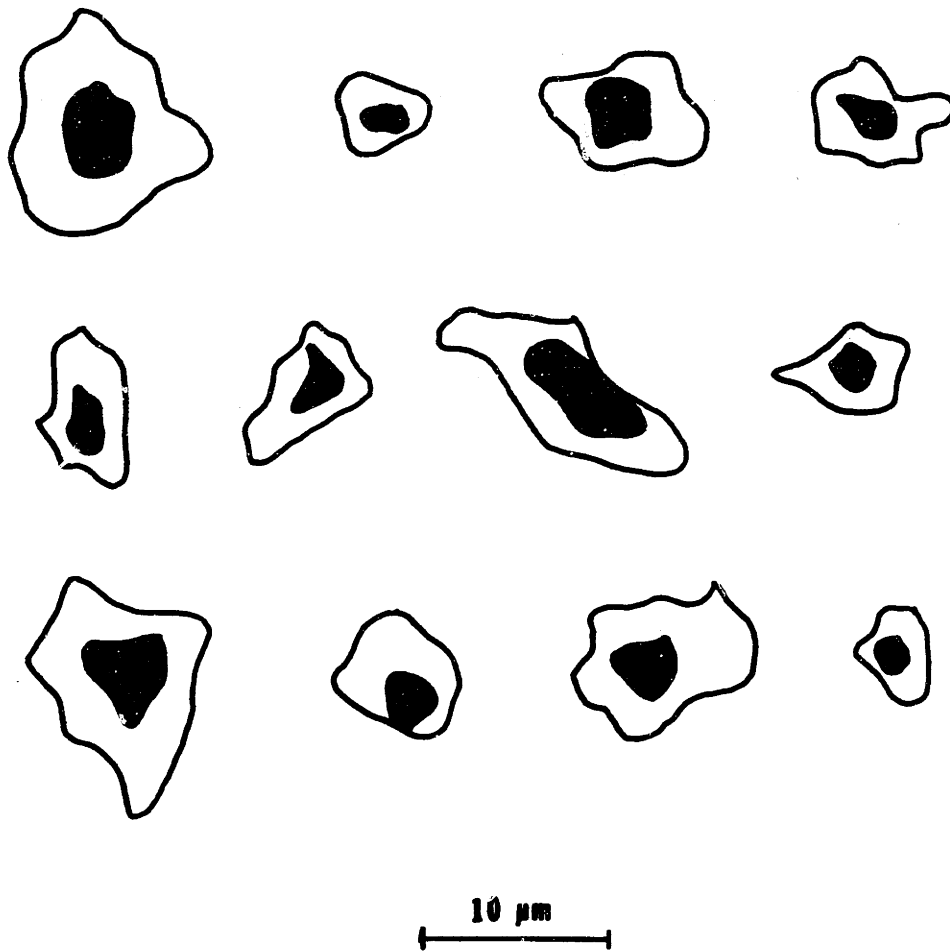


Figure 5.1.9 Schematics of particles and their associated plastic zone traced by hand from enlarged micrographs.

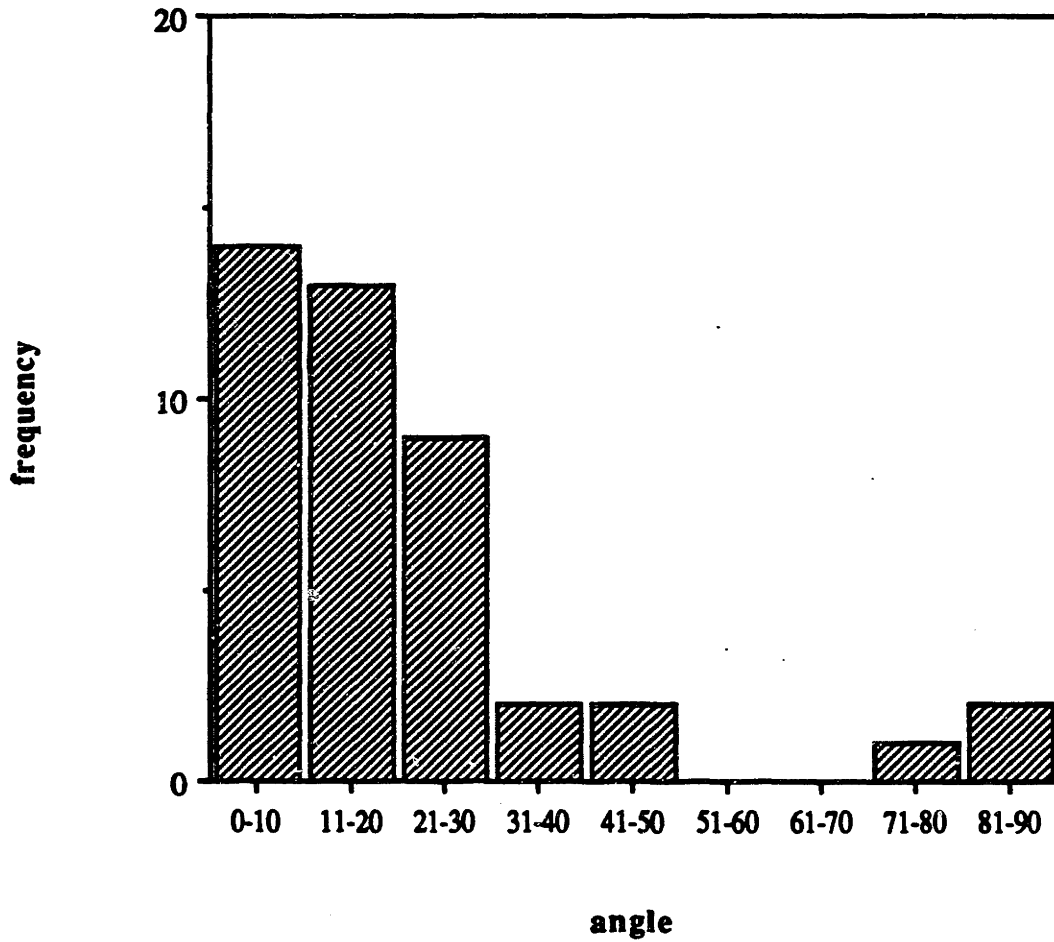


Figure 5.1.11 Plot of the frequency of the punching angle for non-equiaxed particles.

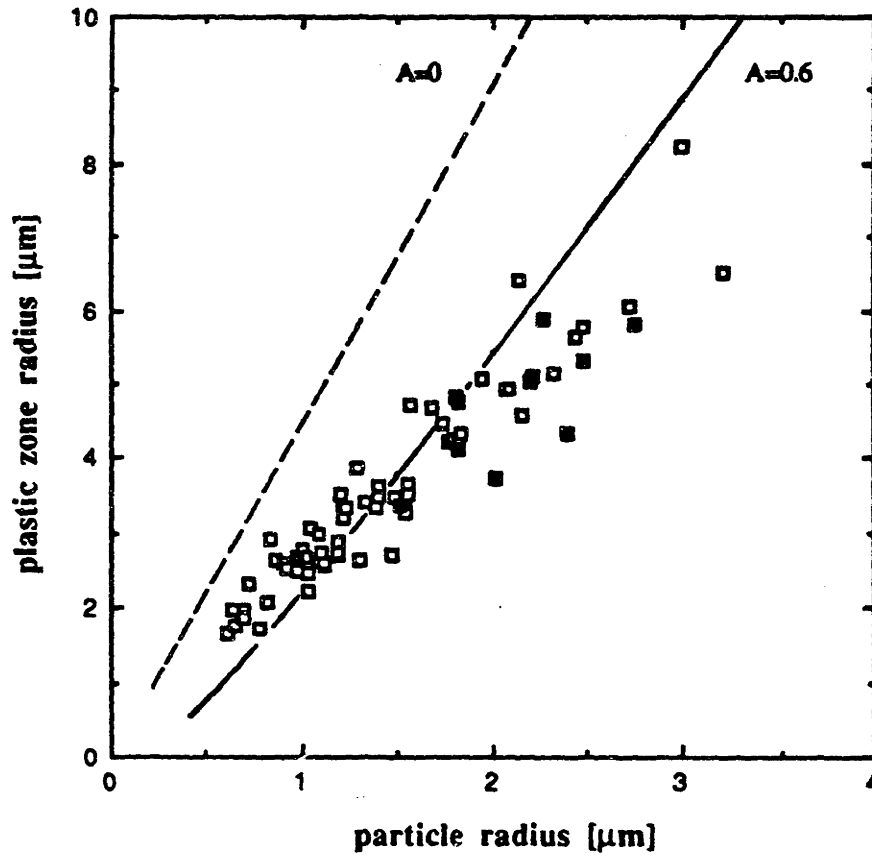


Figure 5.1.12 Equivalent radius of the plastic zone surrounding glass particles in AgCl as a function of the equivalent radius of the corresponding particle. Full squares : plastic zones formed of tangled dislocations and row of loops (Fig.5.1.10); empty squares : plastic zone formed by tangled dislocations only (Fig. 5.1.8). Full curve : strain-hardening matrix with $A=0.6$ (Eq. [3.1.12b]); dotted curves : non strain-hardening matrix (Eq. [3.1.6b]).



Figure 5.1.13 Decorated, pinned dislocations in the plastic zone surrounding an alumina fiber in an AgCl matrix. Due to the stress from the fiber, some dislocations are bowed. The fiber is out of focus, being a few microns off the image plane.

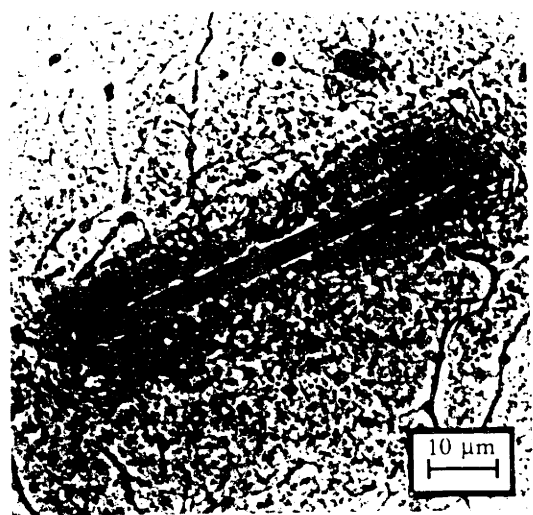


Figure 5.1.14 Decorated rows of prismatic loops punched from a short alumina fiber in an AgCl matrix. After bursting through a subgrain boundary (dark continuous line), the loops change orientation in the second subgrain. Partially resolved dislocation tangles are also decorated around the fiber.

Figure 5.1.15 Peanut-shaped plastic zone around an alumina fiber embedded in AgCl.

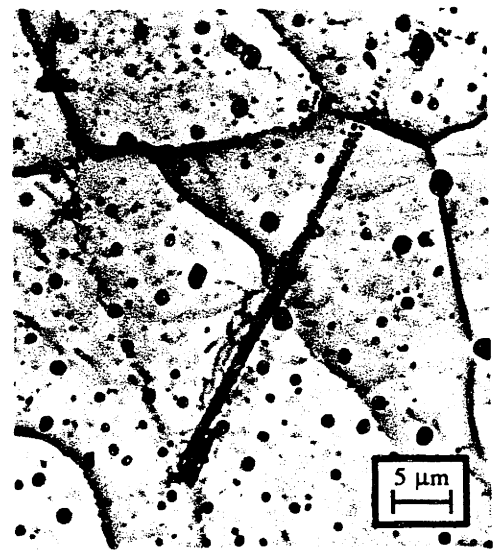
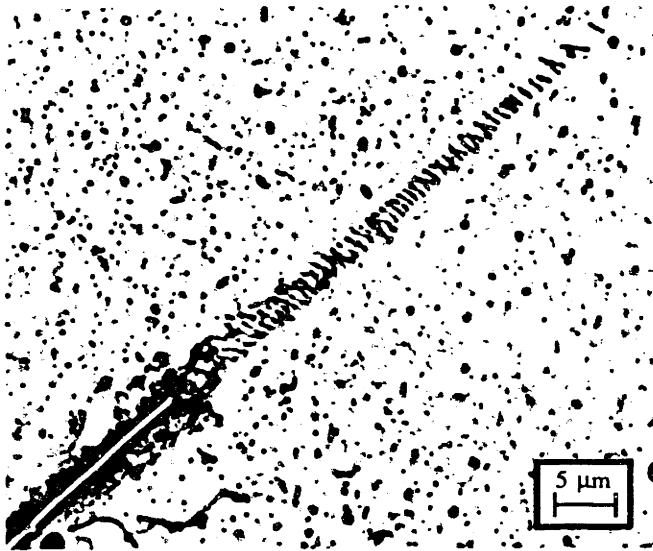


Figure 5.1.16 Row of decorated, prismatic loops emitted by a glass fiber in AgCl. A dark zone formed of unresolved dislocation tangles surrounds the fiber.

Figure 5.1.17 Row of decorated prismatic loops punched from the end of a glass fiber in AgCl. The fiber and part of the row are out of focus. The row bursts through a subgrain boundary and continues in another subgrain. Elongated dislocations are visible along the sides of the fiber.



Figure 5.1.18 Glass fiber with emitted row of prismatic loops punched at an angle in AgCl. The fiber is also surrounded by a plastic zone formed of unresolved dislocations.



Figure 5.1.19 Glass fiber in AgCl with decorated dislocation structure consisting of two rows of elongated loops emitted sideways at the fiber ends and a plastic zone surrounding the fiber (dislocations are not resolved). The linear feature is a subgrain boundary.

Figure 5.1.20 Two rows of decorated loops punched by the tip of a glass fiber in AgCl. Loops are on non-adjacent glide systems.

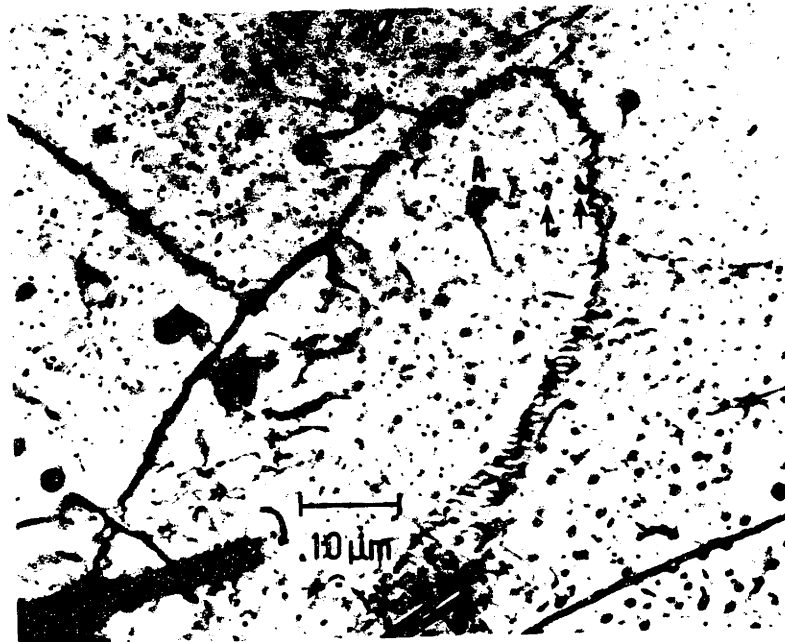


Figure 5.1.21 Rows of elongated, decorated dislocations emanating from the tip of a glass fiber (B) in AgCl. Dislocations rotate away from the fiber and form a wall or subgrain boundary. An out-of-focus inclusion (A) emitted prismatic, decorated loops, two of which are visible (arrow).

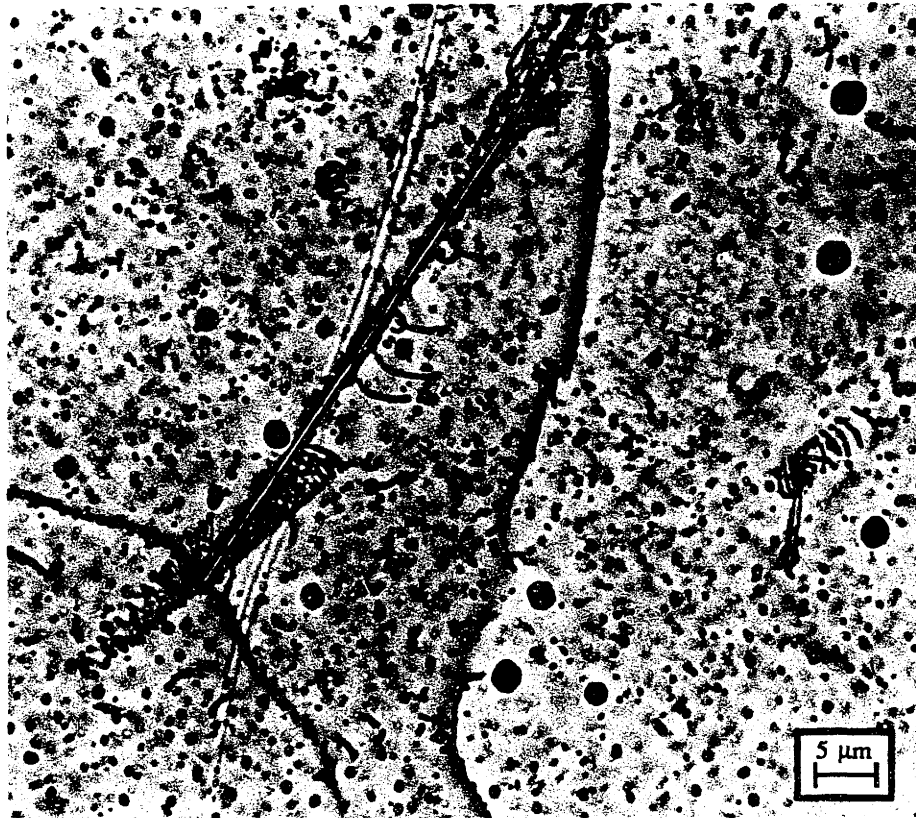


Figure 5.1.22 Two glass fibers in AgCl showing the same dislocation structure: a double row of decorated elongated loops emitted by the tip of the fiber. The outward row is similar in nature to those in Fig. 5.1.18; the inward row is attached to the fiber.

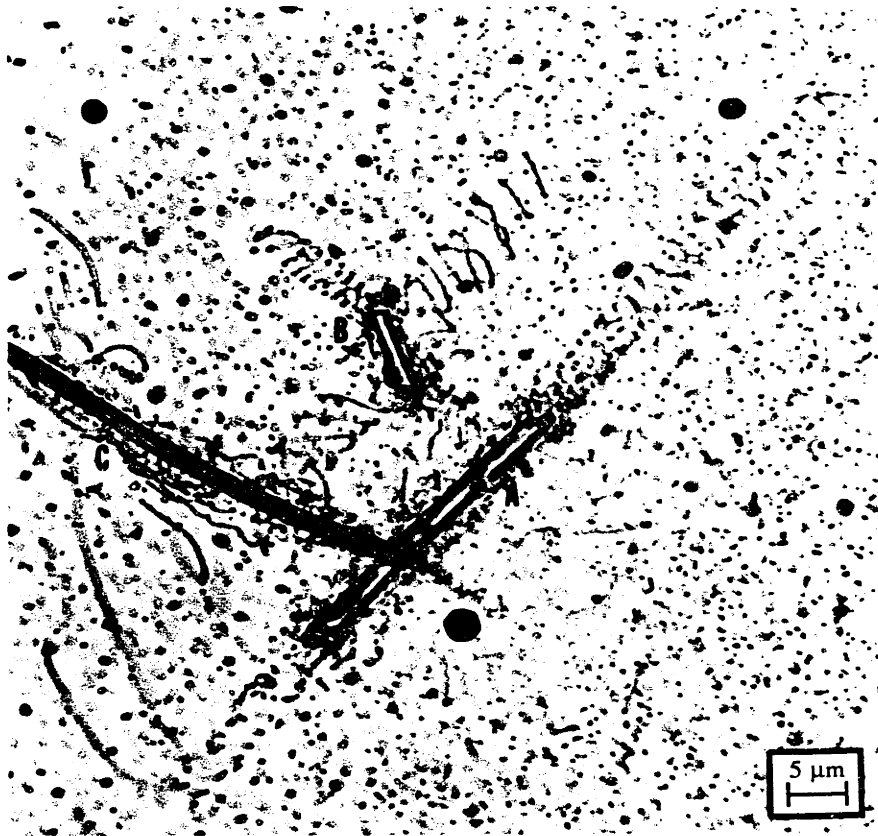


Figure 5.1.23 Three glass fiber having emitted decorated dislocations in AgCl. Fiber A punched a row of loops at each of its end. Fiber B punched four rows, two of which are blocked by fiber A and C. Fiber C is surrounded by a plastic zone in which some dislocations can be resolved.

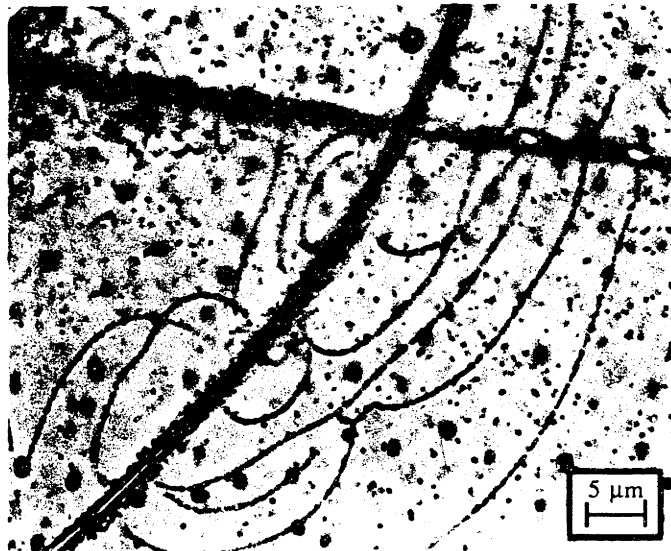


Figure 5.1.24 Glass fiber in AgCl with elongated, decorated loops emitted by its sides. Some of the dislocations are still attached and bowed due to the residual fiber stress.

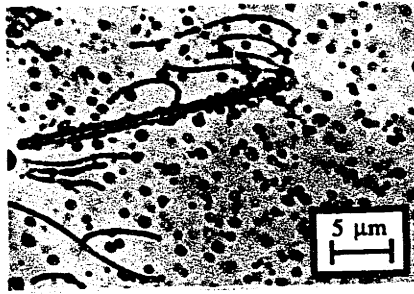


Figure 5.1.25 Long, decorated loops emitted by the sides of a long glass fiber in AgCl. Some loops are still attached to the fiber and all are bowed by its residual stress.



Figure 5.1.26 Decorated dislocations forming the plastic zone surrounding a long glass fiber in AgCl. Some of the dislocations can be resolved.

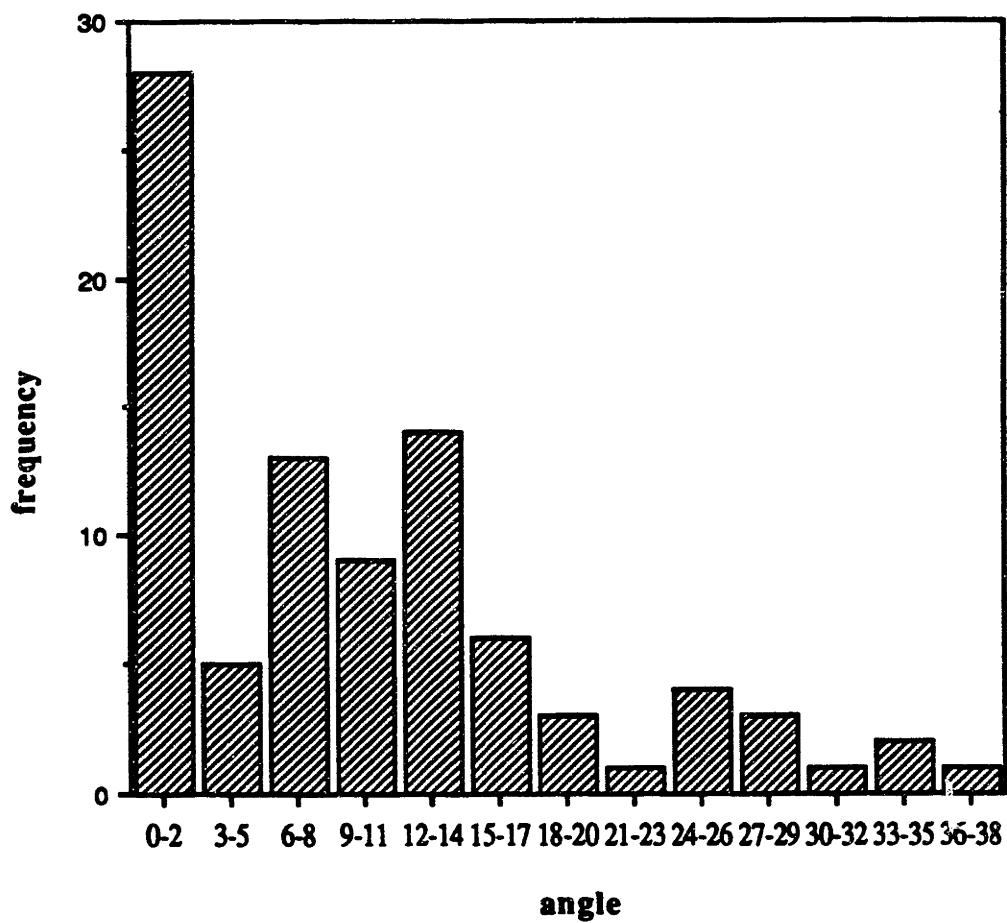


Figure 5.1.27 Plot of the frequency of the angle between the axis of the punched row of loops and that of the emitting alumina fiber.

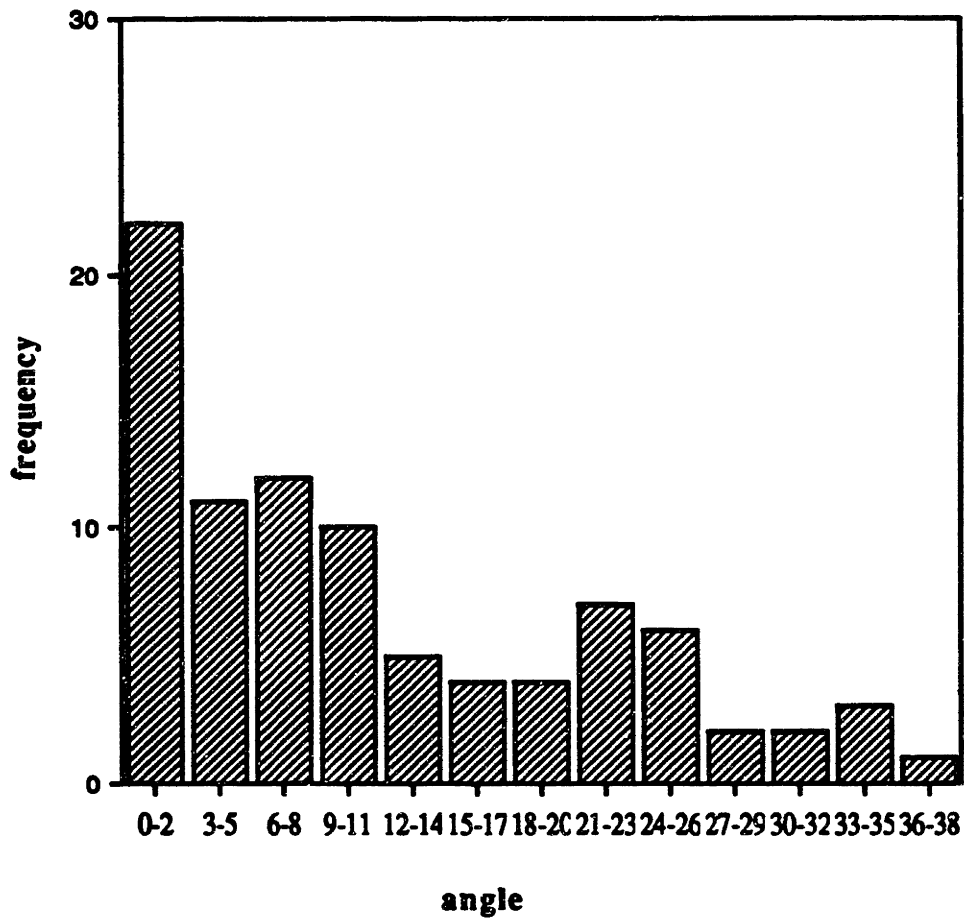


Figure 5.1.28 Plot of the frequency of the angle between the axis of the punched row of loops and that of the emitting glass fiber.

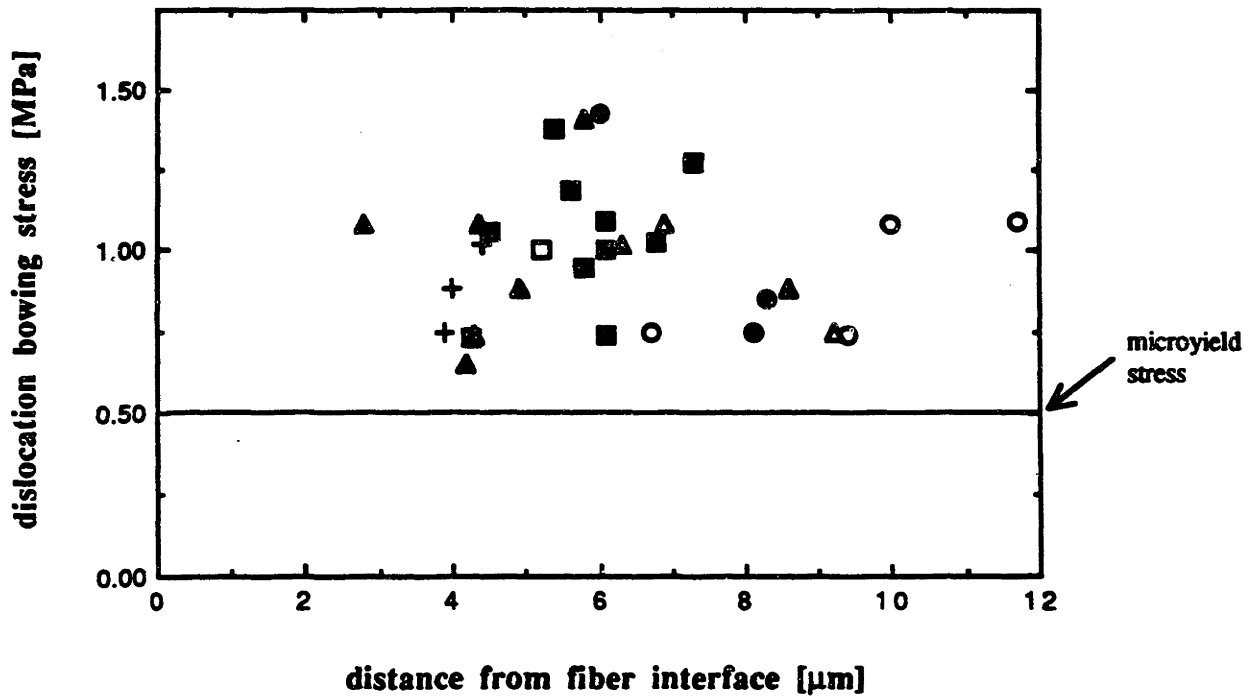


Figure 5.1.29 Stress of pinned dislocations as calculated from Eq. [5.1.2] in the plastic zone surrounding alumina fibers in an AgCl matrix (see Fig. 5.1.13) as a function of radial distance from the interface. The various symbols represent different fibers. The lower horizontal line is the value of the microyield stress in shear as measured by Sprackling (1966) and Haasen and Skrotzki (1981).

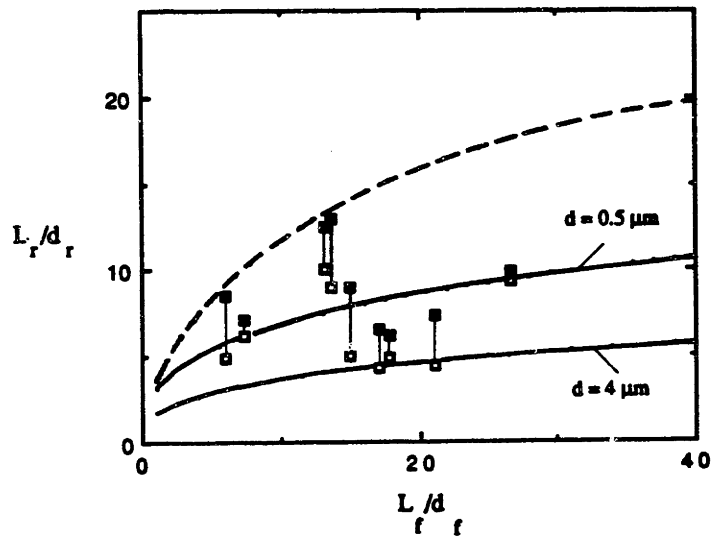
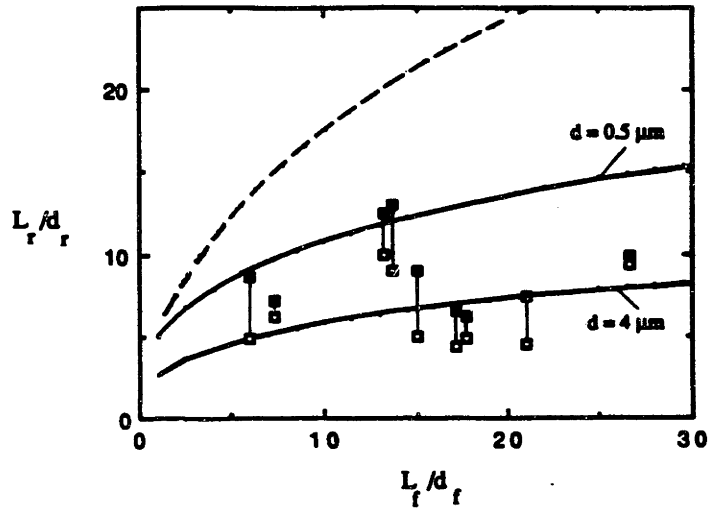


Figure 5.1.30 Plot of the row length (divided by its diameter) versus the fiber aspect ratio. Squares represent experimental data for glass fibers of diameter between $0.5 \mu\text{m}$ and $4 \mu\text{m}$ which punched rows at both their ends; the longer and shorter rows for a given fiber are represented by connected filled and empty symbols respectively. The full lines are calculated from Eqs. [3.4.23] and [3.3.11] and dotted full lines are calculated from Eqs. [1] and [2], App. 5 (Taya and Mori, 1987) for values of the friction stress of 0.25 MPa (upper diagram) and 0.5 MPa (lower diagram) and the above range of diameters.

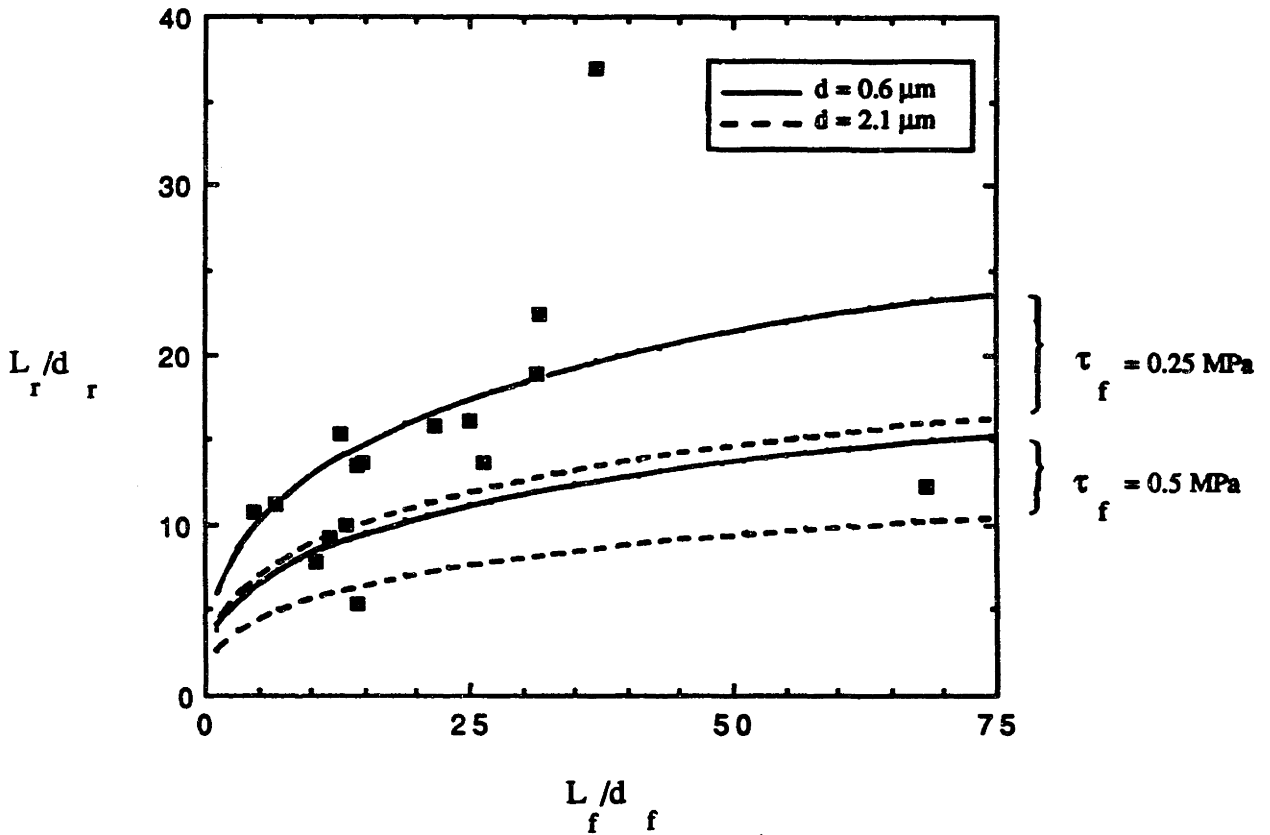


Figure 5.1.31a Plot of the row length (divided by its diameter) versus the fiber aspect ratio. Squares represent experimental data for glass fibers with a diameter between $0.6 \mu\text{m}$ and $2.1 \mu\text{m}$ which had punched a row at only one of their tips. The lines are calculated from Eqs. [3.4.23] and [3.3.11] for the two above diameters and a friction stress of 0.25 MPa and 0.5 MPa .

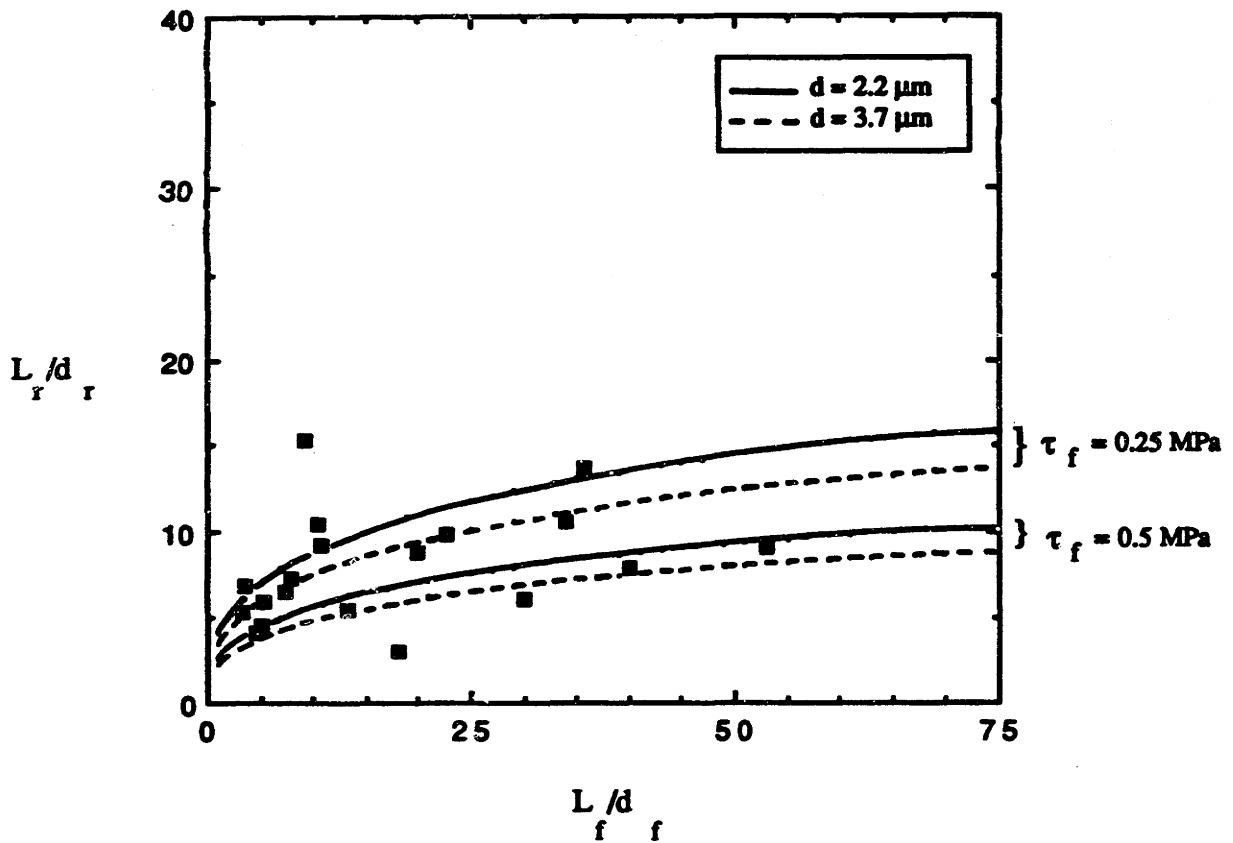


Figure 5.1.31b Plot of the row length (divided by its diameter) versus the fiber aspect ratio. Squares represent experimental data for glass fibers with a diameter between $2.2 \mu\text{m}$ and $3.7 \mu\text{m}$ which had punched a row at only one of their tips. The lines are calculated from Eqs. [3.4.23] and [3.3.11] for the two above diameters and a friction stress of 0.25 MPa and 0.5 MPa .

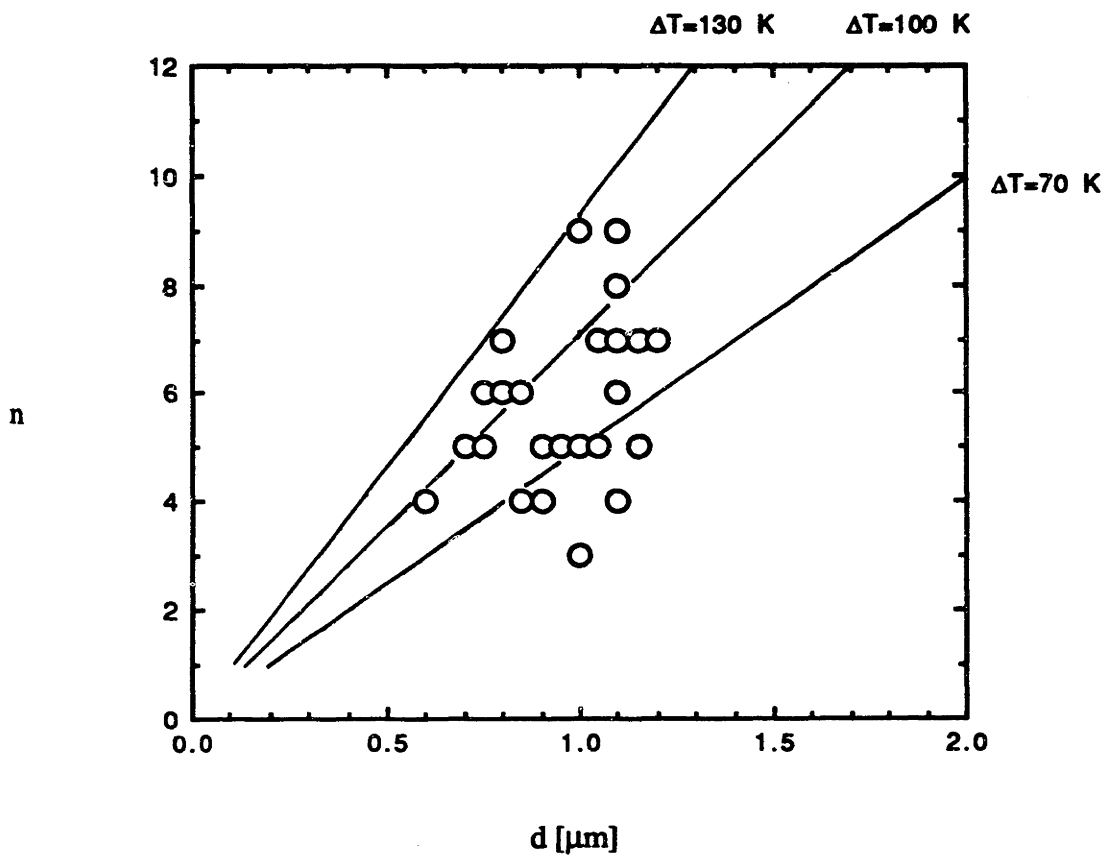


Figure 5.1.32 Plot of the maximum number of loops emitted by the sides of glass fibers as a function of the fiber diameter.

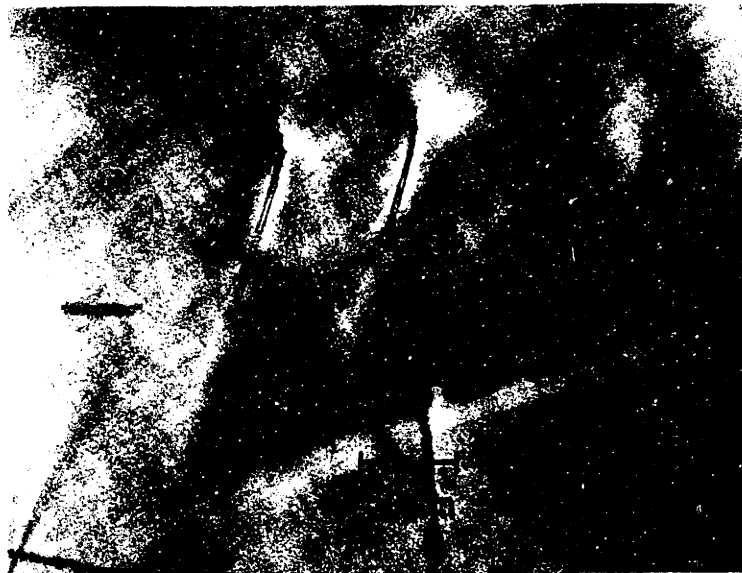


Figure 5.2.1 Large glass fibers in AgCl matrix. One grain shows slip bands visible as parallel region of alternating contrast while the other grain does not show any slip. (cross-polarized filters used).

Figure 5.2.2 Stress concentration at the tip of alumina fibers 3 μm in diameter embedded in AgCl (cross-polarized filters used).



Figure 5.2.3 Stress concentration at the tip of alumina fibers 20 μm in diameter embedded in AgCl (cross-polarized filters used).



Figure 5.2.4 Stress concentration at the tip of a glass fiber 80 μm in diameter embedded in AgCl (cross-polarized filters used).

Figure 5.2.5 Stress concentration at the tip of a glass fiber 80 μm in diameter embedded in AgCl (cross-polarized filters used).

6. DISCUSSION

6.1 Dislocation microstructure

A large body of literature exists on dislocation nucleation and geometry around submicroscopic particles in deformed metals, e.g., Hirsch and Humphreys (1970), Humphreys and Hirsch (1970), Brown and Stobbs (1971), Gould *et al.* (1974), Humphreys and Hirsch (1976). While very detailed TEM observations and mechanical test results have shed considerable light on the dislocation mechanisms operative in such systems, these results are not directly applicable to the present problem because the volume of the second phase in the present study is typically more than three orders of magnitude larger. The completion in an unimpeded manner of such processes as double cross-slip (Hirsch and Humphreys 1970) are much less probable with large inclusions because the length of the involved dislocations is much larger. The probability of interaction before completion of the process is therefore much higher and the activation energy is increased by an order of magnitude. Another important difference is that most of the earlier studies investigated particles submitted to shear whereas in the present study the strains are purely dilatational. Finally, the interface in the present case is incoherent, while many earlier investigators studied systems with coherent interfaces; this has a large effect on the energy considerations involved in such processes as prismatic punching (Brown and Woolhouse, 1970).

While not directly transposable to the problem treated in this study for the reasons mentioned above, these previous investigations indicate however that the total dislocation density we assumed to be generated at the reinforcement is most likely a rough approximation. This relative crudeness is justified by the

absence of detailed information on the specifics of dislocation emission in the tangled regions by large incoherent particles and the simplicity of the resulting expressions (Eqs. [3.1.12] and [3.3.11]) for the plastic zone radius and the number of punched loops.

6.1.1 Spherical inclusions

Plastic zones of irregular size, an example of which is given in Fig. 5.1.4, present a mode of strain relief intermediate between prismatic loop trains punched along crystallographic directions and an isotropic spherical shell of plastically deformed matrix. It seems that prismatic loops were punched out along crystallographic directions but became entangled soon thereafter. TEM investigations to date have generated similar observations on particles over an order of magnitude smaller (Ashby *et al.* 1969, Lewis and Martin 1963). This finding suggests that the spherical plastic shells observed around the majority of the embedded particles (Fig. 5.1.2) - similar to spherical zones of tangled dislocations around submicroscopic particles reported by Kinsman *et al.* (1975) - resulted from punched loops which were entangled early in the punching process. This lends credence to our estimation of the final dislocation density in the regular spherical plastic zones modelled above.

When more than one row of loops emanating from the same particle was found, these were very often at opposite sides of the spheres. No glass sphere was found to have punched loops on two adjacent glide cylinders without the presence of a zone of tangled dislocations between the punched loops and the particle. One of the rows was almost invariably much shorter than the other. This could be due to interactions between loops in the intersection of the glide cylinders close to the sphere (shaded area in Fig. 3.1.2). As pointed out by

Johnson and Lee (1983), it is energetically possible for two loops on adjacent cylinders in an f.c.c. crystal to interact and form a sessile product dislocation. This is likelier to happen the larger the particle, since the intersection volume between glide cylinders increases in size. Thus, for the large spheres investigated here, we expect plastic zones of tangled dislocations to form whenever two adjacent glide cylinders are active. We therefore expect the ratio of the number of inclusions with tangled zones to that with rows of punched loops to be higher for MMCs than for dispersion hardened metals because inclusion dimensions are much larger in MMCs.

The intermediate case illustrated in Fig. 5.1.3 could be due to a first stage of relaxation where the active glide cylinders were not adjacent, followed by the activation of additional glide cylinders leading to tangles. Similar TEM micrographs on submicroscopic particles have been published by Makenas and Birnbaum (1980).

Fig. 5.1.5, showing the total number of punched prismatic loops as a function of the sphere diameter, illustrates the fact that there is no systematic difference in the total number of loops emitted by spheres with one or two rows of loops, i.e., the number of loops in single rows is on the average twice that for double rows for a given sphere diameter. This finding suggests that one row of loops can relax the sphere as efficiently as two on each side, which in turn implies that short range diffusion or glide occurs in the vicinity of the interface. The observation that a row of loops is emitted only along one direction for certain spheres is an indication that nucleation of loops in other directions is perturbed by emission of the first row of dislocations. However, with precipitates of silver in the matrix much smaller than the glass spheres, we observed dislocation punched along most or all crystallographic directions, similar to what has been reported by various investigators in silver chloride (Parasnis and Mitchell 1959, Mitchell

1958) and metals (Lawley and Gaigher 1963, Eikum and Thomas 1964, Bertocci *et al.* 1969, Shinotomai and Hasiguti 1979). This indicates that the mechanisms for relief of thermal mismatch depend on inclusion size. Extrapolation to MMCs of data gathered with dispersion hardened metals will therefore not always be valid.

6.1.2 Particulate inclusions

Fig. 5.1.7 and 10 illustrate that prismatic loop punching is a mode of stress relief operational not only for spheres but also for particles of irregular shape.

The lack of correlation between the shape of the particle and that of its plastic zone (Fig. 5.1.9) might occur because relaxation starts earlier at some places than at others, or because entanglement does not occur at the same distance from the interface. It can be concluded from this observation that large errors will be introduced if TEM measurements (such as dislocation density or plastic zone extent) are made only at one limited region of the interface and are extrapolated to the whole plastic zone. While decoration does not allow the determination of high dislocation densities as TEM does, it gives a full view of the size and shape of an undisturbed plastic zone around the second phase. The two methods therefore complement each other.

Spheres exhibited such regions of high dislocation densities as well, visible either as a regular spherical shell or as a zone of irregular form (see previous paragraph). In several cases, both features described above (loop row and tangled dislocation zone) were observed simultaneously around the same particle or sphere, as in Fig. 5.1.10: the row of loops emitted by the particle is blocked by a subgrain boundary and the loops closest to the particle form an helix. Such a configuration can arise when a straight dislocation combines with a row of loops,

or it could have been formed initially at the interface. Another interesting feature seen in Fig. 5.1.10, and observed in many other instances, is that the row of loops seems to have emanated from the sharp corner of the particle. This observation is consistent with observations with fibers (see next paragraph), the ends of which had punched rows of prismatic loops. It can be explained by the stress concentration effect of cuspidal points which must help nucleation of the loops.

Prismatic punching has been reported by many investigators (e.g., Honeycombe 1984, Lawley and Gaigher 1963) in metals containing submicroscopic particles as well as in silver halide containing microspheres (e.g., Mitchell 1958) and fibers (e.g., Childs and Slifkin 1965). We observed this mechanism to be operative for particles with volumes from about one cubic micron to many hundreds of cubic microns. The scarcity of particles which exhibited trains of loops as their only plastic zone suggests that such prismatic loops are easily entangled after their emission, thus forming the plastic zone of high dislocation density found around particles (Fig. 5.1.8) as well as microspheres (see above paragraph). TEM investigations on submicroscopic particles in metals (e.g., Lewis and Martin 1963, Ashby *et al.* 1969) have shown that such entanglement is common around smaller particles. Similar observations reported in this thesis have been made around spheres and fibers in silver chloride. The hypothesis that the tangled dislocations in the plastic zone were originally prismatic loops is confirmed by the frequent observation of particles and microspheres showing one or more rows of loops in addition to a shell of dense dislocations (Fig. 5.1.7 & 10). Such a configuration will form if relaxation begins with nucleation and emission of prismatic loops on non-adjacent glide cylinders, followed by the activation of additional glide cylinders overlapping with the original ones and subsequent

entanglement. In the spherical case, adjacent glide cylinders overlap, if Hull and Bacon's (1984) geometrical model of maximum shear stress is adopted (Fig. 3.1.2). As shown by Johnson and Lee (1983), it is energetically favorable for two loops on overlapping glide cylinders to combine into a sessile configuration; such locks could induce additional entanglements by subsequent loops and finally lead to the shells of high dislocation density found around particles and spheres. While the positions of the glide cylinders around a particle of irregular shape will vary depending on the exact geometry and orientation of the particle, there is no reason that the cylinders should not overlap, even if they are significantly smaller than the particle mean radius. An additional observation supporting the above hypothesis is that no particle was found with adjacent rows of loops (i.e. with rows forming an angle of 60°). Quite often, two rows were visible outside the shell of tangled dislocations, almost invariably at opposite sides of the particle. These observations thus support the choice of loops geometry made in section 3.1 for the calculation of dislocation density and plastic zone volume.

Due to the relatively small aspect ratio, punching along different directions will happen almost simultaneously in the cooling process, thus leading to rapid entanglement and the absence of long rows of loops. We indeed only rarely observed long rows emanating from such non-equiaxed particles, even for those of large dimension which should punch a large number of loops from volume conservation considerations. The short rows observed are thus formed of loops which nucleated before any other glide direction was activated, at which point entanglement took place. As mentioned earlier, large glass spheres exhibit the same phenomenon, probably for the same reason.

Fig. 5.1.11, which presents for elongated glass particles the frequency of the angle of punching ϕ formed between the axis of the row of loop and the particle main dimension. Small punching angles are observed more often than large ones, an observation made for fibers as well, probably for the same reason: when ϕ is small, the loops formed are small since their size is at most that of the projection of the particle on the plane perpendicular to glide (for a sphere, that projection is a circle, see Fig. 3.1.2); they thus have a smaller probability of interaction with loops on adjacent glide cylinders. This argument is developed in more detail in section 6.1.3.1b.

6.1.3 Fibrous inclusions

Childs and Slifkin (1965) published a micrograph of a 200 μm long dislocation in silver chloride pinned at many places and bowed due to an external stress. Our observations of pinned, bowed dislocations close to fibers are similar (Fig. 5.1.13). The same authors have also published two micrographs of punched trains of dislocation loops at elongated inclusions in silver chloride. In both their and our work, trains of prismatic dislocation loops were found to emanate from the fiber ends. One of their micrographs features loops of dislocations punched along the inclusion length as well, which we only observed in very few instances for alumina fibers, more often for the thinner glass fibers. Relaxation of radial mismatch strains was found in the majority of the fibers to result in the formation of a cylindrical plastic zone containing tangled dislocations. This observation is to be expected in view of the fact that unless the fiber axis is perfectly perpendicular to the glide directions of emitted prismatic loops, significant interference will result between emitted dislocations of differing Burgers vector. Even when the fiber is optimally oriented (as in Fig.

3.1.3), loops on overlapping glide directions will be able to form sessile products as in the case of spherical inclusions.

With short fibers, the peanut-shaped plastic zones we observed (Fig. 5.1.15) are similar to those predicted by Dutta *et al.* (1988) using finite element analysis for an elastic, perfectly plastic matrix. These confirm that the dark unresolved regions found surrounding the glass spheres and the alumina fibers are indeed zones of plastically deformed matrix.

6.1.3.1 Punching by fiber ends

a. Fiber axis parallel to punching direction

In numerous instances, fibers were found to have punched a row of loops in the longitudinal directions in a plane parallel to the sample surface (Fig. 5.1.14 & 16); the row was thus in focus over its whole length. We believe that the fibers which did not exhibit any decorated loops or plastic zone at their tips probably emitted a row of loops at an angle with respect to the sample surface. If the loops were emitted toward the surface, they were attracted by it and annihilated; if they were emitted toward a deeper region of the sample, the limited decoration depth attainable with silver chloride (30 μm maximum) prevented them from being decorated and thus observed in the optical microscope. In rare cases, such as Fig. 5.1.17, the angle between the row of loops and the surface is small enough that part of the train is in focus for a given objective distance. However, we observed a relatively large number of fibers which exhibited a row of loops at their tip. This might be due to two factors: (i) the fibers were laid on a quartz plate prior to being engulfed by the molten halide and mostly conserved their orientation parallel to the surface and (ii) as reported by Mitchell (1957, 1959), silver chloride

grown directionally between two quartz plates tends to nucleate grains whose {100} planes (and occasionally {111} planes) are within a small angle of the plate surfaces. Since both these planes are glide planes which contain the glide direction $\langle 110 \rangle$, the rows of loops tend to be parallel to the sample surface and in focus over long distances.

In most cases, loops could not be counted close to the fiber tip, either because they could not be resolved or because the decoration was fainter there than at some distance from the fiber, possibly because of a depletion of the interstitial silver ions responsible for the decoration due to the high density of dislocations close to the fiber tip. In many cases, punched loops extending far away from the fiber encountered a subgrain boundary which blocked them. In cases such as Fig. 5.1.14 and 5.1.17, the stress at the head of the piled up loops is high enough to nucleate more loops on the other side of the boundary. Another interesting feature was that a minority of the fibers exhibited a row of loops at both of their ends; when it was the case, they generally were of different length. This suggests that the fibers with a single row of loops were either relaxed only on the half length which exhibited a row or that complete relaxation is possible by emission of a single row. This latter hypothesis would require that the loops of vacancies left at the interface be capable of gliding from one tip to the other in order to relax the fiber half length which did not emit any prismatic loops into the matrix. The two situations are shown schematically in Fig. 6.1.1 where only longitudinal strains are considered. The fiber is assumed to be a perfect cylinder, at the surface of which atomic planes (or delocalized vacancy loops) can glide without encountering any obstacle. In practice, the surface of fibers is not perfect and such loops - if they exist in a localized manner - would need to move by a combination of climb and glide to travel along the interface. A similar situation is found for misfitting glass spheres of diameter 1-3 μm in silver chloride

(section 6.1.1) which were often observed to punch loops along a single direction, rather than the 12 necessary for complete relaxation (micrographs published by Mitchell (1958) and Jones and Mitchell (1958) show the same phenomenon). In that case too, relaxation can be achieved by motion of the interfacial vacancy loops left at the interface. It is noteworthy that submicroscopic misfitting particles were observed to punch in all crystallographic directions. It must also be noted that while the total number of loops necessary to relax the fiber in Fig. 6.1.1 is the same, the length of a row of $2n$ loops will be less than the sum of the length of the two rows containing n loops (Eq. 3.3.11).

b. Fiber axis not parallel to punching direction

Fig. 5.1.18 shows an example of a fiber which punched a row of loops at an angle to its axis. Since prismatic loops can only glide along $\langle 110 \rangle$ directions, any fiber with an axis making an angle θ with that direction will only be capable of relaxation by prismatic punching at this angle. The fiber displacement in the longitudinal direction for each loop of Burgers vector b punched at an angle θ is equal to the projection of the Burgers vector on the direction of the fiber axis, i.e., $b \cdot \cos\theta$. The total number of loops to be punched for a given relaxation is thus increased by a factor $1/\cos\theta$. Since two adjacent glide directions make an angle of 60° , the maximum punching angle is 30° . Punching at an angle can thus increase the number of loops for a given relaxation by a factor $2/\sqrt{3}$ (i.e. 15%) at most. For a large number of loops, such a difference will not significantly alter the punching distance since it is only a weak function if the total number of loops (Eq. 3.3.11). We counted the frequency of the punching angle θ and found only a few occurrences of punching angles larger than 30° . These can be explained by the early blocking of punching along the direction with the smaller

angle and the subsequent activation of the less optimal punching direction when the stress becomes large. The higher proportion of fibers with small θ (Figs. 5.1.27 and 29) is surprising at first, since the fibers are oriented randomly in a plane parallel to the sample surface and the $\langle 110 \rangle$ directions are random as well in that plane (but not in space, since the growth of certain crystallographic planes is favored as mentioned above). From a purely geometric stand-point, the largest prismatic loop which can be generated by longitudinal strain mismatch is given by the projection of the fiber half-length on the plane perpendicular to the glide direction; the other half-length can contribute to a loop on the other side of the fiber (Fig. 6.1.2). If the fiber axis and the glide direction are aligned, this projection is a circular loop of same radius as the fiber. If the angle θ is non-zero, the whole fiber half-length can potentially punch elongated loops. The Burgers vector b_1 of such a loop has a component in both longitudinal and radial directions of the fiber and thus relaxes mismatch in both directions. However, there are always two possible glide directions where loops satisfy this condition: the direction closest to the fiber axis and the adjacent one with Burgers vector b_2 (Fig. 6.1.2). While the adjacent one can only contribute little to the longitudinal relaxation, it can also be activated due to the radial mismatch stresses. If this happens, entanglement between loops on both glide system is likely to occur in the intersection volume V (cross-hatched in Fig. 6.1.2) equal to

$$V = \frac{L^2 r}{4\sqrt{2}} \left[\frac{1}{\text{tg}(\theta)} - \text{tg}(\pi/6 - \theta) \right], \quad [6.1.1]$$

where L and r are the fiber length and radius and the angle θ is the angle between the fiber axis and the closest glide direction. For the possible values of θ from 0 to $\pi/6$, the intersection volume given by Eq. [6.1.1] varies almost linearly between

0 and $L^2r/4\sqrt{6}$ with θ . Assuming that the interaction probability between two loops on adjacent glide directions is proportional to the interaction volume, entanglement will be more likely at high values of θ and thus rows will be less likely observed. We believe that this is the reason why rows punched at a large angle are less numerous, rather than because nucleation is inhibited at higher angles. Observation of elongated loops such as that visible in Fig. 5.1.19 support this hypothesis as does the frequent occurrence of a dark zone of unresolved dislocations along the sides of the fibers. The length of such elongated dislocations was however observed to be most of the time less than that of the projection of the fiber half-length. It thus seems that a compromise is reached where punching occurs along some, but not all, the available length of the fiber.

Figs. 5.1.27 and 28 are to be compared to Fig. 5.1.11 featuring the frequency of the punching angle for elongated particles. The same general dependence is found, probably for the same reason as described above.

In most cases, one punching direction is more favorable than others to relax longitudinal stresses, because it makes the smallest angle with the fiber axis (direction 1 in Fig. 6.1.2). However, on occasions, fibers have such orientations with respect to the glide direction that two adjacent glide directions form the same angle with the fiber axis and both can be activated simultaneously as in Fig. 5.1.20. The axis of the left row of elongated loops is parallel to the image plane while that of the right row forms an angle: the farthest loop from the tip is deepest. Since they are not seen edge-on as the loops in the left row, their whole length can be seen. The projected angle between the two rows is about 75° ; the actual angle in space is thus most probably 90° and the two rows are punched along non-adjacent $\langle 110 \rangle$ glide directions. It is nevertheless a rare occurrence since in most such cases the loops of each row interact and become entangled.

Fig. 5.1.21 shows the tip of a fiber which has emitted what seems to be parallel non-coaxial elongated dislocations. These could be prismatic loops since the direction perpendicular to their line forms an angle close to 30° with the axis of the glide cylinder of the particle in the center of the picture (arrow) where two loops are in focus. The parallel elongated dislocations emanating from the fiber form a subgrain boundary; close to the fiber, the dislocation lines form an angle with the image plane and are thus visible as a line in the volume defined by the depth of field; farther away, the dislocations rotate and take a position perpendicular to the image plane and are thus visible as points. Whether the rest of the subgrain boundary is formed by dislocations coming from the same fiber or the other one in the same picture (out of focus due to its greater depth) is unclear. Fig. 5.1.21 clearly demonstrates, however, that dislocations generated by fibers can rearrange themselves to form subgrain boundaries; such boundaries have been observed in many other instances at the outside of the dark decorated plastic zone surrounding fibers.

c. Punching of pairs of rows

In numerous cases, we observed a pair of coaxial rows located on either side of a fiber as illustrated by Fig. 5.1.22. Such pairs of rows were only found at the ends of fibers and the far side of the elongated dislocations were always emanating from the fiber tip. The outward row was completely separated from the fiber and longer than the inward row, the dislocations of which were always connected to the fiber. The inward row is clearly different from the plastic zone of tangled dislocations usually found along the sides of fibers, visible at some distance of the tip of the large fiber in Fig. 5.1.22. While it is quite safe to assume that the outward row is not different from the ones described in the previous section, the

nature of the inward row is less clear. Assuming that they are prismatic, these dislocations are unlikely to be interstitial since their number is too high to be generated by radial misfit (see Eq. [6.2.9]) and since the orientation of their Burgers vector is less favorable than other glide directions with a Burgers vector closer to the radial direction. Also, if that row was produced by radial misfit, it would occur at other places along the fiber also, rather than exclusively at its tip. We propose the hypothesis, explained in more detail in what follows, that the inward row is constituted of vacancy loops formed at the same time as the interstitial loops of the outward row.

Every time a prismatic interstitial loop is created at the interface of a misfitting particle, a vacancy loop of same size is formed by conservation of matter. In most cases, this vacancy loop is not further considered because it is absorbed at the interface, i.e. the volume of the vacancy loop is replaced by the same volume of the expanding inclusion. Fig. 6.1.1 is a schematic example of such a process: the vacancy loop lines are shown at the interface but their volume has been taken by the expansion of the relaxing fiber. These loops actually lose their identity and the half planes marking their location are not different from the other half planes ending at the interface. If, however, the prismatic interstitial loop formed is larger than the volume taken by the misfitting inclusion, a vacancy loop can be formed from the difference of the volume of the interstitial loop and that of the expansion of the inclusion. This basically amounts to the creation of a pair of vacancy and interstitial loops in a strained lattice, where part of the vacancy loop has been absorbed by the expanding inclusion. Unless the loops are not free to glide, such a pair is unstable and will annihilate. If, on the other hand, the loops are created on either side of an obstacle, such as an inclusion, which blocks their motion, it will prevent their recombination. When further pairs are formed on each side of the inclusion, loops in the

respective rows will repel each other while loops from different rows will attract each other. Due to the rapid decay of the elastic fields of prismatic loops, the attractive effect is in most cases small compared to the repulsion between loops of same Burgers vector as calculated in the case of circular loops (see section 3.3 and Fig. 3.3.9). It is thus not possible in the case of interest to differentiate experimentally (by measuring the row length) between the lengths of two interstitial rows and that of a pair of interstitial and vacancy.

While the limited resolution available in silver chloride allows to draw few conclusions concerning the nucleation of such interstitial and vacancy loops, it is noteworthy that the configuration proposed above would indeed relax the longitudinal - and to some extent the radial - mismatch between the fiber and the matrix. The two-dimensional Fig. 6.1.3 illustrates that point, showing the atomic planes before and after the creation of the pair of loops. While the atomic spacing is widely exaggerated for clarity, it is clear that the vacancy loop induces some relaxation at the tip of the fiber, as does the presence of the interstitial loop on the other side of the tip. It is also apparent by observing shear strains in Fig. 6.1.3 that the vacancy loops will tend to stay at the point of maximum atomic plane disregistry, i.e. close to the fiber tip, as observed experimentally.

6.1.3.2 Punching by fiber sides

Fig. 5.1.23 shows a fiber A which punched loops at both its tips at a low angle. The shorter fiber B also punched loops at its tips, as well as longer dislocations along its sides, thus lending credence to the hypothesis that these are elongated prismatic loops punched according to the simple model shown in Fig. 6.1.2. One would therefore expect that the total emitted dislocation length in the plastic zone surrounding the fibers is estimated with reasonable accuracy as that

resulting from elongated punched prismatic loops (Eq. [3.1.9a]). The sides of fiber A are surrounded by a dark plastic zone formed of dislocations which probably became entangled before they could glide away from the interface, as was the case with fiber B. Fiber C also has elongated dislocations on its sides (some of which can be resolved) forming a dense plastic zone. It can be deduced from the angle of 90° between the glide directions in this particular subgrain that the image plane is parallel to a $\{100\}$ plane. Fig. 5.1.24 shows a similar situation in which elongated loops seem to have emanated from the tip of the fiber. This is to be expected due to the stress concentration at the sharp corner of the chopped fibers.

Based on these observations, a hypothesis can be advanced for the formation of elongated loops along the sides of fibers. We propose to extend to a cylindrical inclusion the model presented by Ashby and Johnson (1969) whereby a shear loop nucleates at the surface of a sphere and produces a prismatic loop by cross-slip of its screw component. Fig. 6.1.4 shows such a shear loop nucleated at a region of stress concentration such as the fiber tip or surface roughness. The fiber axis is assumed to be parallel to a $\langle 111 \rangle$ direction. While the edge component of the shear loop glides radially away from the fiber due to the stress field, the screw components of the loop cross slip along the sides of the fiber, "unzipping" in the process a long prismatic loop. The movement stops when the end of the fiber is reached or when the screw components are blocked by obstacles. Another possibility is represented in Fig. 6.1.5 where a long shear loop is nucleated so that its edge portion is parallel to the fiber axis. The screw components glide and annihilate to form a prismatic loop. Both Fig. 5.1.24 and 25 (as well as many others not included in this thesis) show dislocation structures which can be explained by these simple models. In these figures, dislocations are visible with one end still attached to the fiber while the other has glided away from it. Elongated dislocations were however only observed along fibers with the

smallest diameter; for fiber diameters larger than about 2 μm , the dislocations were without exception entangled and formed a dense plastic zone such as that visible in Fig. 5.1.26. This is presumably the case because more dislocations are necessary to relax the radial stresses and the glide system intersection volumes are greater, both leading to entanglement. Both above models are very simplified since they do not consider such situations as surface roughness, interaction with other dislocations on adjacent glide cylinders and obstacles in the matrix, etc.. Energy calculations such as that performed by Ashby and Johnson (1969) predicting the range of misfit and radii for which spheres nucleate prismatic dislocations, are more difficult to perform in the case of the misfitting cylinder since a complete solution of the elastic stress field taking into account the effect of the fiber tip and the stress concentration at the edge is exceedingly complex. Also, the problem is complicated by the effect of the orientation relationship between the fiber and the slip directions. In the extreme case of an infinite cylinder with no longitudinal stresses, the model presented above is not possible since the shear stresses τ_{zx} and τ_{zy} (according to the coordinate system of Figs. 6.1.4 and 5) are zero and therefore the shear loop cannot grow in the plane perpendicular to the z-direction. If however the fiber axis is not perpendicular to the dislocation Burgers vector, these shear stresses are non-zero and, depending on their magnitude, might be sufficient to nucleate a shear loop which transforms into a prismatic loop according to the simple geometric model of Figs. 6.1.4 and 5. This is true as well for a fiber of finite length with longitudinal stresses.

Another interesting feature visible in Figs. 5.1.25 and 26 and observed in many cases is that the dislocations are pinned and bowed away from the fiber, probably because of residual elastic stresses near the fiber. The radius of curvature of the dislocations, which is inversely proportional to the stress on the dislocation (Eq.

[5.1.2]), increases with increasing distance from the fiber, in accord with the above interpretation.

6.2 Dislocation micromechanics

This section is devoted to the comparison and discussion of the data and the theoretical models developed in chapter 3. As in the previous section, we consider in turn microspheres, irregular particles and fibers.

6.2.1 Spherical inclusions

6.2.1.1 Determination of ΔT

Each punched-out prismatic loop of Burgers vector b emitted by a sphere of diameter d_s relaxes the thermal mismatch in the direction of emission of the loops by a strain ϵ_l approximated by:

$$\epsilon_l = \frac{b}{d_s}, \quad [6.2.1]$$

assuming that the emitted loop has the same diameter as the sphere (as observed experimentally) and neglecting strains in the direction where no loops are emitted. The total mismatch strain ϵ_m between sphere and matrix is given by Eq. 3.1.2. Assuming that this mismatch is completely relaxed along one direction by punching of coaxial prismatic loops, the total number of loops n_s is equal to

$$n_s = \frac{\epsilon_m}{\epsilon_l}. \quad [6.2.2]$$

Inserting Eqs. [3.1.2] and [6.2.1] into [6.2.2] yields

$$\Delta T = \frac{n_s \cdot b}{d_s \cdot \Delta \alpha} \quad [6.2.3]$$

The right hand side of Eq. [6.2.3] would be divided by a factor 2 if it were assumed that loops can be punched out along all twelve {110} directions as described by Hull and Bacon (1984). Fig. 5.1.5 shows the measured number of loops n_s as a function of sphere diameter. The only spheres considered were those that did not exhibit any tangled dislocations between the row of loops and the sphere/matrix interface in the glide cylinder direction, i.e. for cases where relaxation took place solely by prismatic loop punching. The best fit line passing through the origin gives a value of 100 K for ΔT using Eq. [6.2.3]; lines corresponding to ΔT values of 70 K and 130 K are also shown on the same figure. While there is considerable scatter in the data, it can be safely assumed that the value of ΔT is 100 ± 30 K. This translates into an absolute temperature for the onset of slip T_c of 400 ± 30 K or an homologous temperature T_c/T_m of 0.55 ± 0.04 , a result in good agreement with the value of 0.50 for sodium chloride given by Frost and Ashby (1982) for the transition from power law-creep to plasticity at the strain rate corresponding to the rate of mismatch due to the experimental cooling rate of 1 K/s. Since sodium chloride and silver chloride are in the same isomechanical group, the homologous temperature of transition from one deformation mechanism to another is expected to be the same. A calculation based on atomic diffusion from the inclusion to the surface (Appendix 6) supports this conclusion. The scatter in Fig. 5.1.5 might be due to loops which disappeared due to combination with point defects produced during quenching,

unresolved loops not counted, superimposed macroscopic stresses, incompletely relieved stresses by the sphere, varying loop diameter, etc.. Most of these factors indicate that ΔT is probably somewhat above 100 K.

6.2.1.2 Plastic zone size

For the case of spherical plastic zones around particles, the plastic zone radius c_s is plotted in Fig. 5.1.6 as a function of sphere radius r_s . As predicted by Eq. [3.1.6b], there is a linear relationship between the radius of the sphere and the radius of the plastic zone. Using values for silver chloride listed in Table 3.1 and a value of $3 \cdot 10^{-6} [K^{-1}]$ for the CTE of glass, Eq. [3.1.6b] yields an unreasonably low value of 18 K for ΔT compared to the previously determined value of 100 K. Alternatively, for $\Delta T=100$ K, Eq. [3.1.6b] yields a value of 5.7 MPa for σ_y which corresponds to the stress value measured in simple tension on silver chloride by Carnahan *et al.* (1961) at a strain of $2.1 \cdot 10^{-4}$, which is equivalent to ϵ_m with $\Delta T=100$ K (Eq. [3.1.2]). Their measurements were made on annealed samples which all showed significant work hardening (ultimate tensile strength more than ten times higher than the microyield stress of 1 MPa measured by Sprackling (1966)), independently of the grain size. Eq. [3.1.12b], on the other hand, gives very good agreement with the data points for values of $\Delta T=100$ K and $A = 0.6$. Eq. [3.1.12b] is plotted in Fig. 5.1.6 for these values as well as for values of A equal to 0.3 and 0.9. For comparison, Eq. [3.1.6b] is also plotted in the same figure with $\Delta T=100$ K and $\sigma_y = 2 \tau_{y0} = 1$ MPa.

6.2.2 Particulate Inclusions

Fig. 5.1.12 displays the experimental measurements as well as the solution of Eq. [3.1.12b], using the physical properties of silver chloride listed in Table 3.1, a value of $5.8 \cdot 10^{-6} \text{ [K}^{-1}\text{]}$ for the CTE of the glass (American Ceramic Society 1988) and values of $\Delta T = 100 \text{ K}$ and $A = 0.6$, as determined for spheres (see section 6.2.1.1). The small temperature interval of 100 K allows to ignore the temperature dependence of the mechanical and physical properties used in the calculation. Observation and theory match very well over the whole range of radii, corresponding to a volume range spanning more than two orders of magnitude. This confirms the validity of the simple geometrical model considering strain hardening developed above. Also plotted in the same figure is the result of Eq. [3.1.6b] which assumes a non strain-hardening matrix. As for spheres, this model clearly does not match the data, even taking into account the experimental error estimated above. The data also prove the assumption - made implicitly by many investigators - that irregularly shaped particles, as they occur in most MMCs, can be treated as equivalent spherical particles of same volume. While the shape of the plastic zone is irregular and cannot be predicted (see Fig. 5.1.9), its volume is very well described by the volume of a spherical plastic zone resulting around a sphere of identical volume in a work-hardening matrix.

6.2.3 Fibrous Inclusions

6.2.3.1 Flow stress of the dislocations

Mitchell (1958) decorated dislocations in silver chloride under load which were formed by an indenter and also observed bowed dislocations pinned at their ends, as did Childs and Slifkin (1965). Careful examination of long dislocations in the plastic zone surrounding fibers in this investigation reveals that, in

several areas, the dislocations were similarly pinned and bowed due to the local stress field (Fig. 5.1.13). Since they were in the vast majority of cases found to be bowed away from the fiber on both of its sides, the stress to which they were subjected can be assumed to emanate from the fiber, rather than from some unknown extraneous source. This local elastic stress is unable to move these particular dislocations any further and is therefore lower than the local yield stress in shear of the matrix. Brown and Stobbs (1971) also observed around submicroscopic silica particles in deformed copper that the dislocations in the plastic zone had high curvature compatible with an increased local flow stress.

The stresses for pinned bowed dislocations such as the ones visible in Fig. 5.1.13 are calculated using Eqs. [5.1.1] and [5.1.2] and plotted in Fig. 5.1.29. It is found that the local stress within the plastic region is independent of the distance from the fiber and varies between 0.6 MPa and 1.45 MPa. The lower bound is in good agreement with a value of 0.5 MPa for the microyield shear stress of pure silver chloride measured at room temperature by other investigators (Sprackling 1966, Haasen and Skrotzky 1981). Haasen and Skrotzky (1981) also found that the presence of 300 and 500 ppm of calcium chloride in the matrix hardly changed the value of the critical resolved shear stress. This indicates that the 500 ppm of cuprous chloride present in the sample used in this investigation should have very little effect on the yield stress of silver chloride, especially since the monovalent cuprous ions are expected to interfere less with dislocations than the divalent calcium ions investigated by Haasen and Skrotzky (1981). In a matrix showing no strain-hardening, one would expect the stress in the plastic zone to be constant and equal to the microyield stress, i.e. around 0.5 MPa. The data shown in Fig. 5.1.29 thus indicate that the matrix is strain hardened, as found by many authors with silver chloride in tension (Stepanow 1934 & 1935, Axilrod and Lamb 1948, Haasen and Skrotzki 1981). The choice of a model taking

into account the strain-hardening of the matrix (Eq. [3.1.12]) is thus further justified.

6.2.3.2 Plastic zone size

The radius of the plastic zone around fibers was measured for 45 alumina fibers of aspect ratio larger than 20, in cases where the plastic zone was a cylinder with a constant radius. For the fibers used in this investigation, which have a radius of $1.5 \mu\text{m}$, the mean radius of the plastic zone was measured as $10.2 \mu\text{m}$, with a standard deviation of $2.7 \mu\text{m}$. Using Eq. [3.1.12a] with the previously determined values of $\Delta T=100 \text{ K}$ and $A=0.6$, we calculate a plastic zone radius c_c equal to $6.2 \mu\text{m}$. Eqs. [3.1.7] and [3.1.10a] predict a value of 2 MPa for the value of the yield stress in shear within the plastic zone. As expected, all measured stress values are below this value (Fig. 5.1.29). Changing the parameters ΔT and A by a factor 30% (i.e. 130 K and 0.42 respectively), yields a value of $7.6 \mu\text{m}$ for c_c , within the interval of confidence of measured values. The yield stress in shear of the strain hardened matrix becomes 1.4 MPa , equal to the maximum value measured experimentally (Fig.5.1.29), as should be the case. The discrepancy of 30% with the values determined for the spheres can be explained by the fact that Eq. [3.1.12a] does not take into account the contribution of the axial mismatch to the radial plastic zone, since the model was developed for an infinitely long fiber. An alternate explanation can be found in the observation that subgrain boundaries were generally found to exist at the interface separating the plastic zone from the unstrained matrix around fibers. A smaller plastic zone size should result due to the locally enhanced dislocation density at these subgrain boundaries within the plastic zone. Eq. [3.1.6a] yields a value of $17.4 \mu\text{m}$ for c_c , far in excess of the range of measured values.

From the above results, it appears that Eqs. [3.1.12] which take into account strain-hardening of the matrix fit well the experimental data for spherical, irregularly shaped and cylindrical inclusions, while Eqs. [3.1.6] which assume a perfectly plastic matrix fail to do so. We conclude that strain-hardening must be taken into account in modelling matrix plastic deformation around reinforcements in MMCs, and that with reinforcement volume fractions below the values given by Eqs. [3.1.16], Eqs. [3.1.12] should yield an adequate estimation of plastic zone size in a coarse-grained, single-phase matrix. As shown in Fig. 3.1.4, dislocations punched by the reinforcing phase should have a significant effect on the size of the plastic zone in pure aluminium. It must however be kept in mind that this effect will become less pronounced with larger values of τ_{y0} typical of alloys. Furthermore, the simple calculation presented above loses its validity when other obstacles (grain and subgrain boundaries, second phases and other reinforcements) also impede dislocation motion in the vicinity of the reinforcement.

6.2.3.3 Punching distance

The length of the rows of loops and that of the glass fiber from which they were punched were measured on micrographs and plotted against each other in Figs. 5.1.30 and 5.1.31. As calculated in section 5.1.3, the maximum deviation for fibers punching at an angle in the number of loops n is about 15%, which translates in a smaller deviation in the length of the row L_r , since L_r is a weak function of n (Eq. [3.3.11]). All data points, independent of the punching angle, were thus included in Figs. 5.1.30 and 5.1.31. The predictions of Taya and Mori's model (Eqs. [1] and [2], App. 5) are plotted in Figs. 5.1.30 only, since their model is only applicable to fibers punching loops at both their tips. Predictions of the model

presented in the theoretical section (Eqs. [3.4.23] and [3.3.11]) are also plotted in Figs. 5.1.30 and 5.1.31. The fiber elastic modulus for glass was taken as 85 GPa (manufacturers information), its Poisson's ratio as 0.22 (Kelly and Macmillan, 1986b) and its CTE as $6.5 \cdot 10^{-6} \text{ K}^{-1}$ (manufacturers information). For the matrix, the Poisson's ratio and Burgers vector listed in Table 3.1 were used, as well as a value of 5.5 GPa for the shear modulus calculated from elastic constants for the [110] direction. A range of fiber diameter values corresponding to that of the glass fibers used in this study are used to generate the curves in Figs. 5.1.30 and 5.1.31, as well as values of the friction stress of 0.5 MPa and 0.25 MPa. The higher value corresponds to the microyield stress in shear of silver chloride as measured by Sprackling (1966) as well as Haasen and Skrotsky (1981), and is therefore likely to represent an upper bound for the actual value of the lattice friction stress. The lower value of 0.25 MPa is thus chosen to illustrate the effect of a smaller friction stress on the shape and location of the theoretically derived curves.

Eq. [3.4.23] was derived for fibers which had punched a row of loops at both their ends (Fig. 6.1.1b). For fibers punching at only one end, we assumed that the whole interface became relaxed as in Fig. 6.1.1c. The number of loops can then be calculated from Eq. [3.4.23], using a corrected fiber length equal to twice the actual fiber length. We thus assume that the number of loops produced by a fiber of length L , with only one punching end, is the same as that produced by an equivalent fiber of length $2L$ punching at both its ends, since in both cases the fiber length being relaxed by a row is the same. This assumption is not entirely correct since, as shown schematically in Fig. 6.1.1c, a stress is exerted by the matrix on the fiber end having not punched, in order to equilibrate the net force produced by the asymmetrical distribution of interfacial shear stress. For the

curves shown in Figs. 5.1.31, we assumed that this effect was small and we inserted twice the measured fiber length in Eq. [3.4.23].

The quantitative correlation between our model and the data shown in Figs. 5.1.30 and 31 is satisfactory, with data points both above and below the theoretically predicted range. As mentioned above, the lower data points can be explained by the blocking of rows of loops by obstacles not visible in the microscope such as undecorated dislocations or submicroscopic inclusions. This effect should become stronger the longer the row, because of the higher probability of encountering an obstacle. Extraneous long-range stresses might also induce scatter in the data points, both elongating and shortening the measured row length. Finally, an effect which might systematically increase the row length is the electrostatic repulsion between charged loops. As discussed in greater details in the next paragraph, this is not expected to induce forces larger than the elastic repulsion on which Eq. 3.3.11 is based and thus can probably be neglected. If however the first few loops of the train are charged to the maximum possible extent, this effect might produce an increase of row length by typically 1 to 10 μm . Given the experimental errors in the measurements cited above as well as the uncertainties connected with some of the physical constants used in the model (the lattice friction stress, the critical interfacial shear stress assumed to be equal to the lattice friction stress, and the temperature excursion of 100 K which has an experimental error of typically 30 K) and the simplifying assumptions made in the model presented in section 3.4 (perfect dislocation nucleation, cylindrical inclusion with smooth surface, etc.), we feel that the agreement between the data and our model is satisfactory. For a value of the friction stress of 0.5 MPa, Taya and Mori's model fits the higher range of experimental data, while our model fits best the lower range. For a value of the friction stress of 0.25 MPa, Taya and Mori's model predictions tend to be too high,

but our model is still within the range of the data. Both models are quite sensitive to the value of the friction stress for which a factor 2 in uncertainty can be reasonably assumed. The small aspect ratios of the fibers investigated does not allow observation of fibers larger than the critical aspect ratio at which Taya and Mori's model predicts suppression of punching and thus quantitatively and qualitatively disagrees with the predictions of our model. While our model predicts a maximum value of the punching distance for fibers of infinite aspect ratios, Taya and Mori's curves in Figs. 5.1.30 reach a maximum and drop to zero for a critical aspect ratio which has a value of 265 for Fig. 5.1.30a and 550 for Fig. 5.1.30b. It would be very difficult to generate experimental data in silver chloride for such high fiber aspect ratio. While this critical aspect ratio is large for silver chloride, it must be noted that it is significantly smaller for matrix materials with higher elastic modulus and friction stress, e.g., about 28 for the system aluminum/silicon carbide submitted to a temperature excursion of 200 K.

It was shown in section 3.4.4 that the fiber residual stress is unlikely to induce major perturbations in the loop row length. We now turn our attention to the electrostatic charging of dislocations in AgCl as another possible cause for the perturbation of loop elastic equilibrium. In what follows, we make a rough approximation of the repulsive electrostatic force between punched prismatic loops. This force must be added to the elastic repulsive force existing between the loops (Eq. [3.3.3]).

Edge dislocations in ionics carry a net charge due to an excess of charged jogs of one sign formed by the absorption by the dislocation line of point defects (Sprackling 1976). At equilibrium, the electroneutrality is preserved because a sheath of point defects of the other sign surrounds the dislocation (Pratt 1958). A fast moving dislocation may however display a net long range charge if it breaks away from the cloud of compensating point defects (Brown 1961). The line

charge density of edge dislocation in NaCl has been measured by many investigators as 10^{-12} to $4 \cdot 10^{-11}$ C/m (Sprackling, 1976). No such information is available for AgCl; a rough estimation of the line charge can be made by assuming that it is proportional to the cubic root of the equilibrium defect concentration. The ratio of the defect concentration at 300 K in AgCl to that in NaCl is 4250 (Kittel, 1983), the cubic root of which is 16, leading to a dislocation line density for AgCl in the range of $2 \cdot 10^{-11}$ to $8 \cdot 10^{-10}$ C/m. Another significant difference between NaCl and AgCl is the nature of the predominant point defects: Schottky-type for NaCl and Frenkel-type for AgCl. Defect mobility is also much higher in AgCl at a given temperature.

Assume that the charges on a loop are spread equally along its circumference. This is an acceptable assumption since the typical distance between two loops is significantly larger than the distance Δ between two jogs of charge $e/2$ on a loop, given by

$$\Delta = e / 2 \rho_q, \quad [6.2.4]$$

where ρ_q is the line charge density. This yields a value for Δ in the range of 0.1 to 4 nm. The lower value, corresponding to a line density of $8 \cdot 10^{-10}$ C/m, is clearly unreasonable since it is less than the interatomic distance in AgCl. We will thus assume an upper value of 10^{-10} C/m for the line density.

The force F_q between the two charged loops separated by a distance x is found by Coulomb's law:

$$F_q = k q^2 / x^2, \quad [6.2.5]$$

where $k=9 \cdot 10^9$ Nm²/C² and q is the total charge carried by one loop or radius r :

$$q = 2 \pi r \rho_q . \quad [6.2.6]$$

The force F_q exerts a shear stress τ_q on a loop

$$\tau_q = F_q / b 2 \pi r . \quad [6.2.7]$$

inserting Eqs. [6.2.5] and [6.2.6] into [6.2.7] and solving for x yields

$$x = \rho_q \sqrt{\frac{2 \pi r k}{b \tau_q}} . \quad [6.2.8]$$

Inserting $\tau_q = \tau_y$ yields the critical distance x_c above which the electrostatic repulsive force does not induce glide between two isolated loops, if their elastic interaction is neglected. Taking a value of $\tau_y = 0.5$ MPa, $r = 1.5$ μm , Eq. [6.2.8] yields a value for x_c equal to 2 μm for the upper bound value of 10^{-10} C/m estimated above. This is to be compared to the critical equilibrium distance of 1-2 μm between two uncharged loops. It thus seems that electrostatic interactions might have a measurable effect on the equilibrium position of closely spaced loops, if their line density is at equilibrium with the defect population in the crystal.

The above estimation is clearly an upper bound value since it was assumed that each loop carries an equilibrium charge. In our experiments however, the loops are punched and glide rapidly to their equilibrium position, typically in the 100 seconds necessary to cool the samples. It is therefore possible that the first few punched loops sweep out the defects as they move on their glide cylinder, resulting in a charging. Since all the loops of the train glide on the same cylinder, they encounter fewer and fewer defects as the number of their

predecessors increases. In the time considered, the typical diffusion distance as estimated by $(Dt)^{1/2}$ is in the order of 30 nm. The total number of defects on a glide cylinder of length 20 μm , radius 1 μm and "wall thickness" 60 nm at 300 K is thus about 1000. If all these defects are swept by the first loop gliding on the cylinder, they induce a line charge on the order of 10^{-11} C/m, depleting completely the diffusion volume and thus preventing the charging of the subsequent loops. If the defects are equally incorporated by the 100 loops of a train of that length, the line charge is 100 times less and has a negligible effect on the equilibrium spacing of the loops (Eq. [6.2.8]).

It can be concluded from the semi-quantitative argument presented above that a row of loops which is at thermal equilibrium with the lattice before it glides might be influenced by electrostatic forces if the loops break away from their atmosphere of defects of opposite sign. On the other hand, if the loops move immediately after they have been nucleated as it is the case in our experiments, the diffusion kinetics are not rapid enough to charge them significantly, and the electrostatic forces will be insignificant compared to the elastic repulsion between the loops. At the most, the first few loops of the train might become charged and their spacing might be larger than that predicted by elastic interactions only.

6.2.3.4 Number of side-punched dislocations

Considering only radial stresses, the number of elongated prismatic dislocations punched by the sides of the fiber can be predicted using the simple geometric model of Fig. 6.1.2. The prismatic dislocations are assumed to nucleate on the fiber surface where the resolved shear stress is maximal, resulting in a dislocation height of $d/\sqrt{2}$, where d is the fiber diameter. The thickness of the region of fiber that the dislocation relaxes thus varies between $d/\sqrt{2}$ at the

nucleation point and d at the fiber diameter. Assuming that the mismatch strain $\Delta\alpha\Delta T$ is totally relaxed by the emission of n loops of Burgers vector b forming an angle θ with the fiber radial direction yields

$$n = \frac{\Delta\alpha \Delta T d \sqrt{2}}{b \cos\theta} \quad [6.2.9]$$

The maximum number of loops n_{\max} is reached for the maximum angle $\theta = 30^\circ$ (as discussed above) and by replacing the factor $\sqrt{2}$ by 1 in Eq. [6.2.9], i.e., considering the maximum mismatch of the fiber at its largest dimension. Using the materials values listed in Table 3.1 for the fiber and the matrix as well as the value of $\Delta T = 100$ K determined for spherical inclusions in section 6.2.1.1, we find a value of 7.1 for the ratio n_{\max}/d . The resulting line is plotted in Fig. 5.1.32, together with those corresponding to $\Delta T=130$ K and $\Delta T=70$ K, the upper and lower bond determined in section 6.2.1.1 and Fig. 5.1.5. The experimental values of the maximum number of side dislocations are plotted in the same figure. The average number was usually smaller by 25% to 50%. The experimental points fall on or below the upper bound calculated above, as expected if the simple geometric model presented above (Fig. 6.1.2) is correct. In most cases, dislocations were tangled in a plastic zone around the fiber (Fig. 5.1.26) and could only be partially resolved; they were thus not used as data. Fig. 5.1.25 shows an example where the side dislocations can be resolved and counted because they glided a considerable distance from the fiber. A small dark zone is still visible around the fiber and might be due to dislocations emitted along other directions.

6.3 Photoelasticity

Fig. 5.2.1 shows two grains in which long glass fibers are embedded. One of the grains deformed plastically and exhibits slip glide bands. The angle of 45° between the slip bands and the fibers indicates that a slip system was close to the plane of maximal resolved shear stress. The other grain does not show any glide band, probably because its crystallographic orientation is such that the critical resolved shear stress is not exceeded. The coexistence of slipped and unslipped grains is typical of a sample only slightly deformed; when samples were deformed extensively under the microscope, slip bands were seen travelling through the whole sample, changing orientation from grain to grain. Such widespread movement is only observable when the glide plane is close to parallel to the sample surface: otherwise glide packets hit quickly the surface and form a step there, visible as a wavy slip line.

Fig. 5.2.2 to 5 show stress concentration at the end of fibers. While the samples were not decorated and dislocations were thus not observable, it can be reasonably expected that the fibers of small diameters were relaxed through emission of punched loops as reported in the previous sections. The photoelastic contrast visible in these figures thus suggests that some residual stresses are present even after relaxation of the matrix by slip, as described in more detail in section 3.4.4. Fig. 5.2.3 is particularly illustrative of the advantage of using silver chloride rather than polymers to simulate the stress state at the tip of mismatching fibers in metals. First, slip most probably occurred, thus duplicating the situation found in MMCs; since polymers do not deform plastically by slip, stress information collected on fiber reinforced polymers is only applicable to metals in the purely elastic state which is, as calculations above have shown, only found with very short fibers. Second, the two fibers of Fig. 5.2.3 induced a different stress concentration in the matrix: the matrix at the tip of the short fiber exhibits a symmetric state field with lobes typical of stress

concentrations due to a discontinuity. The long fiber in the same figure, on the other hand, induced a non-symmetric stress field in the matrix. We believe that this difference is due to the different orientation of the two fibers with respect to the crystallographic orientation of the matrix: the short fiber is probably aligned with a main crystallographic direction and thus induces a symmetric stress pattern similar to these observed in amorphous polymers. The long fiber on the other hand is not well aligned and thus has a more complicated and diffuse stress field. The orientation dependence of the elastic moduli typical of crystalline materials cannot be duplicated in an amorphous polymer.

Fig. 5.2.4 is another good example of the stress concentration at the end of fibers. Of particular interest in this micrograph is the offset between the axis of the fiber and that of the stress concentration region. We believe that it is an expression of the same phenomena described above, i.e., the misalignment between the crystallographic direction and the fiber axis. The same is true for the punching of loops as described in section 6.1.3.1. Fig. 5.2.5 shows the stress concentration at the corners of the fibers; while purely qualitative in nature, this result illustrates the fact that significant disturbances in the stress field are introduced close to the fiber tip, but not far away from it, as calculations above show. It can be argued that since such stress concentrations are only limited to the immediate vicinity of the fiber, they have only a limited effect on the overall elastic stress field of the composite and that fibers can thus be treated as a good approximation as an ellipsoid as in the model of Taya and Mori (1987). We feel however that the effect of corners and cuspidal points on plasticity will be much more important since such stress concentrators can very easily nucleate dislocations as shown in previous paragraphs. The ellipsoid approximation will most likely yield a poor approximation of the fiber from the point of view of plasticity, as it does for dislocation emission by long fibers.

6.4 Figures

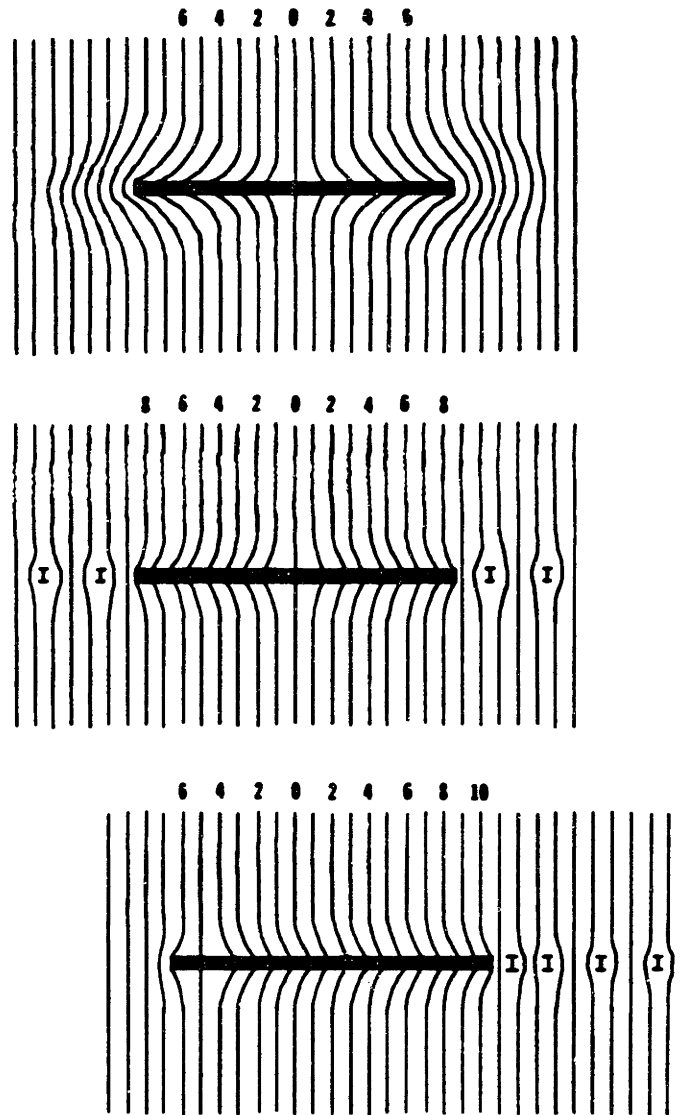


Figure 6.1.1 Schematics of a mismatching fiber in a crystalline matrix deforming by slip. (a) fiber under compression and deformed atomic plane in tension before slip (exaggerated deflections for illustrative purpose). (b) emission of two rows of interstitial loops at both fiber ends and relaxation of the interface. Two atomic planes have been added at each ends of the fiber; they can be considered as delocalized vacancy loops at the interface. (c) emission of a single row of interstitial loops at one end of the fiber and relaxation of the whole interface. The fiber is translated since atomic planes were added only at one end. Force equilibrium dictates that the matrix push against the fiber end which did not punch loops.

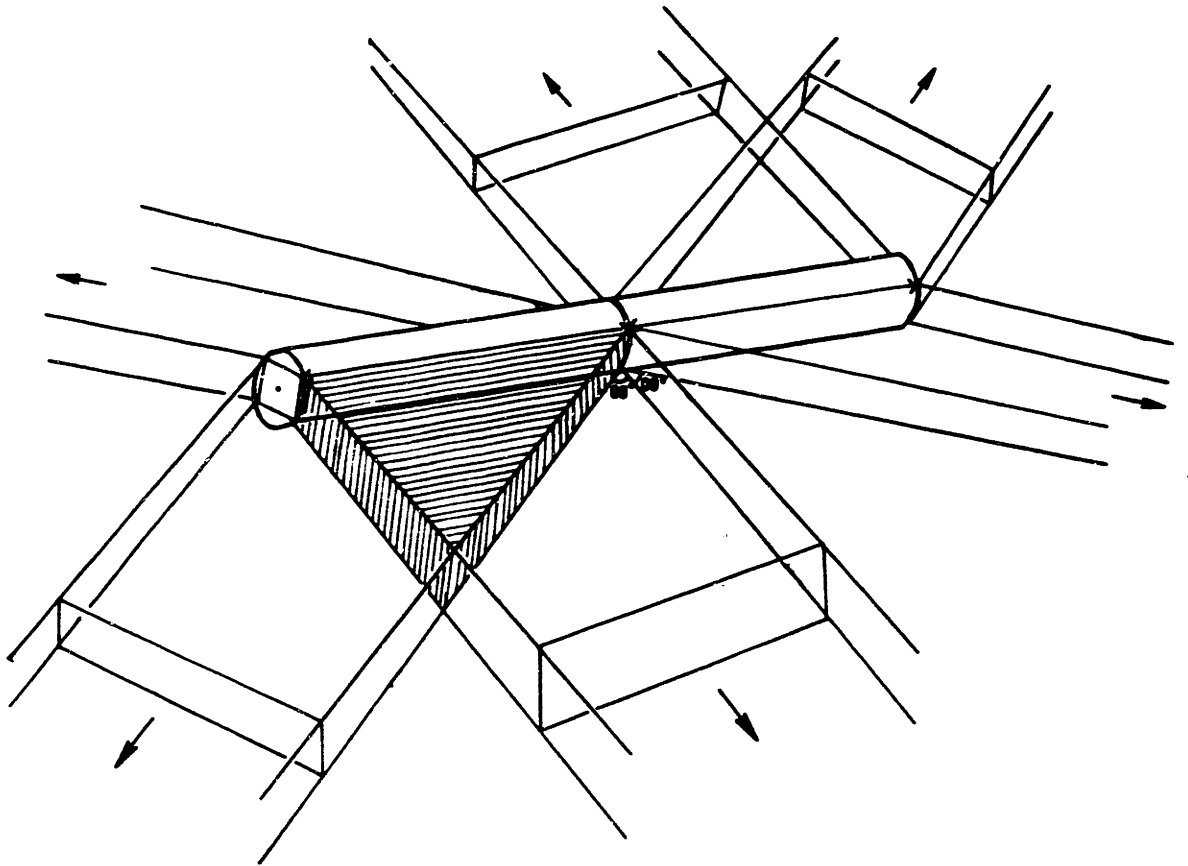


Figure 6.1.2 Schematic of fiber punching elongated dislocation loops along the six directions $\langle 110 \rangle$. Cross-hatched volume correspond to interaction volume between two adjacent glide systems.

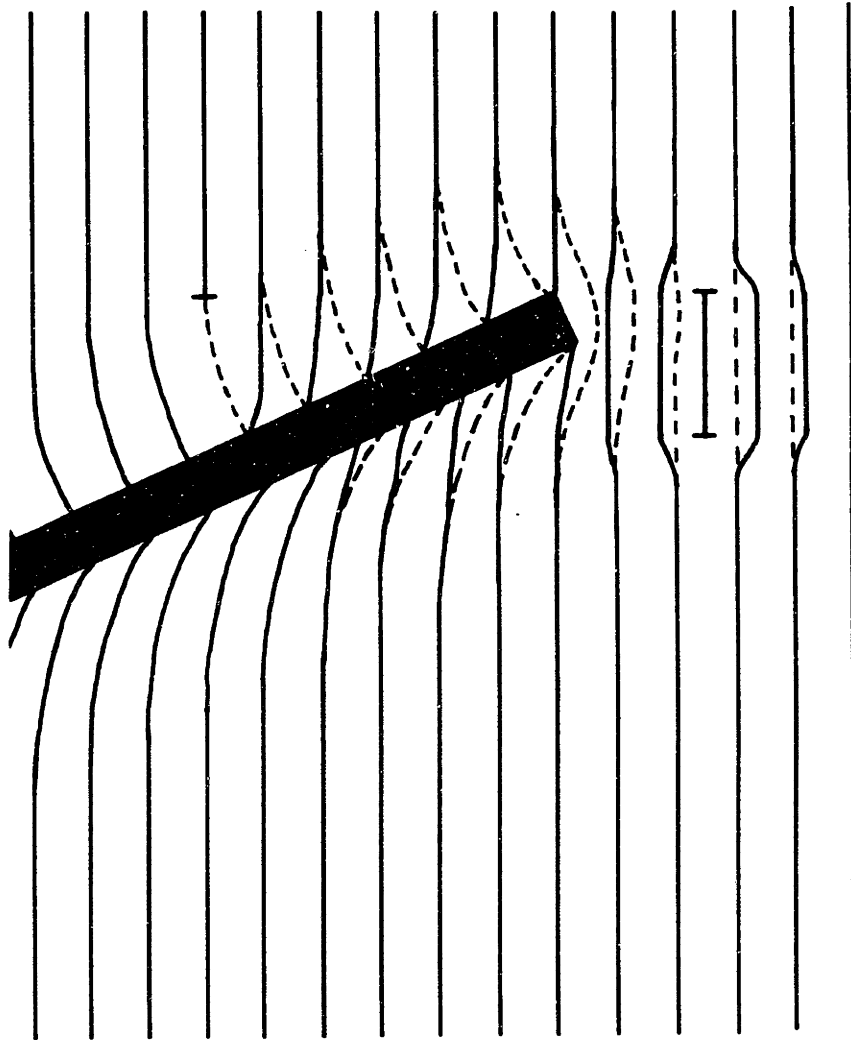


Figure 6.1.3 Schematic drawing proposed as an explanation for the structure of Fig. 5.1.22. Dotted lines : atomic plane stressed by a mismatching fiber before relaxation. Full lines : atomic planes after creation of a pair of prismatic interstitial and vacancy loops on either side of the fiber. The interstitial loop glides away from the fiber while the vacancy loop stays attached to the fiber for maximum relaxation of the interface. Atomic plane deflections are exaggerated for clarity.

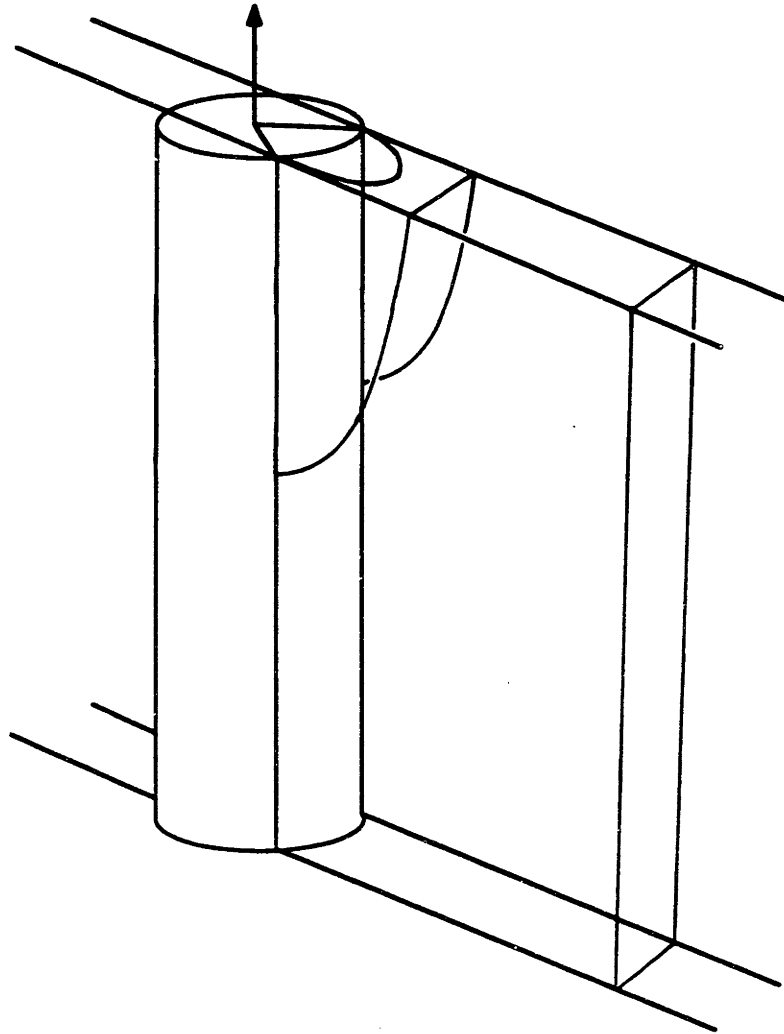


Figure 6.1.4 Proposed mechanism of nucleation of prismatic loops to explain structure in Fig. 5.1.24 and 25. Three stages are shown : (a) formation of a shear loop at fiber end of irregularity, (b) cross-slip of screw segment and (c) fully formed prismatic loop.

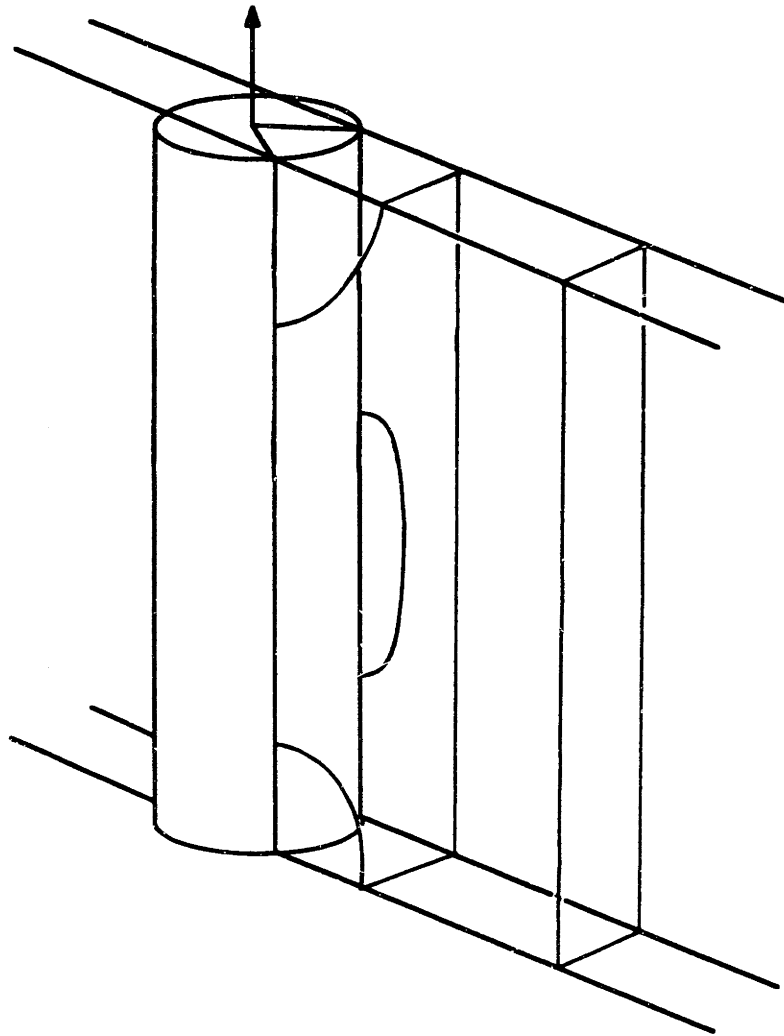


Figure 6.1.5 Variation of Fig. 6.1.4, with formation of the shear loop on another glide plane.

7. CONCLUSIONS

1. Plasticity is induced by thermal mismatch between a matrix of silver chloride and inclusions of different shapes, simulating metal matrix composites: glass microspheres 1 to 5 μm in diameter, glass particles in the same dimension range and glass or alumina fibers 1 to 3 μm in diameter. The resulting dislocations are decorated by photodissociation of the matrix and observed by transmission optical microscopy. This experimental technique has a lower resolution than electron microscopy but presents great advantages for the observation of dislocations around large inclusions, since the whole matrix can be observed.

2. Two main plastic zone morphologies are observed: tangled dislocations forming a sheath around the inclusion and rows of punched prismatic dislocations emanating from the inclusion. Similar observations around equiaxed particles more than three orders of magnitude smaller in volume have been made by TEM. However, the very large volume of the plastic zone around the supramicroscopic inclusions investigated in this thesis leads to more frequent entanglement of punched dislocations. Also, the shape of the plastic zone does not usually follow that of the inclusion. Thus, the wealth of knowledge on submicroscopic particles in metals cannot be systematically applied to metal matrix composites.

3. From the number of prismatic loops punched by microspheres, the highest temperature at which slip is operative is found to be 400 ± 30 K. The maximum number of elongated loops punched radially by fibers is found to match this result as well.

4. Measurements of the radius of curvature of pinned dislocations in the tangled plastic zone show that the matrix is locally strain-hardened. A simple

model to predict the size of this plastic zone around spherical and cylindrical inclusions in a strain-hardening matrix is developed and found to match well the experimental data around microspheres, fibers and particles of irregular shapes.

5. A model predicting the number of loops punched longitudinally by a fiber is presented. Adapting the shear lag model to the case of a partially plastic interface, the model predicts that there is a critical fiber length above which a region in the middle of the fiber is strained to the point that it does not show any mismatch with the matrix anymore and thus does not contribute to punching of loops at fiber ends. The length of the loop row is then calculated using a numerical solution after estimating the effect of the residual elastic field from the fiber on the row length. The predicted row length as a function of the fiber length matches the data satisfactorily, as does another model proposed by Taya and Mori (1987). The model presented above predicts, however, that very long fibers will punch loops, in disagreement with the model of Taya and Mori (1987).

6. Observations are reported for the case where the glide direction of punched loops and the fiber axis do not coincide. In certain cases, two rows of loops are punched by the fiber tip in opposite directions. This structure is interpreted in terms of loops of opposite Burgers vectors.

8. SUGGESTIONS FOR FUTURE WORK

8.1 Decoration experiments

1. Larger decoration depth could be reached by using a pulsed electric field synchronized with actinic light flashes as described in section 4.2. This would open the possibility for the use of larger diameter fibers in the range above 10 μm in diameter and above.

2. The interaction between dislocations emanating from different inclusions could be systematically studied in order to gain a better understanding of the situation at high volume fraction. This could be done with one type of reinforcement or two different types such as fibers and particles, representative of hybrid composites.

3. The influence of the friction stress and yield stress on the extent of the plastic zone and the rows of loops could be investigated by alloying the matrix with other salts such as silver bromide or sodium chloride.

4. The influence of thermal cycling on the size of the plastic zone could be investigated. Questions such as whether the thermally induced dislocations can reversibly disappear upon heating or whether they are irreversibly blocked due to entanglement could be addressed.

5. The influence of grain boundaries on the plastic zone could be examined: most of the work reported in this thesis was done on samples with large grains and dislocation interactions with grain boundaries were absent.

6. This thesis as well as the above suggestions pertain to thermal stresses; all the questions addressed for that particular type of deformation could be asked anew in the case of small mechanical deformations, either unique or repeated. New parameters, such as Poissons ratio difference and generalized matrix slip,

would certainly play an important role. Dislocations could be studied both under stress and in their relaxed configuration.

8.2 Photoelastic experiments

The few photoelastic experiments reported in this thesis were qualitative and exploratory in nature. We believe that a very rich field of research lies unexplored and the following suggestions are only examples of the many possible questions which can be addressed with this technique.

7. Quantitative measurements of the stress field around fibers could be easily made with standard photoelastic compensating methods, either manually or automatically. This would open the possibility for comparison with models of the stress state around inclusions in a matrix deforming by slip, a task exclusively done theoretically by analytical or numerical methods, to the best of our knowledge.
8. Thermal and mechanical deformation, either unique or repeated could be investigated. The stress fields could be analyzed both during the deformation and after it, when the material has relaxed. Time dependent deformation could also be studied *in situ*.
9. The global matrix stress state as well as local stress profile around inclusions could be investigated. The effect of interacting stress fields of neighbouring inclusions could be studied. It would be interesting to vary the composite properties such as the matrix yield stress, the fiber moduli or the deformation regime of the fiber (using plastically deformable tungsten fibers, for instance).
10. The geometry and dynamics of slip bands nucleation and propagation could be of great interest. The temperature, strain rate, reinforcement geometry and

volume fraction as well as the mechanical properties of the matrix are some of the possible parameters which could be varied.

11. Nucleation and growth of cracks in the presence of fibers or particles in a matrix deforming by slip is a whole field open to investigation which could bring new experimental evidence and understanding in the fracture mechanics of MMCs.

12. Recrystallization of two-phase materials could be observed *in situ* with a heated sample slightly strained to bring photoelastic contrast to the grains. This could clarify the role of supramicroscopic inclusions in the nucleation and growth of grains, a subject well understood for multiphase materials with submicroscopic inclusions, but less explored for MMCs.

APPENDIX 1: List of symbols

| | |
|-------------------------------------|---|
| a | equivalent hole radius |
| A | strain-hardening constant |
| A' | projected area |
| A'' | constant defined in Eq. [3.3.10] |
| b | Burgers' vector |
| c | plastic zone radius |
| c' | sum of punching distance and fiber half length |
| C | constant defined in Eq. [3.3.10] |
| C₁, C₂ | constants defined in Eqs. [3.1.14] |
| d | fiber or inclusion diameter |
| D, D₀ | diffusion coefficient |
| e | uniaxial strain |
| e | elementary charge force |
| E | elastic modulus |
| E(x) | complete elliptical integral |
| F | force |
| F_B, F_b | backforce |
| F_F, F_f | friction force |
| F_q | electric force |
| F_R | repulsive force |
| G | shear modulus |
| h | maximum deflection of a bowed dislocation from the line running between its anchor points |
| H | function |

| | |
|------------|--|
| H' | projected height |
| H'' | constant used in Eq. (1) |
| i | loop number |
| J_0, J_1 | flux |
| $J_1(x)$ | Bessel function of first order |
| k | constant in Eq. [6.2.5] |
| K | constant defined in Eq. [3.2.5] |
| $K(x)$ | complete elliptical integral |
| l | dislocation length |
| L | fiber length at low temperature inside the matrix |
| L_b | distance between the anchor points of a bowed dislocation |
| L_f | fiber length at low temperature outside the matrix |
| L_m | matrix hole length at low temperature without fiber |
| L_o | fiber length at high temperature |
| L_p | fiber critical length (elastic/plastic interface) |
| L_r | loop row length |
| L_u | fiber critical length (elastic/plastic/unstrained interface) |
| L_2' | intercept length of the projected area |
| L_3 | intercept length |
| n, n' | dislocation loop number |
| p | fiber load |
| P | packing ratio |
| q | electrical charge |
| r | inclusion radius |
| R | radius of curvature of bowed dislocations |
| R_o | dislocation core distance |
| t | embedding depth |

| | |
|----------------|--|
| T_a | annealing temperature |
| T_c | transition temperature from creep to glide |
| T_m | melting temperature |
| T_o | observation temperature |
| u | displacement |
| v | parameter defined in Eq. [3.3.4] |
| V | volume |
| v^* | critical volume fraction of inclusions |
| w | displacement |
| x | coordinate, distance |
| x_i | dimensionless plastic zone parameter; $i=c$: cylinder, $i=s$: sphere |
| x^* | equilibrium distance between two charged loops |
| z | coordinate |
| α | coefficient of thermal expansion |
| β | parameter defined in Eq. [3.4.4] |
| β' | parameter used in Eq. [3.4.38] |
| β'' | angle between dislocation line and its Burgers vector |
| Γ | constant defined in App. 6 |
| δ | spacing difference |
| δ_{ij} | Kronecker symbol |
| Δ | distance between two charged jogs |
| $\Delta\alpha$ | difference in CTE between matrix and fiber |
| Δr | matrix displacement at the interface of a mismatching inclusion |
| ΔT | temperature difference |
| $\Delta\zeta$ | dimensionless loop spacing |
| ϵ | shear strain |

| | |
|----------------|---|
| ϵ_1 | strain relieved by one prismatic loop |
| ϵ_1 | matrix strain due to inclusion |
| ν | Poisson's ratio |
| λ | Lame's constant |
| Ω | atomic volume |
| ρ | dislocation density |
| ρ' | dimensionless coordinate |
| ρ_q | dislocation line charge density |
| σ | fiber longitudinal stress |
| $\bar{\sigma}$ | average stress |
| σ_b | bowing stress |
| σ_B | backstress |
| σ_e | elastic contribution to fiber stress |
| σ_y | tensile yield stress |
| σ^* | fiber stress at L_p |
| τ | interfacial shear stress |
| τ_c | critical shear stress |
| τ_f | lattice friction stress |
| τ_q | shear stress due to electrical interactions |
| τ_{rz} | shear stress on a loop |
| τ_y | matrix shear flow stress |
| τ_{y0} | matrix intrinsic shear flow stress |
| τ^* | shear stress on glide cylinder |
| ξ | dimensionless coordinate |
| Ξ | constant defined in App. 6 |
| ζ | dimensionless coordinate |

subscripts

| | |
|----------------|--------------|
| c | cylinder |
| e | equivalent |
| f | fiber |
| i | number |
| m | matrix |
| max | maximal |
| p | particle |
| s | sphere |
| r, z, θ | coordinate |
| z | plastic zone |

APPENDIX 2 : Program to calculate the equilibrium of a row of loops

The FORTRAN program listed below was used on MIT's ATHENA system. It seeks the equilibrium configuration of a row of large number of loops using the elastic solution given by Bullough and Newman (1960). The output is the dimensionless position and stress of the loops as defined by these authors. It is shorter to calculate the equilibrium configurations of intermediate trains with increasingly larger number of loops rather than calculating directly the position of the train with the maximum number of loops, because intermediate equilibrium positions can be used as part of the initial position of the train with a larger number of loops. The program thus first calculates the "primordial" initial position for the maximum number of loops n_{\max} ; the loop spacings are independent of n_{\max} since only next neighbours interactions are considered. The first n_1 loops of this primordial train are used as initial conditions for the first train which is then equilibrated. The initial conditions of the second train with n_2 loops is constructed by taking the primordial initial conditions for loops between n_1 and n_2 and the final conditions for the loops between n_1 and a , shifted from the origin to accommodate the $n_2 - n_1$ loops which have just been added. The second train is then equilibrated and used as part of the initial condition for the next one, and so on until the final train with n_{\max} loops is equilibrated. This recurrent method not only yields information on all the intermediate trains, it also takes less time than the calculation of the single train with n_{\max} starting from its initial position. Indeed the choice of initial positions as close as possible to (but not exceeding) the final positions is crucial since the calculation time increases rapidly with the number of loops in the train. The primordial and subsequent initial positions are written in a file while the final configurations are stored in another file.

Starting with the last loop, each position is changed until the loop stress is equal to the lattice friction stress. By changing the position of a given loop, its neighbours which were at equilibrium are not any more. This will be corrected the next time these loops are considered. The equilibrium of the first row is reached when the equilibrium position is reached simultaneously for all loops except the first one which is blocked. Each loop is considered having fixed neighbours and its position is changed in the interval formed by its two nearest neighbours until its stress is within 0.5% of the critical shear stress. Practically, though, the stress position function is so extremely steep that this criterion cannot be used anymore for small loop spacings since a minor displacement makes the stress change from a very large positive to a very large negative value. Since one is interested only by the position of the loops, there is no need to change the position by an infinitesimal fraction to fulfil the stress criterion. Rather, the process is stopped when the equilibrium position is within $\zeta=5 \cdot 10^{-5}$ of the actual loop position: the program considers this loop equilibrated even though the stress criterion is not fulfilled. The error in position is however at most $\zeta=5 \cdot 10^{-5}$ for each loop. To "mark" these loops, their stress in the output is set at exactly the friction stress, a telltale value when the output is considered. Some times, the iteration is unsuccessful and increasingly smaller steps converge to values farther from the equilibrium position than the preset value of $\zeta=5 \cdot 10^{-5}$. In this case, the program repositions the loop at equal distances between its neighbours and start again the procedure of equilibration. When this situation happens more than thrice in a row for a given loop, the program moves on to the next loop giving a screen output "exit", loop number, position and stress. These small errors are of not great importance if they do not happen too often. At the next pass, the freak loop will be equilibrated and the errors are repaired rather than accumulating in an uncontrollable fashion. Finally, it can happen,

due to the lack of precision of numerical variables that a loop is placed at the same position as one of its neighbours; the program then assigns an arbitrary large value to the stress rather than collapsing due to division by zero. Also, from time to time, a loop ends up with a negative value. The program puts this wandering loop back between its two neighbours, provided they both have positive positions. Otherwise, the program exits completely.

After each row iteration, the position of each loop in the newly equilibrated train is compared to its position in the previously calculate row. If this difference in position for every loop in the train is more than 0.5% of the distance from the origin as well as larger than an absolute value of $\zeta=5 \cdot 10^{-3}$, the row is considered not yet at equilibrium and the procedure is repeated. Also, the program stops when the spacing between loops is smaller than a value which can be preset at the beginning of the run.

* this prog. calculates the equilibrium of a train of loops according to the
 * method of Bullough & Newman. Translated from BASIC prog Train5 (March 3, 1990)
 * the output are the x and y axis of their paper.

```

    CHARACTER F1*20, F2*20, cd*1
    INTEGER deltan, BOMB
    DIMENSION x(500), f(500), xold(500)
    DOUBLE PRECISION x, k, Kint, Eint
***** set parameters
1  PRINT *, 'input FILENAME for equilibrium data'
   READ *, F1
   OPEN (UNIT=1, FILE=F1, STATUS='NEW', IOSTAT=BOMB)
   IF (BOMB.NE.0) THEN
     PRINT *, 'TRY ANOTHER NAME'
     GO TO 1
   END IF
2  PRINT *, 'input FILENAME for initial data'
   READ *, F2
   OPEN (UNIT=2, FILE=F2, STATUS='NEW', IOSTAT=BOMB)
   IF (BOMB.NE.0) THEN
     PRINT *, 'try another name...'
     GO TO 2
   END IF
   PRINT *, 'Do you want to set the parameters? (y/n) '
   read *, cd
   IF (cd.EQ.'n') THEN
     GO TO 5
   END IF
   PRINT *, 'reduced Peierls stress '
   READ *, fp
   PRINT *, 'initial number of loops ? (<500) : '
   READ *, nstart
   PRINT *, ' Loop number increment'
   READ *, deltan
   PRINT *, 'maximal number of loops (<500)'
   READ *, nmax
   PRINT *, 'lowest distance between 2 loops before program exits'
   READ *, lowx
   PRINT *, 'set initial distances? (in ascending order) (y/n)'
   READ *, cd
   GO TO 9
5  fp=2.5
   nstart=5
   deltan=5
   nmax=10
   lowx=.0001
   cd = "n"
9  x(nmax)=0
   ntot = nstart
   buf=fp
*calculate initial position of 2 loops with a friction stress equal to
*the number of loops times the real friction stress
   PRINT *, 'n      position      friction stress'
   IF (cd.EQ.'n') THEN
     buf=fp
     DO 17, m=nmax-1,1,-1
       fphigh=1.005*m*buf
       fplow=.995*m*buf
       d=50
       xx=50
13  d=d/2
       IF (d.LT.0.00001) THEN
         GO TO 15
       END IF
       k=1/SQRT(1+xx**2)
       CALL ellint(k,Kint,Eint)
       ff=k*((1-k*k)*Kint)+(Eint*((2*k*k)-1))/xx

```

```

        IF (ff.LT.fplow) THEN
            xx=xx-d
            GO TO 13
        END IF
        IF (ff.GT.fphigh) THEN
            xx=xx+d
            GO TO 13
        END IF
15      x(m)=xx+x(m+1)
        f(m)=ff
        WRITE (2,33) m,x(m),f(m)
17      CONTINUE
        fp=buf
*set initial position of first batch of loops
        PRINT *,'initial position of first train'
        WRITE (1,55) 'total loop #, # increment, friction stress'
        WRITE (1,33) nmax, deltan, fp
        WRITE (2,55) 'initial position of first train'
        DO 20, jj =ntot,1,-1
            WRITE (2,33) jj, x(jj)-x(ntot), f(jj)
            PRINT *,jj,x(jj)-x(ntot),f(jj)
20      CONTINUE
        PRINT *,'calculate equilibrium of first train'
        WRITE (1,55) 'equilibrium position of first train'
        ELSE
            DO 23, jj = ntot-1, 1, -1
                PRINT*, jj
                READ *, x(jj)
23      CONTINUE
            END IF
*****position first loop
25      xold(1) = x(1)
            i=1
            CALL move(f,x,i,fp,ntot)
*****position other loops
27      DO 30, i = 2, ntot-1
            xold(i) = x(i)
            CALL move(f,x,i,fp,ntot)
*error correction...just in case...
            IF (x(i).LT.0) THEN
                IF (x(i+1).GE.0.AND.x(i-1).GE.0) THEN
                    x(i)=(x(i+1)+x(i-1))/2
                    PRINT *, 'position error corrected (high level)',i
                ELSE
                    PRINT *,'STOP, loops have neg. positions',i-1,i,i+1
                    GO TO 50
                END IF
            END IF
30      CONTINUE
            i=ntot
            CALL force(f,x,ntot,i,fp)
*****compares the changes in position
            DO 31, ii = ntot-1,1,-1
                IF ((xold(ii).LT.(0.995*x(ii)).OR.xold(ii).GT.(1.005*x(ii)))
                    $ .AND.(ABS(xold(ii)-x(ii)).GT.0.001)) THEN
                    PRINT *, ntot, ii
                    GO TO 25
                END IF
31      CONTINUE
*****store data
            DO 34, jj = ntot,1,-1
                WRITE (1,33) jj, x(jj)-x(ntot), f(jj)
33      FORMAT (1X,I3,'t',E12.4,'t',E12.4)
                PRINT *, jj,x(jj)-x(ntot),f(jj)
34      CONTINUE
*****exit if minimum spacing is reached

```

```

        IF (x(ntot-1)-x(ntot).LT.lowx) THEN
            PRINT *, 'minimum spacing of loop ', ntot, ' is smaller than ', lowx
            GO TO 50
        END IF
*****position next batch
        ntot = ntot + deltan
        IF (ntot.GT.nmax.OR.x(ntot-deltan).LT.lowx) THEN
            GO TO 50
        END IF
        PRINT *, 'initial position of new train'
        WRITE (2,55) 'initial position of new train'
        DO 40, ii=ntot,1,-1
            PRINT *, ii, x(ii)-x(ntot),f(ii)
            WRITE (2,33) ii, x(ii)-x(ntot),f(ii)
40      CONTINUE
        PRINT *, 'calculate equilibrium of new train'
        WRITE (1,55) 'equilibrium position of new train'
        GO TO 25
*****end of program
50     PRINT *, 'the equilibrium data is in file', F1
        PRINT *, 'the initial data is in file', F2
55     FORMAT(1X,A50)
        CLOSE (1)
        CLOSE (2)
        END
*
*****move loops
        SUBROUTINE move(f,x,i,fp,ntot)
            DIMENSION f(500),x(500)
            DOUBLE PRECISION d,x
            ntab=0
71     ntab=ntab+1
            fphigh=1.005*fp
            fplow=.995*fp
            ncount=0
72     IF (i.EQ.1) then
                d=50
                x(i)=x(i)+50
                CALL force(f,x,ntot,i,fp)
                GO TO 75
            END IF
            CALL force(f,x,ntot,i,fp)
            IF (f(i).GE.fphigh) THEN
                d = ABS(x(i-1)-x(i))
                GO TO 75
            END IF
            IF (f(i).LE.fplow) THEN
                d = ABS(x(i)-x(i+1))
            ELSE
                RETURN
            END IF
75     d=d/2
*****exit procedures
        IF (d.LE.0.0002) THEN
            x(i)=x(i)+d
            call force(f,x,ntot,i,fp)
            fbuf=f(i)
            x(i)=x(i)-2*d
            call force(f,x,ntot,i,fp)
* exits if the error in distance is less than .0002, sets f(i)=fp
            IF ((fp-f(i))*(fp-fbuf).LE.0) THEN
                f(i)=fp
                RETURN
            ELSE
                ncount=ncount+1
                IF (ncount.LE.2) THEN

```

```

        GO TO 72
    ELSE
* exits if cannot find equilibrium after 3 trials
        PRINT *, 'exit', i, x(i), f(i)
        RETURN
    END IF
END IF
END IF
*****control that loop stays between its 2 neighbours
    IF (i.NE.1.AND.i.NE.ntot.AND.((x(i).LE.x(i+1)).OR.
$ (x(i).GE.x(i-1)))) THEN
        x(i)=(.6*x(i+1))+(.4*x(i-1))
        PRINT *, 'error in position fixed (low level)', i, x(i)
        IF (ntab.LE.3) THEN
            GO TO 71
        ELSE
            RETURN
        END IF
    END IF
*****equilibrium procedure
    IF (f(i).GT.fphigh) THEN
        x(i)=x(i)+d
        CALL force(f,x,ntot,i,fp)
        GO TO 75
    END IF
    IF (f(i).LT.fplow) THEN
        x(i)=x(i)-d
        CALL force(f,x,ntot,i,fp)
        GO TO 75
    ELSE
        RETURN
    END IF
END
*
*****calculate total force on a loop (using the formula by Kroupa 1962) from a
***** loops which exert a force at least equal to fp; the output is x(i):dista
*****diameter & f(i):reduced stress as given by Bullough & Newman
    SUBROUTINE force(f,x,ntot,i,fp)
        INTEGER s
        DIMENSION f(500), x(500)
        DOUBLE PRECISION k, Kint, Eint,x
        f(i)=0
        s=0
****error check
        IF (i.NE.1.AND.x(i).EQ.x(i-1)) THEN
            f(i)=-314159265
            RETURN
        END IF
        IF (i.NE.ntot.AND.x(i).EQ.x(i+1)) THEN
            f(i)=314159265
            RETURN
        END IF
****calculation
100     s=s+1
        IF (i+s.GT.ntot) THEN
            bull = 0
            GO TO 110
        END IF
        k = 1/SQRT(1+ABS(x(i)-x(i+s))**2)
        CALL ellint(k, Kint, Eint)
        bull=k*((1-k**2)*Kint)+(Eint*((2*k*k)-1))/ABS(x(i)-x(i+s))
110     IF (i-s.LT.1) THEN
            bul2 =0
            GO TO 115
        END IF
        k=1/SQRT(1+ABS(x(i)-x(i-s))**2)

```

```

CALL ellint(k, Kint, Eint)
bul2=k*((1-k**2)*Kint)+(Eint*((2*k*k)-1))/ABS(x(i)-x(i-s))
115 f(i)=f(i)-bul2+bull
IF (bull.GT.fp.OR.bul2.GT.fp) THEN
    GO TO 100
END IF
RETURN
END
*****calculate elliptical integral (Abramovitz numerical method)
SUBROUTINE ellint(k, Kint, Eint)
DOUBLE PRECISION k, m1, Kint, Eint
m1=1-k
IF (k.GE.1.OR.k.LT.0) THEN
    IF (k.GE.1.) THEN
        PRINT *, 'outside limits ell. integral >1'
        Eint=1
        Kint=11.386294
        RETURN
    END IF
    IF (k.LT.0) THEN
        PRINT *, 'outside limits ell. integral <0'
        Eint=1.570796
        Kint=1.570796
        RETURN
    END IF
    Eint=(1+.4630151*m1+.1077812*m1**2)
    Eint=Eint-((.2452727*m1+.0412496*m1**2)*LOG(m1))
    Kint=(1.386294+.1119723*m1+.0725296*m1**2)
    Kint=Kint-((.5+.1213478*m1+.0288729*m1**2)*LOG(m1))
RETURN
END

```

APPENDIX 3

BASIC program used to determine Eq. [3.3.11], Fig. 3.3.3.

```

REM calculates the # of loops emitted by a fiber according to theory and
REM simple upper limit nmax=LΔaΔT/b
REM alfa, alfa : CTE of matrix and fiber L : length, r : radiusdT : ΔT
REM Gm : matrix shear mod., Em : fiber Young mod., Y : matrix yield strength, Sb : backst
ress
REM b : Burger's vector, v : assumed volume fraction for calculation of beta
OPEN "clip:" FOR OUTPUT AS #1
10 PRINT " variable n n max Lc2[μm]
Lc1[μm]"

low=.000001
high=.0005
stepp=.000005

FOR i = low TO high STEP stepp
alfa = .0000235 : alfa = .000009 : Gm = 3E+10 : Ef = 3E+11 : Y = 1E+07
b = 2.86E-10 : v=.01 : L=.0002 : r=.0000015 : dT=200 : Sb = 0
L=i
dalfa = alfa - alfa
REM shear lag model beta coef.
beta = SQR (2*Gm/(Ef*r*r*LOG(1/SQR(v))))
buf = Y/(Ef*r*dalfa*dT*beta)
Lc2 = LOG((1+buf)/(1-buf))/beta
sto=2*Ef*r*dalfa*dT/(Y*(EXP(beta*Lc2/2)+EXP(-beta*Lc2/2))/2)
Lc1=Lc2-(4*r*Sb/Y)+sto
nmax = dalfa*dT*L/(2*b)
IF L <= Lc2 THEN b$ = "purely elastic" : GOTO 20
IF Lc1 < Lc2 THEN b$ = "lc1 < lc2" : GOTO 20
IF L>Lc1 THEN
L=Lc1 : b$ = "elastoplastic-unstrained"
ELSE
b$ = "elastoplastic"
END IF
integ=(Y/(4*Ef*r))*((L*L)-(Lc2*Lc2)-(8/(beta^2)))+(dalfa*dT*Lc2)+(Sb*L/Ef)
n=((dalfa*dT*L)/(1+(alfam*dT))) - (integ*(1+alfaf*dT)/(1+alfam*dT))/(2*b)
20 PRINT i, n, nmax, Lc2*1000000!, Lc1*1000000!
WRITE #1, n, nmax, Lc1*1000000!, Lc2*1000000!, i
NEXT i

INPUT "again ? (y/n) ", a$
IF a$ = "y" GOTO 10
CLOSE #1
END

```


APPENDIX 4

FORTRAN Program used to determine Eq. [3.3.13], Fig. 3.3.7. This program is a modification of that listed in Appendix 1.

* this prog. calculates the equilibrium of two trains of loops according to the
 * method of Bullough & Newman. the trains are placed symmetrically on each side
 * of the origine and attract each other (one is interstitial, the other vacancy
 * modified from new.f. Lines with ** are deleted statements from new.f (March 22,
 **drop F2

```

    CHARACTER F1*20, cd*1
    INTEGER deltan, BOMB
    DIMENSION x(500),f(500),xold(500)
    DOUBLE PRECISION x,k,Kint,Eint
***** set parameters
  1  PRINT *, 'input FILENAME for equilibrium data'
    READ *, F1
    OPEN (UNIT=1, FILE=F1, STATUS='NEW', IOSTAT=BOMB)
    IF (BOMB.NE.0) THEN
      PRINT *, 'TRY ANOTHER NAME'
      GO TO 1
    END IF
** 2  PRINT *, 'inpute FILENAME for initial data'
**    READ *, F2
**    OPEN (UNIT=2, FILE=F2, STATUS='NEW', IOSTAT=BOMB)
**    IF (BOMB.NE.0) THEN
**      PRINT *, 'try another name...'
**      GO TO 2
**    END IF
**    PRINT *, 'Do you want to set the parameters? (y/n) '
**    read *, cd
**    IF (cd.EQ.'n') THEN
**      GO TO 5
**    END IF
    PRINT *, 'reduced Peierls stress '
    READ *, fp
    PRINT *, 'total number of loops ? (<500) : '
    READ *, nstart
**    PRINT *, ' Loop number increment'
**    READ *, deltan
**      deltan=1
**    PRINT *, 'maximal number of loops (<500)'
**    READ *, nmax
    nmax=ntot
    PRINT *, 'set initial distance in ascending order)'
**    READ *, cd
    GO TO 9
  5  fp=2.9
    nstart=25
    deltan=25
    nmax=150
  9  cd = "y"
    x(nmax)=0
    ntot = nstart
    buf=fp
*calculate initial position of 2 loops with a friction stress equal to
*the number of loops times the real friction stress
**    PRINT *, ' positions of 2 loops under different friction stress'
**    PRINT *, 'n position friction stress'
    IF (cd.EQ.'n') THEN
      buf=fp
      DO 17, m=nmax-1,1,-1
        fphigh=1.005*m*buf
        fplow=.995*m*buf
        d=50
        xx=50
  13  d=d/2
        IF (d.LT.0.00001) THEN
          GO TO 15
        END IF
        k=1/SQRT(1+xx**2)

```

```

        CALL ellint(k,Kint,Eint)
        ff=k*((1-k*k)*Kint)+(Eint*((2*k*k)-1))/xx
        IF (ff.LT.fplow) THEN
            xx=xx-d
            GO TO 13
        END IF
        IF (ff.GT.fphigh) THEN
            xx=xx+d
            GO TO 13
        END IF
15         x(m)=xx+x(m+1)
           f(m)=ff
**         WRITE (2,33) m,x(m),f(m)
17         CONTINUE
           fp=buf
*set initial position of first batch of loops
        PRINT *,'initial position of first train'
        WRITE (1,55) 'total loop #, # increment, friction stress'
        WRITE (1,33) nmax, deltan, fp
**         WRITE (2,55) 'initial position of first train'
        DO 20, jj =ntot,1,-1
**         WRITE (2,33) jj, x(jj)-x(ntot), f(jj)
           PRINT *,jj,x(jj)-x(ntot),f(jj)
20         CONTINUE
        PRINT *,'calculate equilibrium of first train'
        WRITE (1,55) 'equilibrium position of first train'
        ELSE
**CHANGE         DO 23, jj = ntot, 1, -1
                   PRINT*, jj
                   READ *, x(jj)
**NEW
                   x((2*ntot)-jj+1)=-x(jj)
23         CONTINUE
           END IF
*****position first loop
25         xold(1) = x(1)
           i=1
           CALL move(f,x,i,fp,ntot)
**NEW
           x(2*ntot)=-x(1)
*****position other loops
27         DO 30, i = 2, ntot-1
           xold(i) = x(i)
           CALL move(f,x,i,fp,ntot)
**NEW
           x((2*ntot)-i+1)=-x(i)
30         CONTINUE
           i=ntot
           CALL force(f,x,ntot,i,fp)
*****compares the changes in position
        DO 31, ii = ntot-1,1,-1
           IF ((xold(ii).LT.(0.995*x(ii)).OR.xold(ii).GT.(1.005*x(ii)))
           $      .AND.(ABS(xold(ii)-x(ii)).GT.0.001)) THEN
               PRINT *, ntot, ii
               GO TO 25
           END IF
31         CONTINUE
*****store data
        WRITE (1,33) ntot, fp
        DO 34, jj = ntot,1,-1
           WRITE (1,33) jj, x(jj)-x(ntot), f(jj)
33         FORMAT (1X,I3,' \t',E12.4,' \t',E12.4)
           PRINT *, jj,x(jj)-x(ntot),f(jj)
34         CONTINUE
*****position next batch of loops

```

```

ntot = ntot + deltan
IF (ntot.GT.nmax) THEN
  GO TO 50
END IF
PRINT *, 'initial position of new train'
**  WRITE (2,55) 'initial position of new train'
DO 40, ii=ntot,1,-1
  PRINT *, ii, x(ii)-x(ntot),f(ii)
**  WRITE (2,33) ii, x(ii)-x(ntot),f(ii)
40  CONTINUE
PRINT *, 'calculate equilibrium of new train'
WRITE (1,55) 'equilibrium position of new train'
GO TO 25

*
50  PRINT *, 'the equilibrium data is in file', F1
**  PRINT *, 'the initial data is in file', F2
55  FORMAT(1X,A50)
    CLOSE (1)
    END

*
*****move loops
SUBROUTINE move(f,x,i,fp,ntot)
  DIMENSION f(500),x(500)
  DOUBLE PRECISION d,x
  fphigh=1.005*fp
  fplow=.995*fp
  ncount=0
72  IF (i.EQ.1) then
    d=50
    x(i)=x(i)+50
    CALL force(f,x,ntot,i,fp)
    GO TO 75
  END IF
  CALL force(f,x,ntot,i,fp)
  IF (f(i).GE.fphigh) THEN
    d = ABS(x(i-1)-x(i))
    GO TO 75
  END IF
  IF (f(i).LE.fplow) THEN
    d = ABS(x(i)-x(i+1))
  ELSE
    RETURN
  END IF
75  d=d/2
*****exit procedures
  IF (d.LE.0.0002) THEN
    x(i)=x(i)+d
    call force(f,x,ntot,i,fp)
    fbuf=f(i)
    x(i)=x(i)-2*d
    call force(f,x,ntot,i,fp)
***** exits if the error in distance is less than .0002, sets f(i)=fp
    IF ((fp-f(i))*(fp-fbuf).LE.0) THEN
      f(i)=fp
      RETURN
    ELSE
      ncount=ncount+1
      IF (ncount.LE.2) THEN
        GO TO 72
      ELSE
***** exits if cannot find equilibrium after 3 trials
        PRINT *, 'exit', i, x(i), f(i)
        RETURN
      END IF
    END IF
  END IF
END IF

```

```

*
  IF (f(i).GT.fphigh) THEN
    x(i)=x(i)+d
    CALL force(f,x,ntot,i,fp)
    GO TO 75
  END IF
  IF (f(i).LT.fplow) THEN
    x(i)=x(i)-d
    CALL force(f,x,ntot,i,fp)
    GO TO 75
  ELSE
    RETURN
  END IF
END

*
*****calculate total force on a loop (Kroupa 1962) from all other loops which
***** exert a force at least equal to fp
SUBROUTINE force(f,x,ntot,i,fp)
  INTEGER s
  REAL bull, bul2
  DIMENSION f(500), x(500)
  DOUBLE PRECISION k, Kint, Eint,x
  f(i)=0
  s=0
100  s=s+1
  **          IF (i+s.GT.ntot) THEN
  **          bull = 0
  **          GO TO 110
  **          END IF
  k = 1/SQRT(1+ABS(x(i)-x(i+s))**2)
  CALL ellint(k, Kint, Eint)
  bull=k*(((1-k**2)*Kint)+(Eint*((2*k**2)-1)))/ABS(x(i)-x(i+s))
**NEW 3 LINES
  IF ((i+s).GT.ntot) THEN
    bull=-bull
  END IF
110  IF (i-s.LT.1) THEN
    bul2 =0
    GO TO 115
  END IF
  k=1/SQRT(1+ABS(x(i)-x(i-s))**2)
  CALL ellint(k, Kint, Eint)
  bul2=k*(((1-k**2)*Kint)+(Eint*((2*k**2)-1)))/ABS(x(i)-x(i-s))
115  f(i)=f(i)-bul2+bull
*CHANGE
  IF (ABS(bull).GT.fp.OR.bul2.GT.fp) THEN
    GO TO 100
  END IF
  RETURN
END

*****calculate elliptical integral (Abramovitz numerical method)
SUBROUTINE ellint(k, Kint, Eint)
  DOUBLE PRECISION k, ml, Kint, Eint
  IF (k.GE.1.OR.k.LT.0) THEN
    PRINT *, 'outside limits elliptical integral'
    RETURN
  END IF
125  ml=1-k
  Eint=(1+.4630151*ml+.1077812*ml**2)
  Eint=Eint+((.2452727*ml+.0412496*ml**2)*LOG(1/ml))
  Kint=(1.386294+.1119723*ml+.0725296*ml**2)
  Kint=Kint+((.5+.1213478*ml+.0288729*ml**2)*LOG(1/ml))
  RETURN
END

```

APPENDIX 5 : Model by Taya and Mori (1987)

This model predicts the number of loops and the punching distance for a misfitting ellipsoid. The fiber is assimilated to a prolate spheroid with major axis $L/2$ and minor axis $d/2$. The fiber punches loops, thus forming a plastic zone modelled as another prolate spheroid of same minor axis as the fiber and major axis c' equal to the sum of the fiber half length and the punching distance. The punching distance is determined by equating the total work (estimated using Tanaka and Mori's model (1972)) done by the loops against the lattice friction stress τ_f with the elastic energy released during relaxation of the fiber, calculated using Eshelby's equivalent inclusion method. The result is of the form

$$H(c'/d, L/d, G_m, G_f, \lambda_m, \lambda_f, \nu_m) = \frac{\tau_f L}{d \Delta\alpha \Delta T G_m} \quad [1]$$

where $\Delta\alpha$ is the CTE difference between fiber and matrix, ΔT is the temperature excursion, G_m and ν_m are the matrix shear modulus and Poisson's ratio, G_f is the fiber shear modulus and λ_m and λ_f are the matrix and fiber Lamé's constants. H is a complicated function of the punching distance c' and other variables, containing Eshelby's tensors.

A noteworthy feature of this model is that each parameter in Eq. [1] has a critical value for which the punching distance becomes zero, separating a regime of positive and negative punching distances. Taya and Mori (1987) predict that punching is suppressed in the latter regime and explain this result by showing that the energy needed to move the dislocations against the lattice friction stress

is larger than the elastic energy of relaxation. This leads to the unexpected result that the punching length decreases and finally becomes zero as the fiber length (and thus the mismatch) increases. In the regime where loops are emitted, they assume complete longitudinal relaxation of the fiber, which yields by conservation of volume for the total number of loops emitted n_{\max} :

$$n_{\max} = \frac{\Delta\alpha \Delta T L}{2b} . \quad [2]$$

Figs. 3.4.5a-e show this value as dotted lines which drop to zero at a critical value corresponding to the onset of negative punching distance regime predicted by Eq. [1]. The basic program listed below calculates the values c'/c and c/a according to Eqs. [1] and [2].

The following is a list of the BASIC program used to determine Eq. [1].

REM this program calculates the the extend of the plastic zone c/c (called
REM x is this program) as a function of the fiber aspect ratio c/a (called b1)
REM according to theory developed in Taya and Mori, Acta Met. 1987.
REM K = matrix shear modulus* Δ CTE* Δ T/friction stress
REM all other variable defined in program

```

OPEN "clip:" FOR OUTPUT AS #1
5 INPUT "new material constants ? (y/n) ",a$
  IF a$ = "n" THEN nu=.343 : nuf=.21 : E=14.7 : Ef=85 : K=23.5 : GOTO 10
  INPUT "Poisson ratio of matrix",nu
  INPUT "Poisson ratio of fiber",nuf
  INPUT "Young's Modulus of matrix",E
  INPUT "Young's Modulus of fiber",Ef
  INPUT "Beta coefficient",K
10 INPUT "new bounds for c/c (Now : from1 to 9 step 0.25)? (y/n)", a$
  IF a$ = "n" THEN lowbond=1 : highbond = 9 : stepbond = .25 : GOTO 15
  INPUT "lower bond ", lowbond
  INPUT "higher bond ", highbond
  INPUT "step ",stepbond
15 L=E*nu/((1+nu)*(1-2*nu)): Lf=Ef*nuf/((1+nuf)*(1-2*nuf)) : mu=E/(2*(1+nu)) : muf=E
f/(2*(1+nuf))
  a=1 : c=10 : oldb = -99.99
  b1#=c/a : Lbar = Lf - L : mubar = muf - mu

FOR x# = lowbond TO highbond STEP stepbond
  b1# = 10000# : b# =x#*b1#
20 oldb = b1#
  GOSUB compute
  b1#=K*h : b#=b1#*x# : c=b1#*a
  PRINT x#,b1#
  IF b1# < .999*oldb OR b1# > 1.001*oldb GOTO 20
  WRITE #1,x#,b1#
NEXT x#
  INPUT "Again ? (y/n)",q$
  IF q$ = "y" GOTO 5
  CLOSE #1
  END
40 PRINT ERL
INPUT qq
  
```

compute:

REM formulas in Appendix of Taya and Mori (1987)

$$G1=b1#\left(\frac{b1#\left(b1\#*b1\#-1\right)^{.5}-\text{LOG}\left(b1\#+\left(b1\#*b1\#-1\right)^{.5}\right)}{\left(b1\#*b1\#-1\right)^{1.5}}\right)$$

$$G = b^* \cdot ((b^* \cdot (b^* \cdot b\# - 1)^{.5}) - \text{LOG}(b\# + (b^* \cdot b\# - 1)^{.5})) / (b^* \cdot b\# - 1)^{1.5}$$

$$\text{Gdot} = (c / (a^* \cdot (b^* \cdot b\# - 1)^{1.5})) \cdot (1 - 3^* \cdot b^* \cdot b\# / (b^* \cdot b\# - 1)) \cdot (b^* \cdot (b^* \cdot b\# - 1)^{.5} - \text{LOG}(b\# + (b^* \cdot b\# - 1)^{.5})) + 2^* \cdot c^* \cdot b\# / (a^* \cdot (b^* \cdot b\# - 1))$$

$$S111 = (3^* \cdot b1\# \cdot b1\#) / (8^* \cdot (1 - \text{nu})^* \cdot (b1\# \cdot b1\# - 1)) + G1^* \cdot (1 - 2^* \cdot \text{nu} - (2.25 / (b1\# \cdot b1\# - 1))) / (4^* \cdot (1 - \text{nu}))$$

$$S122 = S111$$

$$S211 = (3^* \cdot b^* \cdot b\#) / (8^* \cdot (1 - \text{nu})^* \cdot (b^* \cdot b\# - 1)) + G^* \cdot (1 - 2^* \cdot \text{nu} - (2.25 / (b^* \cdot b\# - 1))) / (4^* \cdot (1 - \text{nu}))$$

$$S222 = S211$$

$$\text{Sd11} = (c/a)^* \cdot ((.75^* \cdot b\# / ((1 - \text{nu})^* \cdot (b^* \cdot b\# - 1))) \cdot (1 - b^* \cdot b\# / (b^* \cdot b\# - 1)) + (.25 / (1 - \text{nu}))^* \cdot (\text{Gdot} \cdot (1 - (2^* \cdot \text{nu}) - 2.25 / (b^* \cdot b\# - 1)) + 4.5^* \cdot G^* \cdot b\# / ((b^* \cdot b\# - 1)^2)))$$

$$\text{Sd22} = \text{Sd11}$$

$$S133 = (.5 / (1 - \text{nu}))^* \cdot (1 - 2^* \cdot \text{nu} + (3^* \cdot b1\# \cdot b1\# - 1) / (b1\# \cdot b1\# - 1) - G1^* \cdot (1 - 2^* \cdot \text{nu} + 3^* \cdot b1\# \cdot b1\# / (b1\# \cdot b1\# - 1)))$$

$$S233 = (.5 / (1 - \text{nu}))^* \cdot (1 - 2^* \cdot \text{nu} + (3^* \cdot b^* \cdot b\# - 1) / (b^* \cdot b\# - 1) - G^* \cdot (1 - 2^* \cdot \text{nu} + 3^* \cdot b^* \cdot b\# / (b^* \cdot b\# - 1)))$$

$$\text{Sd33} = (c / (2^* \cdot a^* \cdot (1 - \text{nu})))^* \cdot (2^* \cdot b^* \cdot (3 - (3^* \cdot b^* \cdot b\# - 1) / (b^* \cdot b\# - 1)) / (b^* \cdot b\# - 1) - \text{Gdot}^* \cdot (1 - (2^* \cdot \text{nu}) + 3^* \cdot b^* \cdot b\# / (b^* \cdot b\# - 1)) - 6^* \cdot G^* \cdot b^* \cdot (1 - b^* \cdot b\# / (b^* \cdot b\# - 1)) / (b^* \cdot b\# - 1))$$

$$S112 = (.25 / (1 - \text{nu}))^* \cdot ((.5^* \cdot b1\# \cdot b1\# / (b1\# \cdot b1\# - 1)) - G1^* \cdot (1 - (2^* \cdot \text{nu}) + .75 / (b1\# \cdot b1\# - 1)))$$

$$S121 = S112$$

$$S212 = (.25 / (1 - \text{nu}))^* \cdot ((.5^* \cdot b^* \cdot b\# / (b^* \cdot b\# - 1)) - G^* \cdot (1 - (2^* \cdot \text{nu}) + .75 / (b^* \cdot b\# - 1)))$$

$$S221 = S212$$

$$\text{Sd12} = (.25^* \cdot c / (a^* \cdot (1 - \text{nu})))^* \cdot (b^* \cdot (1 - b^* \cdot b\# / (b^* \cdot b\# - 1)) / (b^* \cdot b\# - 1) - \text{Gdot}^* \cdot (1 - (2^* \cdot \text{nu}) + .75 / (b^* \cdot b\# - 1)) + 1.5^* \cdot G^* \cdot b\# / (b^* \cdot b\# - 1)^2)$$

$$\text{Sd21} = \text{Sd12}$$

$$S113 = (-.5 / (1 - \text{nu}))^* \cdot (b1\# \cdot b1\# / (b1\# \cdot b1\# - 1) - .5^* \cdot G1^* \cdot (3^* \cdot b1\# \cdot b1\# / (b1\# \cdot b1\# - 1) - 1 + (2^* \cdot \text{nu})))$$

$$S123 = S113$$

$$S213 = (-.5 / (1 - \text{nu}))^* \cdot (b^* \cdot b\# / (b^* \cdot b\# - 1) - .5^* \cdot G^* \cdot (3^* \cdot b^* \cdot b\# / (b^* \cdot b\# - 1) - 1 + (2^* \cdot \text{nu})))$$

$$S223 = S213$$

$$\text{Sd13} = (.5^* \cdot c / (a^* \cdot (1 - \text{nu})))^* \cdot (-2^* \cdot b^* \cdot (1 - b^* \cdot b\# / (b^* \cdot b\# - 1)) / (b^* \cdot b\# - 1) + .5^* \cdot \text{Gdot}^* \cdot (3^* \cdot b^* \cdot b\# / (b^* \cdot b\# - 1) - 1 + (2^* \cdot \text{nu})) + 3^* \cdot G^* \cdot b^* \cdot (1 - b^* \cdot b\# / (b^* \cdot b\# - 1)) / (b^* \cdot b\# - 1))$$

$$\text{Sd23} = \text{Sd13}$$

$$S131 = (-.5 / (1 - \text{nu}))^* \cdot (1 - (2^* \cdot \text{nu}) + 1 / (b1\# \cdot b1\# - 1)) + (.5^* \cdot G1 / (1 - \text{nu}))^* \cdot (1 - (2^* \cdot \text{nu}) + 1.5 / (b1\# \cdot b1\# - 1))$$

$$S132 = S131$$

$$S231 = (-.5 / (1 - \text{nu}))^* \cdot (1 - (2^* \cdot \text{nu}) + 1 / (b^* \cdot b\# - 1)) + (.5^* \cdot G / (1 - \text{nu}))^* \cdot (1 - (2^* \cdot \text{nu}) + 1.5 / (b^* \cdot b\# - 1))$$

$$S232 = S231$$

$$\text{Sd31} = (.5^* \cdot c / (a^* \cdot (1 - \text{nu})))^* \cdot (2^* \cdot b\# / ((b^* \cdot b\# - 1)^2) + \text{Gdot}^* \cdot (1 - (2^* \cdot \text{nu}) + 1.5 / (b^* \cdot b\# - 1)) - G^* \cdot 3^* \cdot b\# / ((b^* \cdot b\# - 1)^2))$$

Sd32=Sd31

$$Q1=(2^{\text{nu}}/(1-2^{\text{nu}}))*(S111+S112+S131-1) + S111 + S112 - 1$$
$$Q2=S113/(1-2^{\text{nu}}) + \text{nu}*(S133-1)/(1-2^{\text{nu}})$$

$$D1=-(1/x\#)*((Lbar+mubar)*S213/\mu + .5*Lbar*(S233-1)/\mu) + (Lf+muf)/\mu$$
$$D2=-(1/x\#)*(.5*Lbar*(2*S213+S233)/\mu + mubar*S233/\mu - .5*(Lbar+2*mubar)/\mu) + Lf/\mu$$

$$D1dot= (1/x\#^2)*((Lbar+mubar)*S213/\mu + .5*Lbar*(S233-1)/\mu)- (1/x\#)*((Lbar+mubar)*Sd13/\mu + .5*Lbar*Sd33/\mu)$$
$$D2dot=(-D2+(Lf/\mu))/x\# - (1/x\#)*(.5*Lbar*(2*Sd13+Sd33)/\mu + mubar*Sd33/\mu)$$

$$B11=((Lbar+mubar)/\mu)*(S111+S112) + Lbar*S131/\mu + 1/(1-2^{\text{nu}})$$
$$B12=((Lbar+mubar)/\mu)*S113 + .5*Lbar*S133/\mu + \text{nu}/(1-2^{\text{nu}})$$
$$B21=(Lbar/\mu)*(S111+S112+S131) + 2*S231*mubar/\mu + 2^{\text{nu}}/(1-2^{\text{nu}})$$
$$B22=(.5*Lbar/\mu)*(2*S113+S133) + mubar*S133/\mu + (1-\text{nu})/(1-2^{\text{nu}})$$
$$B0=B11*B22-B12*B21$$

$$A1=2^{\text{nu}}*(S211+S212+S231-1)/(1-2^{\text{nu}}) + 2*S231$$
$$A2=2^{\text{nu}}*S213/(1-2^{\text{nu}}) + (1-\text{nu})*(S233-1)/(1-2^{\text{nu}})$$
$$A3=S213/(1-2^{\text{nu}}) + \text{nu}*(S233-1)/(1-2^{\text{nu}})$$

$$A1dot=2^{\text{nu}}*(Sd11+Sd12+Sd31)/(1-2^{\text{nu}}) + 2*Sd31$$
$$A2dot=2^{\text{nu}}*Sd13/(1-2^{\text{nu}}) + (1-\text{nu})*Sd33/(1-2^{\text{nu}})$$
$$A3dot=Sd13/(1-2^{\text{nu}}) + \text{nu}*Sd33/(1-2^{\text{nu}})$$

$$h1 = -(A1*(D1*B22-D2*B12)+A2*(D2*B11-D1*B21))/(B0*x\#*x\#)$$
$$h2=h1+((A1dot*(D1*B22-D2*B12)) + (A1*(B22*D1dot-B12*D2dot)))/(B0*x\#)$$
$$h3=h2+((A2dot*(D2*B11-D1*B21)) + (A2*(B11*D2dot-B21*D1dot)))/(B0*x\#)$$
$$h4=h3+((2/B0)*(Q1*(B22*D1dot-B12*D2dot) + Q2*(B11*D2dot-B21*D1dot)))$$
$$h=h4-((A2+2*A3)/(x\#*x\#))+((A2dot+2*A3dot)/x\#)$$

RETURN

Appendix 6 : Determination of the maximum temperature at which mismatch relaxation by slip is operative

Imagine a mismatching sphere of radius r embedded in silver chloride at a depth t below the surface. The temperature T_c at which diffusion is less efficient than slip to evacuate the extraneous matrix material due to the mismatching sphere is calculated in what follows in two different manners.

We first solve the problem by considering creep. We calculate the temperature T_c at which the Nabarro-Herring creep rate $\dot{\epsilon}_c$ given by

$$\dot{\epsilon}_c = \frac{14 \sigma \Omega D}{k T t^2} , \quad [1]$$

is equal to the rate of thermal mismatch $\dot{\epsilon}_t$:

$$\dot{\epsilon}_t = \Delta\alpha \Delta\dot{T} \quad [2]$$

where k is Boltzman's constant, T the temperature, Ω the atomic volume, D the diffusion coefficient, $\Delta\alpha$ the CTE mismatch, $\Delta\dot{T}$ the cooling rate and σ is the stress at the interface at which a loop is nucleated. The diffusion distance t is taken as the distance between the inclusion and the surface.

Charge neutrality dictates that both anions and cations diffuse at the same rate. The rate of removal of matter by diffusion is thus given by the slowest diffusing ion in AgCl (chlorine), for which the diffusion coefficient can be written as

$$D = D_0 \exp(-\Gamma/T) , \quad [3]$$

where D_0 and Γ are constants with values of 13300 [m²/s] and 18600 [K] respectively (Compton and Maurer 1956).

To calculate the dislocation nucleation stress, we use a model by Brown and Woolhouse (1970) which gives a lower bound for the mismatch strain ϵ_{11}^T necessary to nucleate a prismatic loop at the surface of a mismatching sphere. For a sphere radius of 1.2 μm , $\epsilon_{11}^T = 5.6 \cdot 10^{-4}$. This strain corresponds to a displacement at the surface of the sphere of 3.4 Burgers vectors; the number of loops counted in section 6.2.1.1 and used in Eq. [6.2.3] might therefore be underestimated by 2 to 4 dislocations, depending on the radius of the sphere. This error is within the scatter of the data presented in Fig. 5.1.5.

The maximum shear stress at the surface of the sphere can then be calculated from (Asby *et al.* 1969)

$$\tau_{\max} = G \frac{1+\nu}{1-\nu} \epsilon_{11}^T, \quad [4]$$

where G and ν are the matrix shear modulus and Poisson's ratio respectively. Introducing Eqs. [3] and [4] and $\sigma = 2\tau_{\max}$ into Eq. [1] and equating with Eq. [2] yields an equation for T_c :

$$\frac{\exp(-\Gamma/T_c)}{T_c} = \frac{(1-\nu) k t^2 \Delta\alpha \Delta\dot{T}}{28 (1+\nu) G \epsilon_{11}^T \Omega D_0}, \quad [5]$$

Introducing the values of ϵ_{11}^T , D_0 and Γ given above, as well as $\Omega = 1.78 \cdot 10^{-29}$ [m³] (Kittel, 1983) and $t = 10 \mu\text{m}$ yields a value for T_c of 432 K, in good agreement with the range of values determined experimentally in section 6.2.1.1.

We now solve the same problem using diffusion equations. Fick's first law for the flux of atoms J_0 gives

$$J_0 = -D \overrightarrow{\text{grad}}(c) , \quad [6]$$

where D is the diffusion coefficient and c is the local concentration in the gradient between the source (mismatching sphere) and the sink (specimen surface).

We assume that the atoms which must be evacuated from the interface are placed in the matrix as interstitials. A disk of such interstitials would form a prismatic loop. At high temperatures, diffusion is so rapid that the equilibrium concentration of the interstitials is much lower than that necessary to form a full disk of atoms. At lower temperatures, diffusion is slow and interstitials accumulate until their number is large enough to create a loop which can then glide away from the stressed inclusion. While nucleation of loops at mismatching inclusions does not actually occur according to this scenario (condensation of interstitials), it allows to ascribe a concentration c_1 of interstitials at which slip occurs, i.e., one interstitial per atomic site:

$$c_1 = \frac{1}{\Omega} , \quad [7]$$

where Ω is the atomic volume of the chlorine ion. The concentration of interstitial atoms at the sink c_0 is assumed to be zero.

Eq. [6] yields after insertion of Eqs. [3] and [7]:

$$J_0 = \frac{D_0 \exp(-\Gamma/T)}{\Omega t} . \quad [8]$$

The flux J_1 of atoms produced at the source is

$$J_1 = \frac{1}{\pi r^2} \frac{\Delta \dot{V}}{\Omega} , \quad [9]$$

where $\Delta \dot{V}$ is the rate of volume mismatch:

$$\Delta \dot{V} = \Xi 4 \pi r^2 \Delta \alpha \Delta \dot{T} r , \quad [10]$$

where $\Delta \alpha$ is the CTE mismatch, $\Delta \dot{T}$ the cooling rate, taken respectively as $2.1 \cdot 10^{-5}$ [K⁻¹] and 1 [K/s] and Ξ is the ratio of atomic volume of chlorine to that of the AgCl molecule ($\Xi = 0.75$).

Inserting Eq. [10] into Eq. [9], equating to Eq. [8] and solving yields:

$$T_c = \frac{-\Gamma}{\ln\left(\frac{4 \Delta \alpha \Delta \dot{T} r t}{D_0}\right)} , \quad [11]$$

which gives a value of $T_c = 426$ K for $r \cdot t = 15 \mu\text{m}^2$ and $T_c = 405$ K for $r \cdot t = 1.5 \mu\text{m}^2$, corresponding to the experimental range of values for r (0.5 to 1.5 μm) and t (3 to 10 μm). These temperatures are in good agreement with the value calculated above and the range of $T_c = 400 \pm 30$ K determined independently in section 6.2.1.1.

BIBLIOGRAPHY

- Abramowitz M., Stegun I.E. (1972), *Handbook of Mathematical Functions*, 10th Printing, p. 591, National Bureau of Standards, Washington D.C. .
- Allard L.F., Rawal S.P. , Misra M.S. (1986), *J. of Met.* **10**, 40.
- American Ceramic Society (1988), *Ceramic Source*, 234.
- Arsenault R.J. (1984), *Mat. Sci. Eng.* **64**, 171.
- Arsenault R.J. (1986), *Composites '86: Recent Advances in Japan and the United States*, Kawata et al. Ed., Japan Society for Composite Materials, 521.
- Arsenault R.J. (1988), *Ninth Riso International Symposium on Metallurgy and Materials Science*, Andersen et al. Ed., Riso National Laboratory, 279.
- Arsenault R.J., Feng C. R., Shi N. (1986), *Proceedings of the Fourth Japan-US Conference on Composite Materials*, Technomic Publishing Co, 589.
- Arsenault R.J., Fisher R.M. (1983a), *Mechanical Behavior of Materials IV, ICM IV*, Carlsson and Ohlson Ed., Pergamon, 451.
- Arsenault R.J., Fisher R.M. (1983b), *Scripta Metall.* **17**, 67.
- Arsenault R.J., Shi N. (1986), *Mat. Sci. Eng.* **81**, 175.
- Arsenault R.J., Wu S.B. (1988), *Cast Reinforced Metal Composites*, Fishman & Dhingra Eds., ASM, 231.
- Ashby M.F. (1966), *Phil. Mag.* **14**, 1157.
- Ashby M.F. (1970), *Phil. Mag.* **21**, 399.
- Ashby M.F., Gelles S.H., Tanner L.E. (1969), *Phil. Mag.* **19**, 757.
- Ashby M.F., Johnson L. (1969), *Phil. Mag.* **20**, 1009.
- Atkinson C., Avila J., Betz E., Smelser R.E. (1982), *J. Mech. Phys. Sol.* **30**, 97.
- Axilrod B.M., Lamb J.J. (1948), *J. Appl. Phys.* **19**, 213.
- Bailey J.E., Hirsch P.B. (1960), *Phil. Mag.* **5**, 485.
- Barber D.J., Harvey K.B., Mitchell J.W. (1957), *Phil. Mag.* **8,2**, 704.
- Bartlett J.T., Mitchell J.W. (1958), *Phil. Mag.* **8,3**, 334.
- Bartlett J.T., Mitchell J.W. (1960a), *Phil. Mag.* **8, 5**, 445.
- Bartlett J.T., Mitchell J.W. (1960b), *Phil. Mag.* **8, 5**, 799.
- Bartlett J.T., Mitchell J.W. (1961), *Phil. Mag.* **8, 6**, 271.
- Bertocci U., Bertocci C., Young F.W. (1969), *J. Appl. Phys.* **40, 4**, 1674.
- Bever M.B., Holt D.L., Titchener A.L. (1973), *The Stored Energy of Cold Work*, Pergamon.
- Beyer W.H. (1979), *Standard Mathematical Tables*, 25th Edition, CRC Press, 143.
- Blank E., Stoloff N.S. (1987), *Act. Metall.* **35, 9**, 2255.
- Boyer H.E., Gall T.L. Editors (1985), *Metals Handbook, Desk Edition* , A.S.M..
- Brady L.E., Castle J.W., Hamilton J.F. (1968), *Appl. Phys. Let.* **13**, 2,7 6.
- Breinan E.M., Thompson E.R., Tice W.K. (1972), *Metall. Trans.* **3**, 211.
- Brown L.M. (1961), *Phys. Stat. Sol.* **1**, 585.
- Brown L.M., Stobbs W.M. (1971), *Phil. Mag.* **23**, 1201.
- Brown L.M., Woolhouse G.R. (1970), *Phil. Mag.* **21**, 329.
- Bullough R., Newman R.C. (1960), *Phil. Mag.* **8**, 921.
- Carnahan R.D., Johnston T.L., Stokes R.J., Li C.H. (1961), *Trans. Met. Soc. AIME* **221**, 45.
- Castle J.W. (1957), *J. Appl. Phys.* **28, 6**, 743.

- Chawla K.K., Metzger M. (1972), *J. Mat. Sci.* 7, 34.
- Chawla K.K., Metzger M. (1977), *Metall. Trans.* 8A, 1680.
- Childs C.B., Slifkin L.M. (1960), *Phys. Rev. Let.* 5,11, 502.
- Childs C.B., Slifkin L.M. (1965), *Brit. J. Appl. Phys.* 16, 771.
- Chin E.S.C. (1987), *Report # MTL TR 97-7*, U.S. Army Materials Technology Laboratory, Watertown MA.
- Christman T., Suresh S. (1988), *Acta Metall.* 36, 1691.
- Clark P.V., Mitchell J.W. (1956), *J. Phot. Sci.* 4, 1.
- Compton W.D., Maurer R.J. (1956), *Phys. Chem. Sol.* 1, 191.
- Cottrell A.H., Aytakin V. (1950), *J. Inst. Met.* 77, 389.
- Cox H.L. (1952), *Brit. J. Appl. Phys.* 3, 72.
- de Silva A.R.T., Chadwick G.A. (1969), *J. Mech. Phys. Solids* 17, 387.
- Dietz P.R. (1986), *Proceedings of the International Symposium on Photoelasticity, Tokyo 1986*, Nisida and Kawata Eds., Springer, 31.
- Dow N.F. (1963), *General Electric Report R. 63SD61*. Reported by Kelly and Macmillan (1986).
- Dutta I., Bourell D.L., Latimer D. (1988), *J. Comp. Mat.* 22, 829.
- Earmme Y.Y., Johnson W.C. (1981), Lee J.K., *Metall. Trans.* 12A, 1521.
- Eikum A., Thomas G. (1964), *Acta Metall.* 12, 537.
- Eshelby J.D. (1957), *Proc. Roy. Soc.* A241, 376.
- Flom Y., Arsenault R.J. (1985), *Mat. Sci. Eng.* 75, 151.
- Fox S., Flower H.M. (1987), Private communication.
- Frieser H., Haase G., Klein E. Ed. (1968), *Die Grundlagen der photographischen Prozesse mit Silberhalogeniden, 1-3*, Akademische Verlagsgesellschaft, 48.
- Frost H.J., Ashby M.F.(1982), *Deformation-Mechanism Maps*, Pergamon Press.
- Funk W., Blank E. (1988), *Metall. Trans.* 19A, 987.
- Garmong G. (1974), *Metall. Trans.* 5, 2183.
- Garmong G., Williams J.C. (1975), *Metall. Trans.* 6A,1711.
- Gmelins Institut Editor (1971),*Gmelins Handbuch der anorganischen Chemie: Silber B1* , Verlag Chemie.
- Gmelins Institut Editor (1972),*Gmelins Handbuch der anorganischen Chemie: Silber B2* , Verlag Chemie.
- Goodman L.E., Sutherland J.G. (1953), *J. Appl. Phys.* 24, 5, 577.
- Gould D., Hirsch P.B., Humphreys F.J. (1974), *Phil. Mag.* 30, 1353.
- Haasen P., Skrotski W. (1981), *J. de Physique* 42, C3-119.
- Hamilton J.F. (1967), *Phil. Mag.* 8, 16, 1.
- Hamilton J.F., Hamm F.A., Brady L.E. (1956), *J. Appl. Phys.* 27, 8, 874.
- Hancock J.R. (1967), *J. Comp. Mat.* 1, 136.
- Hancock J.R., Grosskreutz J.C. (1968), *Metal Matrix Composites*, ASTM, 134.
- Hansen N. (1977), *Acta Metall.* 25, 863.
- Harding J., Taya M., Derby B., Pickard S. (1987), *Sixth International Conference on Composite Materials*, Matthews et al. Ed., 2.224.
- Haynes J.R., Shockley W. (1951), *Phys. Rev.* 82, 6, 935.
- Head A.K. (1959), *Phil. Mag.* 4, 295.
- Hedges J.M., Mitchell J.W. (1953a), *Phil. Mag.* 7, 44, 223.
- Hedges J.M., Mitchell J.W. (1953b), *Phil. Mag.* 7, 44, 357.

- Hidshaw W., Lewis J.T., Briscoe C.V. (1967), *Phys. Rev.* **2**, 876.
- Hill R. (1950), *The Mathematical Theory of Plasticity*, Oxford.
- Hirsch P.B. (1957), *J. Inst. Met.* **86**, 7.
- Hirsch P.B., Humphreys F.J. (1970), *Proc. Roy. Soc.* **318A**, 45.
- Hirth J.P., Lothe J. (1982), *Theory of Dislocations*, 2nd Edition, Wiley-Interscience, 752.
- Hoffman C.A. (1973), *J. Eng. Mat. Tech.* **95**, 55.
- Hohne M. (1964), *Phys. Stat. Sol.* **7**, 869.
- Honeycombe R.W.K. (1984), *The Plastic Deformation of Metals*, 2nd Edition, ASM, 197
- Hull D., Bacon D.J. (1984), *Introduction to Dislocations*, 3rd Ed., Pergamon, 166.
- Humphreys F.J. (1988), *Ninth Risø International Symposium on Metallurgy and Materials Science*, Andersen et al. Ed., Risø National Laboratory, 51.
- Humphreys F.J., Hirsch P.B. (1970), *Proc. Roy. Soc.* **318A**, 73.
- Humphreys F.J., Hirsch P.B. (1976), *Phil. Mag.* **34**, 373.
- in der Schmitt W., Haasen P. (1961), *J. Appl. Phys.* **32**, 1790.
- Javornicky J. (1974), *Photoplasticity*, Elsevier.
- Johnson W.C., Lee J.K. (1983), *Acta Metall.* **31**, 1033.
- Johnston W.G. (1955), *Phys. Rev.* **98**, 1777.
- Jones D.A., Mitchell J.W. (1957), *Phil. Mag.* **8**, 2, 1047.
- Jones D.A., Mitchell J.W. (1958), *Phil. Mag.* **3**, 1, 1.
- Kanzaki H. (1955), *Phys. Rev.* **99**, 1888.
- Kanzaki H. (1956a), *J. Phys. Soc. Jap.* **11**, 2, 120.
- Kanzaki H. (1956b), *J. Phys. Soc. Jap.* **11**, 2, 126.
- Keh A.S. (1962), *Direct Observation of Imperfections in Crystals*, Interscience, 213.
- Kelly A., Macmillan N.H. (1986a), *Strong Solids*, Oxford Sci. Publi., 263-4.
- Kelly A., Macmillan N.H. (1986b), *ibid.*, 392.
- Kim C.T., Lee J.K., Plichta M.R. (1990a), *Metall. Trans.* **21A**, 673.
- Kim C.T., Plichta M.R., Lee J.K. (1990b). *Fundamental Relationships between Microstructure and Mechanical Properties of Metal Matrix Composites*, Liaw & Gungor Eds., TMS, 371.
- Kinsman K.R., Sprys J.W., Asaro R.J. (1975), *Acta Metall.* **23**, 1431.
- Kittel C. (1983), *Einführung in die Festkörper Physik*, 6. Auflage, 577.
- Kroupa F. (1960), *Czech. J. Phys.* **10**, 284.
- Kuznetsov B.A. (1956), *Sov. Phys.-Tech. Phys.* **1**, 1570.
- Landau L.D., Lifshitz E.M. (1959), *Theory of Elasticity*, Pergamon, 29.
- Lang A.R. (1959), *J. Appl. Phys.* **30**, 11, 1748.
- Lawley A., Gaigher H.L. (1963), *Phil. Mag.* **8**, 1713.
- Layer H., Miller M.G., Slifkin L.M. (1962), *J. Appl. Phys.* **33**, 1, 478.
- Lee J.K., Earmme Y.Y., Aaronson H.I., Russell K.C. (1980), *Metall. Trans.* **11A**, 1837.
- Lewis M.H., Martin J.M. (1963), *Acta Metall.* **11**, 1207.
- Li Q., Megusar J., Masur L.J., Cornie J.A. (1989), *Mat. Sci. Eng.* **A117**, 199.
- Liu J.S., Balluffi R.W. (1984), *Mat. Res. Soc. Symp. Proc.* **25**, 261.
- Liu Y.L., Hansen N., Jensen D.J. (1989), *Metall. Trans.* **20A**, 1743.

- Livingston J.D. (1962), *Acta Metall.* **10**, 229.
- Mader S., Seeger A., Thieringer H. (1963), *Conference on the Relation Between Structure and Strength in Metals and Alloys*, Tedington.
- Makenas B.J., Birnbaum H.K. (1980), *Acta Metall.* **28**, 979.
- Matta K.M., Vavrinec E. (1970), *Czech. J. Phys.* **B 20**, 284.
- Matejec R. (1961), *Z. wiss. Photogr.* **55**, 121.
- Matejec R. (1962), *Z. Elektrochem.* **66**, 326.
- Mees E.K., James T.H. (1966), *The Theory of Photographic Process*, Third Edition, Macmillan.
- Mitchell J.W. (1957), *Dislocations and Mechanical Properties of Crystals*, Wiley, 69.
- Mitchell J.W. (1957b), *Rep. Prog. Phys.* **20**, 433.
- Mitchell J.W. (1958), *Growth and Perfection of Crystals*, J. Wiley, 386.
- Mitchell J.W. (1959), *Faraday Soc. Disc.* **28**, 242.
- Mitchell J.W. (1962), *Direct Observation of Imperfections in Crystals*, Interscience, 3.
- Mitchell J.W. (1980), *Proc. Roy. Soc. Lond.* **A371**, 149.
- Mitchell J.W. (1983), *J. Phot. Sci.* **31**, 227.
- Mitchell J.W. (1987a), *J. Imag. Sci.* **31**, 1, 1.
- Mitchell J.W. (1987b), *J. Imag. Sci.* **31**, 6, .
- Mitchell J.W. (1988), private communication.
- Mori T., Taya M. (1986), *Composites '86: Recent Advances in Japan and the United States*, Kawata et al. Ed., Japan Society for Composite Materials, 563.
- Newkirk J.B. (1959), *Phys. Rev.* **6**, 1465.
- Ninomiya T., Sonoike S. (1958), *Photographic Sensitivity*, Tokyo Symposium, Maruzen, 81.
- Nye J.F. (1948), *Nature* **4088**, 367.
- Nye J.F. (1949a), *Proc. Roy. Soc. A* **198**, 190.
- Nye J.F. (1949b), *Proc. Roy. Soc. A* **200**, 47.
- Nye J.F., Spencer R.D., Sprackling M.T. (1957), *Phil. Mag.* **8**, 2, 772.
- Ogin S.L., Brown L.M. (1980), *Dislocation Modelling of Physical Systems*, Bullough et al. Ed., 579.
- Parasnis A.S., Frank F.C., Mitchell J.W. (1963), *Phil. Mag.*, 1503.
- Parasnis A.S., Mitchell J.W. (1959), *Phil. Mag.* **8**, 4, 171.
- Pashley D.W. (1950), *Acta Cryst.* **3**, 163.
- Pattnaik A., Lawley A. (1974), *Met. Trans.* **5**, 111.
- Pedersen O.B. (1988), *Ninth Riso International Symposium on Metallurgy and Materials Science*, Andersen et al. Ed., Risø National Laboratory, 157.
- Phan Thien N. (1979), *Fibre Sci. Tech.* **12**, 235.
- Pinnel M.R., Lawley A. (1970), *Met. Trans.*, **1**, 1337.
- Pinnel M.R., Lawley A. (1971), *Met. Trans.*, **2**, 1415.
- Pratt P.L. (1958), *Vacancies and Other Point Defects in Metals*, Inst. Met. at AERE, Harwell, 99.
- Puls M.P., So C.B. (1980), *Phys. Stat. Sol.* **98A**, 87.
- Rawal S.P., Allard L.F., Misra M.S. (1986), *Interfaces in Metal Matrix Composites*, A.K. Dhingra and S.G. Fishman Eds., A.I.M.E., 211.

- Rawal S.P., Allard L.F., Misra M.S. (1987), *Sixth International Conference on Composite Materials*, Matthews, Buskell, Hodginson Eds., Elsevier, 2.169.
- Rühle M., Evans A.G. (1988), *High Temperature/High Performance Composites*, *Mat. Res. Soc. Symp. Proc.*, 120, 293.
- Schneider G.J., Conway H.D. (1969), *J. Comp. Mat.* 3, 116.
- Schuster D.M., Scala E. (1964), *Trans. Met. Soc. AIME* 230, 1635.
- Shimotomai M., Hasiguti R.R. (1979), *Jap. Inst. Met. J.*, 43, 292.
- Skillman D.C., Berry C.R. (1964), *Phot. Sci. and Eng.*, 8, 2, 65.
- Slifkin L.M., Childs C.B. (1961), *Bull. Am. Phys. Soc.*, 2, 6, 23.
- Sprackling M.T. (1960), *Phil. Mag.* 8, 5, 441.
- Sprackling M.T. (1964), *Phil. Mag.* 9, 739.
- Sprackling M.T. (1966), *Phil. Mag.* 13, 1293.
- Sprackling M.T. (1968), *Phil. Mag.* 18, 691.
- Sprackling M.T. (1976), *The Plastic Deformation of Simple Ionic Crystals*, Academic Press.
- Sprackling M.T. (1980), *J. Phot. Sci.* 28, 189.
- Stanford-Beale C.A., Clyne T.W. (1988), *Ninth Riso International Symposium on Metallurgy and Materials Science*, Andersen et al. Ed., Riso National Lab., 479.
- Stepanov A.V., Eidus I.M. (1955), *Zh. Eksperim. i Teor. Fiz.*, 29, 669.
- Stepanow A.W. (1934), *Phys. Z. Sowjet.* 6, 312.
- Stepanow A.W. (1935), *Phys. Z. Sowjet.* 8, 25.
- Stohr J.F., Khan T. (1982), *Introduction aux matériaux composites vol. 2*, Naslain Ed., CNRS, 263.
- Stowell M. J. (1962), *Phil. Mag.* 8, 7, 677.
- Süptitz P. (1958), *Z. fur Phys.* 153, 174.
- Süptitz P. (1959), *Z. Elektrochem.* 63, 400.
- Tanaka K., Mori T. (1972), *J. Elasticity* 2, 199.
- Taya M., Mori T. (1987), *Acta Met.* 35, 155.
- Taylor G.I. (1934), *Proc. Roy. Soc.* 145A, 362.
- Tyson W.R., Davies G.J. (1965), *Brit. J. Appl. Phys.* 16, 199.
- Underwood E.E. (1970), *Quantitative Stereology*, Addison Wesley, 90.
- Underwood E.E. (1972), *J. Microscopy* 95, 25-44.
- Vallin J. (1967), *Arkiv. Fysik.* 34, 367.
- Vavra F. (1969), *Czech. J. Phys.* 19B, 776.
- Venables J.A. (1962), *Phil. Mag.* 7, 1969.
- Vogelsang M., Arsenault R.J., Fisher R.M. (1986), *Metall. Trans.* 17A, 379.
- Walter J.L. (1982), *In Situ Composites IV*, Lemkey et al. Ed., Elsevier, 85.
- Walter J.L., Cline H.E., Koch E.F. (1969), *Trans. AIME* 245, 2073.
- Webb J.H. (1955), *J. Appl. Phys.* 26, 11, 1309.
- Williams D.R., Fine M.E. (1985), *Fifth International Conference on Composite Materials*, Harrigan et al. Ed., 639.
- Williams J.C., Garmong G. (1975), *Metall. Trans* 6A, 1699.
- Zhitnikov R.A., Stepanov A.V. (1958a), *Sov. Phys.-Tech. Phys.* 3, 2004.
- Zhitnikov R.A., Stepanov A.V. (1958b), *Sov. Phys.-Tech. Phys.* 3, 2011.
- Zhitnikov R.A., Stepanov A.V. (1958c), *Sov. Phys.-Tech. Phys.* 3, 2048.
- Zhitnikov R.A., Stepanov A.V. (1958d), *Sov. Phys.-Tech. Phys.* 3, 2055.